UiT
THE ARCTIC
UNIVERSITY
OF NORWAY

Faculty of Science and Technology
Department of Physics and Technology

KAIRA — The Kilpisjärvi Atmospheric Imaging Receiver Array

Design, operations and first scientific results

—

Derek McKay

A dissertation for the degree of Philosophiae Doctor – May 2018

Abstract

The Kilpisjärvi Atmospheric Imaging Receiver Array (KAIRA) is a phased-array radio detector located in Arctic Finland, where auroral electron precipitation is common. This unique deployment of a modern radio telescope in an unconventional location has resulted in a novel and powerful instrument capable of carrying out a large variety of remote-sensing, geoscience experiments. This work presents a selection of these and introduces the interferometric imaging riometry method. This new technique has been utilised to investigate high-energy particle precipitation and the dynamic structural variation of the D region of the ionosphere. Observations rely on the measurement of incoming cosmic radio noise emissions (typically Galactic synchrotron emission in the 20–60 MHz range) resulting in a spatially continuous radiogram of the entire sky. The map of the received power at each time may then be compared to the equivalent map from geomagnetically quiescent conditions, allowing the morphology of ionospheric radio absorption to be ascertained. The first such interferometric imaging riometry was carried out using KAIRA in late 2013 and, since then, multi-frequency and high time resolution capability has been added. Using all-sky interferometry gives distinct advantages for absorption measurements. The spatial coverage is continuous, preventing uneven areas of sensitivity on the sky, which is a limitation for multi-beam riometers. Unlike optical techniques, it is optimal at lower altitudes (D Region) and its use of radio frequencies means that it can make measurements during daylight (including the midnight-sun season) and cloudy conditions. The imaging method reduces the effects of radio-frequency interference (RFI), as transmitters can be localised and their signals thus excised from the data. The same benefit also applies to the ionospheric scintillation of the cosmic radio sources Cas A and Cyg A, although the strong and temporal nature of the fluctuations poses some limitations. A multi-frequency, software-based correlator is described. The use of multi-frequency riometry for the determination of three-dimensional electron density mapping has been considered. However, it is concluded that unambiguous altitude profiles of electron density cannot be obtained. Since the commencement of operations, a large data set of many auroral substorms has been accumulated, with events being compared to co-located, co-temporal observations made at optical wavelengths. The results, in conjunction with the energy-derivation based on the optical observations, indicate discrepancies in our current understanding and have led to the discovery of unexpected electron precipitation.

Tiivistelmä

KAIRA eli Kilpisjärvi Atmospheric Imaging Receiver Array on Pohjois-Suomessa Kilpisjärvellä sijaitseva vaiheistettuihin antenniryhmiin perustuva radiovastaanotin. Alueella revontulet ja niihin liittyvät elektronipresipitaatio on yleistä. KAIRA on moderni radioteleskooppi epätyypillisessä paikassa, mikä on mahdollistanut useiden uusien kaukokartoitus- ja geofysikaalisten kokeiden kehittämisen. Tässä työssä esitellään näitä kokeita sekä niin kutsuttu interferometrisen kuvantavan riometrin menetelmä. Tätä uutta tekniikkaa on hyödynnetty korkeaenergisten hiukkasten presipitaation tutkimukseen ja ionosfäärin D-kerroksen dynaamisen rakenteen vaihtelun selvittämiseen. Havainnot perustuvat kosmisen radiokohinan emissioiden mittaamiseen (tyypillisesti galaktista synkrotroniemissiota taajuusalueella 20–60 MHz), jonka lopputuloksena saadaan spatiaalisesti jatkuva koko taivaan radiogrammi. Vertaamalla koko taivaan hetkellistä radiokuvaa geomagneettisesti hiljaisten jaksojen keskiarvokarttoihin päästään tutkimaan kosmisen säteilyn absorptiota ilmakehässä. Ensimmäinen tämänkaltainen kuvantaminen toteutettiin KAIRAlla vuoden 2013 loppupuolella. Sen jälkeen monitaajuisen ja korkean aikaresoluution kapasiteettia on lisätty. Koko taivaan interferometrian käyttö tarjoaa selkeitä etuja absorption mittaamiseen. Perinteisten kuvantavien riometrien absorptiokartoissa mittausherkkyys jakautuu epätasaisesti riometrikeilojen paikkojen ja kokojen vaikutuksesta. Inteferometrisen absorptiokartan herkkyysjakauma on tasainen, sillä erillisiä keiloja ei ole. Radiotekniikka sopii ihanteellisesti ionosfäärin alempien kerrosten mittaamiseen. Toisin kuin optisia revontulihavaintoja, ilmakehän radioaaltomittauksia voidaan tehdä myös päiväsaikaan (mukaan lukien kesän yöttömän yön kausi) ja pilvisissä olosuhteissa. Kuvantamismenetelmä vähentää radiohäiriöiden vaikutuksia, koska häiriölähteet voidaan paikantaa ja näin ollen niiden signaalit voidaan poistaa aineistosta. Sama hyöty saadaan myös kosmisten säteilylähteiden Cas A ja Cyg A aiheuttaman skintillaation suhteen, vaikkakin vaihteluiden voimakkuus ja aikariippuvainen luonne asettaa joitakin rajoitteita. Työssä arvioidaan myös monitaajuisen, ohjelmistopohjaisen käyttökelpoisuutta kolmiulotteisen elektronitiheyden ratkaisumenetelmänä. Tulokset osoittavat, ettei elektronitiheyden korkeusjakaumaa voida määrittää yksikäsitteisesti. KAIRAn toiminnan aloittamisen jälkeen revontulipurkauksista on karttunut laaja aineisto, jota on verrattu optisilla aallonpituuksilla tehtyihin samanaikaisiin havaintoihin. Tulokset osoittavat puutteita nyky-ymmärryksessämme ja ne ovat johtaneet energeettisen elektronipresipitaation havaitsemiseen jo ennen revontulipurkauksen alkua.

Sammendrag

Kilpisjärvi Atmospheric Imaging Receiver Array (KAIRA) er en fasestyrt radiomottaker i arktisk Finland, hvor elektronnedbør ofte observeres i forbindelse med nordlys. Denne unike plasseringen av et radioteleskop, på et ukonvensjonelt sted, har resultert i et nytt og kraftig verktøy for fjernmåling, egnet for et stort spenn av eksperimenter innen geovitenskap. I denne avhandlingen presenteres et utvalg av disse eksperimentene og en metode for interferometrisk avbildende riometri introduseres. Denne teknikken blir brukt for å studere høyenergetisk partikkelnedbør og den dynamiske strukturvariasjonen av D-laget i ionosfæren. Observasjonene benytter den kosmiske bakgrunnsstrålingen (typisk galaktisk synkrotronstråling i området 20–60 MHz) til å danne et romlig kontinuerlig radiogram av hele himmelen. Radiogrammet kan så sammenlignes med tilsvarende målinger gjort under rolige geomagnetiske forhold, for å identifisere morfologien til absorpsjonen av radiobølger i ionosfæren. Den første av disse avbildningsstudiene ble utført med KAIRA i slutten av 2013. Siden da har kapasiteten til instrumentet blitt utvidet med flere frekvenser og høyere tidsoppløsning. All-sky-interferometri har betydelige fordeler fremfor tradisjonelle multi-stråle riometre siden den romlige dekningen er kontinuerlig, og den romlige variasjonen i følsomhet er fraværende. I motsetning til optiske teknikker er denne teknikken optimal for lavere høyder (D-laget), og på grunn av bruken av radiofrekvenser kan eksperimenter også foregå i dagslys (inkludert midnattssol) og uavhengig av skydekke. Avbildningmetoden reduserer effekten av interferens, siden radiosendere kan lokaliseres og signalet fra dem dermed ekskluderes fra målingene. De samme fordelene gjelder også for ionosfærisk scintillasjon av signalet fra de sterke radiokildene Cas A og Cyg A, selv om dette begrenses noe av de store variasjonene i signalstyrken fra dem. En programvarebasert multifrekvens-korrelator er beskrevet. Bruken av multifrekvens-rionometri for bestemmelse av tredimensjonal avbildning av elektrontetthet er diskutert med en redegjørelse for hvorfor teknikken ikke kan brukes til å produsere entydige høydeprofiler av elektrontetthet. Siden de første målingene har et stort datasett med mange aktive nordlyshendelser (substorm'er) blitt samlet og videre sammenlignet med samtidige og samlokaliserte optiske observasjoner. Resultatene, i sammenheng med energiberegninger basert på de optiske målingene, viser avvik i vår nåværende forståelse av nordlyshendelser og har ført til oppdagelsen av uventet elektronnedbør.

Contents

Preface

"Watch the skies, traveller."
— Skyrim

This thesis is the result of the long intertwining of various strands of development. After an extended time working in astrophysics, observatory operations and telescope engineering, I had participated in the design study phase of the next generation incoherent scatter radar project : EISCAT_3D. Together with Ian McCrea, I was editor for the final report, bringing together the collective results of all the different aspects of that programme. This had brought me into contact not only with Arctic geophysics, but also with the members of the EISCAT community — both engineering and scientific. Following that project I returned to astrophysics. In 2009, I become involved in the LOFAR-UK project and took over as project manager for the construction and commissioning of that facility in 2010. The LOFAR station UK608 at Chilbolton, England, was successfully completed and was officially opened by Dame Jocelyn Bell Burnell on 20 September 2010.

Meanwhile, the EISCAT_3D project had continued, and had reached the point of building prototypes and demonstrators. Sodankylä Geophysical Observatory had applied for, and was awarded, a grant from the European Regional Development Funds of Lapland, supplemented by funding from the University of Oulu, in order to build a LOFAR-type facility in northern Finland for the testing of concepts related to the EISCAT_3D preparatory phase.

Because of my earlier involvement with EISCAT, and the experience gained from the recently completed LOFAR-UK facility, I was invited by Sodankylä Geophysical Observatory to oversee the design and construction. Thus began my involvement with the KAIRA project from those very early stages through to the demonstration of incoherent scatter radar detections in late 2012 and the subsequent official opening of the facility by Rector Lauri Lajunen on 6 June 2013.

During that time, it was recognised that KAIRA could be used to carry out a number of other geophysical experiments. I realised that the interferometric aperture synthesis imaging used in radio astronomy could be applied to the ionospheric measurement technique of riometry. This became the core concept of this thesis.

Overview of this thesis

Chapter 1 provides a very brief overview of the radio observational history of the ionosphere leading up to the existing EISCAT incoherent scatter radar facilities and EISCAT_3D (McCrea et al., 2015). This establishes the context for the KAIRA project, and a description of it is provided in Chapter 2. Although KAIRA was initially conceived as an EISCAT_3D technical demonstrator, it could also be applied to many other radio observations. These range from middle-atmospheric measurements to radio astronomy. Chapter 3 provides a sampler of these programmes and explains how KAIRA contributes to scientific advances in these areas.

One of the significant types of experiments that KAIRA can perform is the measurement of ionospheric cosmic noise absorption. The theory for this technique, known as riometry, is described in Chapter 4, which also explains the advantages of conducting riometric measurements at multiple frequencies. Consideration is given to whether the determination of electron density profiles can be attempted using an inverse problem technique. The core thesis of this dissertation is the development of a new method of conducting cosmic noise absorption measurements using interferometric aperture synthesis imaging. Chapter 5 explains this melding of phased-array interferometric imaging with the riometric technique and demonstrates a selection of observations. The limitations and ancillary techniques are also described. In Chapter 6, the method is applied to the study of the aurora. A discussion of future work, the conclusions and references follow thereafter.

Then included are three peer-reviewed journal papers and one conference paper, which contain the scientific contributions of this thesis.

The deployment of a phased-array radio telescope in an Arctic location for the purposes of geophysical measurement has resulted in a number of interesting observations from a technical perspective. It is important to include this development process and design decisions, as they pertain equally to future installations of a similar nature — not least, the EISCAT_3D project itself. These accounts are therefore provided as appendices.

A complete list of the abbreviations used is given in Appendix A. Tables of the technical parameters of KAIRA, are likewise provided as appendices.

Derek McKay,
Tromsø, 2018

List of papers

This thesis consists of a subject introduction (with supplementary material included in appendices) and the following peer-reviewed scientific papers:

I McKay-Bukowski, D., *et al.* (2015) *KAIRA: The Kilpisjärvi Atmospheric Imaging Receiver Array — System Overview and First Results*, in IEEE Transactions on Geoscience and Remote Sensing, 53, 3, 1440–1451, March 2015.
doi: 10.1109/TGRS.2014.2342252.

II McKay, D., R. Fallows, M. Norden, A. Aikio, J. Vierinen, F. Honary, S. Marple, and T. Ulich (2015), *All-sky interferometric riometry*, Radio Sci., 50, 1050–1061, October 2015. doi:10.1002/2015RS005709.

III McKay, D., N. Partamies, J. Vierinen (2018), *Pulsating aurora and cosmic noise absorption associated with growth-phase arcs*, Annales Geophysicae, 36, 59–69, January 2018, doi:10.5194/angeo-36-59-2018.

A fourth article is also included. It is a conference paper, but one which contains relevant material to this thesis topic, supplementing the techniques described herein. This paper is:

IV McKay, D., N. Partamies, K. Kauristie (2017), *Acquisition of optical and riometric keograms for studying auroral electron precipitation*, in: XVIII Geofysiikan Päivät, Geofysiikan seura r.y., 35–38, 2017 available at: `https://geofysiikanseura.yhdistysavain.fi/@Bin/174016/GFP2017_kirja.pdf`

In the text, these first-author papers will be referred to by their Roman numerals.

Additional publications

Throughout his career, the author has been author or co-author to numerous papers, reports and circulars on a variety of scientific topics. The following publications (listed alphabetically, by first author) are a small subset of those, and include only works which are relevant to KAIRA and the application of KAIRA to geoscience, and which were completed during the duration of the PhD programme. In addition, the author has written many technical documents for the KAIRA construction and project management, which are part of the KAIRA technical documentation archive, held at Sodankylä Geophysical Observatory and Rutherford Appleton Laboratory.

1. Chau, J. L., **McKay, D.**, Vierinen, J. P., La Hoz, C., Ulich, T., Lehtinen, M., and Latteck, R.: Multi-static spatial and angular studies of polar mesospheric summer echoes combining MAARSY and KAIRA, Atmospheric Chemistry and Physics Discussions, 2018, 1–23, doi: 10.5194/acp-2018-210, URL `https://www.atmos-chem-phys-discuss.net/acp-2018-210/`, 2018.

2. Fallows, R. A., Coles, W. A., **McKay-Bukowski, D.**, Vierinen, J., Virtanen, I. I., Postila, M., Ulich, T., Enell, C.-F., Kero, A., Iinatti, T., Lehtinen, M., Orispää, M., Raita, T., Roininen, L., Turunen, E., Brentjens, M., Ebbendorf, N., Gerbers, M., Grit, T., Gruppen, P., Meulman, H., Norden, M. J., de Reijer, J.-P., Schoenmakers, A., and Stuurwold, K.: Broadband meter-wavelength observations of ionospheric scintillation, Journal of Geophysical Research (Space Physics), 119, 10 544, doi: 10.1002/2014JA020406, 2014.

3. Garsden, H., Girard, J. N., Starck, J. L., Corbel, S., Tasse, C., Woiselle, A., McKean, J. P., van Amesfoort, A. S., Anderson, J., Avruch, I. M., Beck, R., Bentum, M. J., Best, P., Breitling, F., Broderick, J., Brüggen, M., Butcher, H. R., Ciardi, B., de Gasperin, F., de Geus, E., de Vos, M., Duscha, S., Eislöffel, J., Engels, D., Falcke, H., Fallows, R. A., Fender, R., Ferrari, C., Frieswijk, W., Garrett, M. A., Grießmeier, J., Gunst, A. W., Hassall, T. E., Heald, G., Hoeft, M., Hörandel, J., van der Horst, A., Juette, E., Karastergiou, A., Kondratiev, V. I., Kramer, M., Kuniyoshi, M., Kuper, G., Mann, G., Markoff, S., McFadden, R., **McKay-Bukowski, D.**, Mulcahy, D. D., Munk, H., Norden, M. J., Orru, E., Paas, H., Pandey-Pommier, M., Pandey, V. N., Pietka, G., Pizzo, R., Polatidis, A. G., Renting, A., Röttgering, H., Rowlinson, A., Schwarz, D., Sluman, J., Smirnov, O., Stappers, B. W., Steinmetz, M., Stewart, A., Swinbank, J., Tagger, M., Tang, Y.,

Tasse, C., Thoudam, S., Toribio, C., Vermeulen, R., Vocks, C., van Weeren, R. J., Wijnholds, S. J., Wise, M. W., Wucknitz, O., Yatawatta, S., Zarka, P., and Zensus, A.: LOFAR sparse image reconstruction, A&A, 575, A90, doi: 10.1051/0004-6361/201424504, 2015.

4. Grandin, M., Kero, A., Partamies, N., **McKay, D.**, Whiter, D., Kozlovsky, A., and Miyoshi, Y.: Observation of pulsating aurora signatures in cosmic noise absorption data, Geophysical Research Letters, 44, 5292–5300, doi: 10.1002/2017GL073901, URL `http://dx.doi.org/10.1002/2017GL073901`, 2017.

5. Kallunki, J., Uunila, M., and **McKay-Bukowski, D.**: Multi-frequency solar observations at Metsähovi Radio Observatory and KAIRA, Astronomische Nachrichten, 336, 566, doi: 10.1002/asna.201512194, 2015.

6. Kero, A., Vierinen, J., **McKay-Bukowski, D.**, Enell, C.-F., Sinor, M., Roininen, L., and Ogawa, Y.: Ionospheric electron density profiles inverted from a spectral riometer measurement, Geophys. Res. Lett., 41, 5370–5375, doi: 10.1002/2014GL060986, 2014.

7. Mann, G., Breitling, F., Vocks, C., Aurass, H., Steinmetz, M., Strassmeier, K. G., Bisi, M. M., Fallows, R. A., Gallagher, P., Kerdraon, A., Mackinnon, A., Magdalenic, J., Rucker, H., Anderson, J., Asgekar, A., Avruch, I. M., Bell, M. E., Bentum, M. J., Bernardi, G., Best, P., Bîrzan, L., Bonafede, A., Broderick, J. W., Brüggen, M., Butcher, H. R., Ciardi, B., Corstanje, A., Gasperin, F. d., Geus, E. d., Deller, A., Duscha, S., Eislöffel, J., Engels, D., Falcke, H., Fender, R., Ferrari, C., Frieswijk, W., Garrett, M. A., Grießmeier, J., Gunst, A. W., van Haarlem, M., Hassall, T. E., Heald, G., Hessels, J. W. T., Hoeft, M., Hörandel, J., Horneffer, A., Juette, E., Karastergiou, A., Klijn, W. F. A., Kondratiev, V. I., Kramer, M., Kuniyoshi, M., Kuper, G., Maat, P., Markoff, S., McFadden, R., **McKay-Bukowski, D.**, McKean, J. P., Mulcahy, D. D., Munk, H., Nelles, A., Norden, M. J., Orru, E., Paas, H., Pandey-Pommier, M., Pandey, V. N., Pizzo, R., Polatidis, A. G., Rafferty, D., Reich, W., Röttgering, H., Scaife, A. M. M., Schwarz, D. J., Serylak, M., Sluman, J., Smirnov, O., Stappers, B. W., Tagger, M., Tang, Y., Tasse, C., ter Veen, S., Thoudam, S., Toribio, M. C., Vermeulen, R., van Weeren, R. J., Wise, M. W., Wucknitz, O., Yatawatta, S., Zarka, P., and Zensus, J. A.: Tracking of an electron beam through the solar corona with LOFAR, A&A, 611, A57, doi: 10.1051/0004-6361/201629017, 2018.

8. Martin, P. L., Scaife, A. M. M., **McKay, D.**, and McCrea, I.: IONONEST — A Bayesian approach to modeling the lower ionosphere, Radio Science, 51, 1332–1349, doi: 10.1002/2016RS005965, 2016.

9. Szponarski, P., Honary, F., and **McKay-Bukowski, D.**: Climatology of high-latitude ionospheric scintillation based on 38.2 MHz IRIS riometer measurements in Northern Finland, AGU Fall Meeting Abstracts, 2015.

10. **McKay-Bukowski, D.**, Lehtinen, M., Orispää, M., Teppo, T., Turunen, E., Th., U., Vierinen, J., Virtanen, I., Hellgren, H., Sarrala, S., Sutinen, S., Mansikkaniemi, K., Fletcher, M., Solonen, V., Tallkvist, T., Mäkivaara, J., Pulkkinen, J., Tuomi, M., Rantamäki, S., and Johansson, L.: EISCAT_3D Preparatory Phase 7.1 — Final report summarising the work done in WP7, Sodankylä Geophysical Observatory Report, 65, 2014a.

11. **McKay-Bukowski, D.**, Orispää, M., Lehtinen, M., Vierinen, J., Ettus, M., Hellgren, H., Fletcher, M., and Mäkivaara, J.: EISCAT_3D Preparatory Phase 7.1 — Prototype signal processing unit readiness, Sodankylä Geophysical Observatory Report, 64, 2014b.

12. **McKay-Bukowski, D.**, Orispää, M., Teppo, T., Lehtinen, M., Vierinen, J., Hellgren, H., Fletcher, M., Mäkivaara, J., Borg, J., and Johansson, L.: EISCAT_3D Preparatory Phase 7.1 — Field testing and proof of concept, Sodankylä Geophysical Observatory Report, 63, 2014c.

13. Turunen, E., Ulich, T., Orispaa, M., Vierinen, J., Lehtinen, M., Hellgren, H., Makivaara, J., **McKay-Bukowski, D.**, Teppo, T., Virtanen, I., and Fletcher, M.: System development and demo equipment for EISCAT_3D SDR concept, in: 40th COSPAR Scientific Assembly. Held 2-10 August 2014, in Moscow, Russia, Abstract C0.3-9-14., vol. 40 of *COSPAR Meeting*, p. 3424, 2014.

14. van Haarlem, M. P., Wise, M. W., Gunst, A. W., Heald, G., McKean, J. P., Hessels, J. W. T., de Bruyn, A. G., Nijboer, R., Swinbank, J., Fallows, R., Brentjens, M., Nelles, A., Beck, R., Falcke, H., Fender, R., Hörandel, J., Koopmans, L. V. E., Mann, G., Miley, G., Röttgering, H., Stappers, B. W., Wijers, R. A. M. J., Zaroubi, S., van den Akker, M., Alexov, A., Anderson, J., Anderson, K., van Ardenne, A., Arts, M., Asgekar, A., Avruch, I. M., Batejat, F., Bähren, L., Bell, M. E., Bell, M. R., van Bemmel, I., Bennema, P., Bentum, M. J., Bernardi, G., Best, P., Bîrzan, L., Bonafede, A., Boonstra, A.-J., Braun, R., Bregman, J., Breitling, F., van de Brink, R. H., Broderick, J., Broekema, P. C., Brouw, W. N., Brüggen, M., Butcher, H. R., van Cappellen, W., Ciardi, B., Coenen, T., Conway, J., Coolen, A., Corstanje, A., Damstra, S., Davies, O., Deller, A. T., Dettmar, R.-J., van Diepen, G., Dijkstra, K., Donker, P., Doorduin, A., Dromer, J., Drost, M., van Duin, A., Eislöffel, J., van Enst, J., Ferrari, C., Frieswijk, W., Gankema, H., Garrett, M. A., de Gasperin, F., Gerbers, M., de Geus, E., Grießmeier, J.-M., Grit, T., Gruppen, P., Hamaker, J. P., Hassall, T., Hoeft, M., Holties, H. A., Horneffer, A., van der Horst, A., van Houwelingen, A., Huijgen, A., Iacobelli, M., Intema, H., Jackson, N., Jelic, V., de Jong, A., Juette, E., Kant, D., Karastergiou, A., Koers, A., Kollen, H., Kondratiev, V. I., Kooistra, E., Koopman, Y., Koster, A., Kuniyoshi, M., Kramer, M., Kuper, G., Lambropoulos, P., Law, C., van Leeuwen, J., Lemaitre, J., Loose, M., Maat, P., Macario, G., Markoff, S., Masters, J., McFadden, R. A., **McKay-Bukowski, D.**, Meijering, H., Meulman, H., Mevius, M., Middelberg, E., Millenaar, R., Miller-Jones, J. C. A., Mohan, R. N., Mol, J. D., Morawietz, J., Morganti, R., Mulcahy, D. D., Mulder, E., Munk, H., Nieuwenhuis, L., van Nieuwpoort, R., Noordam,

J. E., Norden, M., Noutsos, A., Offringa, A. R., Olofsson, H., Omar, A., Orrú, E., Overeem, R., Paas, H., Pandey-Pommier, M., Pandey, V. N., Pizzo, R., Polatidis, A., Rafferty, D., Rawlings, S., Reich, W., de Reijer, J.-P., Reitsma, J., Renting, G. A., Riemers, P., Rol, E., Romein, J. W., Roosjen, J., Ruiter, M., Scaife, A., van der Schaaf, K., Scheers, B., Schellart, P., Schoenmakers, A., Schoonderbeek, G., Serylak, M., Shulevski, A., Sluman, J., Smirnov, O., Sobey, C., Spreeuw, H., Steinmetz, M., Sterks, C. G. M., Stiepel, H.-J., Stuurwold, K., Tagger, M., Tang, Y., Tasse, C., Thomas, I., Thoudam, S., Toribio, M. C., van der Tol, B., Usov, O., van Veelen, M., van der Veen, A.-J., ter Veen, S., Verbiest, J. P. W., Vermeulen, R., Vermaas, N., Vocks, C., Vogt, C., de Vos, M., van der Wal, E., van Weeren, R., Weggemans, H., Weltevrede, P., White, S., Wijnholds, S. J., Wilhelmsson, T., Wucknitz, O., Yatawatta, S., Zarka, P., Zensus, A., and van Zwieten, J.: LOFAR: The LOw-Frequency ARray, A&A, 556, A2, doi: 10.1051/0004-6361/201220873, 2013.

15. Vierinen, J., Ulich, T., Raita, T., **McKay-Bukowski, D.**, and Lehtinen, M.: Kilpisjärvi Atmospheric Imaging Receiver Array, in: 39th COSPAR Scientific Assembly, vol. 39 of *COSPAR Meeting*, p. 2089, 2012.

16. Vierinen, J., **McKay-Bukowski, D.**, Lehtinen, M., Kero, A., and Ulich, T.: Kilpisjärvi Atmospheric Imaging Receiver Array — First results, in: Phased Array Systems & Technology, 2013 IEEE International Symposium on, pp. 664–668, doi: 10.1109/ARRAY.2013.6731909, 2013.

17. Vierinen, J., Lehtinen, M., and **McKay-Bukowski, D.**: EISCAT_3D Preparatory Phase 7.1 — Proposed implementation of digital signal processing, Sodankylä Geophysical Observatory Report, 62, 2014.

18. Virtanen, I. I., **McKay-Bukowski, D.**, Vierinen, J., Aikio, A., Fallows, R., and Roininen, L.: Plasma parameter estimation from multistatic, multibeam incoherent scatter data, Journal of Geophysical Research (Space Physics), 119, 10 528, doi: 10.1002/2014JA020540, 2014.

19. Zucca, P., Morosan, D. E., Rouillard, A. P., Fallows, R., Gallagher, P. T., Magdalenic, J., Klein, K., Mann, G., Vocks, C., Carley, E. P., Bisi, M. M., Kontar, E. P., Rothkaehl, H., Dabrowski, B., Krankowski, A., Anderson, J., Asgekar, A., Bell, M. E., Bentum, M. J., Best, P., Blaauw, R., Breitling, F., Broderick, J. W., Brouw, W. N., Bruggen, M., Butcher, H. R., Ciardi, B., de Geus, E., Deller, A., Duscha, S., Eisloffel, J., Garrett, M. A., Grießmeier, J. M., Gunst, A. W., Heald, G., Hoeft, M., Horandel, J., Iacobelli, M., Juette, E., Karastergiou, A., van Leeuwen, J., **McKay-Bukowski, D.**, Mulder, H., Munk, H., Nelles, A., Orru, E., Paas, H., Pandey, V. N., Pekal, R., Pizzo, R., Polatidis, A. G., Reich, W., Rowlinson, A., Schwarz, D. J., Shulevski, A., Sluman, J., Smirnov, O., Sobey, C., Soida, M., Thoudam, S., Toribio, M. C., Vermeulen, R., van Weeren, R. J., Wucknitz, O., and Zarka, P.: Shock location and CME 3D reconstruction of a solar type II radio burst with LOFAR, ArXiv e-prints, 2018.

Acknowledgements

This PhD thesis was completed at UiT – The Arctic University of Norway, with supervision from Juha Vierinen, Noora Partamies, Björn Gustavsson and Tom Grydeland. Before moving to UiT, my supervisors at the University of Oulu were Thomas Ulich and Anita Aikio, and the follow-up group committee was Elena Kozlovskaya, Timo Asikainen and Jyrki Manninen.

KAIRA was funded by the Infrastructure Funds of the University of Oulu and is operated by Sodankylä Geophysical Observatory with assistance from the University of Tromsø, Norway. Development work was funded by the European Regional Development Funds of Lapland through the Regional Council of Lapland as well as by the 7th Framework Preparatory Phase project '*EISCAT_3D: A European Three-Dimensional Imaging Radar for Atmospheric and Geospace Research*'. The KAIRA build team itself comprised: Toivo Iinatti, Arttu Jutila, Oula Kalttopää, Marko Kauranen, Stuart Keenan, Antti Kero, Joona Keskitalo, Pasi Lakkala, Markku Lehtinen, Nikiforos Nikiforou, Pertti Nissinen, Rauno Oikarainen, Mikko Orispää, Jussi Paulamäki, Markus Peltoniemi, Fabio Pereira, Aleksi Postila, Markku Postila, Tero Raita, Eero Rantakokko, Santtu Rantakokko, Timo Rantala, Jussi Rauhala, Lassi Roininen, Mikko Tilja, Paavo Törmänen, Lars-Aslak Tornensis, Johannes Turunen, Thomas Ulich, Juha Vierinen, Han Wessels and Pertti Ylitalo.

Further support from Sodankylä Geophysical Observatory was provided by Maxime Grandin, Ari Keskitalo, Alexander Kozlovsky, Jussi Markkanen, Tomi Teppo, Esa Turunen and Jaana Yli-Suvanto.

The Low Frequency Array (LOFAR) was designed and constructed by the Netherlands Foundation for Radio Astronomy (ASTRON), with notable Dutch assistance to the KAIRA project provided by: Michiel Brentjens, Nico Ebbendorf, Matys Eikelboom, Richard Fallows, Marchel Gerbers, Teun Grit, Peter Gruppen, Henri Meulman, Harm Munk, Menno Norden, Jan-Pieter de Reijer, Arno Schoenmakers, Klaas Stuurwold, Corina Vogt, Sefan Wijnholds and Michael Wise.

The staff of the Kilpisjärvi Biological Station have been vital to the project, providing a welcoming home, superlative meals and helping hands to the weary KAIRA build teams. *Kiitos paljon:* Aki Aintila, Pirjo Hakala, Kirsi Holstila, Ulla Hyvönen, Oula Kalttopää, Karoliina Kehus, Tuula Kotavuopio, Vuokko Lapinniemi, Kalevi Laurila, Hannele Maikkula, Maija Miettinen, Rauni Partanen, Ritva Ruokojärvi, Saara Sipola *ja* Anna-Liisa Välitalo.

Likewise, Chilbolton Observatory is another such home and I acknowledge the formative LOFAR-UK project that ultimately led to the KAIRA adventure. I am grateful to: John Bradford, Mal Clarke, Owain Davies, Alan Doo, Jon Eastment, Elena Jackson, Dave King, Darcy Ladd, Jan Lass and all the others from Chilbolton Observatory.

I am grateful to the generous support and encouragement from Rutherford Appleton Laboratory. I wish to thank: Ivan Finch, Richard Harrison, Richard Holdaway, Ian McCrea, Chris Mutlow, Jane Porter and Bruce Swinyard.

I would like to thank Tuula Paavilainen, Noora Partamies, Lassi Roininen, Jussi Norberg, Antti Kero, Theresa Rexer, Tom Grydeland, Magnar Johnsen and Andreas Kvammen for assistance with the translations of the abstract.

Countless others have also contributed to the KAIRA endeavour in some way, or have supported me in my work. Amongst them are: James Anderson, Philip Best, Izabela Bukowska, Jorge Chau, John Davis, Chris de la Force, Griffin Foster, Annette Haas, Farideh Honary, Alex Hyne, Virpi Jussila, Juha Kallunki, Kirsti Kauristie, Michael Kesteven, Steve Marple, Poppy Martin, Brian McClave, Doris Merkl, Jussi Norberg, Steve Rawlings, Harry Smith, John Storey, Minttu Uunila, Mark Wieringa and Olaf Wucknitz. Most recently, I note the camaraderie of fellow students at the University of Tromsø. *Mange takk til:* Tarjei Antonsen, Knut Ola Dølven, Marcus Floer, Andreas Kvammen *og* Theresa Rexer. *Sitten niin paljon kiitokset:* Seppo, Sinikka, Päivi *ja* Sulo-Katti! *ja revontulitutkimusassistenttini*, Tuula Paavilainen.

Contributions of co-authors to the included papers are acknowledged. All photographs, diagrams and illustrations in this work are by the author unless indicated otherwise. Any material from others is used with permission.

The support of numerous organisations is given due recognition: UiT – The Arctic University of Norway, Rutherford Appleton Laboratory, Chilbolton Observatory, Sodankylä Geophysical Observatory, University of Oulu, Finnish Meteorological Institute, the Kilpisjärvi Biological Station of the University of Helsinki, Finnish Geodetic Institute (incl. *karttapaikka* service), University Centre in Svalbard (UNIS), RF-shamaanit Oy, EISCAT Scientific Association, Leibniz Institute of Atmospheric Physics Kühlungsborn, Netherlands Foundation for Radio Astronomy (ASTRON), Lancaster University, and the University of Southampton. LOFAR is operated by the International LOFAR Telescope (ILT) foundation, and has benefited from these major funding sources: CNRS-INSU, Observatoire de Paris & Université d'Orléans, France; BMBF, MIWF-NRW, MPG, Germany; Science Foundation Ireland, Dept. Business, Enterprise & Innovation, Ireland; NWO, The Netherlands; and STFC, UK.

The design, production and operation of a major scientific instrument, such as KAIRA, is a long and complex task, spanning many years, and involving many individuals and organisations. It is, perhaps, impossible to include every name here, but their efforts and sacrifices are nevertheless greatly appreciated.

Finally, this work is dedicated to everyone who was in some way involved in the building of the KAIRA facility.

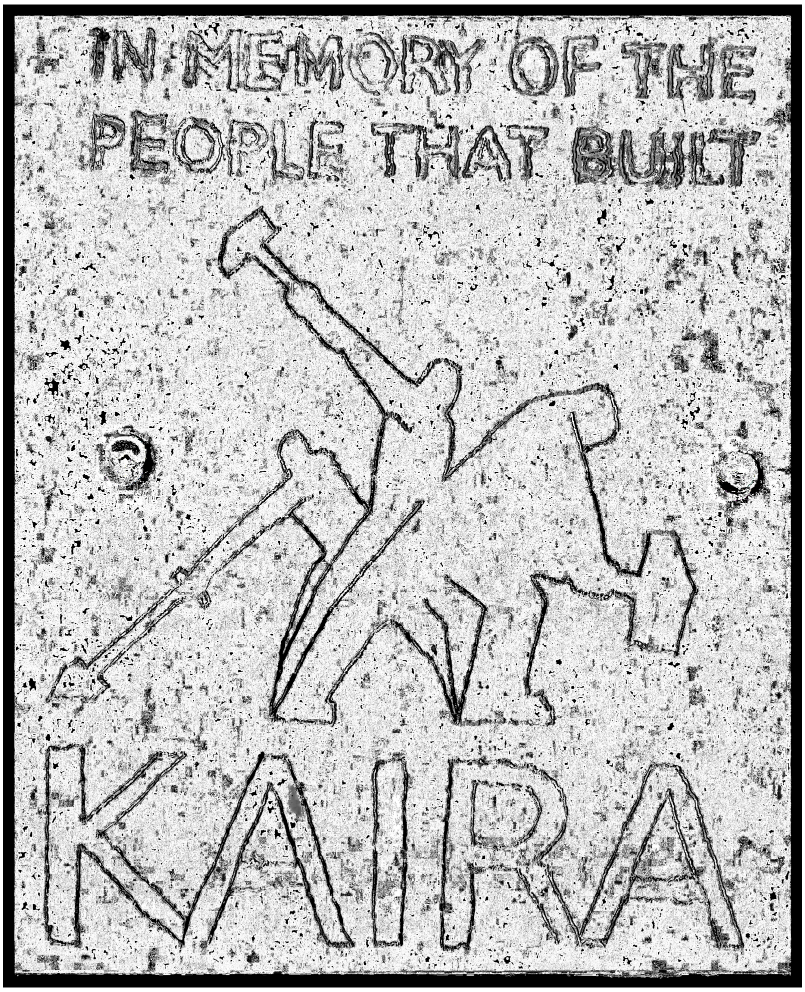
IN MEMORY OF THE
PEOPLE THAT BUILT
KAIRA

Chapter 1

Introduction

This volume describes the construction and operation of a new scientific facility: the Kilpisjärvi Atmospheric Imaging Receiver Array (KAIRA). It discusses the scientific programme being carried out and the advances in one specific area of investigation. The panoply of different experiments spans the dominions of astronomy and geophysics. Although a general overview of all of them will be given, the particular focus of this work is the study of the lower ionosphere and the radio phenomena that occur therein as a result of the interaction of charged particle precipitation with the existing particle populations.

The Ionosphere

The ionosphere is a layer of the Earth's atmosphere. Unlike the atmosphere at ground level, the ionosphere is partially ionised, containing free electrons and ions, as well as neutral species. Overall, the charge of the ionosphere is neutral and, although ionisation exists, the total number of neutral particles greatly exceeds the numbers of those that are charged. The main generalised regions of the ionosphere are designated D, E, F1, and F2, with very approximate characteristics indicated in Table 1.1. The typical electron densities vary by an order of magnitude, depending on solar photo-ionisation, solar activity and latitude. In the D and E regions, recombination times are short and the electron density drops at night in the absence of photo-ionisation. Only auroral charged particle precipitation creates significant additional ionisation at this time[1]. The F region has longer recombination times and therefore persists. At low latitudes it splits into two distinct regions (F1 and F2) during sunlit conditions, but this is rarely seen at the latitude of KAIRA. The regions are characterised by a complex interaction of physical and chemical processes, including electrons which precipitate from the plasmasphere (Hunsucker and Hargreaves, 2002, p 209). General ionisation from these electrons has been investigated throughout the history of the field, and is summarise in the recent review paper by Mironova et al. (2015).

---

[1] This thesis does not consider the effects of a nearby supernova.

Region	Height	Electron density		Collision frequency
	km	m^{-3}	cm^{-3}	s^{-1}
D region	60–90	10^8–10^{10}	10^2–10^4	10^7–10^5
E region	90–160	10^{11}	10^5	10^4–10^3
F1 region	160–180	10^{11}–10^{12}	10^5–10^6	10^3
F2 region	max.$\approx$300	10^{12}	10^6	10^3

Table 1.1: Summary of approximate peak daytime characteristics of the ionosphere regions (Aggarwal et al., 1979; Hunsucker and Hargreaves, 2002, p 13–15).

A major component of this thesis pivots on the radio absorption properties of the ionosphere. Absorption triangulation methods, supplemented with radar measurements, indicate that absorption of cosmic radio noise occurs in the D region (Wild et al., 2010), where the absorption is determined by the electron density and the frequency of collisions between electrons and neutral particles (Hunsucker and Hargreaves, 2002, p 229–231).

The inaccessible altitudes of the ionosphere have resulted in an observational history dominated by remote sensing. Even with the advent of space flight, this boundary region of the Earth's atmosphere remains elusive for satellites and aircraft alike.

Therefore, the scientific community is continuously experimenting with new remote-sensing techniques to study it. The work and results described in this thesis are one thread of this investigation and, in order to put it in context, an overview of the observational history of the ionosphere is presented.

A selected history of ionospheric observations

The earliest scientific hypothesis for the existence of the ionosphere is provided by Gauss (1839) who, in regard to variations in the Earth's magnetic field, considered internal (subterranean) and external (atmospheric) possibilities. Gauss wrote:

> *Die atmosphärische Luft ist kein Leiter solcher Ströme, der leere Raum auch nicht: unsre Kenntnisse verlassen uns also, wenn wir einen Träger für galvanische Ströme in den obern Regionen suchen. Allein die räthselhaften Erscheinungen des Nordlichts, bei welchem allem Anscheine nach Elektricität in Bewegung eine Hauptrolle spielt, verbieten uns, die Möglichkeit solcher Ströme bloß jener Unwissenheit wegen geradezu zu läugnen, und bleibt jedenfalls interessant, zu untersuchen, wie die aus denselben hervorgehende magnetische Wirkung auf der Erdoberfläche sich gestalten würde.*

This I translate as follows:

> The atmospheric air is no conductor of such current, nor is empty space: our knowledge abandons us when we search for a medium of galvanic current in the upper regions. The enigmatic phenomenon of the Northern Lights, in which it seems electricity-in-motion plays a critical role, denies us the possibility to dismiss such currents merely through such lack of knowledge, and in any case it remains interesting to investigate how they would manifest themselves in the magnetic effects on the Earth's surface.

Following the "great solar disturbance" of 1859 (Carrington, 1859; Hodgson, 1859), the first association between disruption to the Earth's magnetic field and extra-terrestrial phenomena was made by Stewart (1860). This led Thomson and others to renew the speculation on the existence of an electrically charged layer of the Earth's atmosphere (Kaiser, 1962).

During the late 19th century experiments in radio telegraphy had been developing, leading to the famous trans-Atlantic radio communication from Cornwall, England to Newfoundland by Marconi in 1901. This feat led Kennelly and Heaviside independently in 1902, to suggest that this radio communication would be possible if the upper atmosphere were electrically conducting (Appleton, 1932, and references contained therein). This implied that there would be a tendency for the electromagnetic waves to be guided around the Earth, constrained between the two concentric shells of the surface and the electrically conducting layer above, and thus not lost into space (Appleton and Barnett, 1925b).

In the 1920s, the hypothesis of an electrical layer was confirmed experimentally by Appleton and Barnett (1925a), who noted arrival of incidence, radio fading and elliptical polarisation, leading them to estimate an electron density, N_e, of 10^{11} m^{-3}. The following year, Breit and Tuve (1926) successfully demonstrated this using a "vertical incidence sounding" technique and detecting the transmitted and received pulses separately, with the reflection occurring "between 50 and 130 miles" (80–209 km). The technique gives information about N_e as a function of height, and gave rise to type of active radio sounding instrument, known as the ionosonde.

This electrical stratum in the atmosphere was referred to as the E region (Appleton, 1932), with the D and F regions named in sequence for those regions lying below and above the E region, respectively. The naming of the ionosphere was attributed to Watson-Watt in 1926, who added the definition: "the ionosphere is that region of the atmosphere (or gaseous envelope) surrounding a solar system body where significant numbers of low energy, free electrons and ions are present." (Gardiner, 1969)

It was realised that the majority of the ionisation was on the dayside but during the Second International Polar Year (1932–1933); Appleton et al. (1937) were able to use an ionosonde to demonstrate that the aurora were associated with N_e increases in the ionosphere.

In the same year, Jansky published that certain radio noise was of cosmic origin, and was associated with the Galaxy, thus founding a new branch of science — Radio Astronomy (Jansky, 1933). Shain (1951) observed the absorption of this cosmic radio noise by the ionosphere. This led to the development of new instruments specifically designed for using this phenomenon to investigate the ionosphere. The first dedicated instruments to measure the absorption effect were developed by UK scientists shortly thereafter (e.g. Machin et al., 1952). One later example built by Little and Leinbach (1959) — the R.I.O.M.E.T.E.R (for *Relative Ionospheric Opacity Meter for Extra-Terrestrial Emissions of Radio noise*) — gave the name "riometer" to this generic class of instrument and the term "riometry" for the measurement of cosmic noise absorption by the ionosphere.

At a similar time to the development of riometers, the field of incoherent scatter radar (ISR) measurements was being established. Initial predictions were made by Gordon (1958), and the first measurements reported by Bowles (1958). Unlike the ionosonde technique, the ISR method is also capable of measuring the upper ionosphere above the F-region maximum.

During the 1970s, a large ISR system was planned for northern Fenno-Scandinavia. This was the European Incoherent Scatter (EISCAT) facility with the first of its systems, the UHF incoherent scatter radar, starting observations in 1981 (Rishbeth and Williams, 1985). In the early 2000s, it was planned to conduct a major upgrade of this facility. Termed "EISCAT_3D", this replacement will use modern phased-array technology in place of the large parabolic dishes which had been used successfully with the current EISCAT system for more than 30 years (Ulich et al., 2010).

The KAIRA project was started in 2010, after EISCAT_3D had completed its initial design study (van Eyken et al., 2009). The motivation for the construction of KAIRA and its close connection with the EISCAT_3D endeavour are discussed in the next chapter.

Chapter 2

KAIRA overview

The facility used for this thesis is the Kilpisjärvi Atmospheric Imaging Receiver Array (KAIRA). This chapter complements the description of the instrument given in Paper I and provides the context for KAIRA's construction and operation.

2.1 Description

KAIRA was built as a technology pathfinder for the EISCAT_3D project, in order to assess the capabilities of using a modern wide-band phased-array radio telescope system for incoherent scatter radar measurements. Its location was chosen to be in Finland, but at a suitable distance from the EISCAT radar transmitter at Ramfjordmoen, Norway, so as to permit a favourable observing angle for bistatic incoherent scatter measurements ($\approx 45^\circ$ at 80–100 km altitude above the transmitter). The KAIRA site is near the village of Kilpisjärvi and the relationship between this place and other significant locations for this work is shown in Figure 2.1. Position parameters are given in Table B.1 (page 140).

A further aim of the KAIRA project was to experiment with radio telescope technology for conducting other active and passive geophysical remote sensing experiments, as described in Chapter 3. These experiments are typically not possible with existing incoherent scatter facilities due to the narrow bandwidth and narrow beam-pattern of those radars. Another limitation of previous experiments was the lack of digital beamforming, which precluded multiple intersection points of the radar transmit beam.

A photograph of the KAIRA site and the surrounding landscape is shown in Figure 2.2. The site itself is a reused roadworks landfill, which provided a stable "mound" which sits 5–7 m proud of the surrounding terrain.

The instrument comprises two phased arrays, each of 48 dual-polarisation antennas; the Low-Band Antenna (LBA) array spans a nominal frequency range of 10–80 MHz and the High-Band Antenna (HBA) array spans 110–270 MHz. The intervening gap is the broadcast allocation of FM radio, which is deliberately excluded.

Figure 2.1: Regional map of northern Fenno-Scandinavia showing the locations of scientific instruments at places mentioned in this thesis. Universities at Tromsø and Oulu, EISCAT VHF transmitter at Ramfjordmoen, EISCAT receiver sites at Kiruna and Sodankylä, MAARSY radar at Andenes, KAIRA and IRIS at Kilpisjärvi and FMI-ASC sites at both Abisko and Kilpisjärvi.

Recent advances in signal processing and computing are utilised, resulting in the rapid control of these antennas using digital beamforming techniques permitting multiple directions to be observed with different frequency channels simultaneously.

The antenna and signal-processing system chosen for KAIRA is the same as that used in the Low Frequency Array (LOFAR) International Telescope, a radio telescope network intended for low frequency astronomy, designed and produced by the Netherlands Institute for Radio Astronomy (ASTRON) and Dutch industry (van Haarlem et al., 2013).

Because the first stages of LOFAR had been completed, the system was already tested and a user community existed for support. The capabilities required for the EISCAT_3D bistatic receiver were a subset of those offered by the LOFAR system. As the LOFAR system is a phased array with no moving parts, it is beneficial in an Arctic environment, where it can be bitterly, bitterly cold. The LOFAR design makes use

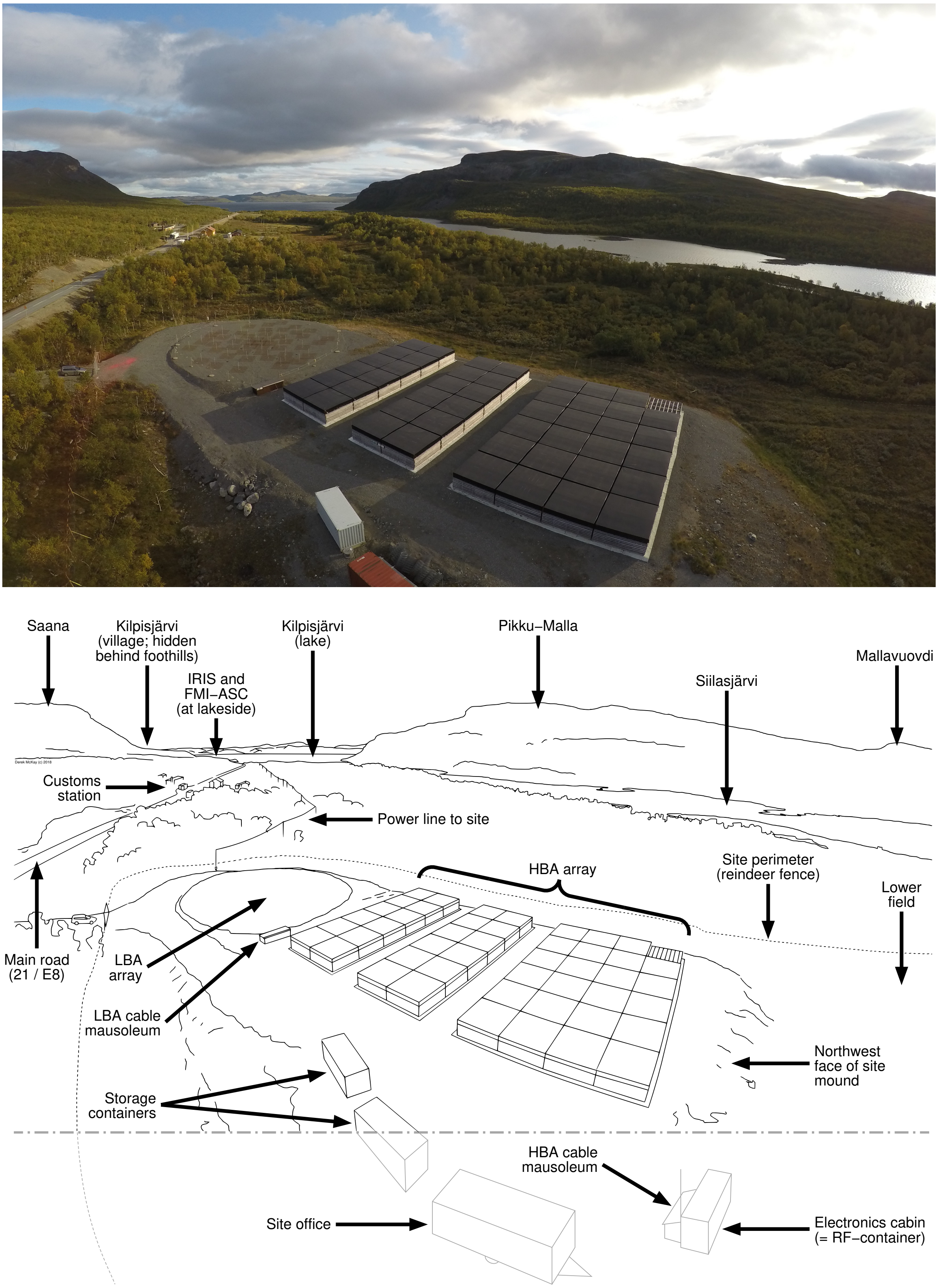

Figure 2.2: Overview of the Kilpisjärvi Atmospheric Imaging Receiver Array (KAIRA) looking south, on 1 September, 2015. The annotated line-drawing indicates key parts of the site, including some features not in the field of view of the camera (delineated with a dash-dot line). Aerial photograph: Craig Heinselman, EISCAT.

of mass-produced, low-cost components that are moderately quick to deploy and commission. An exposition of the KAIRA facility is given in Paper I, the technical parameters are listed in Appendix B, and the design decisions and construction details are given in Appendix E. The following sections give a general overview of the form and capability of KAIRA.

2.2 Antenna arrays

The antennas used in the two arrays have been designed to optimise their performance and deployment within their designed frequency range. The motivation to use two arrays is partly due to the difficulty of designing a single system which can operate efficiently over the large frequency range of 10–270 MHz (wavelength range of 30–1.1 m). The HBA array actually has a much denser packing of antennas, which is impractical with the LBA array, due to the longer wavelength and the resultant antenna size. Additionally, interference from FM-radio stations (88–108 MHz) is extremely strong. Especially at the LOFAR sites, in populated areas of Europe, the prevalence of strong FM broadcast signals would make it difficult to achieve full frequency coverage in a satisfactory way with a single antenna field. Although there are relatively few FM-radio stations in the Kilspijärvi area, these transmitters still cause significant interference. The location of the transmitter tower on the top of the nearby mountain, Saana (elevation $\approx 6^\circ$), is considerably higher than at other LOFAR sites which have transmitters on the horizon (effectively elevation 0°), which would be at the null of the antenna elements.

HBA array

The 48 HBAs that were installed each comprise 16 one-meter-wide crossed bow-tie antenna elements packed into a plastic-covered, polystyrene frame, to form “tiles”. Within each tile, the elements are spaced 1.25 m apart. An exposed section of a tile is shown in Figure 2.3. In the base of each tile is an earthed metal wire grid to serve as a common ground plane. Each tile is 5 m by 5 m and stands approximately 0.5 m tall. In the case of LOFAR sites, these are anchored into level ground. For KAIRA, it was not desirable to have the tiles placed as such due to possible accumulation of drift snow and the difficulties presented in terms of cable installation and protection. Instead, as shown in Figure 2.4, the tiles were mounted on “framesets” — open timber lattices which stand 1.5 m tall. Each tile is placed on top of a frameset and connects directly to it with elastic. The framesets are then anchored to the ground in the same manner as conventional LOFAR systems. The ability to connect the anchors to arbitrary points on the timber frameset makes it easier to deploy these systems over uneven ground. The use of the framesets raises the top of the tiles 2 m above the mound-level (which itself is raised some 5–7 m above the surrounding landscape). This increased elevation allows a natural clearing of light snow due to the wind shear.

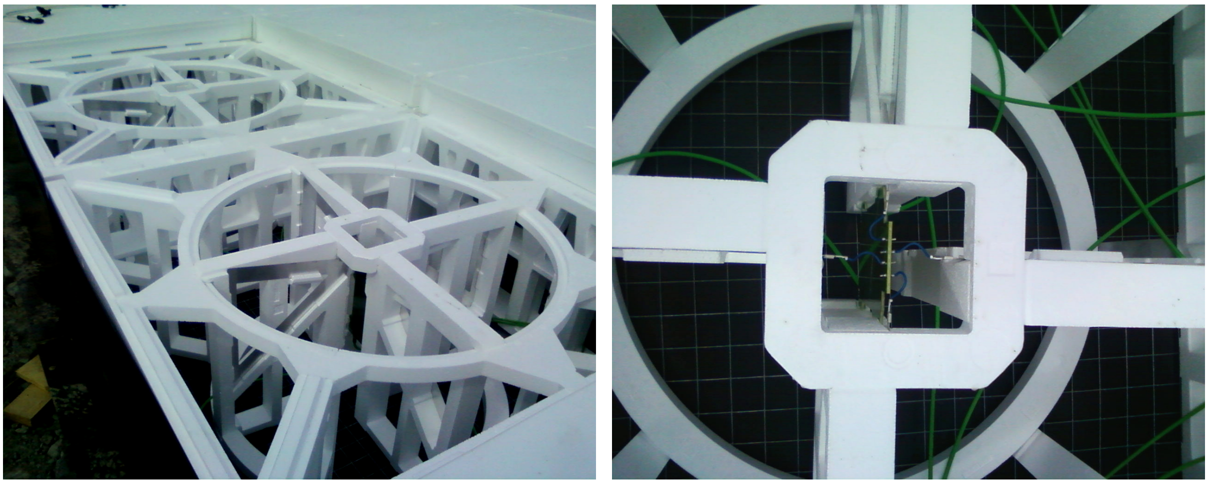

Figure 2.3: Two exposed cells in an HBA tile, showing the polystyrene skeleton that holds the antenna blades in place (left) and a detail of the amplifier board at the centre of each cell (right). Note the wire-mesh at the base of the tile.

Figure 2.4: An example HBA tile (#H31). The top cover of the tile is anchored onto the supporting timber frameset, holding the tile in place. Each tile stands independently of neighbouring tiles.

The signals from the 16 antenna elements within each HBA tile are combined with a remotely controlled analogue beamformer. This hierarchy means that each of the 48 tiles still only has two outputs, one for each polarisation. Because of the size and number of receiving sub-elements, these are packed within each tile in a regular grid and the tiles themselves are also regularly spaced across the field.

On 8 March 2014, a blizzard resulted in the total loss of one HBA tile (see Appendix E.20). Since then, KAIRA has operated with only 47 HBA tile elements.

LBA array

The 48 LBAs are crossed inverted-V-dipole aerials, standing 1.8 m tall, above a 3 m by 3 m steel grid ground plane as shown in Figure 2.5. The antennas are scattered in a quasi-random pattern across a field 34 metres in diameter to give a good beam-profile with low sidelobes. It matches the layout of the inner section of a LOFAR "remote station" (van Haarlem et al., 2013) enabling direct comparison. In the LOFAR case, there are two outlying aerials used for calibration. For KAIRA, these two additional aerials are placed within the compact array area at locations selected to improve sidelobe suppression.

Figure 2.5: An example LBA aerial (#L35) in the foreground, amongst numerous others. The small structure with the sloped roof is the LBA array cable mausoleum (Appendix E.15) and the southeast edge of the HBA array is also visible.

Array layout

The layout of the LOFAR antennas at the KAIRA site is shown in Figure 2.6. The VHF arrow marks the azimuthal direction towards the VHF-transmitter at Ramfjordmoen, near Tromsø in Norway, which is used with some of KAIRA's experiments.

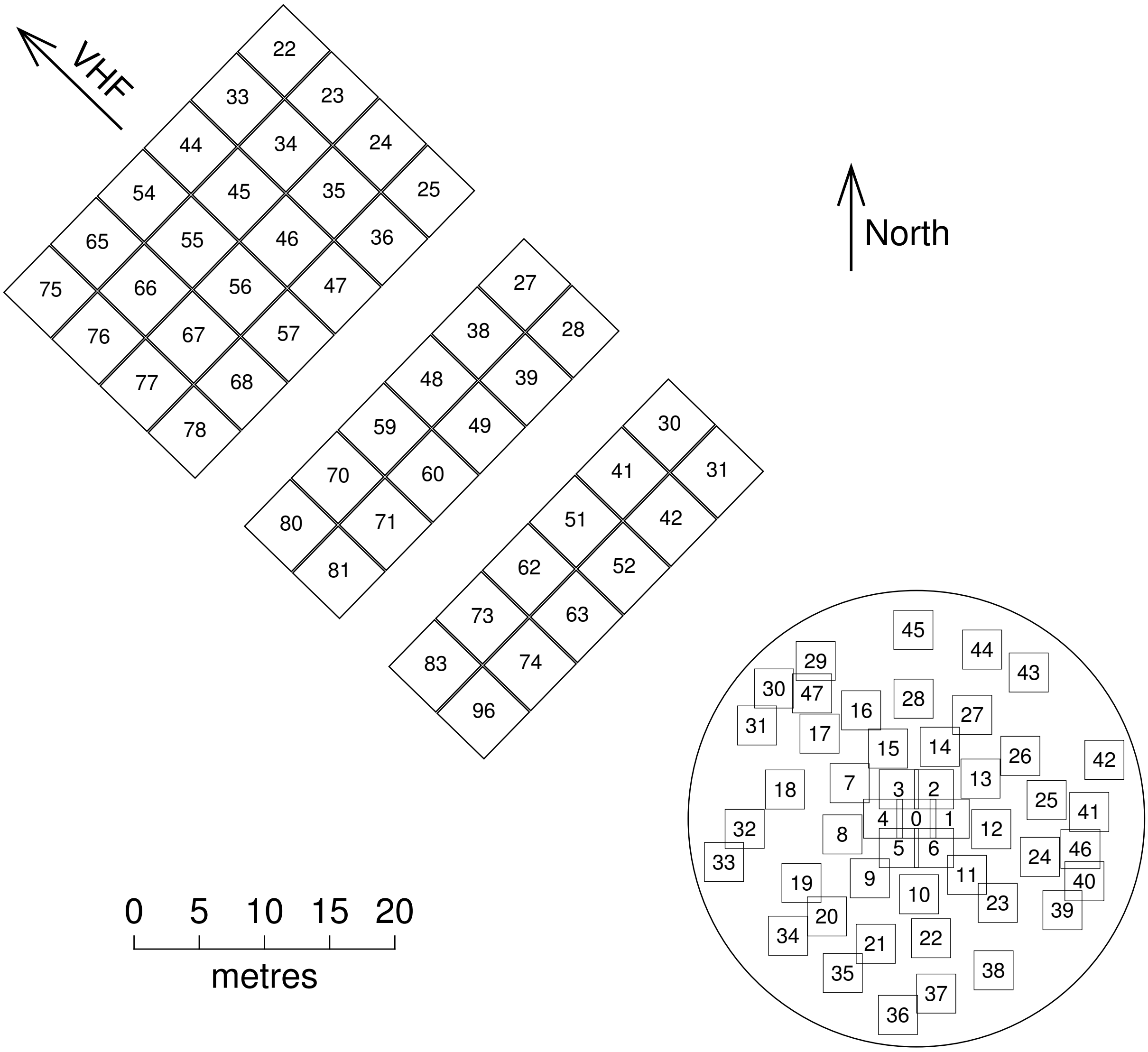

Figure 2.6: Scale layout of the KAIRA antennas. The numbers are the identification codes of the individual HBA tiles and LBA aerials. The circle indicates the LBA array, and the HBA array is aligned with the direction of the EISCAT VHF radar transmitter at Ramfjordmoen.

The HBA array layout was chosen as a compromise between beam-pattern for imaging the region of the atmosphere illuminated by the EISCAT radar and ease of construction and maintenance in a snow-heavy region. The layout is consistent with a 96-antenna layout of a large LOFAR site (known as an "international station"), with the only exception being HBA #96, which is not coincident with any LOFAR layouts. While this permits KAIRA to be upgraded without requiring the repositioning of existing antennas, it does present a non-standard patching between HBA number and RCU number. Design methodologies for the HBA and LBA array design are given in Appendices E.3 and E.13, respectively, and the performance of the arrays is discussed in Section 2.4.

The system permits rapid pointing with multiple beam formation and has high sensitivity. Furthermore, the broad-band nature of this system also ensures that many different transmitters can be received simultaneously.

2.3 Signal processing

Recent advances in digital signal processing and computing are utilised, resulting in the rapid control of these antennas using digital multi-beamforming techniques.

Each polarisation signal cable from each antenna is connected to a receiver unit (RCU). In the case of the LBA array, these are numbered sequentially, where LBA #00 patches to RCUs 0 and 1; LBA #01 patches to RCUs 2 and 3; and so on. In the case of the HBA array, the layout is designed to match that of a LOFAR international station, so the numbering is non-sequential. (See Table B.2 for the assignment of the antenna polarisation and RCUs and Appendix E.3 for an explanation of the array layout design.)

Each RCU has three inputs: two LBA inputs (referred to as LBL and LBH) and one HBA input. Within each RCU, there are filters and amplifiers to condition the signal, and an analogue-to-digital converter (ADC). Each RCU has 7 different filter modes of operation (listed in Table B.4 and explained in Appendix E.18). These RCU modes refer to the input selected (LBL, LBH, or HBA) and the configuration of filters. Sample quantisation of the ADC is 12-bit, which can be transported digitally using a 16-bit word, or clipped and transported as an 8- or 4-bit word. This quantisation choice is called the “bit-mode”. While the RCU mode may vary between RCUs, the bit-mode is common to the entire array. Collectively, the RCUs are configured by a control computer (the Local Control Unit, LCU).

Digital signal processing is handled by the Remote Signal Processing (RSP) circuit boards. There are 12 RSP boards, each handling 8 RCUs. Each signal (which is a single polarisation signal from each antenna) is split into 512 “subbands” via a polyphase filter bank. Each subband is of equal bandwidth, which is governed by the sampling clock used (de Vos et al., 2009). The sampling clock is common to all signal processing chains, and can be set to 160 or 200 MHz, resulting in a subband width of ≈156.25 or ≈195.31 kHz, respectively. The relationship of the subband number, s, to its centre frequency, ν_{mid}, is given by:

$$\nu_{\text{mid}} = \frac{s \times \nu_{\text{clk}}}{2 \times 512} \tag{2.1}$$

where ν_{clk} is the sampler clock frequency.

Beamformed signals are generated by each RSP board digitally delaying its signals and adding them, passing the partial beamformed product to the next RSP board, which in turn adds its digitally delayed signals. This continues in a ring until the fully-formed beamformer products are complete, after which they are directed to an output network switch.

Depending on the level of quantisation used, a number of these subbands, each from an arbitrary set of antennas and for both polarisations, can be selected and combined into “beamlets” using a complex-weighted, phase-rotated beamformer. Such a beamlet is therefore a signal associated with a pointing direction on the sky and subband. The pointing directions can be set in either topocentric (Azimuth & Elevation), or celestial (Right Ascension & Declination) coordinates, with the control system introducing the necessary signal delays to facilitate the pointing and tracking of the phased-array beams.

Further details of the signal processing, along with schematic diagrams and photographs, are listed in Appendix E.18.

2.4 System performance

An overview of the system performance of KAIRA is a key component of Paper I. Included therein are the beam patterns and spectral system equivalent flux densities (SEFD; sensitivity). Additional discussion of the evaluation of the instrument performance is given in Appendix J. However, a summary of the important points will also be given here.

The beamsize of the array in radians, θ, is given by the conventional diffraction limit, based on the equivalent synthetic aperture. This is:

$$\theta = \alpha\lambda/D \tag{2.2}$$

where λ is the wavelength and the D is the effective array diameter; both in the same units, typically meters. The scaling parameter, α, used is 1.02±0.01 for the HBA array and 1.10±0.02 for the LBA array (van Haarlem et al., 2013). The beamsize is elongated in the elevation axis by sec(Z), where Z is the zenith angle. This may be used as a first-order approximation, although at low elevation angles, the beam pattern of the array is complicated by the increase in antenna coupling and the convolution with the beam pattern of individual elements in the array. The case of the HBA array, the array beam is additionally convolved with the beam pattern of individual tiles. The zenith beam sizes and sample beam patterns are plotted in Figures 8, 9 and 10 of Paper I.

Figure 2.7 shows the spectra of RCU modes 3, 5 and 7, which are currently used. The spectrum and performance of the additional RCU mode 6 is discussed in Paper I. Spectral response and spectral sensitivity are given in Figures 7 and 11 of Paper I, respectively, with the method described in Appendix J. The narrow features at exactly 100 and 200 MHz are harmonics of the sampler clock. Spectral features present in Figure 2.7, but which are not a result of KAIRA’s implementation, include radio-frequency interference (RFI) from shortwave radio (10–25 MHz), local FM radio stations (88–108 MHz), DAB radio stations (174–230 MHz) and military satellite communications (240–270 MHz). Other sources of RFI include over-the-horizon radar, radio noise from passing vehicular traffic, power-line static discharges, and radio traffic from local military operations. Isolated and unidentified RFI is occasionally present, and poses a challenge to observations (discussed in Section 5.4). Self-interference from KAIRA itself is effectively eliminated by the use of an electronics cabin (known as the “RF-container”) where all electronics are enclosed in a Faraday enclosure (described in Appendix E.18).

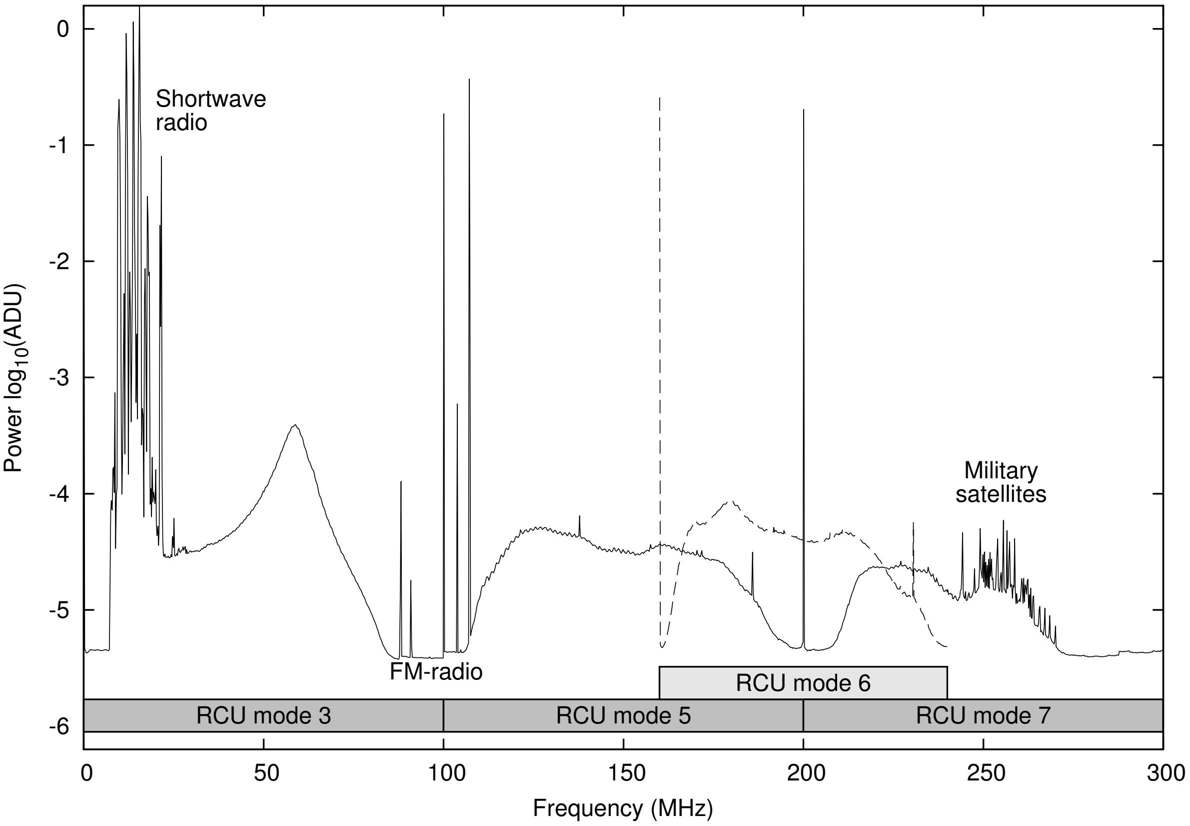

Figure 2.7: Bandpasses for the commonly-used RCU modes (from Figure 7, Paper I). Note the strength of certain signals, even though they are in strongly filtered parts of spectrum. Signals at exactly 100, 160 and 200 MHz are the aliased sampler clock.

At 38.1 MHz (the frequency often used at KAIRA for imaging riometry measurements), the system equivalent flux density (SEFD) is 39±4 kJy. At 224 MHz (the transmitter frequency of the EISCAT VHF ISR), the SEFD is 2.7±0.5 kJy. The main source of the difference is from the HBA array having 16-times the number of antennas (there are 16 crossed bow-tie antennas per tile). Individual antenna shape, as well as amplifier and filter responses, cause secondary variation across the bands.

2.5 Operation and data

Configuration parameters built into the control system, provide the necessary coordinates of antennas, default cable lengths, delay-line calibration and amplifier response levels. Observations using KAIRA are then accomplished by setting:

- Data transport size for the array (the bit-mode: 4, 8 or 16-bit)
- Filter configuration for each RCU (the RCU mode: 0–7)
- Frequency of the sampler clock (160 or 200 MHz)
- Beamlet specification (antenna, subband and pointing direction per beamlet)
- Integration time for statistics data (integer number of seconds)
- Station correlator mode (single- or swept-frequency: XST or ACC)

Once this has been done, data products are generated automatically and may be optionally recorded. For KAIRA, the array control settings are configured by software designed to run semi-autonomously (Appendix F.1).

The LOFAR control system and data formats are described by Virtanen (2012). In addition to the standard LOFAR data products, KAIRA has a number of bespoke data acquisition software packages, which have been specifically written to accomplish its geoscience observations (Appendix F.3).

Standard operating modes

The standard operating mode uses 8-bit data transport, as a compromise between number of beamlets and dynamic range. This results in 488 beamlets with no need for additional attenuation to accommodate saturation. A single RCU mode is used (typically RCU mode 3) with the 200 MHz sampler clock.

Subband, beamlet and cross-correlation statistics are collected for each linear polarisation at a 1 second cadence. Faster beamlet data is accumulated at a data rate of approximately 100 samples per second, recorded as Stokes parameters. Data formats and rates are described in Appendix F.3. The current KAIRA experiment is given in Appendix K as an example of the beamlet configuration. For very long baseline interferometry (VLBI) and incoherent scatter radar (ISR) measurements, raw data is captured with 5.12 μs samples, using linear polarisations.

2.6 Special operating modes

Experimentation with a number of unconventional observing modes has been carried out with KAIRA. This has been motivated by the nature of the geophysical phenomena being observed which have different requirements compared to the astrophysical phenomena for which the technology was originally developed. This experimentation has formed a key part of the early development stages of KAIRA and has resulted in some unique observations. A number of these observing modes also became of interest to the LOFAR community and have since been adopted for use in astronomical applications.

Mode 357

The RCU modes 1–7 define the input and filters used for each RCU. Most are designed to use the 200 MHz sampling clock. However RCU mode 6 has a filter set optimised to use the 160 MHz sampling clock in order to observe the frequencies around 200 MHz (which would normally be aliased in the other modes). RCU modes 1 and 2 are for the LBL inputs and are not used at KAIRA.

Because each individual receiver unit has both an LBA and an HBA polarisation connected to it, it is not possible to observe with both of these simultaneously on the one RCU. Furthermore, because of the filters used in the RCUs, it is not possible to observe across the entire frequency range of the HBA simultaneously either. A single RCU mode must be selected for each given channel.

It is typical for astronomical observations to require the maximum bandwidth and collecting area possible, in order to detect weak cosmic radio emissions. As a result, typically all antennas would be used with a common RCU mode to maximise sensitivity.

However, in the geophysics case, there are occasions where the incoming radio signal is very strong, so it is not necessary to concentrate detecting resources. In these circumstances, a variety of different RCU modes (collectively referred to as “Mode-357”) can be used and the overall system split up into “sub arrays”. A third of the LBA dipoles (RCU mode 3) were used in combination with a third of the HBA tiles receiving in RCU mode 5 and a further third of the HBA tiles receiving in RCU mode 7. An example is given in Figure 2.8. Each beamlet only forms data productions from one of the sub-arrays. This technique was developed by the author as part of the KAIRA commissioning and has since been used at KAIRA and other LOFAR stations for scintillation and solar observations.

Figure 2.9 is example data taken at KAIRA, plotting beamlet power at given frequencies as a function of time. The allocation of subbands to beamlets does not need to be sequential and, using non-uniform subband allocation, it allows nearly complete coverage of the VHF band to be achieved.

The horizontal striping is due to RFI and the different antenna and filter responses. In particular, the faded sections at 100 and 200 MHz are due to the anti-aliasing filters used to select the different Nyquist zones for the RCU modes. The “speckled” horizontal lines (for example at approx. 20 and 260 MHz) are RFI.

The trade-offs made in using this mode are reduced sensitivity and a larger beam-

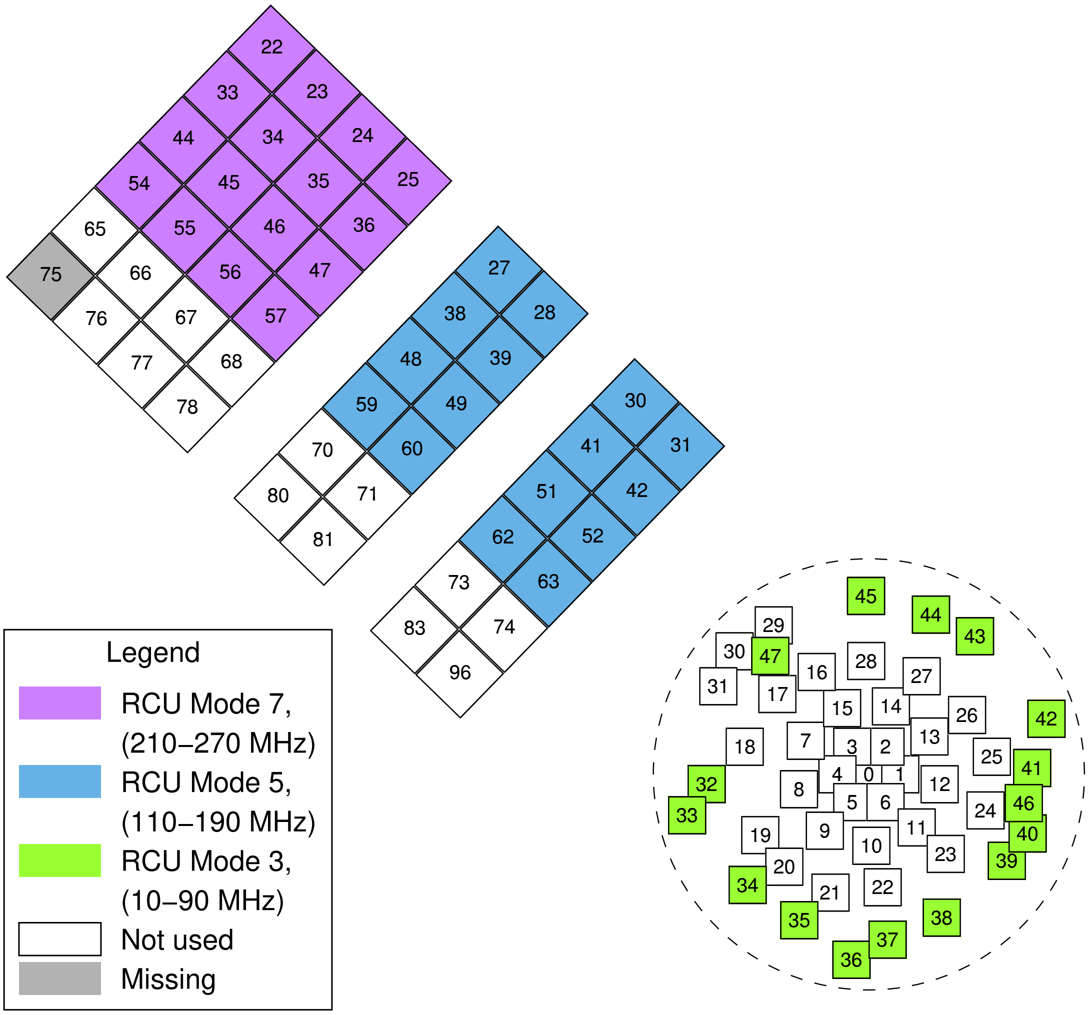

Figure 2.8: An array-status map of the KAIRA antenna layout, showing different sub-arrays used for the Mode-357 observation made for Figure 2.9.

size; both as a result of a reduced number of antennas for any given frequency. In the case of bright sources (scintillation of Cas A or solar flares), this loss of sensitivity and resolution is not problematic.

Observing with 4-bit data

The use of 8-bit sampling, allowing the formation of up to 488 beamlets, has become a regular observing mode with LOFAR. However, a series of experiments was carried out using KAIRA to evaluate 4-bit sampling. This allows the formation of up to 976 beamlets, making it possible to provide complete frequency coverage of available frequencies within the filter limits from 10 to 244 MHz for a single pointing direction. The disadvantage is the reduced headroom for observing strong radio sources and identifying RFI. This is a particular issue with LBA observations where the sharp peak in the antenna response at 58 MHz saturates when observing with

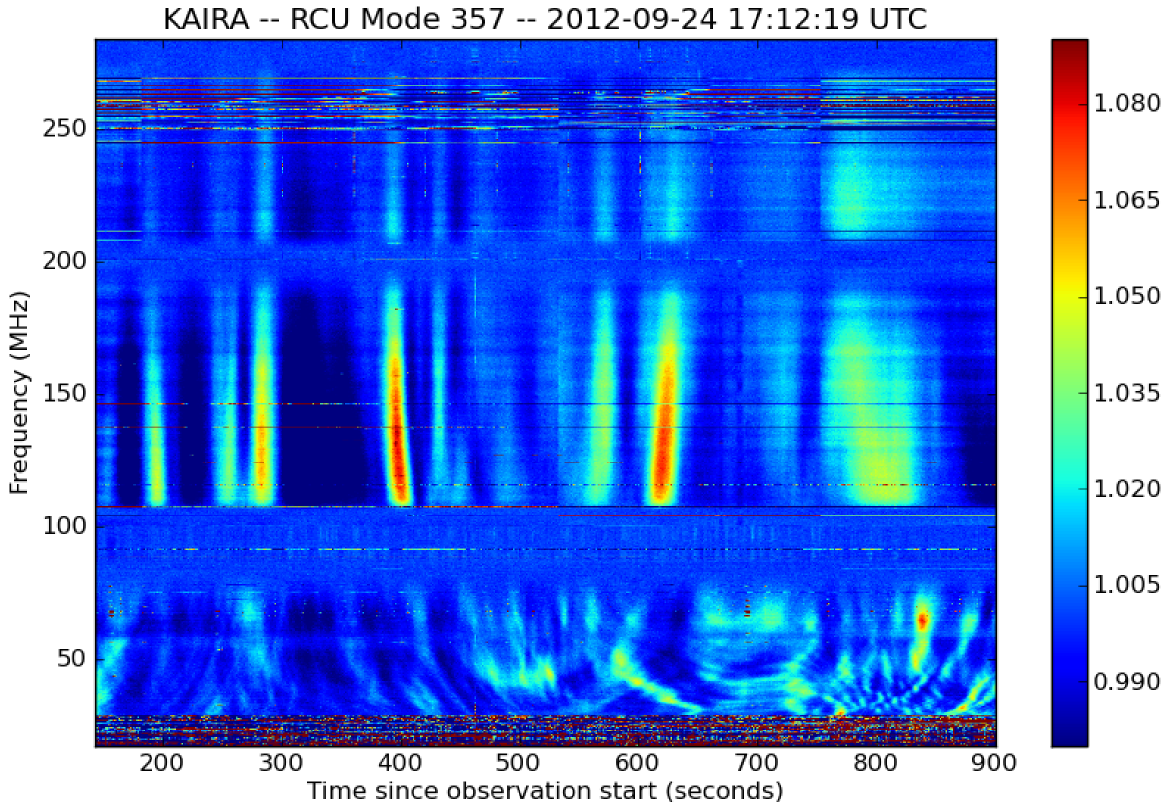

Figure 2.9: An early observation making use of mode-357. The observation is of Cas A and the features are ionospheric scintillation, showing the transition from strong-scintillation at low frequencies, transitioning to weak-scintillation at high frequencies. The data for each subband are mean-divided, raw analogue-to-digital converter units (ADU), on a dB-scale.

4-bit sampling. This is shown in Figures 12 and 13 of Paper I. The effect can be mitigated by applying varying levels of attenuation. The system has the ability to insert up to 31 levels of attenuation in 0.25 dB increments.

Ultimately, the disadvantages of the 4-bit mode outweigh the advantages it offers. For broad spectrum observing using Mode-357, the technique now employed is to observe in 8-bit mode. At low frequencies a solid packing of subbands is used, but at higher frequencies, this is spread out, using every second or every third subband, and interpolating in between. Physical processes, such as ionospheric scintillation and the emission from solar flares, do not show such dramatic frequency variation at the high VHF frequencies as they do in the upper HF band, meaning that a sparse frequency sampling method can be used successfully.

Reduced HBA array sampling

For incoherent scatter radar measurements, such as those described in Section 3.2, the presence of pronounced grating sidelobes from the HBA array is not significant. This is because the transmitted signal from the radar is of known location through the timing, thus removing any directional ambiguity. However for imaging applications, the reduction of grating lobes from the system is necessary. This can be facilitated by using an individual crossed bow-tie antenna element (or subset of antenna elements) from each HBA tile. Doing this results in a reduction in the number of redundant baselines, thus improving the instantaneous sidelobe pattern. Additionally, the beamsize of the individual tiles increases, thus allowing imaging of a larger sky area, albeit with lower sensitivity. This method is described in Paper I, where Figure 14 in the paper shows the improved response pattern.

Multi-frequency correlator

The LOFAR system has a hardware-implemented station correlator, which generates signal covariances for each polarisation and each antenna pair. These antenna pair covariances can be inverted using a Fourier transform to generate all-sky images (Chapter 5). The limitation of the LOFAR station correlator is that it can only process a single subband at a time, and integrates at 1 second cadence.

A multi-frequency correlator has been developed that permits faster integration and can operate at several frequencies simultaneously. This is achieved by dividing the array into sub-arrays, where there is only a single antenna in each sub-array. The outputs from each sub-array are then correlated in real-time using a software correlator. The number of simultaneous subbands (frequencies), N_s, that can be imaged is given by $N_s = \text{int}(N_b/N_a)$, where N_b is the number of beamlets (488, for 8-bit mode) and N_a is the number of antennas in the array (48, for the full LBA array). By reducing the number of antennas in the array, additional subbands can be observed. An example of 10 subbands imaged simultaneously is shown in Figure 2.10.

Additional details about the software correlator, and the array reduction technique, are given in Appendix H. The system was originally developed for use in multifrequency riometry. However, there are a number of limitations of that technique, which means that it was not effective to pursue that line of research. This is described in Section 4.3.

2.7 Strengths and capabilities

KAIRA provides improvements compared to existing Arctic passive-VHF facilities in four key measurement areas: enhanced sensitivity, improved time resolution, better spatial coverage and extended term of data collection. The planned minimum operational life-time of the KAIRA facility is at least one complete solar cycle (11–12 years). However, KAIRA should be effective as a long-term facility, aided by remote operation over the Internet and robust hardware, which is resilient to Arctic conditions and operates with a minimum of moving parts.

The use of modern digital signal processing technology gives KAIRA great flexibility

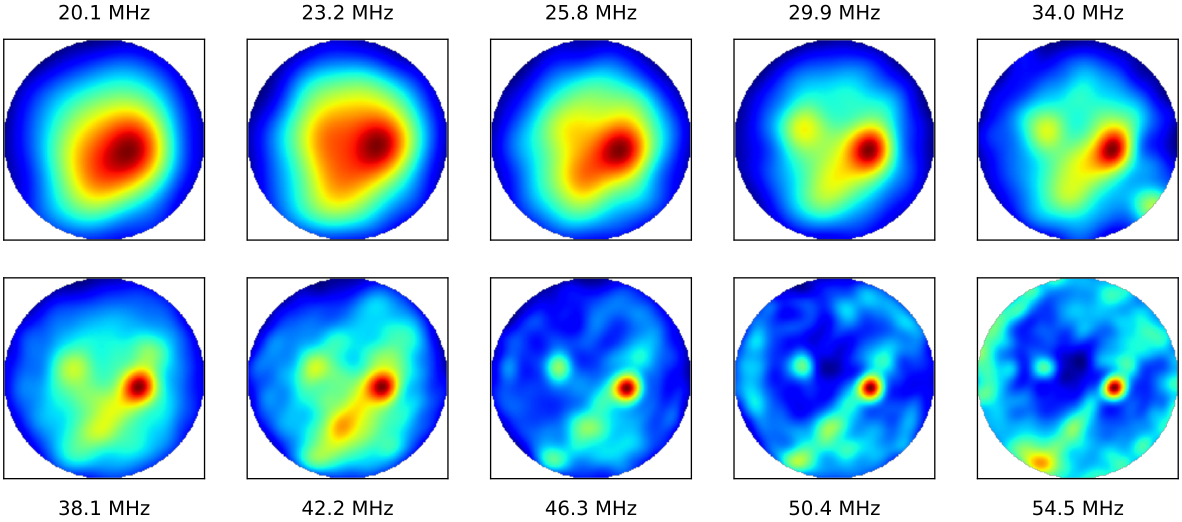

Figure 2.10: All-sky images taken simultaneously using the KAIRA Software Correlator on 10-August, 2016 at 22:00 UTC. The integration time is 73 ms, and the bandwidth of each individual image is 195 kHz. Figures are geographic (East to the right), in orthographic projection. Auto-scaling using the jet colour scheme is applied to each image using a logarithmic scale.

in conducting multiple experiments simultaneously. KAIRA is located at a position ideally suited for bistatic incoherent scatter measurements with the EISCAT VHF transmitter, and is also capable of detecting radio echoes from other nearby radar systems. It is the only such system located in the auroral-zone, which is optimal for studying energetic particle precipitation. This is discussed in detail in Chapters 5 and 6. The region where KAIRA is placed is remote and has relatively little RFI compared to other locations in Finland. Being north of the Arctic Circle means there are times of the year when the sun is always above the horizon, permitting continuous solar monitoring during that season.

This new capability, placed in this special location, permits new and unique scientific investigations and a rich science programme has been developed, which will be discussed in the next chapter.

Chapter 3

KAIRA science programme

The LOFAR radio telescope faces challenges in its astronomical observations as a result of geophysical phenomena — effects which become more extreme at high latitudes. However, these effects are interesting in their own right and form the basis for the radio remote-sensing techniques that can be used to study the Earth's near-space environment. Recently, there has been an initiative for using LOFAR for space weather (LOFAR4SW) has been proposed, which would follow on from many of the innovations that have already been established with KAIRA.

The relevant geoscience research interests of KAIRA focus on the study of the Earth's ionised upper atmosphere, in the range of approximately 60–1000 km. Although this is nominally the edge of space, the entire region is permeated by the Earth's atmosphere, and interacts with the lower layers and the magnetosphere. It is a region which has significant effect on radio communications and navigation aids, and through which low-earth-orbit satellites pass. The instrument is in the vicinity of the auroral oval, where magnetospheric-ionospheric coupling effects play an important role.

The lifetime of KAIRA will span multiple years, and the instrument is operated 24-hour-per-day. Compared to "campaign-based" radar experiments, the continuous KAIRA observations will provide seasonal statistics and help better understand the coupling relationship over the course of a solar cycle. This includes the relationship of the solar wind driving of the ionosphere (McPherron et al., 2009) and the ionospheric interaction with the lower atmosphere, in particular in relation to climatic changes (Gulyaeva and Gulyaev, 1993). This will also assist in improving understanding of the reciprocal interaction between the thermosphere and ionosphere (Rishbeth and Roble, 1992).

Particle precipitation has an effect on the chemistry of the upper atmosphere (Semeniuk et al., 2011). KAIRA provides direct measurements of energetic electron precipitation and can therefore be used as an input source for studies of variations in ionospheric composition.

KAIRA is able to observe solar-proton events, relativistic electron events, solar flares and electron precipitation during substorms. This allows assessment of the molecular population models (such as [N_2] and [O]) and the chemical changes due to geomagnetic activity (Sinnhuber et al., 2016). As a result, KAIRA observations can contribute to the refinement of the current chemistry models, e.g. the Sodankylä Ion Chemistry (SIC) modelling of nitric oxide (NOx) species produced in the mesosphere, which affect the ozone chemistry in the stratosphere (Seppälä et al., 2009). This also ties in with investigations of the space-climate relationship (Tanskanen et al., 2011).

3.1 Overview of the science programme

The scientific aims of KAIRA are illustrated in Figure 3.1; initially published by Vierinen et al. (2013), but later adapted for Paper I. The KAIRA experiments shown therein can be broadly categorised into active and passive measurements.

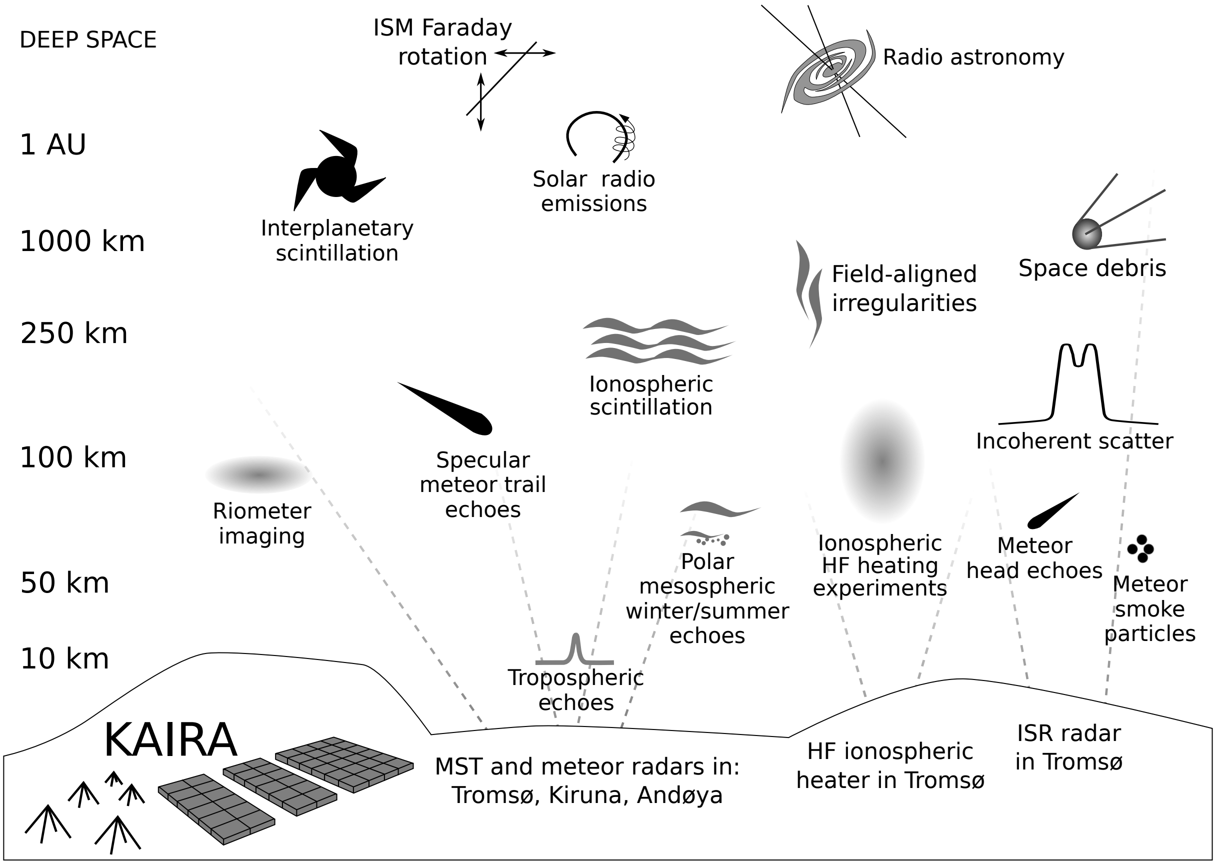

Figure 3.1: The KAIRA science diagram (Vierinen et al., 2013; Paper I, Figure 1; etc.).

Active measurements are made in conjunction with transmissions from other facilities, either coordinated or as by-products of other transmission motivations, including observations during ionospheric modification experiments with high-power HF-radiowave pumping with the EISCAT Tromsø HF heating facility (Rietveld et al., 2016). Multi-static micrometeor head-echo trajectory measurements (Close et al., 2002; Szasz et al., 2008) will be possible in conjunction with the EISCAT Tromsø VHF radar, and specular trail echoes in association with any of the many Mesosphere-Stratosphere-Troposphere (MST) and meteor radars. It is also planned to image high signal-to-noise-ratio radar targets, such as Naturally Enhanced Ion-Acoustic Line (NEIAL) events (Schlatter et al., 2013) and to track artificial hard radar targets (large debris and satellites). Additionally, multi-static, multi-frequency measurements can be made of polar mesospheric winter and summer echoes (Kelley et al., 1987).

Passive observations include measurements of interplanetary scintillation (Fallows et al., 2013; Hewish et al., 1964), solar radio emission studies (e.g. Raulin and Pacini, 2005), ionospheric scintillation (Fallows et al., 2014; Meyer-Vernet et al., 1981), and wide-band imaging riometry.

Although the primary aim is not radio astronomy, astronomical measurements are still planned, as KAIRA can be used to significantly increase the longest baseline of the LOFAR Very Long Baseline Interferometry (VLBI) network (Wucknitz, 2010). The facility complements other planned or existing radio telescopes, such as SKA (Dewdney et al., 2009; Schilizzi et al., 2010), MWA (Lonsdale et al., 2009; Tingay et al., 2013), LWA (Ellingson et al., 2009), LOFAR (van Haarlem et al., 2013), providing demonstration test beds, validation and cross-checking and accomplishing cross-discipline astrophysical and geophysical science goals.

3.2 Incoherent Scatter Radar

Multi-beam, multi-static incoherent scatter radar measurements offer the possibility of measuring instantaneously a full profile of vector velocities, which can be used, e.g., to derive ionospheric neutral winds and electric fields (Heinselman and Nicolls, 2008; Nicolls et al., 2006; Nygrén et al., 2011; Virtanen et al., 2014).

Figure 3.2 shows data from the first multi-beam, bistatic incoherent scatter radar measurement. This was performed on 21 August 2012 together with the EISCAT VHF radar shown in Figure 3.3. The transmitter is located at Ramfjordmoen, Norway, approximately 85 km northwest from KAIRA (for a map, see Figure 2.1). In this experiment, 30 dual-polarised KAIRA beams were set up, intersecting the EISCAT VHF vertical beam at altitudes between 90 km and 2000 km. The incoherent scatter autocorrelation functions were estimated using a lag-profile inversion of coded long-pulse echoes (Virtanen et al., 2008).

Since these initial measurements, KAIRA has been regularly used for bistatic ISR observations together with the EISCAT VHF radar, giving estimates of ion velocity vectors and plasma temperature anisotropies, as well as providing improved accuracy for the other parameter estimates (Virtanen et al., 2014). KAIRA is able to detect moderately-high electron densities with coarse height resolution and, in some cases, with better accuracy than the EISCAT VHF operating monostatically.

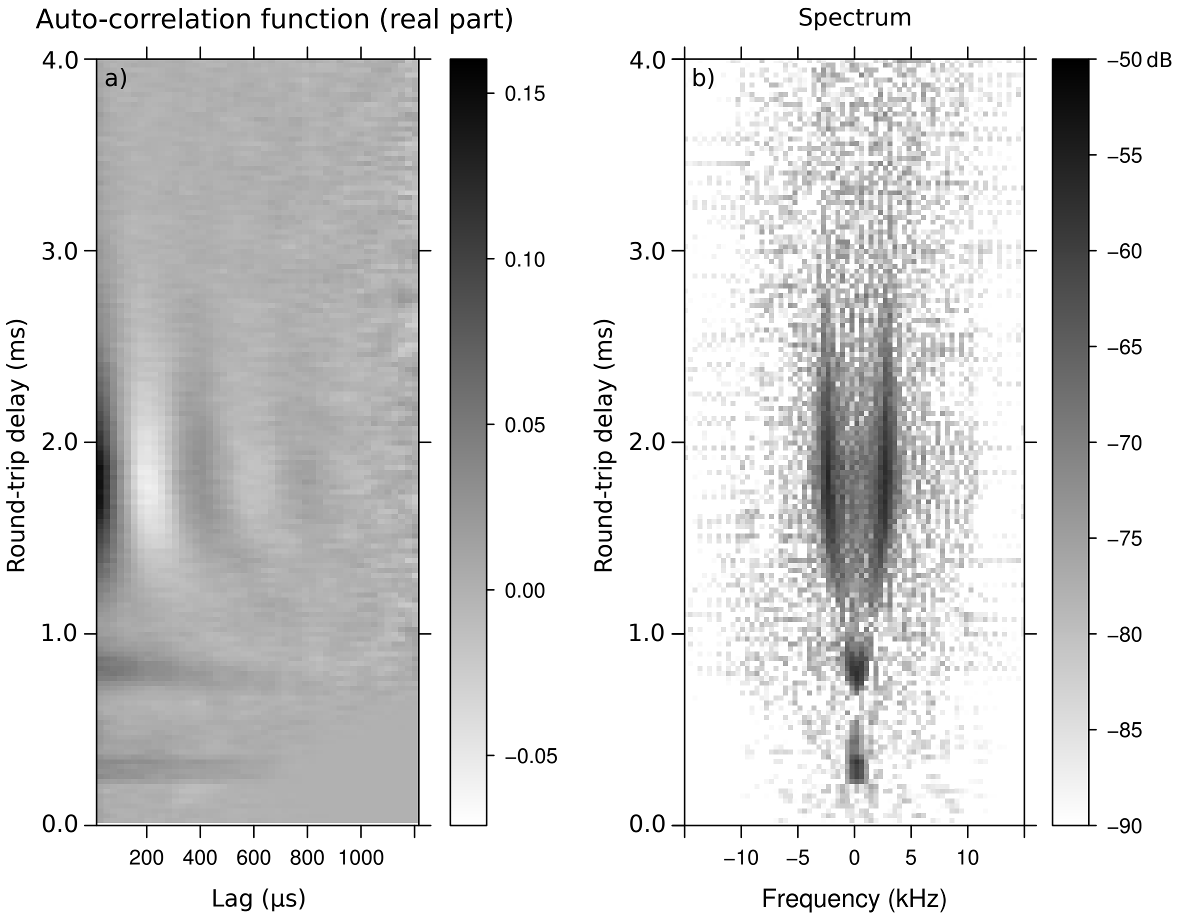

Figure 3.2: First multi-beam bistatic incoherent scatter radar measurement from KAIRA demonstrating the measurement of the lag profile auto-correlation function (a), and the derived full ionospheric incoherent scatter spectrum profile (b) with respect to the transmitter frequency (224 MHz). The vertical axis is the total round-trip delay of the signal from transmission to reception. (Paper I)

Narrower beams and higher transmitter power (such as that being proposed for EISCAT_3D) will result in higher signal-to-noise ratios.

Tetrastatic measurements

In addition to the VHF transmitter at Ramfjordmoen, the EISCAT Scientific Association has two remote receivers located at Kiruna, Sweden, and Sodankylä, Finland (see the map in Figure 2.1), each comprising a fully-steerable 32 m parabolic antenna. At the end of 2012, these were converted to operate at 224 MHz VHF operation. This permitted not only tristatic measurement with EISCAT at VHF frequencies, but with KAIRA there is a fourth station providing the ability for tetrastatic measurements. Additionally, the multi-beam capability of KAIRA means that bistatic observations can be carried out for a large altitude range along the VHF transmission

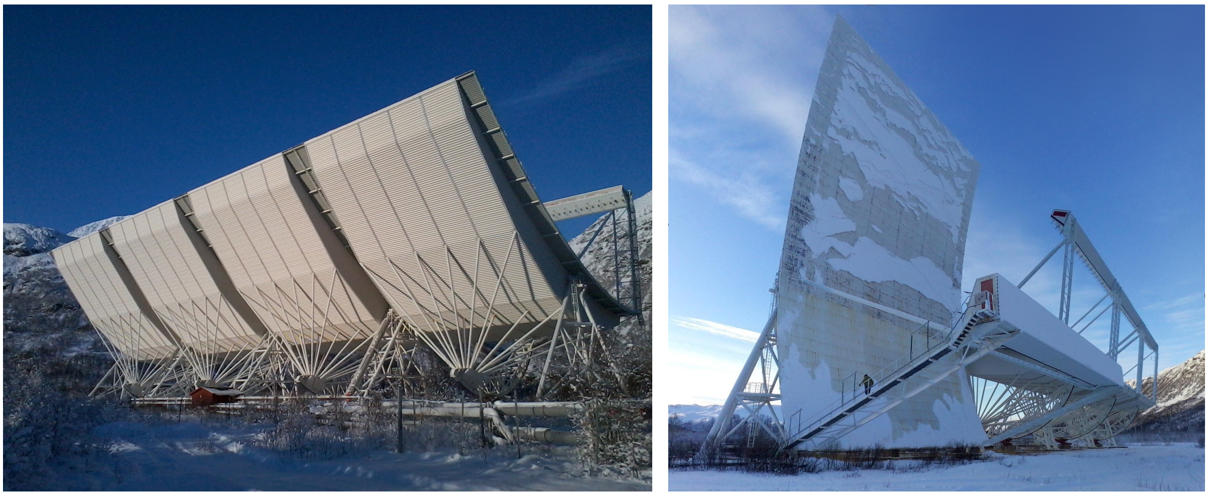

Figure 3.3: EISCAT VHF radar at Ramfjordmoen, comprising four off-axis cylindrical parabolic antennas, fed with phased-array dipoles located on a “feeder bridge”. In the left image, all four panels are aligned to create a vertical beam as used for bistatic measurements with KAIRA. In the right image, seen from the other side, one panel has been tipped forward, showing the phased array feeder bridge. Note the size of the person for scale.

beam in addition to the 3D spot measurements provided by the EISCAT remote stations.

An alternative configuration to tetrastatic would be multiple altitudes of bi- or tristatic. For example, KAIRA could receive radar echoes from the D region, while the EISCAT remote stations receive signals from higher altitudes.

3.3 Radio astronomy

VLBI

Because the KAIRA station is not directly connected to the LOFAR network, it is currently unable to participate in standard international LOFAR observations. For certain special projects requiring the highest possible resolution, KAIRA can nevertheless be an important contribution for “Very Long Baseline Interferometry” (VLBI) with LOFAR. The baseline to LOFAR station FR606 (Nançay, France) of 2600 km is twice as long as the longest within LOFAR between stations FR606 and SE607 (Onsala, Sweden).

The first successful technical test was performed on 26 March 2013 in which KAIRA and the DE601 LOFAR station (2185 km baseline) observed the bright pulsar B0809+74 in the high band in short blocks of a few minutes each. This demonstration was repeated on 13 May 2013. The results, reported in Paper I, indicated that the instrumental properties of the KAIRA–LOFAR system are not only well understood, but also that (at least during this experiment) the ionosphere is sufficiently benign to permit a robust and stable calibration and to do low-frequency VLBI on baselines of several thousand kilometres.

Pulsar environments

Since the initial tests, KAIRA has established itself as a reliable, although logistically-challenging station, but one which offers major benefits to low-frequency VLBI. At the time of writing, KAIRA was participating in monthly observations of the pulsar B1508+55.

The pulsar B1508+55 is a high-velocity pulsar, with a well-established distance due to parallax measurements (Chatterjee et al., 2005). The pulsar shows a complex pulse profile, where pulse components are seen which are the result of the radio signal either being scattered or being refracted by the interstellar medium in the vicinity of the pulsar. VLBI allows high-resolution images to be formed, which provide two spatial dimensions, with information about the third dimension being inferred from the pulse timing. The quasi-three-dimensional imaging indicates not only the morphology of the echoes, but also registration of the proper motion of the pulsar.

In addition to the sensitivity afforded by additional bandwidth, multi-frequency observations permit measurement of the dispersion of the signal and any refractive components. The alignment of any scattering indicates the nature of the interstellar medium and whether the scattering components are comparatively linear, planar or volumetric in nature (e.g. Brisken et al., 2010). Due to interstellar scintillation the measured power both varies with frequency and also with relative motion, which manifests as a time variation. By providing long-baselines to the main LOFAR network, KAIRA plays an important role in this ongoing study.

3.4 Total Electron Content

The Total Electron Content (TEC) is defined as the integral along a line of sight through the ionosphere, and is measured in TEC units (TECU):

$$\mathsf{TEC} = \int_{\ell=0}^{\infty} N_{\mathsf{e}}(\ell)\ \mathsf{d}\ell \tag{3.1}$$

where one TECU is 10^{16} electrons m^{-2} and N_{e} is the free electron density at a given distance on the path length, ℓ. Bulk changes can occur to the TEC of the ionosphere, such as the increase in ionisation at dawn.

There are two well-established techniques in radio astronomy for determining TEC. The first is a technique from VLBI which allows determination of dispersive and non-dispersive delay from dual-station cross-correlation spectra. The other is determination by analysis of Faraday rotation from a known polarised source. Both techniques are relative TEC measurements, but the first one requires a second station (and measures the relative TEC difference between them). The Faraday rotation technique can often only be used to measure relative changes along the line of sight in the direction of the ground station, because the polarisation state or the number of rotations is not known. KAIRA can register changes in rotation measure due to the ionosphere by measuring Stokes Q and U parameters for polarised sources (such as pulsars).

With EISCAT_3D, it would be possible to measure absolute Faraday rotation altitude profiles from ISR echoes, much in the same way that is done with the Jicamarca Radar (Farley, 1969).

3.5 Solar radio emissions

Radio waves are emitted and affected by the complex plasma environment in the solar atmosphere. Radiation at mm-wavelengths is a result of gyro-resonance emission above sunspots and free-free (thermal Bremsstrahlung) emission from plasma in active loops (Shibasaki et al., 2011). At frequencies below 3 GHz, plasma emission dominates (Benz, 2005). This makes diverse radio observations important in the study of solar physics and KAIRA has been used in this capacity. The HF and VHF frequencies of KAIRA complement the 11.2 and 37 GHz frequencies that are observed by the Aalto University Metsähovi Radio Observatory (MRO), also located in Finland, which has a long solar observation time-series measured in the mm- and cm-wavelength range.

The data measured with three instruments at MRO were used in a joint-study with KAIRA for the summer of 2014 (between April and October). One solar radio event, measured on 18 April 2014, was studied in detail. Seven solar flares were recorded with at least two of the three instruments at MRO, and with KAIRA during the chosen time period (Kallunki et al., 2015). It was possible to investigate flare pulsations, flare statistics and radio spectra of single flares, due to the broad frequency range of the observations. The multi-frequency data gives information about different depths in the solar corona.

Due to local RFI, frequencies below 200 MHz at Metsähovi cannot be used for observations. However, at the KAIRA site, RFI is not as problematic as at MRO, which reasserts KAIRA's value in solar observations. Another asset of KAIRA is that its sensitivity is very high compared to the standard solar instrumentation used at MRO and other solar observatories worldwide.

Both KAIRA and MRO have flexible observing policies, which enables easy scheduling of joint measurements. The northern location of both MRO and KAIRA make 15-hour joint solar observations possible during summer. KAIRA has incorporated a solar observing programme as part of its routine observing to provide solar monitoring statistics and to improve the chances of observing more significant events. (Figure K.2 is an example of a Type II solar radio burst, observed with KAIRA.)

3.6 Ionospheric scintillation scattering regimes

When a wave passes through a medium it may be subjected to diffraction and refraction effects. In the case of radio waves passing through a plasma, local variation in the plasma parameters can result in fluctuations of the detected phase and amplitude of the signal, referred to as scintillation. Between the source of the radiation and the observer, there are multiple environments where this can occur (with corresponding resultant scintillation). These are the Interstellar medium (Interstellar Scintillation), the interplanetary medium (Interplanetary Scintillation, IPS) and the Earth's ionosphere (Ionospheric Scintillation).

The wide bandwidth capability of KAIRA at HF and VHF frequencies, combined with its high-latitude location in the ionospherically-dynamic auroral zone has resulted in significant advances in the study of ionospheric scintillation (Paper I). For example, the evolution of scintillation from weak to strong scattering regimes has been directly observed in dynamic spectra. An example of the broadband ionospheric scintillation signature can be seen in Figure 2.9. "Scintillation arcs", seen previously in two-dimensional power spectra from interstellar scintillation observations, have been noted for the first time using observations of ionospheric scintillation, which allows the study of the plasma structures giving rise to the scintillation (Fallows et al., 2014). These allow measurement of the transverse speed of the ionosphere.

KAIRA has been measuring broadband Cas A flux continuously since January 2015. These measurements have been used for statistical studies of ionospheric scintillation (Szponarski et al., 2015).

Scintillation-producing irregularities

Magnetic field-aligned irregularities with scale sizes from meters to tens of kilometres are generated by different plasma instabilities and may cause disruption to VHF radio waves. These high-latitude scintillations are caused by density gradients associated with polar-cap patches (Carlson, 2012). Polar cap patches are defined as 100 km scale regions with F-region plasma densities 2–10 times larger than the background density in the polar cap, and the gradient drift instability is considered as the dominant instability mode. However, Prikryl et al. (2011) found evidence that cusp irregularities are driven by polar cap patches while night-side auroral scintillations seem to be driven by energetic electron precipitation.

3.7 Polar mesospheric echoes

Polar mesospheric summer echoes (PMSEs) are strong radar echoes that result from neutral air turbulence in combination with a significantly reduced electron diffusivity. The diffusion inhibitor is the presence of charged ice aerosol particles, and this results in long lifetimes of resultant turbulent plasma structures (Rapp and Lübken, 2004). They occur in the D-region (with a peak at 84–86 km), are much narrower (typically 1.5 km thick) and may occur in multiple layers. They can also move in altitude, indicating the passage of acoustic-gravity waves (Williams et al., 1989). They occur in summer (typically June–August, with maximum in July).

Experiments using the full beam-steering and beam-forming capabilities of MAARSY and KAIRA, respectively permit better resolution of the spatial and temporal characteristics of PMSEs. Additionally, the bistatic nature of the MAARSY–KAIRA baseline will assist in constraining the angular dependence of PMSE (Chau et al., 2018).

3.8 Riometry

All of the above observations are detecting radio waves, whether naturally occurring, or the reflection of artificially generated radio signals from radars and other transmitters. However, one technique, is looking for the absence of radio waves, rather than the radio waves themselves. This is riometry, and the theory and practice of it is described in detail in Chapter 4. Riometry is a major part of the KAIRA science programme and multiple riometry observations modes are employed.

In the first instance, a riometer measures the power of these cosmic radio emissions. Radio waves are naturally attenuated by collisions between free electrons and neutrals, typically in the ionospheric D region (70–90 km) and, at times of ionospheric disturbance such as during aurorae or other particle precipitation events, increases in the electron density cause enhanced absorption of the radio signals (Hargreaves, 1995).

Polar-cap absorption and solar proton events

Solar coronal mass ejections may generate large fluxes of protons, which may enter the Earth's magnetosphere where they are guided by the magnetic field to precipitate into the polar cap region (Patterson et al., 2001). As the protons can have very high energies, up to tens of MeVs, they may reach down to the mesosphere and stratosphere, providing a direct connection between the Sun and the Earth's middle atmosphere.

In such cases of geomagnetic storms, polar radio blackouts can occur lasting several days due to an enhancement of ionisation in the D region. These are known as polar-cap absorption (PCA) events, categorised as such when riometric absorption exceeds 1 dB at 30 MHz. On average there are 6 PCA events per year, and each can last several days (median is 2.5) (Hunsucker and Hargreaves, 2002). Because Kilpisjärvi is in the auroral zone (at magnetic L-shell of L=5.9) and not directly in the polar cap, the absorption there will be reduced, although the effect is still discernible.

The effective recombination rate in the lower ionosphere varies due to changes in composition and the fraction of negative ions, so one use of the PCA events is to measure the coefficient variations over a range of heights in the mesosphere. The proton spectrum may be measured by satellites and the ionisation rate can be computed using a model of the neutral atmosphere. Electron density profiles can be determined from rocket measurements or by incoherent-scatter radar. However, there is a large spread in the observational data and rockets and ISR do not permit routine monitoring. Multi-frequency riometry measurements — possible with KAIRA — allow the observation of these extreme events and makes it possible to derive information about electron densities at low altitudes ($\approx$50 km).

Because the proton influx during a PCA decays relatively slowly, the effects of daily variations in the complex chemistry of the region may be detected. Comparisons can be made between magnetically conjugate stations. The dominant effect is the diurnal variation in absorption, typically by a factor of five. This is variation of the ratio of the concentrations of the electrons and negative ions — in a dark ionosphere, electrons combine with molecular oxygen to for O_2^- ions. Only ionospheric electrons contribute to absorption, which changes with the altering ratio of species, even if the production rate remains constant (Verronen et al., 2005).

Nitric oxide (NOx) production during a PCA event can exceed the annual production of that produced by cosmic rays (Verronen et al., 2005). NOx acts a catalyst to destroy ozone up to a factor of four, depending on height. Thus NOx production is part of a complex chain of effects that relate PCA particle precipitation with changes in atmospheric chemistry.

Interferometric riometry

Until now, riometers have typically been one of two designs: *wide-beam* and *imaging* (Honary et al., 2011). The imaging case is achieved by forming multiple, narrow beams on the sky. Each one then constitutes a “pixel” in the riometric image. However, with the advent of wide-field phased-array radio telescope systems, it may now be possible to use an interferometric technique to accomplish riometric imaging. Unlike a multibeam imaging riometer, which has discrete beams, the interferometric imaging riometer has continuous coverage.

Another limitation of existing riometers is that they operate at a single frequency (typically 30–50 MHz). However, it has been demonstrated that multi-frequency riometry can be used to determine electronic density height profiles (Kero et al., 2014).

The development of a Fourier-based interferometric riometer technique for measuring electron density induced ionospheric opacity is a major component of this thesis. It will be discussed in depth in Chapters 4 and 5.

3.9 Other envisaged uses

In addition to the research that has been outlined in this chapter, there are numerous areas of scientific investigation which are well within the capability of KAIRA, but have not been attempted. Therefore, to conclude this chapter a small selection of these are discussed.

Despite the relatively low frequency, KAIRA has several possibilities for contributing to space debris monitoring and space situational awareness. Measurement of beacon satellites formed part of the early initiative during the commissioning phase of the instrument. There is also potential to use the instrument for bistatic observations in conjunction with the forth-coming EISCAT_3D.

KAIRA can also be used for meteor studies. It can observe meteor head echoes and trail echoes from a number of radar transmitters. For example the MAARSY radar at Andenes (Latteck et al., 2010, 2012). Multi-static head echo observations are useful for studies of micro-meteoroid radiants (Szasz et al., 2008). Multi-static specular trail echo observations on the other hand are useful for determining regional neutral winds (Stober and Chau, 2015).

The measurement of interplanetary scintillation (IPS) has been used for many years as a remote sensing technique for studying the solar wind. This, complements localised single-point measurements from spacecraft. Tomography from multiple measurements is used to estimate solar wind density and speed. In-depth analysis of single observations can be used to study solar wind streams and Coronal Mass Ejections along the line-of-sight. At the time of writing, IPS measurements with KAIRA have not yet been attempted although KAIRA has been used to verify IPS measurements (Fallows et al., 2016). However, the technique is valid and thus may well be attempted in future. The high-latitude of KAIRA means that long-duration IPS observations would be possible in summer months.

The use of the LOFAR radio telescope has been proposed for monitoring space weather conditions (Oberoi and Kasper, 2004) and KAIRA would be capable of contributing to such a programme.

The multibeam capability of KAIRA would permit imaging of tropospheric and stratospheric echoes (e.g. Woodman, 1980). With the implementation of EISCAT_3D, it would be possible to carry out interferometric radar imaging, allowing any spatial structure to be discerned.

From all of the above cases, both attempted and proposed, the multi-purpose geophysical remote sensing capability of KAIRA is clear. The flexibility of observing modes, combined with the versatile nature of the radio phased array, promises many opportunities to tackle challenging scientific problems during the lifespan of the facility.

Chapter 4

Ionospheric absorption of cosmic radio noise

Electromagnetic radiation is generated naturally throughout the universe. The primary source of emission in the 10–1000 MHz range is radio synchrotron emission from the Galaxy (e.g. de Oliveira-Costa et al., 2008). In addition to this, there are bright “radio stars” (Baars et al., 1977). The brightest two are the radio galaxy Cygnus A (Cyg A) and supernova remnant Cassiopeia A (Cas A). Although there are many other discreet sources, these are not bright enough to be significant for radio absorption experiments at KAIRA. The Sun is a variable radio source which can range from between being undetected with KAIRA to being the brightest source in the sky by several orders of magnitude (Kallunki et al., 2015). The times that the Sun can be detected are sporadic and, for the most part, the static Galactic synchrotron and radio stars form the radio sky for KAIRA, as shown in Figure 4.1.

As cosmic radio waves pass through the ionosphere, they are subjected to various effects, such as refraction, dispersion and absorption. The magnitude of these effects is determined by plasma parameters such as the magnetic field, the electron density and the electron-neutral collision frequency. These conditions vary significantly as a function of altitude within the ionosphere. They are also dependent on the wavelength of the incoming radiation and local magnetic field strength.

Although some electron-ion collisions results in F-region absorption, the absorption effect is typically more significant in the ionospheric D region (80–90 km), where there is sufficient ionisation or electron influx, but the densities remain sufficiently high to ensure a high rate of collisions of these species. Ionisation of that part of the atmosphere is typically caused by high-energy particle precipitation as well as UV radiation and X-rays. At times of ionospheric disturbance, such as during aurorae or other particle precipitation events, increases in the electron density cause enhanced absorption of the radio signals (e.g. Hunsucker, 1991).

The riometer is a stable radio receiver with steerable (or fixed, known) pointing direction and known beam-pattern. The riometer operates at some frequency above the penetration frequency of the ionosphere so that it receives the signal coming

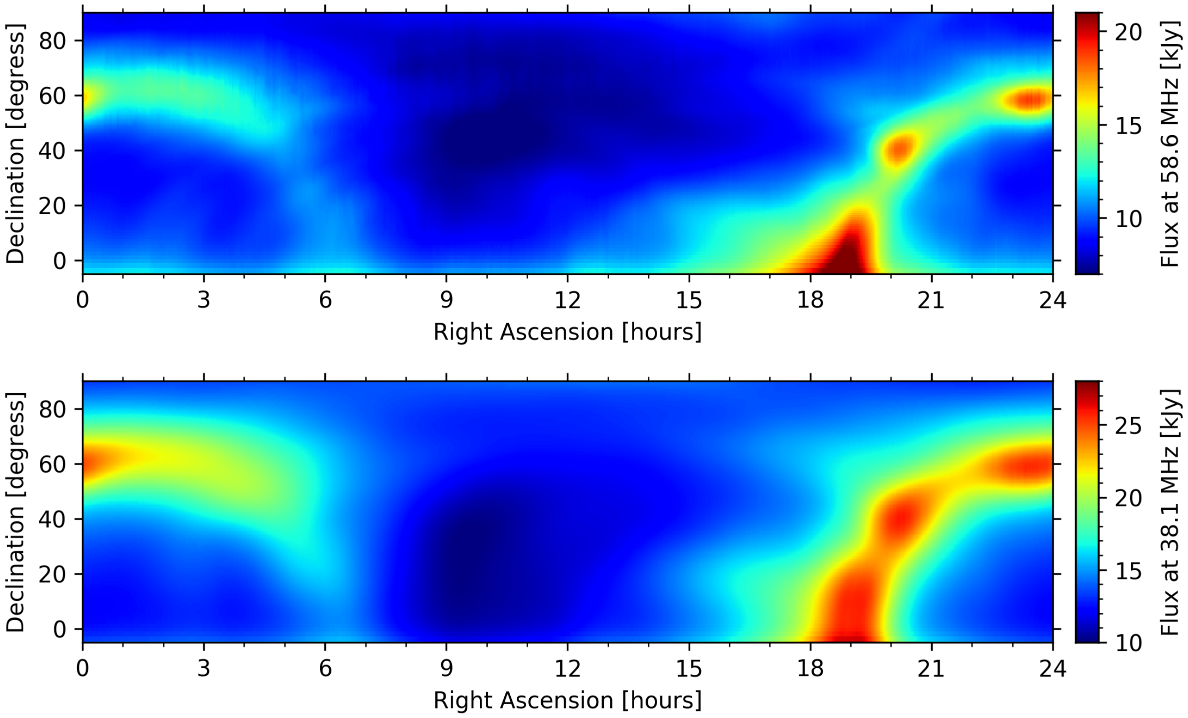

Figure 4.1: The northern radio-sky at 58.6 and 38.1 MHz observed with KAIRA. Flux at negative declinations starts to be unreliable, as that direction is close to the elevation limit of the LBA aerials. The discrete bright sources at 20.0h,41° and 23.4h,59° are the radio galaxy Cyg A and supernova remnant Cas A, respectively.

from space (the cosmic radio noise). Since the intensity of the cosmic radio noise does not change appreciably over the course of the observations, reductions in the received power are interpreted to mean that the signal has been absorbed somewhere in the ionosphere. Anomalous absorption at a given time is determined by comparing the received signal to the signal that would be expected as the result of transmission through an undisturbed ("quiet") ionosphere.

4.1 Radio absorption

This section gives a brief overview of the key points of radio propagation theory which are needed to understand riometric absorption. Definitions of wave related functions as used in this work are presented to provide context for the theoretical development.

Wave theory

If a source causes an oscillating displacement, $A = A_0 \cos \omega t$, which propagates at a speed v in the x-direction, then the displacement at distance x from the source is defined as

$$A = A_0 \cos\omega(t - x/v) \tag{4.1}$$

$$= A_0 \cos(\omega t - 2\pi x/\lambda) \tag{4.2}$$

where t is the time since emission and λ is the wavelength of the wave. Here x and t are conventional position and time variables, respectively. The angular frequency, ω (rad.s^{-1}), is related to the frequency in hertz, ν by $\omega = 2\pi\nu$.

Refractive index

The phase velocity of a wave depends on the medium through which it travels. For an electromagnetic wave in a vacuum, $v = c$, the speed of light. For all other media, the phase velocity is given by

$$v = c/n \tag{4.3}$$

where n is the *refractive index*. If the refractive index varies as a function of frequency, then the medium is said to be dispersive and the result is that waves of different frequencies travel at different speeds.

Appleton-Hartree Equation

The general formula for the refractive index of HF radio waves in an ionised medium with a background magnetic field was developed in parallel by various scientists in the 1920s and 30s. The resultant equation for the refractive index is generally referred to as the Appleton-Hartree equation (Appleton, 1932) and is shown in condensed form in Equation 4.4.

$$n^2 = 1 - \frac{X}{1 - iZ - [\frac{Y_\perp^2}{2(1-X-iZ)}] \pm [\frac{Y_\perp^4}{4(1-X-iZ)^2} + Y_\parallel^4]^{\frac{1}{2}}} \tag{4.4}$$

where n is the complex refractive index, with complex components as $n = \mu - i\chi$ (Hargreaves, 1992, pp 21–22). The X, Y and Z terms are frequency ratios, defined as:

$$X = \omega_\mathrm{N}^2/\omega^2; \quad Y = \omega_\mathrm{B}/\omega; \quad Y_\parallel = \omega_{\mathrm{B}_\parallel}/\omega; \quad Y_\perp = \omega_{\mathrm{B}_\perp}/\omega; \quad Z = \nu/\omega; \tag{4.5}$$

where ω_N is the plasma frequency, ω_B is the gyrofrequency and ν is the electron-neutral collision frequency. The parameters $\omega_{\mathrm{B}_\parallel}$ are the quasi-transverse and quasi-longitudinal components respectively of ω_B with respect to the direction of propagation. Hargreaves (1992) defines θ as the angle between the propagation direction and the magnetic field, thus giving

$$\omega_{\mathrm{B}_\perp} = \omega_\mathrm{B} \sin\theta; \tag{4.6}$$

$$\omega_{\mathrm{B}_\parallel} = \omega_\mathrm{B} \cos\theta; \tag{4.7}$$

Gyrofrequency

The theory and examples for the determination of the electron gyrofrequency are set out in Hargreaves (1992, pp 14–15) and are used as the basis for the explanations shown here. In a magnetic field, a moving charged particle will be subjected to a Lorentz force and therefore orbit in circles. This force, **F** is given by

$$\mathbf{F} = q \cdot \mathbf{v} \times \mathbf{B} \tag{4.8}$$

where q is the charge on the particle, **v** is the electron's velocity and **B** is the magnetic flux density. The direction of this force is normal to both **v** and **B**. The radius of the circle, r_B, can be determined by equating the Lorentz force with the equation of centripetal force:

$$\mathbf{F} = q \cdot \mathbf{v} \times \mathbf{B} = mv^2/r_\mathrm{B} \tag{4.9}$$

$$r_\mathrm{B} = mv/|q|B \tag{4.10}$$

where B is the strength of the magnetic field, $B = |\mathbf{B}|$. The circumference of the circle is $2\pi r_\mathrm{B}$ and thus the orbital period P is given by

$$P = 2\pi r_\mathrm{B}/v = 2\pi m/|q|B \tag{4.11}$$

This gives an angular frequency, referred to as the *gyrofrequency*, as:

$$\omega_\mathrm{B} = 2\pi/P = |q|B/m \tag{4.12}$$

In ionospheric plasmas, particles typically are singularly ionised (single electrons or singularly-ionised ions), so q is typically e (the electron charge). Therefore it is typically the mass of the species and strength of the magnetic field that will affect the gyroradius and gyrofrequency.

Above KAIRA, the strength of the magnetic field is approximately 50 μT. The charged species are either electrons or a variety of ionised species (atomic ions, molecular ions, clusters of ions and charged dust). In the case of an electron the charge and mass are q_e =-1.6×10^{-19} C and m_e =9.1×10^{-31} kg, respectively. Using Equation 4.12, the electron gyrofrequency, $f_e = \omega_e/2\pi$ ≈1.4 MHz.

Ions and other larger species have much higher masses, resulting in a drastically lower gyrofrequency. For example, an oxygen ion, O$^+$ has mass, $m_{\mathrm{O}^+} = 2.7 \times 10^{-26}$ kg which results in a gyrofrequency of ≈48 Hz.

When $\omega_\mathrm{B} \ll \omega$, where ω is the angular frequency of a radio wave, then the effect of the gyrofrequency on the radio propagation is negligible. As a result the terms from the ions can be ignored in subsequent calculations.

Plasma frequency

The electrons have a significantly smaller mass than the ions in the plasma and are thus more easily displaced. If the electrons are collectively displaced from the ions in the plasma environment, a displacement field is created. The *plasma frequency* is then the natural oscillation frequency for electrostatic perturbations within a plasma. Hargreaves (1992, pp 16–17) derives the electron plasma angular frequency using the simplest charge separation model.

$$\omega_{\mathsf{N}} = \sqrt{\frac{N_{\mathsf{e}} e^2}{\epsilon_0 m}} \tag{4.13}$$

(in units of rad.s^{-1}). For electrons, the plasma frequency only depends on physical constants and the electron density, N_{e}, per cubic metre.

$$\omega_{\mathsf{N}} \approx 56.4\sqrt{N_{\mathsf{e}}} \tag{4.14}$$

Collision frequency

The collision frequency refers to the average rate of collision between charged particles and neutral species in a plasma. At D-region altitudes, the atmosphere is only a partially-ionised plasma and a comparatively large number of neutral species are present. Even at the E region, the degree of ionisation is only of the order of one part per million (Rees, 1989).

Although the collisions themselves are random, the collision frequency is well-defined for Maxwellian particle distributions. As a result, the use of a single number for its characterisation suffices in most situations (Stubbe, 1981).

The collision frequency is defined as:

$$\nu = N\sigma(v)\,v \tag{4.15}$$

where N is the volume density of the background medium and $\sigma(v)$ is the collisional cross-section of the particle for a given collisional velocity, v. A more recent, detailed treatment is given by Zawdie et al. (2017), which compares the differences between the traditional Appleton-Hartree equation (Equation 4.4) and a ray-tracing approach.

In the case of the Earth's atmosphere, the molecular species and the atmospheric density determine the collision frequency. When required, this thesis uses a nominal profile based on the experimental results published by Aggarwal et al. (1979). For the purposes of this work, only the electron collision frequency is significant. It is referred to as simply collision frequency, ν, for sake of brevity.

4.2 Riometric absorption

The absorption of HF radio waves in the ionosphere is treated by several sources (e.g. Davies, 1965; Hunsucker and Hargreaves, 2002). If collisions are present $(Z \neq 0)$ and magnetic field terms are neglected, then the refractive index is

$$n^2 = 1 - \frac{X}{1 - iZ} = 1 - \frac{\omega_{\mathsf{N}}^2}{\omega(\omega - i\nu)} \tag{4.16}$$

Here, the refractive index is complex $(n = \mu - i\chi)$ and a wave propagating through the medium in the positive x-direction varies with time, t, and distance, x, as

$$\exp(-x\chi\omega/c)\cos\omega(t - x\mu c) \tag{4.17}$$

The exponential term gives the decay of the wave amplitude with distance with the absorption coefficient, κ, being

$$\kappa = \chi\omega/c \tag{4.18}$$

expressed in nepers per metre. In other words, the amplitude falls to $1/e$ of the original magnitude in a distance of $1/\kappa = c/\chi\omega$. Applying the expression for the plasma frequency to Equation 4.16 and expressing it as an absorption coefficient in the form of Equation 4.18, the following is obtained.

$$\kappa = \frac{\omega}{c}\cdot\frac{1}{2\mu}\cdot\frac{XZ}{1+Z^2} \quad = \quad \frac{e^2}{2\epsilon_0 mc}\cdot\frac{1}{\mu}\cdot\frac{N_\mathrm{e}\nu}{\omega^2+\nu^2} \tag{4.19}$$

If the collision frequency, ν, is small relative to the angular wave frequency, ω, then the absorption coefficient is proportional to the product of the electron density, N_e, and the collision frequency.

The absorption can be measured by taking the ratio of the measured power, P, and the power that could be expected in the case when there is no abnormal absorption activity. This is referred to as the' 'quiet" power, P_q. The measured power is proportional to the square of the radio signal amplitude. Thus the absorption can be expressed in units of decibels (dB) as:

$$A = 10\log_{10}(P_\mathrm{q}/P) \tag{4.20}$$

This can be related to Equation 4.19, and the physical constants can be replaced with a single numerical ratio constant term:

$$\frac{e^2}{2\epsilon_0 mc} = 5.307\times10^{-6}\ (\mathrm{Np}) \tag{4.21}$$

The neper is the natural-logarithmic ratio unit, related to the decibel — a base-10 logarithm system — via:

$$1\ \mathrm{Np} = 20\log_{10} e\ \ \mathrm{dB}\ \ \approx 8.686\ \mathrm{dB} \tag{4.22}$$

Equation 4.19 can thus have the physical constants quantified and convert from nepers to decibels. The simplification that $\mu = 1$ is made, because $\omega_N^2/\omega^2 \ll 1$. This is the non-deviative absorption case where the velocity is not altered and thus no wave deflection or bending occurs.

The resultant expression is then:

$$A = 4.611\times10^{-5}\int_L \frac{N_\mathrm{e}\nu}{\omega^2+\nu^2}\,\mathrm{d}\ell\ (\mathrm{dB}) \tag{4.23}$$

where $d\ell$ is an incremental length over the total radio path, L. Equation 4.23 is the absorption when there is no magnetic field present. To add the magnetic field effects, there are two approximations which are considered: these are the quasi-longitudinal and quasi-transverse conditions. The treatment has been described in several works (e.g. Davies, 1965; Hargreaves, 1992; Hunsucker, 1991). The quasi-transverse is irrelevant. For the quasi-longitudinal approximation and non-deviative absorption, combined with values of $\mu^2 \gg X^2$, it is possible to rewrite Equation 4.19 as:

$$\kappa = \frac{e^2}{2\epsilon_0 mc} \cdot \frac{N_\mathrm{e}\nu}{(\omega \pm |\omega_{\mathrm{B}_\parallel}|)^2 + \nu^2} \tag{4.24}$$

From this, the generalised riometry equation can be derived in a similar manner:

$$A = 4.611 \times 10^{-5} \int_L \frac{N_\mathrm{e}\nu}{\nu^2 + (\omega \pm \omega_{\mathrm{B}_\parallel})^2}\, \mathrm{d}\ell\ (\mathrm{dB}) \tag{4.25}$$

Simplifications

It is possible to avoid the more complicated treatment with some further approximations to simplify the relationship. Since the collision frequency decreases sharply with altitude, most non-deviative absorption occurs in the lower ionosphere, and the integrand is maximised when the terms of the denominator of Equation 4.25 are equal. Additionally, the gyrofrequency may be neglected if it is much smaller than the radio frequency, which is the case at frequencies greater than approx. 30 MHz, in which case Equation 4.25 simplifies to:

$$A(\mathrm{dB}) = \frac{1.168 \times 10^{-18}}{[f(\mathrm{MHz})]^2} \int_L N_\mathrm{e}\nu\, \mathrm{d}\ell \tag{4.26}$$

for the total absorption over the path, where $f(\mathrm{MHz})$ is the observing radio frequency in megahertz. As the dependency is inversely proportional to the square of the observing frequency, it is possible reduce observations to a common frequency (e.g. 30 MHz) for comparison between instruments Hunsucker and Hargreaves (2002, p 340) with:

$$A(30\,\mathrm{MHz}) = A(f)\, 30^2/f^2 \tag{4.27}$$

Unlike conventional riometers, the multi-frequency capability of KAIRA allows specific frequency selection, allowing direction comparison to be made with conversion.

4.3 Multi-frequency riometry

Equation 4.25 is also a function of the observing frequency. Historically, riometers have typically been single-frequency, with narrow bandwidth (Honary et al., 2011). The inverse-squared dependency of absorption the observing frequency (Equation 4.26), means that lower frequencies leads to larger absorption, limited only by the presence of shortwave radio communication RFI at frequencies of approximately 25 MHz and below. Additionally, a narrow bandwidth avoids calibration issues associated with absorption frequency dependency across the band. Most riometers therefore operate in the 25–45 MHz range, with bandwidths of order 100–200 kHz. The interferometric riometry described in Chapter 5 is also of this nature, with the bulk of the observations being made at 38.1 MHz with 195 kHz bandwidth. An example of multi-frequency absorption caused by a substorm event is shown in Figure 4.2. The use of riometry for substorm research is discussed in detail in Chapter 6.

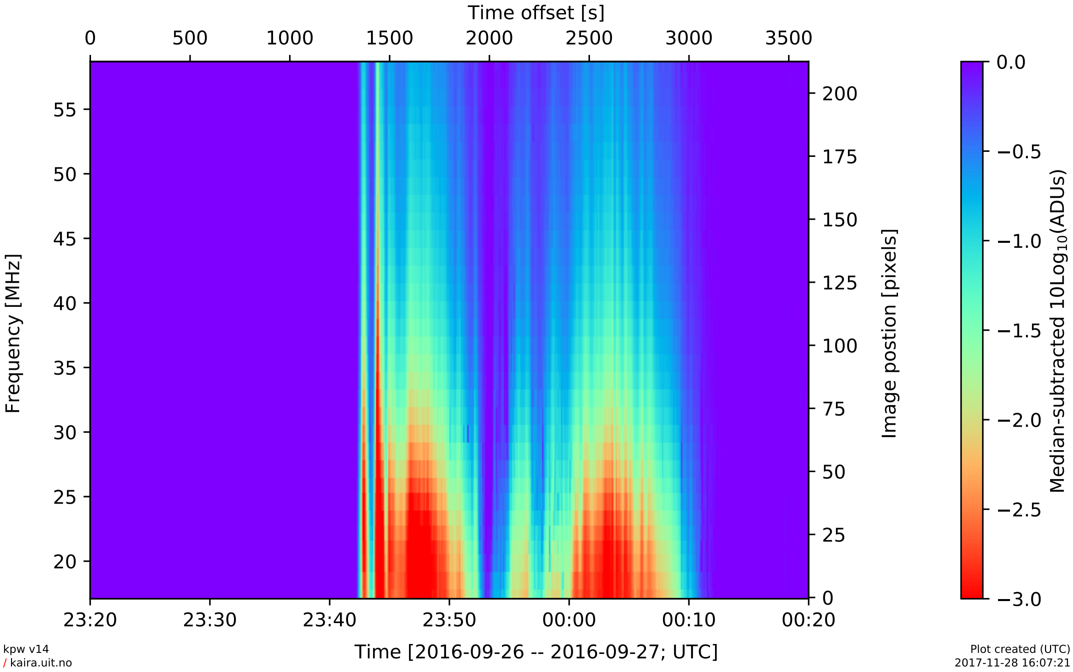

Figure 4.2: Regridded, median-subtracted power spectrum for the zenith beam.

However, there is good motivation to implement riometers which are capable of operating at multiple frequencies.

Measuring a wide-bandwidth is not necessarily helpful due to the potential incursion of RFI. However, observing a range of frequencies on independent channels results in the same increase in sensitivity. This is important for small variations in absorption caused, for example, by pulsating aurora (Grandin et al., 2017).

Increasing the number of frequency channels measured makes the instrument more robust to RFI. The availability of different signal streams makes identification of the RFI easier, and also allows contaminated channels to be dropped without significant loss of total bandwidth coverage by the measurement. These improvements apply not just to the absorption measurement itself, but also to the determination of the quiet-day calibration.

In addition to the artificial RFI which pervades this frequency band, there is also "natural interference" from Type II and Type III solar radio bursts. These are associated with heightened solar activity and thus also with ionospheric CNA. Although it is possible to use external instrumentation to identify such events, it is nevertheless useful to have the capability in the riometer itself to recognise, and thus exclude, this interference.

The use of multiple frequencies also helps mitigate the effects of scintillation. Geophysical conditions where strong absorption is present are often the same as those causing strong scintillation of bright radio stars (at these frequencies, particularly Cas A and Cyg A). Even if not in the direction of observation, these sources can result in strong sidelobe contamination, resulting in a degradation of the riometry measurement.

While it is possible to time-average the data to reduce this effect, that also results in the loss of information about rapidly changing absorption features. The scintillation has a different frequency signature to that of the absorption, allowing modelling of the absorption which reduces the scintillating effect.

4.4 Electron-density inversion

The full riometry equation (Equation 4.25) suggests that there is a frequency and polarisation relationship between absorption and the electron-density profile. Therefore it is of interest to investigate the possibility of deriving the electron density as a function of height using multifrequency measurements.

The determination of electron density profiles, primarily in the D and E region of the ionosphere, can be attempted using inverse problem techniques and radio absorption data. The original work done on the inversion problem was by Parthasarathy et al. (1963). In that work, three parameters were fitted. Since then, various authors have attempted the determination of the maximum likelihood model coefficients (Belikovich et al., 1964; Lavergnat and Berthelier, 1973). More recently, Kero et al. (2014) and Martin et al. (2016) have indicated that this technique produces results comparable to those obtained using an alternative method (specifically, incoherent scatter radar), although both acknowledge that the problem is not well-posed. For this work, a standard inverse problem technique was used. The relation between electron density and absorption (Equation 4.25) can be expressed as:

$$\mathbf{d} = \mathbf{G}\mathbf{m} \tag{4.28}$$

where **d** is the data, **G** is the forward model and **m** is the model. Here, the data, **d**, is the absorption measured at a given frequency and polarisation mode. The frequency is defined by the subband channel of KAIRA and the polarisation mode (O-mode or X-mode) is determined from the Stokes parameters that can be measured when raw-voltage sampling is used.

To model KAIRA observations, we add artifical noise, η, which follows a normal distribution, comparable with one-tenth of typical KAIRA observation noise. The model, **m**, is the electron density, $N_e(h)$ for a given height. The range of heights used can be varied, but for this initial test a range of 65–110 km was selected, which spans the D region, and includes lower altitudes (which would be subject to electron-density enhancements, in the event of hard precipitation).

The forward model, **G**, is a linear algebraic representation of the riometry equation (Equation 4.25). The riometry equation is continuous, so this is discretised as:

$$A = 4.611 \times 10^{-5} \sum_{h=h_{\mathrm{min}}}^{h_{\mathrm{max}}} \frac{N_{\mathrm{e}}\nu}{\nu^2 + (\omega \pm \omega_{\mathrm{B}_{\parallel}})^2} \, \Delta h \; (\mathrm{dB}) \tag{4.29}$$

This can be expressed in matrix form as

$$\begin{bmatrix} A_{o1} \\ A_{o2} \\ \vdots \\ A_{oN} \\ \\ A_{x1} \\ A_{x2} \\ \vdots \\ A_{xN} \end{bmatrix} = \begin{bmatrix} \frac{k\nu_1\Delta h}{\nu_1^2+(\omega_1+\omega_{\mathrm{B}_\parallel})^2} & \frac{k\nu_2\Delta h}{\nu_2^2+(\omega_1+\omega_{\mathrm{B}_\parallel})^2} & \cdots & \frac{k\nu_M\Delta h}{\nu_M^2+(\omega_1+\omega_{\mathrm{B}_\parallel})^2} \\ \frac{k\nu_1\Delta h}{\nu_1^2+(\omega_2+\omega_{\mathrm{B}_\parallel})^2} & \frac{k\nu_2\Delta h}{\nu_2^2+(\omega_2+\omega_{\mathrm{B}_\parallel})^2} & \cdots & \frac{k\nu_M\Delta h}{\nu_M^2+(\omega_2+\omega_{\mathrm{B}_\parallel})^2} \\ \vdots & \vdots & \ddots & \vdots \\ \frac{k\nu_1\Delta h}{\nu_1^2+(\omega_N+\omega_{\mathrm{B}_\parallel})^2} & \frac{k\nu_2\Delta h}{\nu_2^2+(\omega_N+\omega_{\mathrm{B}_\parallel})^2} & \cdots & \frac{k\nu_M\Delta h}{\nu_M^2+(\omega_N+\omega_{\mathrm{B}_\parallel})^2} \\ \\ \frac{k\nu_1\Delta h}{\nu_1^2+(\omega_1-\omega_{\mathrm{B}_\parallel})^2} & \frac{k\nu_2\Delta h}{\nu_2^2+(\omega_1-\omega_{\mathrm{B}_\parallel})^2} & \cdots & \frac{k\nu_M\Delta h}{\nu_M^2+(\omega_1-\omega_{\mathrm{B}_\parallel})^2} \\ \frac{k\nu_1\Delta h}{\nu_1^2+(\omega_2-\omega_{\mathrm{B}_\parallel})^2} & \frac{k\nu_2\Delta h}{\nu_2^2+(\omega_2-\omega_{\mathrm{B}_\parallel})^2} & \cdots & \frac{k\nu_M\Delta h}{\nu_M^2+(\omega_2-\omega_{\mathrm{B}_\parallel})^2} \\ \vdots & \vdots & \ddots & \vdots \\ \frac{k\nu_1\Delta h}{\nu_1^2+(\omega_N-\omega_{\mathrm{B}_\parallel})^2} & \frac{k\nu_2\Delta h}{\nu_2^2+(\omega_N-\omega_{\mathrm{B}_\parallel})^2} & \cdots & \frac{k\nu_M\Delta h}{\nu_M^2+(\omega_N-\omega_{\mathrm{B}_\parallel})^2} \end{bmatrix} \cdot \begin{bmatrix} m_1 \\ m_2 \\ \vdots \\ m_M \end{bmatrix} \tag{4.30}$$

In Equation 4.30, $m_1, m_2, \ldots m_M$ are the model parameters; i.e. the electron density at a given height, $m_i = N_e(h_i)$, where i is the height array index for a given height, h_i. The size of a height increment, Δh, is the distance between heights, h_i and h_{i+1}. The data are the measured absorptions in decibels for the O- and X-mode polarisations, A_{o_j} and A_{x_j} respectively, where j is the frequency channel array index. The series $\nu_1, \nu_2, \ldots \nu_M$ is the electron collision frequency profile, where $\nu_i = \nu(h)$, where i is the height array index for a given height, h. Nominal collision frequencies were used based on values from Aggarwal et al. (1979).

To test the possibility of solving Equation 4.30 for electron densities, four sample profiles were generated: a quiescent case, Q, and three cases of enhanced electron density, A, B and C, with enhancement altitudes of 80, 90 and 100 km, respectively and enhancement widths of 10 km each. The quiescent case is based on a typical electron density profile from Gnanalingam and Kane (1975), with the enhancements being gaussian, shown in Figure 4.3 (top-left).

From these model profiles, we generate the absorption curves, to which we add the noise. The noise term of η=0.01 dB is used, which is approximately 10-times less noise than could be achieved with KAIRA. The inverse problem is solved with a zeroth-order Tikonov-regularised inversion. The inversion generates a nonsense solution Figure 4.3 (bottom-left), which is an arbitrary solution reflecting mathematical and computational artefacts (such as floating-point round-off error). Also shown are the expected absorptions for the O- and X-mode for both the true simulated data and the model recovered by the inversion.

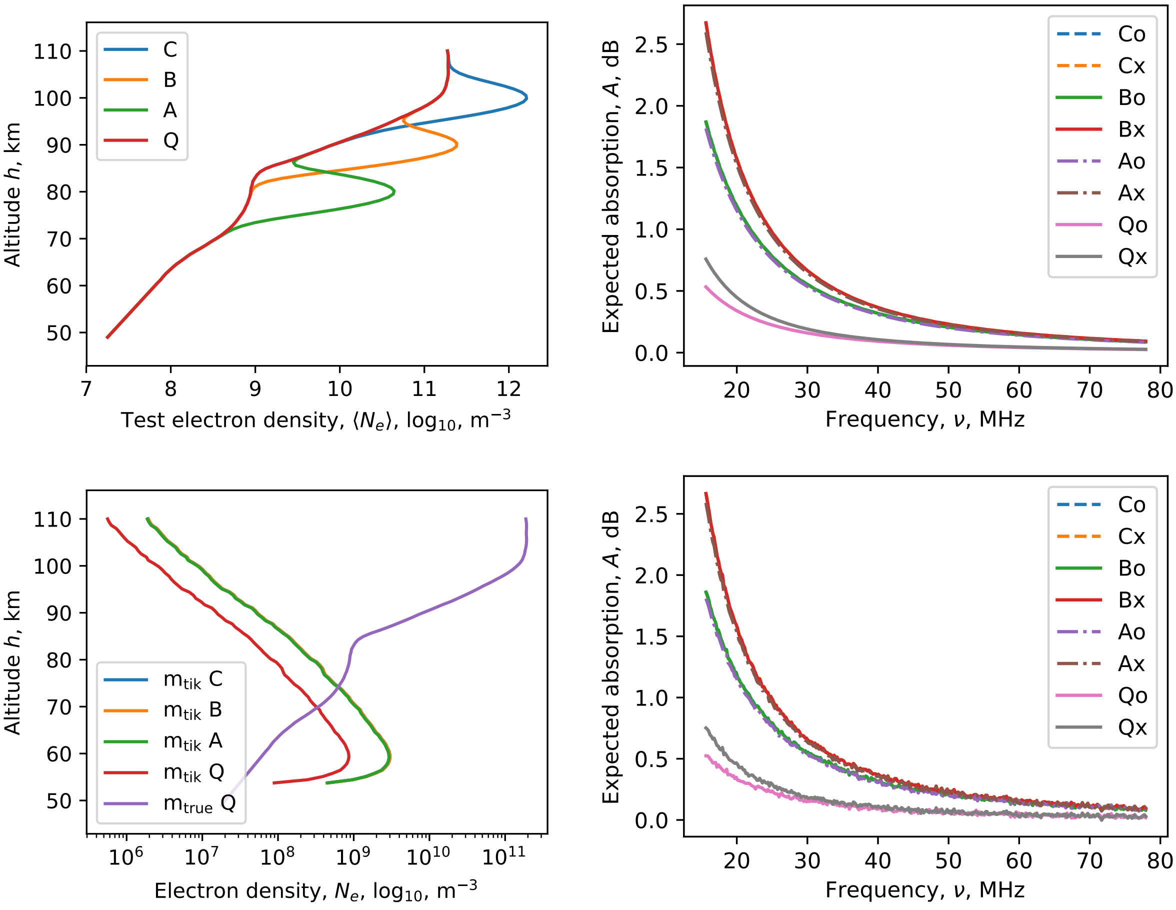

Figure 4.3: Top-left: a nominal quiescent electron density profile (Q), with three additional profiles with enhancement at different altitudes. Top right: application of the forward model to determine the expected absorption. The "o" and "x" mode cases for each model are shown. Bottom left: inversion problem solutions, with true quiescent value shown for comparison. Bottom right: the application of the forward model to the solved solution.

Figure 4.4 shows the residual between the application of the forward model to the inverse problem solution and the application of the model to the original profile. The residual values are small ($<$0.01 dB), which is considered well beyond the noise limit of current instrumentation. There is no information that can be recovered from this scenario. In fact, the situation is even worse, as shortwave radio interference prevents the use of frequencies below $\approx$25 MHz in nearly all cases.

In principle, the electron density could be constrained in the E region, possibly determined by ISR measurements. This would prevent the inverse problem from producing a solution governed by mathematical artefacts. However, since the ab-

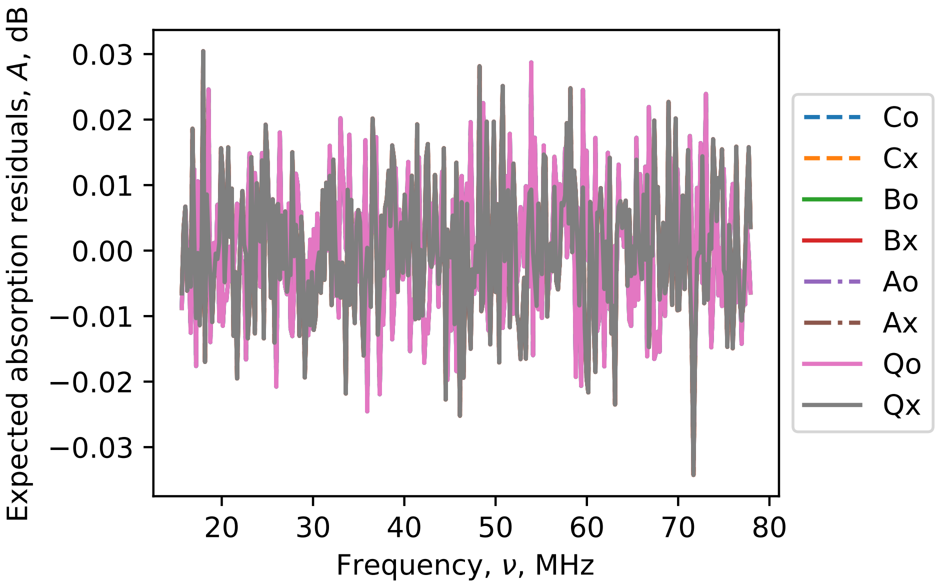

Figure 4.4: Residual absorption between the application of the forward model to the inverse problem solution and the application of the model to the original profile.

sorption curves remain all identical for N_e enhancements at different altitude, there would still be no difference in the reconstructed profiles.

Even in an ideal case with the physical response of the array compensated, the ability to derive electron-density profiles is not possible, as the inverse problem is too ill-posed. Nevertheless some information about high-energy (low-altitude) electron precipitation may be gleaned. Thus, multi-frequency riometry remains a useful technique, but not revolutionary in its ability to carry out three-dimensional electron density reconstruction.

Chapter 5

Interferometric riometry

The early riometers were single-detectors with a wide antenna beam pattern, which provides a single CNA measurement associated with a particular location on the Earth. General spatial distribution can discovered by operating multiple riometers over a large geographical region, such as the Finnish Riometer Chain operated by the Sodankylä Geophysical Observatory (Ranta and Ranta, 1974).

Narrow-beam riometers, both fixed and scanning, have been developed, relying on temporal measurements to provide information about small-scale structures. However, it is more effective to use multi-beam riometers (Honary et al., 2011). These were developed in the 1990s (Detrick and Rosenberg, 1990) and developed with enhanced signal processing, initially Butler matrices (e.g. IRIS, Section 5.3) and later digital beam-forming (e.g. KAIRA, when using beamformed mode).

In these systems, each beam measures its own power and thus operates as a quasi-independent, narrow-beam riometer for that pointing direction. Each beam is, in effect, a "pixel" on the sky from which primitive images of CNA can be formed. This leads to these systems being referred to as imaging riometers. They allow spatial distribution of CNA to be measured in different directions but are still limited in that each beam is discrete. Discontinuities between detection directions and undersampling of the spatial absorption results in uncertainties regarding the temporal movement and evolution of CNA.

5.1 Interferometry

Like in riometry, the scientific field of radio astronomy also measures cosmic radio noise. Historically, radio astronomers have deployed a variety of techniques and instruments. However, following the work of Ryle et al. (1959), the main development in radio telescopes has been dominated by interferometric systems comprising multiple detectors, from which the signals are combined and processed in the Fourier domain. The interferometer provides superior imaging capability and the ability to use extended baselines for improved angular resolution.

The principle of electromagnetic interferometry, was identified by van Cittert who established that a correlation function between sampled signals in a plane is independent of the incidence angle of that plane, and corresponds to the diffraction function defined by the separation of those sample points (van Cittert, 1934). Zernike formalised this in statistical terms and defined the concept of *degree of coherence* between two points to represent the amplitude of the diffraction pattern and, by using a suitable coordinate system, expressed this using the Fourier theorem (Zernike, 1938). The relationship between the covariance of signals received at two different points (often termed as the correlation) is referred to as the van Cittert-Zernike theorem and is expressed as follows:

$$V_\nu(u,v) = \iint I_\nu(\ell,m)\, e^{-2\pi i(u\ell+vm)}\, \mathrm{d}\ell \mathrm{d}m \tag{5.1}$$

where $V_\nu(u,v)$ is the complex visibility as a function of the baseline displacement (u,v) (Thompson, 1999). For interferometric riometry at KAIRA the third dimension of the baseline displacement (namely in the direction of the source, typically notated as w) can always be set to zero, as the nominal image centre is zenith and KAIRA is a level, co-planar array. The synthesised image, $I_\nu(\ell,m)$, is a plane normal to the w-direction, where ℓ,m are proportional to the sines of the angles measured from the tangent point of the plane, which is zenith in the topocentric case (Thompson, 1999). This is a two-dimensional orthographic projection:

$$\ell = \sin(Z)\sin(A); \;\; m = \sin(Z)\cos(A) \tag{5.2}$$

where A is the azimuth and Z is the zenith angle. Figure 5.1 shows a one-dimensional slice of this projection.

Sampling of the Fourier domain is accomplished by the distribution of antennas in the uv-plane. By randomising the distribution of those antennas, grating effects which cause enhanced sidelobes in the beam pattern, can be reduced. This applies especially in the case where there is comparatively few antennas; a motivating factor for the quasi-random distribution of the 48 LBA aerials at KAIRA, compared to the 768 bow-tie antennas embedded in the HBA tiles. Additionally, with small numbers, the logistics of cable-routing and antenna packing are less problematic.

Instantaneous sampling using wide-beamwidth antennas, distributed on an array with sufficient uv-coverage, allows all-sky, high time resolution imaging. With the ability to make rapid, all-sky radio power images, it was realised that the interferometric technique could be also used for riometry. The application of all-sky interferometric imaging to riometry is the basis of Paper II.

In principle, the technique could have been attempted earlier; systems such as LOFAR operate in a suitable frequency range and have the benefit of nearly all-sky coverage. However, strong absorption events are not common at lower latitudes. Until recently there have been no similar systems deployed in geographical areas where intense absorption occurs. KAIRA thus presented the first opportunity to accomplish this.

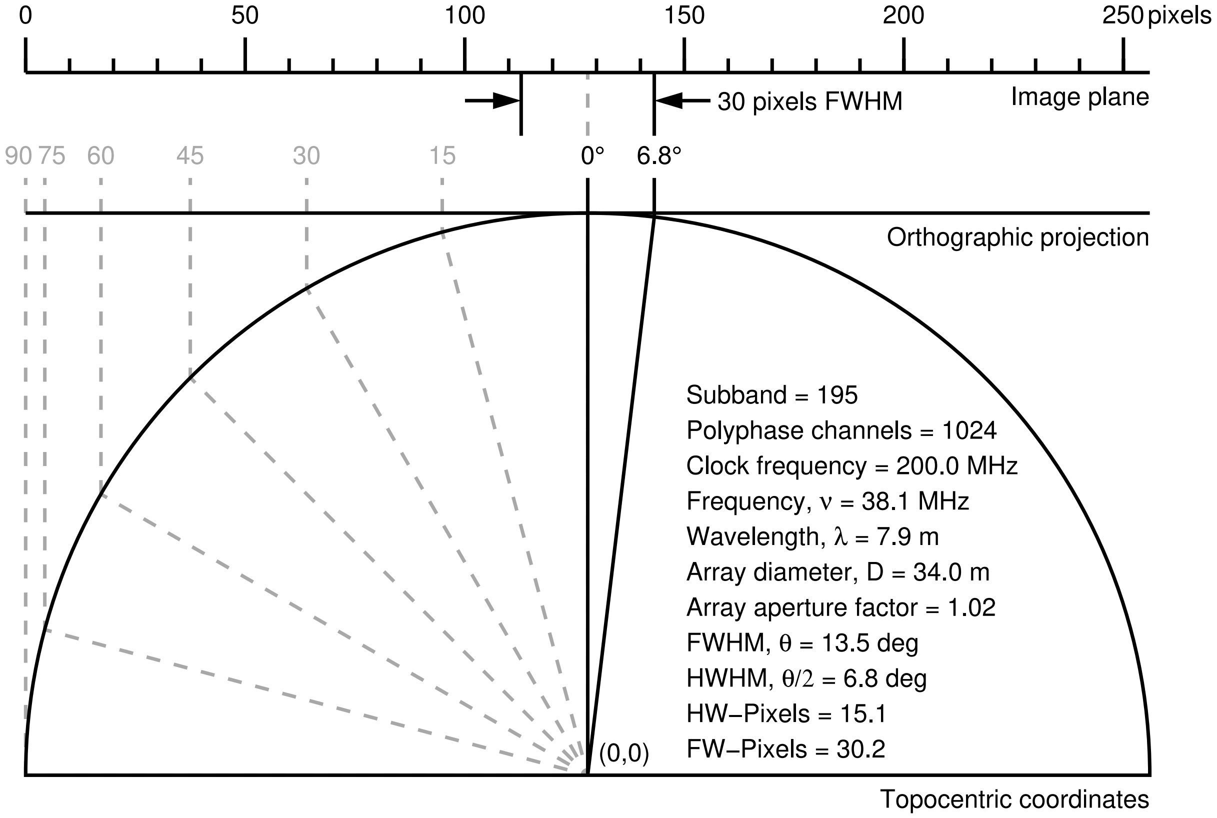

Figure 5.1: Lateral representation of resolution and projection parameters for interferometric observations made with KAIRA. The number of pixels and the choice of frequency is arbitrary, but the relationships are general.

5.2 Implementation

In practice, a discretised version of Equation 5.1 is used to generate images from the antenna covariances. In the case of KAIRA, the correlator produces covariances, V_ν, for every combination of antenna pairs at a given frequency, ν (in the case of KAIRA, this means a given subband, s). Each antenna pair is referred to as a *baseline* and has an associated (u, v)-coordinate, defined as:

$$\left.\begin{aligned} u &= (e_j - e_i)/\lambda \\ v &= (n_j - n_i)/\lambda \end{aligned}\right\} \tag{5.3}$$

where e and n are the topocentric coordinates (in the east and north directions, respectively) of the array (Appendix C) and λ is the wavelength associated with the subband that was observed (Equation 2.1). Consider an image comprising $X \times Y$ pixels. The pixel index, p, is given by $p = yX + x$ and the image plane coordinates are $(\ell, m) = (x - X/2, y - Y/2)$. A two-dimensional matrix, M, is formed such that:

$$M(p, b) = e^{2\pi i(u\ell + vm)} \tag{5.4}$$

where p is the pixel index of the image and b is the baseline index. The discretised version of Equation 5.1 is:

$$I_{s,p} = \sum_b V_s \, e^{2\pi i(u\ell + vm)} \tag{5.5}$$

and the image $I_{s,p}$ can be determined using linear algebraic methods, namely:

$$\mathbf{I} = \mathbf{M} \cdot \mathbf{V} \tag{5.6}$$

where **I**, **M** and **V** are the matrices of $I(s,p)$, $M(p,b)$ and $V(s,b)$, respectively. As software libraries for numerical linear algebra are efficient, these products can be determined rapidly (sub-second). The image has Cartesian coordinates l, m in range $[-1, 1]$, defined as $l = \sin(Z)\sin(a);\ \ m = \sin(Z)\cos(a)$, where Z is the zenith angle and a is the azimuth.

The normal station correlator at KAIRA creates u, v-data at a cadence of one-per-second. The multi-frequency correlator, Appendix H), is faster, but was not used for Paper II.

To determine the quiet-sky power, the median of all-sky images for the equivalent sidereal time for each day over the previous two weeks is used. As the beamsize of KAIRA is large (of the order of degrees, see Equation 2.2), the equivalent sidereal time can be within a minute, thus increasing the number of images to 14×60. This smooths the data of scintillation, RFI, etc., and removes anomalies from substorm electron precipitation. The quiet-sky image is divided by the observation image to generate the absorption image. Figure 5.2 shows such an example.

Riometric keograms

In addition to all-sky imaging, both KAIRA and the Finnish Meteorological Institute's All-Sky Camera (FMI-ASC) generate routine keograms, sampled from points along the meridian, averaged to 1-minute intervals. For the FMI-ASC, this is typically for the green (557.7 nm) filter. For KAIRA to achieve the same effect as an optical keogram, only a 1-D Fourier transform of the meridian pixels is made for each time sample, thus forming a *riometric keogram*. The resolution and orthographic projection are shown in Figure 5.1.

The quiet-sky power derived from a median of meridian slices from equivalent sidereal times, over a period of 14 days prior to the observation. The use of keograms, as opposed to full two-dimensional interferometry reduces processing time and allows them to be generated as part of standard daily data products. A large dataset has be accumulated without special computational effort and keograms provide an overview visualisation of riometric conditions. Detail of this method, and some sample results are shown in Paper IV.

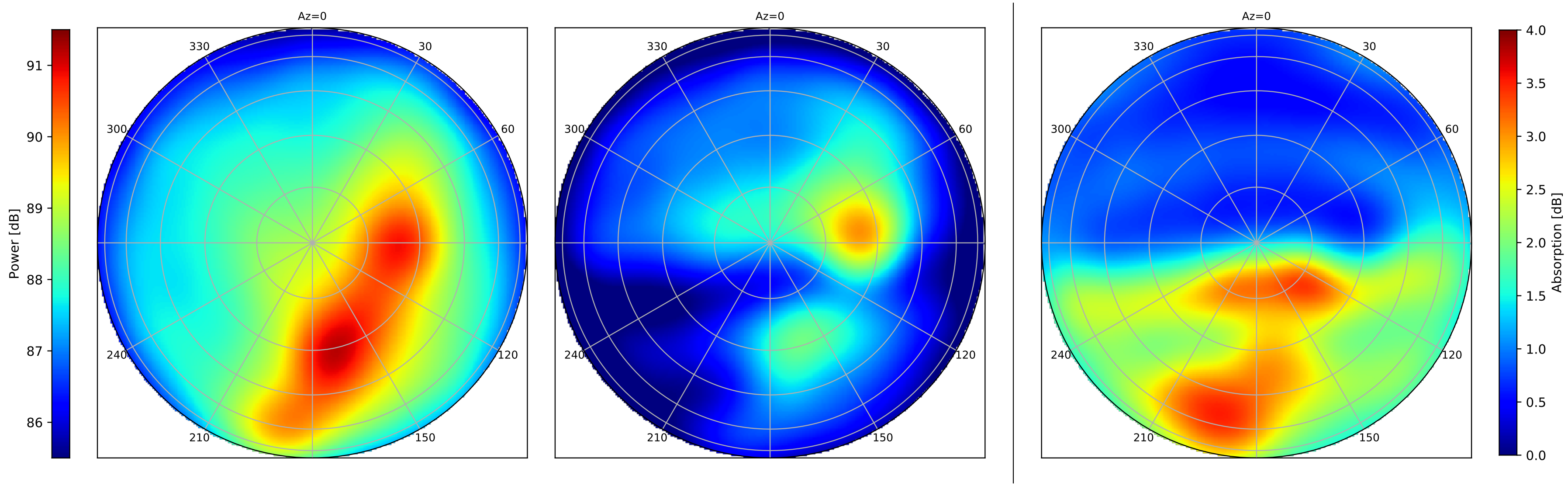

Figure 5.2: CNA event from 30 September 2016, 17:45:00 UTC, showing the quiet-sky power derived from two weeks of LST-equivalent data (left) and the measured power at the time of the event (centre). These are both shown with the same colour-scale. The absorption is calculated from these two images using Equation 4.20 (right). The images are top-down, orthographic projection, with zenith angle marked in 15-degree increments and azimuth in 30-degree increments.

5.3 Comparison studies

IRIS

In addition to KAIRA, there is a multibeam imaging riometer in the same area — Imaging Riometer for Ionospheric Studies (IRIS), located approximately 2.2 km from KAIRA and operated by the University of Lancaster (Browne et al., 1995). It comprises an array of dipole antennas, as shown Figure 5.3. Using a Butler matrix, the signals from these antennas are used to form a 49-beam riometer, operating at 38.2 MHz (equivalent to KAIRA's subband 195). This permitted a direct comparison between the two instruments, using KAIRA in both a multi-beam and interferometric imaging mode.

Figure 5.3: Southeast view across part of the dipole antenna matrix of the IRIS instrument. The building with the singularly-sloped roof has the FMI optical all-sky camera. The mountain in the left background is Saana.

The KAIRA data compares favourably to the data from IRIS. A total of 556 hours of common observing time was compared. This revealed a DC-bias in the IRIS data. As the interferometric data from KAIRA does not have a zero-u, v-spacing, it is less susceptible to this effect. Additionally, KAIRA has a quasi-random layout, compared to the grid-like arrangement of IRIS, which means that KAIRA has better sidelobe suppression for a similar number of antennas.

Details of the comparison between the instruments is found in Paper II. Figures 9 and 10 in that paper demonstrate the stability of KAIRA compared to IRIS.

Optical-riometric comparisons

The Finnish Meteorological Institute (FMI) operates an electron-multiplying charged coupled device (EMCCD) all-sky camera (ASC) at Kilpisjärvi (Sangalli et al., 2011b). It is co-located at the IRIS site in its own building with perspex observing dome, visible in the background of Figure 5.3. As the FMI-ASC is only 2.27 km distant from KAIRA, the proximity means that for observations of ionospheric phenomena in the D and E region (90 and 115 km, for the measurements made here), they have effectively co-incident sky-coverage. This permits direct comparison between the interferometric riometry and ASC images.

The FMI-ASC has a 24 mm, F/4 fisheye lens with a 180° field-of-view. Although partially obscured eastwards due to artificial lighting and terrain, the north-south meridian is clear to the horizon. A mechanical wheel selects filters of 557.7, 427.8 and 630.0 nm with bandwidth of 2.0 nm, and exposures are typically 800 to 2000 ms. During regular observations, the filter wheel is used to alternate between different wavelengths, resulting in a typical sparse cadence at any particular wavelength of 10 seconds.

However, KAIRA is collecting uv-data continuously and can operate at a cadence and integration of 1 second. Although the data could be decimated to match the cadence of the FMI-ASC, instead a bracket of riometric images is used. These are combined as a median and, with the exception of extremely-rapidly moving events, the process does not cause any perceptible degradation in data quality. The relationship between frames of FMI-ASC data and the KAIRA median-sequence is illustrated in Figure 5.4.

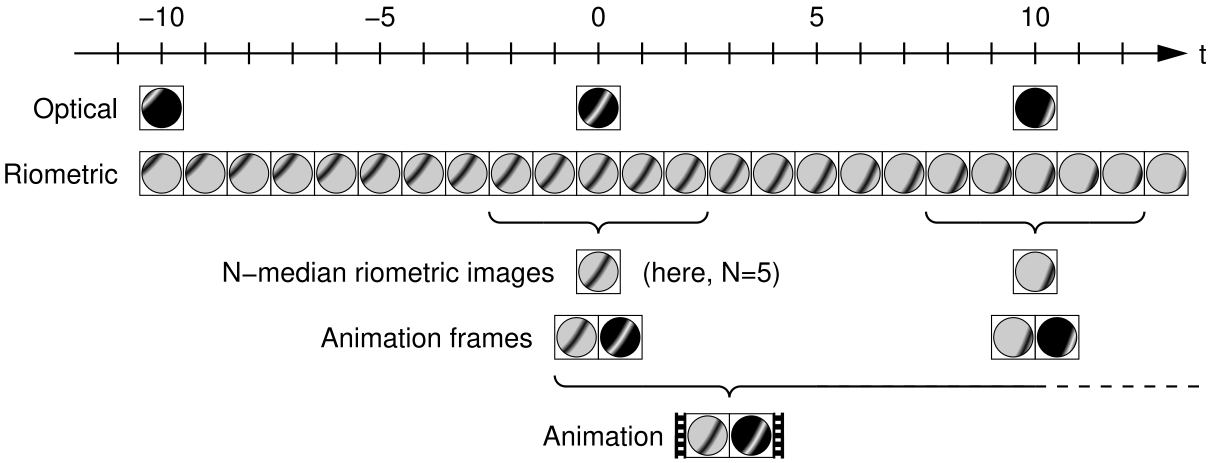

Figure 5.4: Schematic timeline showing the combination of mixed-cadence optical and riometric images for the sequence used in Figure 5.5.

The use of the median image for KAIRA is useful in suppressing the effects of ionospheric scintillation on bright radio sources (Section 5.4).

In general, interferometric riometry provides an additional imaging facility for the study of processes that occur during auroral onset. Although CNA associated with onset has been well known for many decades (e.g. Ortner et al., 1962), the interferometric technique allows it to be directly imaged without sensitivity variation imposed by fixed-beam systems. Figure 5.5 shows a sequence of images comparing KAIRA results directly to that of the FMI-ASC.

5.4 Challenges

The interferometric riometry technique is an effective means of carrying out spatial investigations of electron precipitation into the atmosphere. However, it is subject to a number of limitations, which will be discussed in this section.

Resolution

The effect of CNA by the ionosphere increases with decreasing frequency (Equation 4.26), thus making it more effective to observe at lower frequencies, at least as far as the limitations imposed by shortwave radio RFI. However, the beamsize increases with wavelength (Equation 2.2), making it desirable to use higher frequencies to increase the resolution of the instrument. At the frequency of 38.1 MHz, the full-width half-maximum of the LBA array beam is 13.5 degrees. KAIRA has two main data series at subbands 195 and 300, corresponding to 38.1 and 58.6 MHz, respectively. Experience has shown that the higher frequency was not efficient and that the loss in sensitivity outweighed any benefit in increased resolution. Since October 2014, KAIRA has used 38.1 MHz as its standard interferometric riometry frequency.

The only way to improve the resolution for a given frequency is to construct a physically larger array, although this is subject to limitations. This remains the subject of a future design study.

RFI

Radio sources with variable power result in discrepancies between the quiet-sky power and CNA-power measurements and thus lead to spurious results. The Sun is the only dominant variable radio source and Type II and Type III solar flares can result in such spurious effects. At KAIRA, the sun is below the horizon during the winter months. Even being low to the horizon (elevation $<$15 degrees, and thus below the on-sky beampattern of an individual LBA aerial) is sometimes not enough, given the magnitude of radio emission from solar flares (Kallunki et al., 2015). However, these events are uncommon and it is unusual for the sun to cause disruption of riometric observations at KAIRA.

The other source of natural transients is the electromagnetic pulse from a lightning discharge. The region around KAIRA has occasional thunderstorms in the summer months, which results in this interference. However the duration of in-

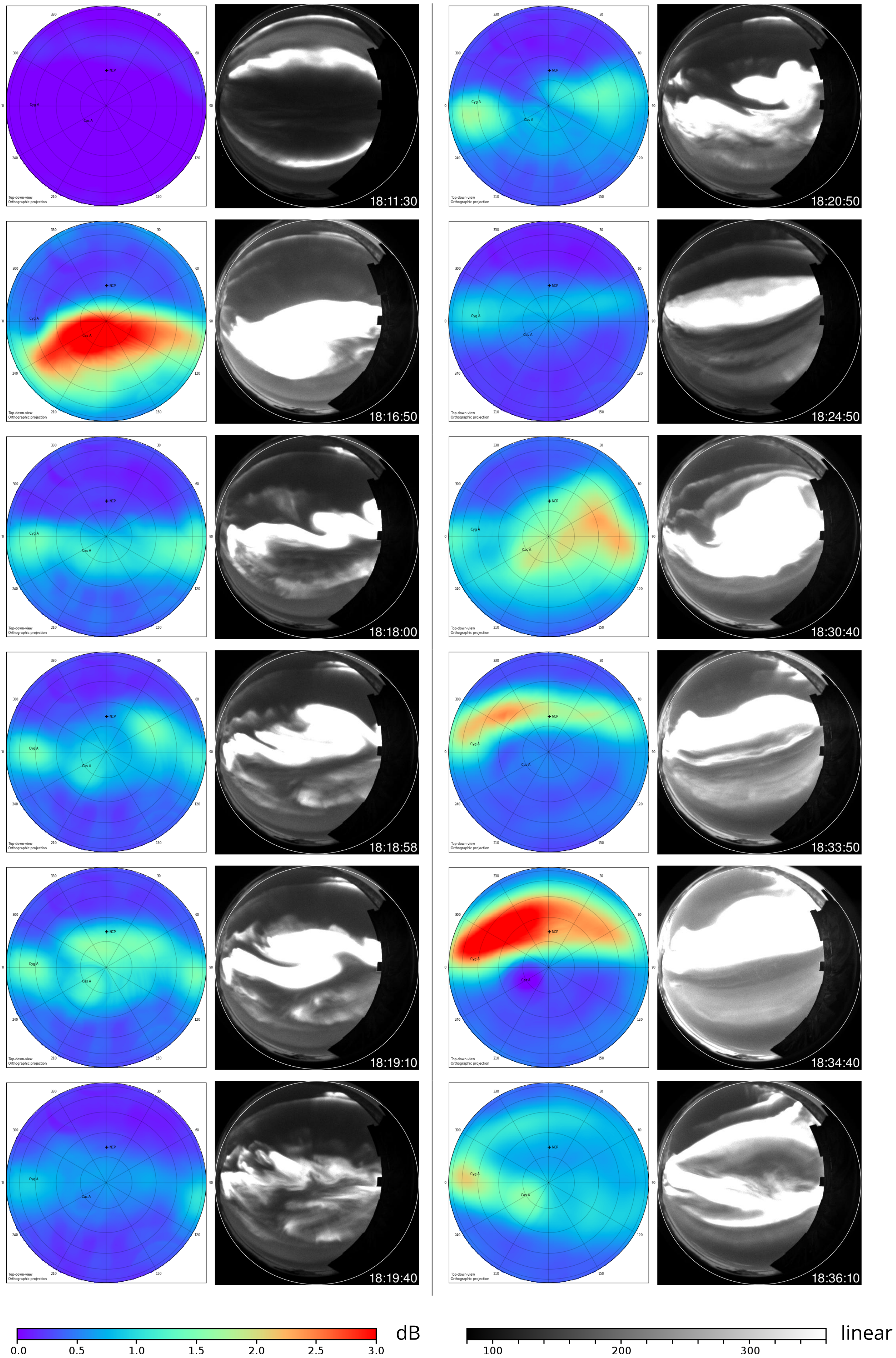

Figure 5.5: Sequence of interferometric riometry (top-down, orthographic projection) and optical 557.7 nm images from KAIRA and the Kilpisjärvi FMI-ASC from 9 December, 2014.

dividual bursts is shorter than a single 1-second sample and the emission is strong and broadband. Thus excising such signals is straightforward.

Another source of problems for experiments is artificial radio signals. In the case of KAIRA, the choice of a radio-quiet environment, coupled with the ability of the interferometric technique to readily discern directions, makes identification and avoidance of artificial sources relatively straightforward. The beam pattern of the LBA aerials at KAIRA suppresses signals close to the horizon (which is the typical location of RFI). Nevertheless, broadband RFI remains detrimental to observations. The full spectrum of KAIRA, along with common RFI sources, has been presented in Section 2.4.

Snow and ice

One limitation of the Arctic location is the accumulation of snow and ice. Although the riometric technique makes use of empirically-determined quiet-sky power levels, the alteration made by precipitation (this time of tropospheric water, not ionospheric electrons), results in a change in the RF-characteristics of the antennas. In the case of heavy snow and rain there is a significant change in the dielectric constant (Frolov and Macheret, 1999). This causes a change in the electrical ground plane, resulting in a narrower beam. This manifests as an increase in absorption at low elevations. At times when the snow melts (typically in May), there is again a large degradation of the riometry data quality.

Figure 5.6 shows the difference between the zenith and horizon absorption, in decibels. The points are daily medians, which excludes most of the effects of electron precipitation, which are on timescales of hours. The horizontal axis is the time of the year, with the start of each month being marked. Note the pronounced effect in May when the annual snow melt occurs.

Field alignment

Precipitation is aligned with the magnetic field. Therefore, when attempting to determine the spatial distribution of absorption associated with aurorae, riometry maps are reliant on imaging a “thin-screen”. For typical cases, this condition holds, with the imaging corresponding to the D region (Wild et al., 2010). If the ionisation as a result of the electron precipitation is spread over a range of altitudes, then absorption detected in directions other than field-aligned will be complicated.

A corollary of this is that creating multiple narrow-beam, field-aligned riometers would allow geographically more precise measurements to be made. As there are isochasms of equi-magnetic-field strength across the earth’s surface, building “line-riometers” which are oriented normal to the isochasms would exploit this. The line-riometer is a linear phased array of antennas, which provide good spatial resolution in the direction normal to the isochasm and all-sky coverage in the direction parallel to the isochasm.

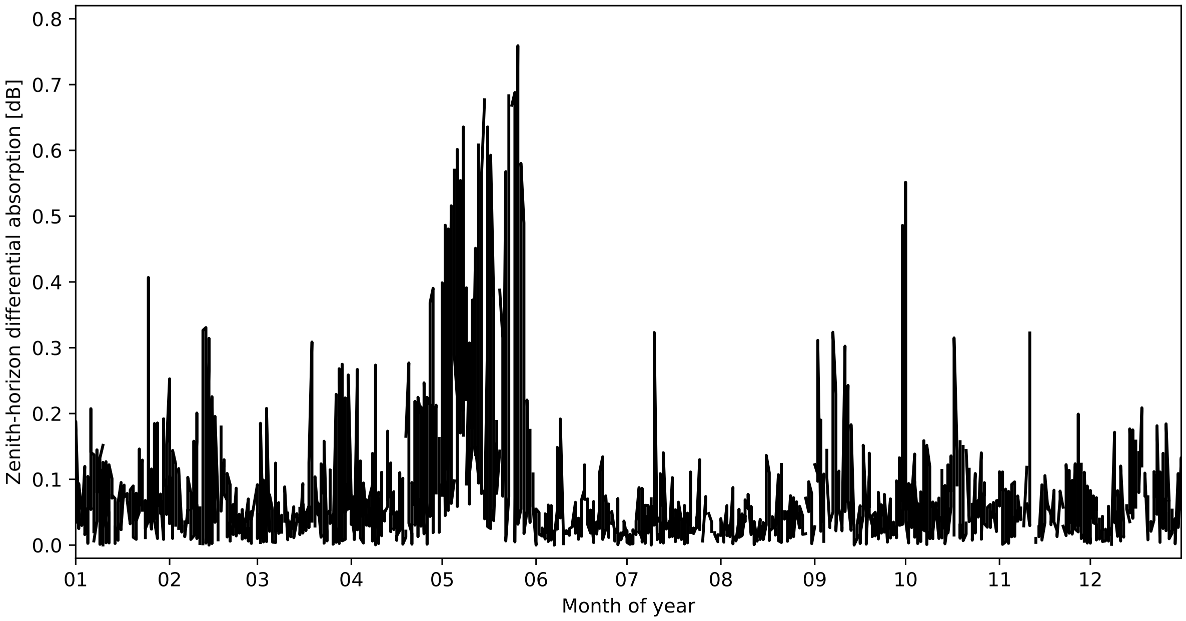

Figure 5.6: The difference between the absorption measured at the horizon and that measured at zenith, as a function of the time of year (for all available KAIRA data spanning July 2013 to April 2018). Variations are a result of changes in the RF ground-plane.

Scintillation

Ionospheric scintillation is caused by rapid fluctuations in electron density in a local patch of the ionosphere along the observed path length between the observer and an extraterrestrial radio source. When the radio source is a point source, there is a fluctuation in intensity, as the signal power is refracted or scattered into or out of the line of sight. This is interesting in its own right (as discussed in the KAIRA science programme, Section 3.6.)

The intensity variations of the bright radio stars Cas A and Cyg A, result in localised absorption (and negative absorption) in their respective directions. The negative absorption is an effect caused by an intensity enhancement from the scintillation. The scintillation brightening makes the radio star exceed the typical value which is present in the quiet-sky power, which then manifests as a negative absorption in the processed data.

These scintillation effects are convolved with the sidelobe pattern of the array, resulting in fluctuations in absorption in other parts of the riometric image. Attempts have been made to use a two-dimensional least-squares fitting routine to map the sidelobe pattern for a given location of Cas A and Cyg A in the CNA map. This is successful when there is scintillation present, and the CNA is uniform in distribution. However, the mechanism breaks down when the CNA is localised, as it is difficult to automatically discern radio-star scintillation from localised CNA.

This remains the topic of on-going work. Until a satisfactory solution can be found, ionospheric scintillation poses a limitation to CNA mapping. In particular it presents challenges for the detection of CNA pulsations associated with optical pulsating aurorae (Grandin et al., 2017, e.g.).

5.5 Multi-frequency interferometric riometry

The flexibility of the LOFAR digital signal processing, which is used at KAIRA, permitted the development of a correlator that is capable of processing multiple subbands simultaneously. A description of this correlator is provided in Appendix H and an example of the multi-frequency all-sky results has been previously shown in Figure 2.10.

The existence of over 40 other LOFAR-based systems across northern Europe means that the KAIRA multi-frequency station correlator could be easily deployed at many other locations, providing even more complete coverage and allowing the study of geographical variation of absorption events.

Nevertheless, the benefits of multi-frequency riometry are limited (Section 4.3) and the loss of flexibility in carrying out such observations is curbed due to the demands of the correlator. The additional digital signal processing (DSP) resources that must be dedicated to the multi-frequency correlator configuration cannot then be used for other experiments. This technical limitation renders this implementation impractical, other than for demonstrative purposes.

5.6 Impact

The interferometric riometry allows high-time-resolution all-sky imaging of absorption in the D-region. It permits the investigation electron precipitation from substorms, as well as solar proton events, relativistic electron precipitation and other interactions between the magnetosphere and the atmosphere. By using aperture-synthesis imaging, the technique is more robust than conventional single- or multi-beam techniques. It provides spatially continuous imaging and is more resilient to misinterpretation of RFI contaminated results.

Riometric observations can be made at times when conventional optical methods fail (such as during the daytime — including months of midnight sun during summer — as well as periods of bright moonlight of cloudy weather). These continuous measurements contribute to the understanding of the impact of space weather on the atmosphere, especially for the highly-dynamic polar atmosphere. In the next chapter, this will be demonstrated in the application of auroral studies.

Chapter 6

Riometric study of aurorae

6.1 Processes

Ionisation in the upper atmosphere can be caused by multiple different processes with peak ionisation occurring at different heights, as shown in Figure 6.1 (See also Table 1.1, page 2).

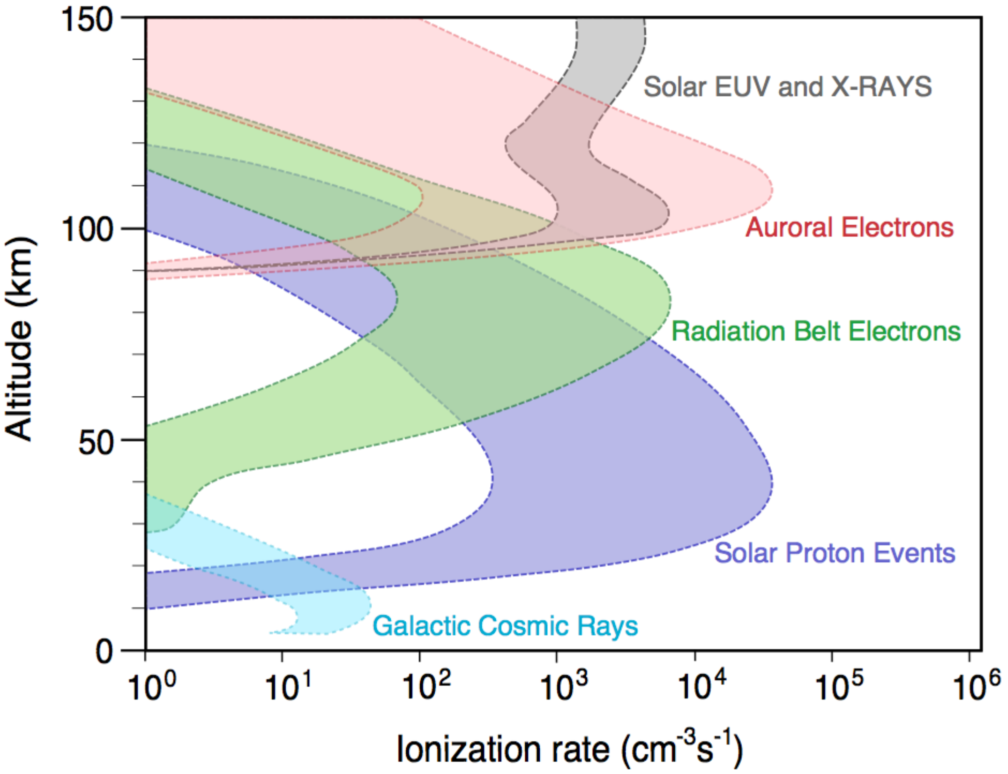

Figure 6.1: Ionisation rates as a function of altitude, categorised by the source of the ionisation. From Mironova et al. (2015).

Although all production of electrons may affect the CNA measured using KAIRA, it is the precipitation of high-energy auroral electrons and electrons from the radiation belt that result in observable events. During a polar magnetospheric substorm, there is significantly increased electron precipitation, which results in an increase in the ionisation rate in the ionosphere. The level of the increase depends on the total electron flux and the altitude of the ionisation depends on the energy of the precipitating particles.

The electron density enhancements in the ionosphere are often the result of polar-magnetospheric substorms (e.g. Hunsucker and Hargreaves, 2002). Earlier studies (e.g. Jussila et al., 2004) have determined that neither plasma instabilities nor enhanced electron temperatures in the E region played a significant role in causing the CNA and concluded that CNA is caused by energetic electron precipitation reaching down into the D region, with a maximum between 80 and 90 km.

The substorm is a magnetospheric-scale phenomenon, where energy from the solar wind that has been loaded into the magnetotail is suddenly released, leading to a characteristic sequence of ionospheric responses. The precipitation changes as the substorm progresses through its different phases. Akasofu (1964, *et al.*) proposed the concept of phases of an auroral substorm. The sequence comprises:

1. Appearance of a latitudinally narrow auroral arc, which extends hundreds of kilometres east-west, which gradually drifts equatorward over the course of about one hour. This period is referred to as the *growth phase*, first categorically described by McPherron (1970).

2. Abrupt complex and conspicuous activity occurs, resulting in an increase in auroral intensity lasting 10–30 minutes and resulting in dynamic aurora of north-south, as well as east-west, extent. It is accompanied by a deviation from the mean ground-level magnetic field and an increase in high-energy precipitation (Wing et al., 2013). This is the *expansion* phase and the moment this phase commences is called the *onset*. Active auroral features move eastward and westward, the latter being referred to as the *westward-travelling surge*.

3. Following the expansion phase, auroral structures have now fragmented and dissipate over the period of 3–5 hours. Often pulsating aurora are observed during this time. This phase is referred to as the *recovery phase*, during which time magnetospheric conditions return to a pre-substorm, quiescent state.

The local morphology of substorms is complicated. The westward-travelling surge in particular comprises multiple smaller features. These localised brightenings are called *surges*, last only a few minutes and do not move far individually. As each completes a new surge forms to its west, thus the whole aurora appear to move westwards quantised by these individual surges (Hunsucker and Hargreaves, 2002, p 311). Some brightenings of the aurora do not develop into full substorms. They remain limited to a few hundred kilometres and have relatively short duration. Such events are called *pseudo-breakups* (Pulkkinen, 1996).

The difficulty in obtaining an overview of the optically-visible phenomena, has led to the categorisation of the substorm phases using the ground-level magnetic signature, e.g. IL-index (Kallio et al., 2000). The growth phase is marked by the first deviation of the north-south component of ground magnetic field and the onset can be identified by an abrupt decrease of this component (e.g. local index IL of more than 80 nT in 15 minutes (Tanskanen, 2009). The time at which the IL index reaches its minimum value is often used to mark the end of the expansion phase. The substorm then enters the recovery phase (with the IL index returning to the pre-substorm values). The substorm recovery process usually lasts 1–3 hours (Tanskanen, 2009).

During the growth phase, energy is transferred to the magnetotail from the solar wind. This causes the magnetotail to stretch with the result that the ionospheric footprint of move equatorward. Finally, there is an abrupt release of energy (the substorm onset), which is often triggered by an abrupt decrease of energy inflow into the magnetotail, e.g. from a decrease in IMF B$_Z$ (Lessard et al., 2007).

Other auroral arcs can form poleward but, by tracing the magnetic field lines into the magnetotail, it can be seen that it is the equatorward arc that maps to the inner edge of the plasma sheet where there are significant gradients in plasma properties, which facilitate instabilities leading to the onset (Fukunishi, 1975).

The growth-phase arc is the optically bright emission band. However a broad region of diffuse emission lies equatorward. This diffuse region has been shown to be caused by proton precipitation (Ono et al., 1987). Lessard et al. (2007) show that the regions of diffuse proton aurora and the bright electron aurora of the growth-phase arc clearly overlap in latitude. They also point out the separation in latitude between the peak emission in the electron and proton bands and that the arcs appear to form in a region where the electrons and protons overlap.

These energetic particles released into the atmosphere originate from the plasma sheet (Wing et al., 2013). They travel along the field lines and precipitate into the ionosphere. Pytte et al. (1976) noted that high-energy electron precipitation associated with arcs during the growth phase occurs when there has been a quiet period between substorms. During the events they studied, there was low- to moderate-geomagnetic conditions ($K_p = 2 - 6$). The choices of events made for Paper III were chosen similarly, so that there were no remnants of previous substorm which might contribute energetic precipitation.

Aurora-related phenomena

Aurorae are one phenomena associated with the substorms, exhibiting association with solar activity, zonal occurrence — the Auroral Oval; typically Lat. 65–80°, but capable of expanding equatorward under magnetically disturbed conditions.

KAIRA lies within this latitude range and so is well located. But the effects of electron precipitation may be divided into different related phenomena, depending on the remote-sensing technique used for their measurement:

1. luminous, optical aurora (the Northern/Southern Lights)
2. radar aurora (electron density enhancements, as detected by ISR)
3. auroral radio absorption (as detected by a riometer)
4. auroral X-rays
5. magnetic disturbances
6. electromagnetic emission at VLF and ULF bands.

All of these phenomena are a consequence of the complex interaction between the solar wind, the magnetosphere and the ionosphere. This results in the precipitation of energetic electrons, producing ions and secondary electrons, which then leads to the excitation of atmospheric atomic and molecular species. The connections between the auroral phenomena, along with the typical techniques used for their detection, are shown in Figure 6.2.

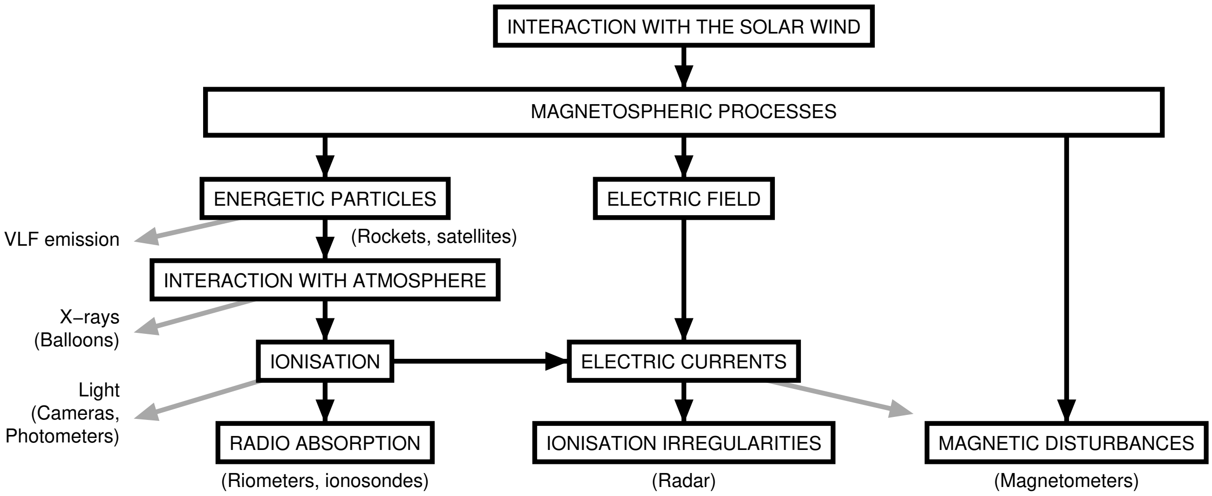

Figure 6.2: Links between auroral phenomena. Techniques are shown in brackets. Based on an original figure from Hargreaves (1969, Figure 21).

Optical aurorae are typically found in the E region, with red oxygen aurora in the F-region, but can extend down to the D region during precipitations of electrons with energy $\gtrapprox$30 keV. They are highly structured and dynamic, and features can be as thin as 100 m and temporal changes can be as rapid as 10 s^{-1}. In the E region, the electron density may reach 10^{12} m^{-3}, which can reflect directly incident radio waves at frequencies up to 20 MHz, and higher frequencies if obliquely incident.

More energetic electrons penetrate into the D region and ionisation at these altitudes causes the frequency-dependent absorption of radio waves, and may thus be imaged using KAIRA's interferometric riometry. Although KAIRA does not have the spatial resolution to discern small-scale auroral structure, it does have good temporal resolution. A study using this was carried out and the results are presented in Paper III. In order to understand the significance of those results, a brief overview of the relationship between substorm dynamics and the ionosphere is included.

The E Region at high-latitude

The E region is an active part of the ionosphere at heights 100-130 km, and one which has different plasma processes at high latitudes (compared to mid- and low-latitudes) as a result of the significant impact of substorm electron precipitation. This is the energy-depletion layer for electrons of energies in the range 1–10 keV, giving rise to a rate of ionisation of 10^8 electrons.cm^{-2}.s^{-1}. This leads to the subsequent optical emission, high-conductivity and electrojet currents.

As the neutral density is increasing exponentially with decreasing height, energy deposition is mostly at the end of the precipitation path. As the density is relatively high, recombination occurs quickly. The relationship between visual aurora and auroral E-region ionisation has been studied by Hunsucker (1975) using simultaneous all-sky camera, ionosonde and incoherent-scatter radar data during the transition of auroral arcs through the fields of view of the instruments with the E region electron density being greatly increased within the arc.

The D Region at high-latitude

The D region has higher neutral densities, complex chemistry and, due to an increased electron-neutral collision frequency, the electric currents are inhibited. Here it is the higher-energy precipitation which is important, as lower-energy electrons will fail to penetrate through the E region to reach these altitudes. As the energy increases (10–100 keV), the characteristic peak altitude of the D region is lowered (Rees, 1989). Earlier studies (e.g. Jussila et al., 2004) have determined that neither plasma instabilities nor enhanced electron temperatures in the E region play a significant role in causing the CNA and concluded that CNA is caused by energetic electron precipitation reaching down into the D region, with a maximum between 80 and 90 km. The diurnal occurrence of CNA peaks just before magnetic midnight and again in the morning sector between 06:00 and 10:00 MLT (Hunsucker and Hargreaves, 2002, p 350).

Some absorption occurs in the mid-latitude D region, but it is at high-latitudes (60°–75° geomagnetic latitude) that D-region absorption dominates. There are two main phenomena:

- *Auroral radio absorption (AA)* — resulting from precipitating electrons from the magnetosphere
- *Polar-cap absorption (PCA)* — resulting from energetic protons emitted from the Sun, typically at the time of a major flare.

To the first order, radio propagation is affected by evolving AA. This is patchy in extent (tens to hundreds of kilometres), and occasionally elongated east-west. Altitudes of AA are typically 90 km, although variation occurs with precipitation of different energy.

AA is caused by the auroral substorm and involve particle precipitation from the outer Van Allen radiation belt. Precipitating electrons have energies in the range of tens to hundreds of kilo-electron volts — generally greater than those which produce the visual aurora. AA is usually present somewhere in the auroral zone and is generally hemispherically conjugate, with equivalent AA occurring in the northern and southern hemispheres. Statistically, it occurs at similar times and with similarly intensities, but exact patterns do not match (Hunsucker and Hargreaves, 2002, p 410). The magnetic field of the magnetosphere is not known in detail. Therefore, variations of the ground-footprint of ± 85 km may be expected compared to computed conjugate points. The interhemispheric event which appears first is stronger than its conjugate counterpart and the interhemispheric ratio depends on the direction of the IMF carried by the solar wind.

The other significant D-region absorption is polar-cap absorption (PCA), which typically produce higher absorption, but occur much less frequently. PCA is caused by precipitation of 1–1000 MeV protons of solar origin. It produces a fairly uniform blanketing of the polar cap down to $\approx 60^\circ$ geomagnetic latitude, resulting in trans-polar HF-blackouts persisting for several days. PCA is not common; rates vary between 0 and 20 per year, correlated with solar activity (Gurman, 2018).

6.2 Auroral radio absorption

AA was initially discovered by Appleton et al. (1933) by observing ionosonde blackouts. Although detectable using ionosondes, riometers — particularly imaging riometers — are better suited for investigating spatio-temporal aspects of this phenomenon. However, riometers rely on trans-ionospheric propagation and thus do not directly indicate the height of the absorption. Hargreaves (1995) presents a selection of different AA phenomena. At times typically just before magnetic midnight and associated with auroral activity, sudden CNA occurs referred to as *sharp-onset events*. This absorption signature has a rise time of minutes and a duration ranging from 30 minutes to a few hours. These can be isolated or occur as part of more general CNA activity. There may also be a dramatic “spike” in absorption, in which case the event is a *spike event*. The spike is highly dynamic and lasts 1–2 minutes with variable absorption between 1 and 6 dB (Hunsucker and Hargreaves, 2002, p 351).

They are not necessarily associated with the injection of energetic particles associated with substorm onset (Spanswick et al., 2007). The physical size of spike events is not well established, but is of the order of tens of kilometres across. Wide-beam riometers have previously underestimated the size of spike events, but the imaging capability of KAIRA allows better limits to be established. The peak absorption invariably moves polewards and that there is considerable variation in magnitude with a quasi-period of 30–60 s (Hargreaves, 1970). An example spike event measured with KAIRA is shown in Figure 6.3, coinciding with modest magnetic activity ($\Delta B_H \approx$180 nT).

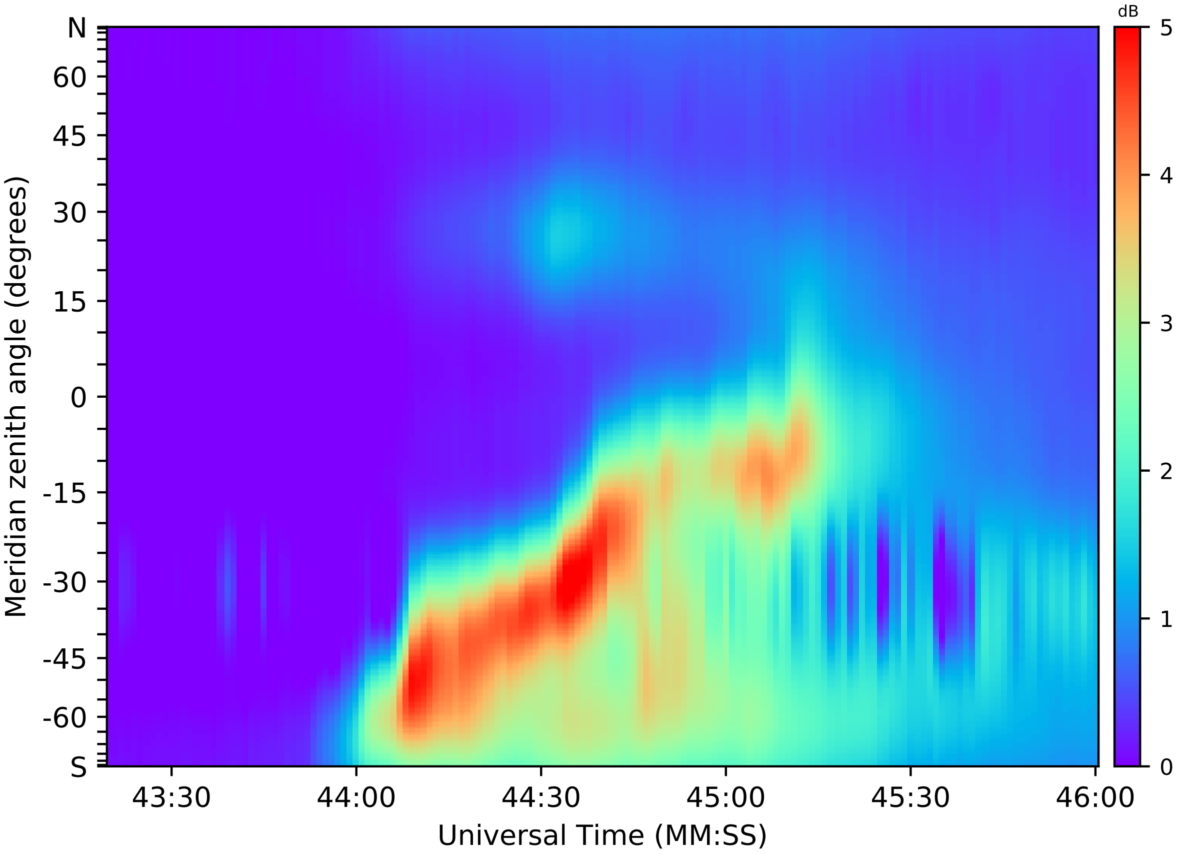

Figure 6.3: Riometric keogram of a spike event occurring shortly after 17:44 UTC on 30 September, 2016. The observation was made at KAIRA using subband 195 (38.1 MHz). The 0 dB striation occurring after 17:45 UTC at a meridian zenith angle of $-35°$ is scintillation from the radio galaxy Cyg A.

Larger spike events are not observed in the day sector, but smaller ones have been observed by day at high latitude in the northern hemisphere occurring between 1200 and 1800 LMT, with mode at 1500–1600 (Stauning and Rosenberg, 1996). Durations are comparable with the nighttime equivalents, but intensity is typically only 0.2–0.5 dB.

Starting 1–1.5 h before the substorm onset, there is occasionally a related weak absorption event (40–60 min; the *pre-onset absorption* or the *preceding bay*). Imaging riometers have identified this as an arc extending east-west across the field of view, but only 60–100 km wide in the north-south direction. The CNA arc is associated with the optical growth-phase auroral arc. The weak absorption bay that may precede an onset moves equatorward at a typical speed of a few hundred m.s^{-1}. This can be measured using geographically separated riometers, or it can be measured with an imaging riometer (Hunsucker and Hargreaves, 2002, Figure 7.7)). These arcs were studied in Paper III (in particular, see Figure 3).

6.3 High-energy electron precipitation in growth-phase arcs

Traditionally a network of riometers was needed to measure the motion of auroral absorption. However, imaging riometers permit this to be measured at higher spatial resolution with a single instrument. This is the main apsect of the study carried out by KAIRA, the results of which are presented in Paper III.

Optical and riometer observations of precipitating electrons provide two complimentary views of the electron energies associated with auroral precipitation. Optical emissions originate at altitudes over 100 km and are caused by electrons of energies in the range 1 to 10 keV, whereas riometer observations identify ionisation of the lower mesosphere for energies typically higher than 10 keV, even up to 1 MeV. Simultaneous observations in two energy ranges allows one to make better estimates of the spatio-temporal distribution of auroral precipitation at a wider range of energies.

As the optical emission and CNA occur at different heights, to compare the relative position and velocity of the growth-phase arc and the CNA arc, the position of the maximum intensity of each arc is projected to a common plane. A height of 110 km is assumed for the optical emission (Sangalli et al., 2011a). This is an approximation as emission occurs over a range of altitudes. An altitude of 90 km is assumed for the CNA (Wild et al., 2010). This is also an approximation as the absorption can cover a range of altitudes, with the altitude of the maximum being dependent on the electron energy distribution (Kero et al., 2014).

In Paper III, a census of growth-phase arcs was conducted, comparing optical keograms from the Kilpisjärvi all-sky camera and riometric keograms made using the KAIRA radio telescope. The main findings of that study are:

1. Before an isolated substorm, auroral emission may comprise a diffuse optical component extending east-west with a bright arc on the poleward edge and CNA arc on the boundary between the bright and diffuse emission. The bright arc and CNA appear 60–90 minutes before the substorm onset and drift equatorward.

2. The CNA that appears on the border between the diffuse emission region and the bright arc is consistently equatorward of the discrete arc, but still contained within the region of diffuse aurora.

3. Optical pulsations are seen in the border region between the diffuse emission region on the equatorward side and the bright growth-phase arc on the poleward side. CNA is detected in the same region.

4. Investigation of the optical pulsations in the border region has led to the detection of hitherto unreported auroral transients (referred to as "lumikot"), which are associated with the CNA arc.

5. Once the equatorward drift starts, it proceeds at constant speed of $70 \pm 5\,\mathrm{m.s}^{-1}$, with uniform separation between the growth-phase arc and CNA of $40 \pm 10\,\mathrm{km}$.

These results are significant because optical pulsating aurora have hitherto been associated with the post-onset phase of the substorm. Although the pulsations seen in those periods are more prominent than those seen during the growth phase, the growth-phase case has not been complicated by disturbed magnetic conditions, thus allowing the source of the pulsation-generating particles to be constrained to the outer radiation belt. This, in turn, allows the mechanism of optical pulsating aurora in the expansion and recovery phases to be better understood. It also means that the occurrence of high-energy precipitation may be much higher than previously thought if the growth phases also regularly contribute.

Occurrence of auroral absorption

Several efforts (Hunsucker and Hargreaves, 2002, and references therein) have attempted to model the distribution and have noted a latitudinal dependency:

$$A_m = A_0 \exp\Big(- \frac{(\lambda - \lambda_0)^2}{2\sigma^2}\Big) \tag{6.1}$$

where A_m is median absorption, λ is the invariant latitude and σ is the half-width of the absorption zone. This distribution corresponds to the outer auroral zone.

AA is more frequent and more intense when geomagnetic activity is high. The relationship is with the magnetic activity, rather than the sunspot number. In some solar cycles, the magnetic activity does not vary in the same way as the sunspot number. KAIRA could be used in future to study the detailed relationship of solar wind driving and energetic particle precipitation.

Geophysical significance

Riometers have typically been calibrated against electron-density profiles based on EISCAT and rocket data, but variations of up to a factor of two have been noted. This is consistent with the discrepancy seen in recent measurements between KAIRA and IRIS (Paper II), suggesting deficiencies in the absolute calibration of early riometers.

The height of the absorbing layer and its thickness are computed from rocket profiles and EISCAT data. Maxima range over 90 to 95 km, but may be lower (75 km) by day. The absorbing layer can be quite thick (15–20 km) between points where the incremental absorption is half the maximum. About 80% of the total absorption occurs within this slab. The specific absorption coefficient increases downward, and the absorption peaks some 5-15 km (depending on the energy spectrum) below the peak in electron density. That is, the absorption layer occurs roughly on the underside of the electron-density layer, although it is a column effect. The daytime spectrum is typically "harder". An important element is the effective recombination coefficient as a function of altitude (Hunsucker and Hargreaves, 2002, Section 1.3.3), which relates the rate of electron-ion production to the resulting electron density. This can be approximated from other experimental results (ISR, rockets, and even low-orbiting satellites) or from ion-chemistry models.

Electron precipitation, particularly the electrons typical for pulsating aurora, is a significant driver for the D-region ion chemistry. Auroral precipitation is thought to have a role in the production of nitric-oxide species in the mesopause region. These species can in turn be transported into the lower atmosphere and can impact ozone chemistry in the mesosphere during the high-latitude spring. Observations of the characteristic energies associated with different types of auroral forms can help characterise the contributions to the D-region chemistry.

Chapter 7

Future work

The deployment of a powerful radio interferometer in a new location has opened up many opportunities for engineering development and scientific research. In particular, the experimentation with new riometric techniques has led to interesting possibilities which warrant investigation, but which are beyond the scope of this thesis.

7.1 Further advances in riometry

Aperture synthesis interferometry, coupled with modern digital signal processing, has opened up numerous possibilities for the measurement of cosmic noise absorption (CNA). Although interesting features have been found using the 1-second measurement cadence, there may be other interesting features that occur at even shorted time scales. Some initial work has been done with 10- and 100-Hz sampling, but these studies are by no means comprehensive. The multi-frequency software correlator (Appendix H), as well as the beam-formed data acquisition, are capable of even more rapid sampling (to 5.12 μs). This will permit the study of fast time domain features, such as pulsating aurorae and rapidly-evolving spike events, which has not been readily possible with existing instruments, and will complement the new generation of fast-sampling cameras that are being planned for optical observations of aurorae.

Although this work indicates that there are deficiencies in the application of the inverse problem technique to recovering electron density height profiles (Section 4.3), a more comprehensive investigation is required.

Experimentation with removal of redundant baselines has been carried out to accommodate more frequencies in the correlator (Appendix H). However, it is possible to expand the array with the inclusion of LBA aerials located at longer baselines, and thus improve the spatial resolution. There are a number of locations where new aerials could be placed on the KAIRA site, while still maintaining co-planarity and remaining within cable-limitation distance. Additional channels within the KAIRA digital signal processing system means that such experiments could be carried out without disrupting the existing array hardware.

All of these advances lead to speculation about next-generation instruments. Before any such proposals can be made a comprehensive design study of the maximum practical size of the interferometric imaging riometer must be completed. As the size of the array increases (in order to improve resolution), a limit is reached where the beamsize of the array projected onto the ionosphere (assuming a given height and observing frequency) becomes smaller than the physical size of the array.

Improvements in calibration

The implementation of interferometric technique in this thesis provides sufficient results for demonstrating the principle and utilising it to answer scientific questions. However, a more rigorous treatment could be applied. The calculation of the signal-to-noise ratio and flux calibration of the array could be improved and ionospheric corrections (such as refraction terms) applied to improve the spatial accuracy. Better modelling and measurement of the antenna element primary beam pattern would permit more rigorous calibration of data.

The processing of the CNA data in this work, has relied on the dense spatial sampling in Fourier space (i.e. uv-coverage) to achieve its high image fidelity. However the aperture is still undersampled and deconvolution techniques, as used in the radio astronomy field, could be applied.

The radio-astronomy technique of deconvolution may be used to remove the point-spread function of the strong radio sources Cas A and Cyg A, thus suppressing sidelobe effects caused by variations in location and power of these sources during periods of strong ionospheric scintillation. This deconvolution has been used to attempt to remove scintillation artefacts from the CNA data, but this technique was not successful (as discussed in Section 5.4). Nevertheless, investigation in this area is warranted in search of further improvements. Spatial removal of RFI sources using a deconvolution approach may also be possible.

Quiet-sky determination in Fourier space

Another approach to preparing CNA data relies on calculating the expected “quiet-sky” in the domain of the signal covariances; that is, the Fourier space, referred to as uv-space in the field of aperture synthesis. Determining the quiet-sky model in uv-space saves are large number of computations, as the Fourier transform is only performed on the final product, rather than on every individual frame. Additionally the average is calculated on the number of baselines in the array (in the case of KAIRA LBA array, this is 1128), as opposed to the number of pixels in the resultant image (which is variable, but is typically $256 \cdot 256 \cdot \pi/4 = 51472$ pixels; corners outside the circular orthographic projection are not computed).

Averaging Cartesian components of the antenna covariances, $(\mathrm{Re}(V), \mathrm{Im}(V))$, results in decorrelation when large phase errors are present. It is more robust to convert visibilities to polar notation, (S, ϕ), and compute the mean amplitude, $\bar{S}$ and the mean phase, $\bar{\phi}$, the latter of which is a circular mean, defined as:

$$\bar{\phi} = \mathrm{arctan}_2 \Big(\sum_i \sin(\phi_i), \sum_i \cos(\phi_i) \Big) \tag{7.1}$$

This is computationally more intensive than a linear mean, but operating in uv-space is still more efficient. Circular median calculation is even more computationally demanding.

Rapid determination of quiet-sky power levels permits real-time riometric monitoring. Already KAIRA produces live all-sky images at the minute level, and riometric keograms every few hours. The slow network connection between the site and the Internet remains a limitation for real-time presentation, but even so, all-sky riometric images could be produced at the minute-level permitting live monitoring and easy recovery and inspection of events.

7.2 Statistics and forecasting

Rapid generation of processed data is critical to the provision of real-time products for forecasting. The work carried out at KAIRA has meant that it is the only LOFAR radio telescope with a live, public, web-based monitoring system. There are plans to make use of LOFAR (and LOFAR-like) systems for tracking space weather using interplanetary scintillation and Faraday rotation measurements, and KAIRA would be well suited for inclusion in such an endeavour. The all-sky capability of the system, combined with the ability to conduct multiple experiments simultaneously, make it suitable for inclusion in long-term monitoring programmes. The northern location of KAIRA, compared to other radio systems, means that long-day solar monitoring is possible in the summer months (although it is precluded completely during polar night).

The robust, automated operation of KAIRA, combined with multi-faceted experiments, means that long-term trend studies can be carried out. KAIRA has been in routine operation since 2013, so it is now becoming feasible to derive statistics from the accumulated data set. One area of potential investigation is CNA variation as a function of time of day and time of year to examine effects of seasonal loading. The imaging capability of KAIRA gives improvements over existing single-beam riometers, and the high-cadence and multi-frequency operation mean that investigations can be made of the frequency and distribution of high-energy precipitation events, which is important for understanding the magnetospheric-ionospheric coupling.

Also of interest is the long-term statistics of ionospheric scintillation. At KAIRA, the radio star Cas A is circumpolar. It is tracked routinely as part of the standard experiment (Appendix K) which has resulted in a substantial database. A preliminary overview has been made (Szponarski et al., 2015), but this remains an area for more detailed investigation, in particular looking for seasonal and solar-cycle dependencies.

7.3 Future auroral investigations

Although pulsations in CNA during the recovery phase have been reported before (Grandin et al., 2017), no evidence of CNA pulsations have been seen in the interferometric riometry images made for this study. Although optical pulsating aurora is considered to be a thin horizontal layer of emission, the electrons contributing to the CNA are not necessarily limited to a single altitude in the D region, and absorption occurs over a range of heights (Kero et al., 2014). When observing across field lines, then different regions with different pulsation signatures may interfere with each other masking the effect (Section 5.4). However, post-onset pulsating aurora does form in large patches and narrow-height ranges and field-line limitations do not affect the measurement. This opens up the possibility for future studies to look the statistics of pulsating optical and absorption signatures and therefore derive information about the source populations for the particles. Additional work is also required to investigate alternative methods for extricating pulsations in CNA from interference from ionospheric scintillation of radio stars. This may provide sufficient sensitivity to reliably discern CNA pulsations, and therefore place constraints on energy distribution of the underlying mechanism.

Additionally, the growth-phase optical pulsating aurora noted in Paper III have been reported but no detailed study has been made regarding the statistics, or the other associated optical transients (the so-called “lumikot”) which have been observed in the high-energy border between the growth-phase arc and the diffuse emission.

As KAIRA builds up a large database of CNA measurements, it will become possible to start investigating auroral absorption image statistics. The occurrence of spike events is not well understood and a detailed study of their occurrence is warranted. This may lead to an explanation of their quasi-unrelated appearance with respect to the auroral onset this is an area of potential contribution to the understanding of substorm processes.

More generally, KAIRA is a versatile instrument and there remains a plethora of interesting scientific projects that could be carried out to exploit its location and capabilities.

Chapter 8

Conclusion

The KAIRA facility was successfully planned, constructed and commissioned between 2010 and 2012. The system has been used for VHF incoherent scatter radar reception, thus fulfilling its purpose as a demonstration for suitable technologies for the EISCAT_3D project, conducting for the first time bistatic, multi-beam ISR observations.

Additionally, wide-band multi-beam measurements are being routinely carried out, permitting a variety of other radio-observations (Paper I). The use of this form of technology has a direct and effective application to geoscience experiments and, due to the flexibility of the underlying technology, many other possible types of innovative experiments have been realised. Very long baseline interferometric fringes have been achieved, indicating not just technical performance and calibration, but also compatibility with other radio telescope systems. With this, KAIRA grants significant improvements in spatial resolution to the LOFAR-VLBI network, thus making a useful contribution to radio astronomy. The high-latitude also permits long-duration solar observations during the summer months and the facility is able to participate in solar research.

It has long been recognised that LOFAR systems would be able to make significant contributions to solar and terrestrial physics (Oberoi and Kasper, 2004). KAIRA is in a unique location to carry out the necessary ionospheric observations, where the ionosphere is most dynamic.

An interferometric technique has been developed with KAIRA allowing spatially-continuous imaging of cosmic-noise absorption (Paper II). The method is compatible with other geoscience experiments carried out at KAIRA and thus a long-term monitoring programme has been established (Paper IV).

The new technique, used in conjunction with the FMI All-Sky Camera has permitted the characterisation of radio absorption and optical emission signatures associated with the growth-phase arcs of isolated auroral substorms (Paper III). The observations have determined the location of the precipitation within growth-phase arcs at optical energy ($<$10 keV) and riometer energy ($>$10 keV), and show that the peak of the absorption arc is equatorward of the optical emission arc. This CNA is contained within the region of diffuse aurora on the equatorward side. This investigation has led to the discovery of pulsating aurorae in the border zone between the diffuse emission on the equatorward side and the bright growth-phase arc on the poleward side. CNA is detected in the same area, although there is no evidence of pulsations in the CNA. The fact that pulsations are also seen in a fairly localised region during the growth phase is important because it shows that the substorm expansion-phase dynamics are not required to closely precede pulsating aurora.

References

Aggarwal, K. M., Nath, N., and Setty, C. S. G. K.: Collision frequency and transport properties of electrons in the ionosphere, Planetary and Space Science, 27, 753–768, doi: 10.1016/0032-0633(79)90004-7, 1979.

Akasofu, S.-I.: The development of the auroral substorm, Planetary and Space Science, 12, 273–282, doi: 10.1016/0032-0633(64)90151-5, 1964.

Appleton, E. V.: Wireless Studies of the Ionosphere, Wireless Section, Institution of Electrical Engineers - Proceedings of the, 7, 257–265, doi: 10.1049/pws.1932.0027, 1932.

Appleton, E. V. and Barnett, M. A. F.: On Some Direct Evidence for Downward Atmospheric Reflection of Electric Rays, Proceedings of the Royal Society of London Series A, 109, 621–641, doi: 10.1098/rspa.1925.0149, 1925a.

Appleton, E. V. and Barnett, M. A. F.: Local reflection of wireless waves from the upper atmosphere, Nature, 115, 333, 1925b.

Appleton, E. V., Naismith, R., and Builder, G.: Ionospheric Investigations in High Latitudes, Nature, 132, 340–341, doi: 10.1038/132340a0, 1933.

Appleton, E. V., Naismith, R., and Ingram, L. J.: British Radio Observations during the Second International Polar Year 1932-33, Philosophical Transactions of the Royal Society of London Series A, 236, 191–259, doi: 10.1098/rsta.1937.0002, 1937.

Baars, J. W. M., Genzel, R., Pauliny-Toth, I. I. K., and Witzel, A.: The absolute spectrum of CAS A - an accurate flux density scale and a set of secondary calibrators, Astronomy and Astrophysics, 61, 99–106, 1977.

Belikovich, V. V., Itkina, M. A., and Rodygin, L. V.: Frequency of Appearance of Anomalous Ionization in the F2 Layer at High Altitudes, Geomagnetism and Aeronomy, 4, 612, 1964.

Benz, A. O.: Radio Emission of Solar Flare Particle Acceleration, in: Sixth International Workshop on Planetary and Solar Radio Emissions Graz, April 20 - 22, 2005, pp. 325–338, , 2005.

Bowles, K. L.: Observation of Vertical-Incidence Scatter from the Ionosphere at 41 Mc/sec, Phys. Rev. Lett., 1, 454–455, doi: 10.1103/PhysRevLett.1.454, 1958.

Breit, G. and Tuve, M. A.: A Test of the Existence of the Conducting Layer, Physical Review, 28, 554–575, doi: 10.1103/PhysRev.28.554, 1926.

Brisken, W. F., Macquart, J.-P., Gao, J. J., Rickett, B. J., Coles, W. A., Deller, A. T., Tingay, S. J., and West, C. J.: 100 μas Resolution VLBI Imaging of Anisotropic Interstellar Scattering Toward Pulsar B0834+06, Astrophys. J., 708, 232–243, doi: 10.1088/0004-637X/708/1/232, 2010.

Browne, S., Hargreaves, J., and Honary, B.: An imaging riometer for ionospheric studies, Electronics Communication Engineering Journal, 7, 209–217, doi: 10.1049/ecej:19950505, 1995.

Carlson, H. C.: Sharpening our thinking about polar cap ionospheric patch morphology, research, and mitigation techniques, Radio Science, 47, RS0L21, doi: 10.1029/2011RS004946, 2012.

Carrington, R. C.: Description of a Singular Appearance seen in the Sun on September 1, 1859, Mon. Not. R. Astron. Soc., 20, 13–15, doi: 10.1093/mnras/20.1.13, 1859.

Chatterjee, S., Vlemmings, W. H. T., Brisken, W. F., Lazio, T. J. W., Cordes, J. M., Goss, W. M., Thorsett, S. E., Fomalont, E. B., Lyne, A. G., and Kramer, M.: Getting Its Kicks: A VLBA Parallax for the Hyperfast Pulsar B1508+55, Astrophys. J. (Lett.), 630, L61–L64, doi: 10.1086/491701, 2005.

Chau, J. L., McKay, D., Vierinen, J. P., La Hoz, C., Ulich, T., Lehtinen, M., and Latteck, R.: Multi-static spatial and angular studies of polar mesospheric summer echoes combining MAARSY and KAIRA, Atmospheric Chemistry and Physics Discussions, 2018, 1–23, doi: 10.5194/acp-2018-210, 2018.

Close, S., Oppenheim, M., Hunt, S., and Dyrud, L.: Scattering characteristics of high-resolution meteor head echoes detected at multiple frequencies, Journal of Geophysical Research: Space Physics, 107, doi: 10.1029/2002JA009253, 2002.

Davies, K.: Ionospheric radio propagation, Monograph, U. S. Dept. of Commerce, National Bureau of Standards; for sale by the Superintendent of Documents, U. S. Govt. Print. Off., URL `https://books.google.no/books?id=lQ1RAAAAMAAJ`, 1965.

de Oliveira-Costa, A., Tegmark, M., Gaensler, B. M., Jonas, J., Landecker, T. L., and Reich, P.: A model of diffuse Galactic radio emission from 10 MHz to 100 GHz, MNRAS, 388, 247–260, doi: 10.1111/j.1365-2966.2008.13376.x, 2008.

de Vos, M., Gunst, A. W., and Nijboer, R.: The LOFAR Telescope: System Architecture and Signal Processing, IEEE Proc., 97, 1431–1437, doi: 10.1109/JPROC.2009.2020509, 2009.

Detrick, D. L. and Rosenberg, T. J.: A phased-array radiowave imager for studies of cosmic noise absorption, Radio Science, 25, 325–338, doi: 10.1029/RS025i004p00325, 1990.

Dewdney, P. E., Hall, P. J., Schilizzi, R. T., and Lazio, T. J. L. W.: The Square Kilometre Array, IEEE Proc., 97, 1482–1496, doi: 10.1109/JPROC.2009.2021005, 2009.

Ellingson, S. W., Clarke, T. E., Cohen, A., Craig, J., Kassim, N. E., Pihlstrom, Y., Rickard, L. J., and Taylor, G. B.: The Long Wavelength Array, IEEE Proc., 97, 1421–1430, doi: 10.1109/JPROC.2009.2015683, 2009.

Fallows, R. A., Asgekar, A., Bisi, M. M., Breen, A. R., and ter-Veen, S.: The Dynamic Spectrum of Interplanetary Scintillation: First Solar Wind Observations on LOFAR, Solar Physics, 285, 127–139, doi: 10.1007/s11207-012-9989-5, 2013.

Fallows, R. A., Coles, W. A., McKay-Bukowski, D., Vierinen, J., Virtanen, I. I., Postila, M., Ulich, T., Enell, C.-F., Kero, A., Iinatti, T., Lehtinen, M., Orispää, M., Raita, T., Roininen, L., Turunen, E., Brentjens, M., Ebbendorf, N., Gerbers, M., Grit, T., Gruppen, P., Meulman, H., Norden, M. J., de Reijer, J.-P., Schoenmakers, A., and Stuurwold, K.: Broadband meter-wavelength observations of ionospheric scintillation, Journal of Geophysical Research (Space Physics), 119, 10 544, doi: 10.1002/2014JA020406, 2014.

Fallows, R. A., Bisi, M. M., Forte, B., Ulich, T., Konovalenko, A. A., Mann, G., and Vocks, C.: Separating Nightside Interplanetary and Ionospheric Scintillation with LOFAR, Astrophys. J. (Lett.), 828, L7, doi: 10.3847/2041-8205/828/1/L7, 2016.

Farley, D. T.: Faraday Rotation Measurements Using Incoherent Scatter, Radio Science, 4, 143–152, doi: 10.1029/RS004i002p00143, 1969.

Finnish Public Recommendation, 197: JHS 197 EUREF-FIN -koordinaattijärjestelmät, niihin liittyvät muunnokset ja karttalehtijako, in: JUHTA - Julkisen hallinnon tietohallinnon neuvottelukunta, JUHTA - Julkisen hallinnon tietohallinnon neuvottelukunta, pp. 1–15, http://docs.jhs-suositukset.fi/jhs-suositukset/JHS197_liite4/JHS197_liite4.pdf, 2016.

Frolov, A. D. and Macheret, Y. Y.: On dielectric properties of dry and wet snow, Hydrological Processes, 13, 1755–1760, 1999.

Fukunishi, H.: Dynamic relationship between proton and electron auroral substorms, JGR, 80, 553–574, doi: 10.1029/JA080i004p00553, 1975.

Gardiner, G.: Origin of the term ionosphere, Nature, 224, 1096, 1969.

Gauss, C. F.: Allgemeine Theorie des Erdmagnetismus, in: Resultate aus den Beobachtungen des magnetischen Vereins im Jahre 1838, edited by Gauss, C. F. and Weber, W., p. 234, Weidmannsche Buchhandlung, Leipzig, https://books.google.no/books?id=TYI5AAAAcAAJ, 1839.

Gnanalingam, S. and Kane, J. A.: A study of electron density profiles in relation to ionization sources and ground-based radio wave absorption measurements, NASA STI/Recon Technical Report N, 75, 1975.

Gordon, W. E.: Incoherent Scattering of Radio Waves by Free Electrons with Applications to Space Exploration by Radar, Proceedings of the IRE, 46, 1824–1829, doi: 10.1109/JRPROC.1958.286852, 1958.

Grandin, M., Kero, A., Partamies, N., McKay, D., Whiter, D., Kozlovsky, A., and Miyoshi, Y.: Observation of pulsating aurora signatures in cosmic noise absorption data, Geophysical Research Letters, 44, 5292–5300, doi: 10.1002/2017GL073901, 2017.

Gulyaeva, T. L. and Gulyaev, R. A.: Climate change in the ionosphere parameters dependent on solar and geomagnetic activity, Advances in Space Research, 13, 63 – 66, doi: http://dx.doi.org/10.1016/0273-1177(93)90250-F, 1993.

Gurman, J. B.: Solar Proton Events Affecting the Earth Environment, in: U.S. Dept. of Commerce, NOAA, Space Weather Prediction Center, edited by Gurman, J. B. and Rutledge, R., NASA Goddard Space Flight Center, ftp://ftp.swpc.noaa.gov/pub/indices/SPE.txt, 2018.

Guzmán, A. E., May, J., Alvarez, H., and Maeda, K.: All-sky Galactic radiation at 45 MHz and spectral index between 45 and 408 MHz, Astronomy & Astrophysics, 525, A138, doi: 10.1051/0004-6361/200913628, 2011.

Hargreaves, J. K.: Auroral absorption of HF radio waves in the ionosphere: A review of results from the first decade of riometry., IEEE Proc., 57, 1348–1373, 1969.

Hargreaves, J. K.: Conjugate and closely-spaced observations of auroral radio absorption - IV. The movement of simple features, Planetary and Space Science, 18, 1691–1705, doi: 10.1016/0032-0633(70)90003-6, 1970.

Hargreaves, J. K.: The solar-terrestrial environment. an introduction to geospace - the science of the terrestrial upper atmosphere, ionosphere and magnetosphere, Cambridge University Press, 1992.

Hargreaves, J. K.: The Solar-Terrestrial Environment, Cambridge University Press, 1995.

Heinselman, C. J. and Nicolls, M. J.: A Bayesian approach to electric field and E-region neutral wind estimation with the Poker Flat Advanced Modular Incoherent Scatter Radar, Radio Science, 43, RS5013, doi: 10.1029/2007RS003805, 2008.

Helmboldt, J. F. and Kassim, N. E.: The Evolution of Cassiopeia A at Low Radio Frequencies, Astronomical Journal, 138, 838–844, doi: 10.1088/0004-6256/138/3/838, 2009.

Hewish, A., Scott, P. F., and Wills, D.: Interplanetary Scintillation of Small Diameter Radio Sources, Nature, 203, 1214–1217, doi: 10.1038/2031214a0, 1964.

Hodgson, R.: On a curious Appearance seen in the Sun, Mon. Not. R. Astron. Soc., 20, 15–16, doi: 10.1093/mnras/20.1.15, 1859.

Honary, F., Marple, S. R., Barratt, K., Chapman, P., Grill, M., and Nielsen, E.: Invited Article: Digital beam-forming imaging riometer systems, Review of Scientific Instruments, 82, 031 301, doi: 10.1063/1.3567309, 2011.

Hunsucker, R. D.: Chatanika radar investigation of high latitude E-region ionization structure and dynamics, Radio Science, 10, 277–288, doi: 10.1029/RS010i003p00277, 1975.

Hunsucker, R. D.: Radio techniques for probing the terrestrial ionosphere., Physics and Chemistry in Space, 22, doi: 10.1007/978-3-642-76257-4, 1991.

Hunsucker, R. D. and Hargreaves, J. K.: The High-Latitude Ionosphere and its Effects on Radio Propagation, Cambridge University Press, 2002.

Jansky, K. G.: Radio Waves from Outside the Solar System, Nature, 132, 66, doi: 10.1038/132066a0, 1933.

Jussila, J. R. T., Aikio, A. T., Shalimov, S., and Marple, S. R.: Cosmic radio noise absorption events associated with equatorward drifting arcs during a substorm growth phase, Annales Geophysicae, 22, 1675–1686, doi: 10.5194/angeo-22-1675-2004, 2004.

Kaiser, T.: The first suggestion of an ionosphere, Journal of Atmospheric and Terrestrial Physics, 24, 865, 1962.

Kallio, E. I., Pulkkinen, T. I., Koskinen, H. E. J., Viljanen, A., Slavin, J. A., and Ogilvie, K.: Loading-unloading processes in the nightside ionosphere, Geophys. Res. Lett., 27, 1627–1630, doi: 10.1029/1999GL003694, 2000.

Kallunki, J., Uunila, M., and McKay-Bukowski, D.: Multi-frequency solar observations at Metsähovi Radio Observatory and KAIRA, Astronomische Nachrichten, 336, 566, doi: 10.1002/asna.201512194, 2015.

Kelley, M. C., Farley, D. T., and Röttger, J.: The effect of cluster ions on anomalous VHF backscatter from the summer polar mesosphere, Geophysical Research Letters, 14, 1031–1034, 1987.

Kero, A., Vierinen, J., McKay-Bukowski, D., Enell, C.-F., Sinor, M., Roininen, L., and Ogawa, Y.: Ionospheric electron density profiles inverted from a spectral riometer measurement, Geophys. Res. Lett., 41, 5370–5375, doi: 10.1002/2014GL060986, 2014.

Latteck, R., Singer, W., Rapp, M., and Renkwitz, T.: MAARSY - the new MST radar on Andøya/Norway, Advances in Radio Science, 8, 219–224, doi: 10.5194/ars-8-219-2010, 2010.

Latteck, R., Singer, W., Rapp, M., Vandepeer, B., Renkwitz, T., Zecha, M., and Stober, G.: MAARSY: The new MST radar on Andøya – System description and first results, Radio Science, 47, RS1006, doi: 10.1029/2011RS004775, 2012.

Lavergnat, J. and Berthelier, J. J.: An iterative mathematical technique for deriving electron-density profiles from multifrequency riometer data, Radio Science, 8, 641–649, doi: 10.1029/RS008i007p00641, 1973.

Lessard, M. R., Lotko, W., LaBelle, J., Peria, W., Carlson, C. W., Creutzberg, F., and Wallis, D. D.: Ground and satellite observations of the evolution of growth phase auroral arcs, Journal of Geophysical Research (Space Physics), 112, A09304, doi: 10.1029/2006JA011794, 2007.

Little, C. G. and Leinbach, H.: The Riometer – A Device for the Continuous Measurement of Ionospheric Absorption, Proceedings of the IRE, 47, 315–320, doi: 10.1109/JRPROC.1959.287299, 1959.

Lonsdale, C. J., Cappallo, R. J., Morales, M. F., et al.: The Murchison Widefield Array: Design Overview, IEEE Proc., 97, 1497–1506, doi: 10.1109/JPROC.2009.2017564, 2009.

Machin, K. E., Ryle, M., and Vonberg, D. D.: The design of an equipment for measuring small radio-frequency noise powers, Electrical Engineers, Journal of the Institution of, 1952, 137–138, doi: 10.1049/jiee-2.1952.0042, 1952.

Martin, P. L., Scaife, A. M. M., McKay, D., and McCrea, I.: IONONEST — A Bayesian approach to modeling the lower ionosphere, Radio Science, 51, 1332–1349, doi: 10.1002/2016RS005965, 2016.

McCrea, I., Aikio, A., Alfonsi, L., Belova, E., Buchert, S., Clilverd, M., Engler, N., Gustavsson, B., Heinselman, C., Kero, J., Kosch, M., Lamy, H., Leyser, T., Ogawa, Y., Oksavik, K., Pellinen-Wannberg, A., Pitout, F., Rapp, M., Stanislawska, I., and Vierinen, J.: The science case for the EISCAT_3D radar, Progress in Earth and Planetary Science, 2, 21, doi: 10.1186/s40645-015-0051-8, 2015.

McPherron, R. L.: Growth phase of magnetospheric substorms, JGR, 75, 5592, doi: 10.1029/JA075i028p05592, 1970.

McPherron, R. L., Baker, D. N., and Crooker, N. U.: Role of the Russell-McPherron effect in the acceleration of relativistic electrons, Journal of Atmospheric and Solar-Terrestrial Physics, 71, 1032–1044, doi: 10.1016/j.jastp.2008.11.002, 2009.

Meyer-Vernet, N., Daigne, G., and Lecacheux, A.: Dynamic spectra of some terrestrial ionospheric effects at decametric wavelengths - Applications in other astrophysical contexts, Astronomy and Astrophysics, 96, 296–301, 1981.

Mironova, I. A., Aplin, K. L., Arnold, F., Bazilevskaya, G. A., Harrison, R. G., Krivolutsky, A. A., Nicoll, K. A., Rozanov, E. V., Turunen, E., and Usoskin, I. G.: Energetic Particle Influence on the Earth's Atmosphere, Space Science Rev., 194, 1–96, doi: 10.1007/s11214-015-0185-4, 2015.

Nicolls, M. J., Sulzer, M. P., Aponte, N., Seal, R., Nikoukar, R., and González, S. A.: High-resolution electron temperature measurements using the plasma line asymmetry, Geophysical Research Letters, 33, doi: 10.1029/2006GL027222, 2006.

Nijboer, R., Pandey-Pommier, M., and de Bruyn, A.: LOFAR imaging capabilities and system sensitivity, 2009.

Nygrén, T., Aikio, A. T., Kuula, R., and Voiculescu, M.: Electric fields and neutral winds from monostatic incoherent scatter measurements by means of stochastic inversion, Journal of Geophysical Research (Space Physics), 116, A05305, doi: 10.1029/2010JA016347, 2011.

Oberoi, D. and Kasper, J. C.: LOFAR: The potential for solar and space weather studies, Planetary and Space Science, 52, 1415 – 1421, doi: 10.1016/j.pss.2004.09.009, 2004.

Ono, T., Hirasawa, T., and Meng, C. I.: Proton auroras observed at the equatorward edge of the duskside auroral oval, Geophysical Research Letters, 14, 660–663, doi: 10.1029/GL014i006p00660, 1987.

Ortner, J., Hultqvist, B., Brown, R. R., Hartz, T. R., Holt, O., Landmark, B., Hook, J. L., and Leinbach, H.: Cosmic Noise Absorption Accompanying Geomagnetic Storm Sudden Commencements, Journal of Geophysical Research, 67, 4169–4186, doi: 10.1029/JZ067i011p04169, 1962.

Parthasarathy, R., Lerfald, G. M., and Little, C. G.: Derivation of Electron-Density Profiles in the Lower Ionosphere Using Radio Absorption Measurements at Multiple Frequencies, Journal of Geophysical Research, 68, 3581–3588, doi: 10.1029/JZ068i012p03581, 1963.

Patterson, J. D., Armstrong, T. P., Laird, C. M., Detrick, D. L., and Weatherwax, A. T.: Correlation of solar energetic protons and polar cap absorption, Journal of Geophysical Research, 106, 149–164, doi: 10.1029/2000JA002006, 2001.

Prikryl, P., Jayachandran, P. T., Mushini, S. C., and Chadwick, R.: Climatology of GPS phase scintillation and HF radar backscatter for the high-latitude ionosphere under solar minimum conditions, Annales Geophysicae, 29, 377–392, doi: 10.5194/angeo-29-377-2011, 2011.

Pulkkinen, T. I.: Pseudobreakup or substorm? (Invited), in: International Conference on Substorms, edited by Rolfe, E. J. and Kaldeich, B., vol. 389 of *ESA Special Publication*, p. 285, 1996.

Pytte, T., Trefall, H., Kremser, G., Jalonen, L., and Riedler, W.: On the morphology of energetic ($\geq$30 keV) electron precipitation during the growth phase of magnetospheric substorms (Paper I), Journal of Atmospheric and Terrestrial Physics, 38, 739–755, doi: 10.1016/0021-9169(76)90112-4, 1976.

Ranta, H. and Ranta, A.: Study of latitudinal, diurnal and seasonal variation of ionospheric absorption according to observations of the riometer network in Finland, Geophysica, 1, 1974.

Rapp, M. and Lübken, F.-J.: Polar mesosphere summer echoes (PMSE): Review of observations and current understanding, Atmospheric Chemistry & Physics, 4, 2601–2633, 2004.

Raulin, J.-P. and Pacini, A. A.: Solar radio emissions, Advances in Space Research, 35, 739–754, doi: 10.1016/j.asr.2005.03.138, 2005.

Rees, M. H.: Physics and Chemistry of the Upper Atmosphere, Cambridge University Press, 1989.

Rietveld, M. T., Senior, A., Markkanen, J., and Westman, A.: New capabilities of the upgraded EISCAT high-power HF facility, Radio Science, 51, 1533–1546, doi: 10.1002/2016RS006093, 2016.

Rishbeth, H. and Roble, R. G.: Cooling of the upper atmosphere by enhanced greenhouse gases — modelling of thermospheric and ionospheric effects, Planetary and Space Science, 40, 1011 – 1026, doi: http://dx.doi.org/10.1016/0032-0633(92)90141-A, 1992.

Rishbeth, H. and Williams, P.: The EISCAT Ionospheric Radar: the System and its Early Results, Q. Jl. R. Astr. Soc., 26, 478–512, 1985.

Ryle, M., Hewish, A., and Shakeshaft, J.: The synthesis of large radio telescopes by the use of radio interferometers, IEEE Transactions on Antennas and Propagation, 7, 120–124, doi: 10.1109/TAP.1959.1144745, 1959.

Sangalli, L., Gustavsson, B., Partamies, N., and Kauristie, K.: Estimating the peak auroral emission altitude from all-sky images, Opt. Pura Apl., 44, 593–598, 2011a.

Sangalli, L., Partamies, N., Syrjäsuo, M., Enell, C.-F., Kauristie, K., and Mäkinen, S.: Performance study of the new EMCCD-based all-sky cameras for auroral imaging, International Journal of Remote Sensing, 32, 2987–3003, doi: 10.1080/01431161.2010.541505, 2011b.

Schilizzi, R. T., Dewdney, P. E. F., and Lazio, T. J. W.: The square kilometre array, in: Society of Photo-Optical Instrumentation Engineers (SPIE) Conference Series, vol. 7733 of *Society of Photo-Optical Instrumentation Engineers (SPIE) Conference Series*, doi: 10.1117/12.856344, 2010.

Schlatter, N. M., Grydeland, T., Ivchenko, N., Belyey, V., Sullivan, J., La Hoz, C., and Blixt, M.: Radar interferometer calibration of the EISCAT Svalbard Radar and a additional receiver station, Journal of Atmospheric and Solar-Terrestrial Physics, 105, 287–292, doi: 10.1016/j.jastp.2012.11.017, 2013.

Semeniuk, K., Fomichev, V. I., McConnell, J. C., Fu, C., Melo, S. M. L., and Usoskin, I. G.: Middle atmosphere response to the solar cycle in irradiance and ionizing particle precipitation, Atmospheric Chemistry & Physics, 11, 5045–5077, doi: 10.5194/acp-11-5045-2011, 2011.

Seppälä, A., Randall, C. E., Clilverd, M. A., Rozanov, E., and Rodger, C. J.: Geomagnetic activity and polar surface air temperature variability, Journal of Geophysical Research (Space Physics), 114, A10312, doi: 10.1029/2008JA014029, 2009.

Shain, C. A.: Galactic Radiation at 18.3 Mc/s., Australian Journal of Scientific Research A Physical Sciences, 4, 258, 1951.

Shibasaki, K., Alissandrakis, C. E., and Pohjolainen, S.: Radio Emission of the Quiet Sun and Active Regions (Invited Review), Solar Physics, 273, 309–337, doi: 10.1007/s11207-011-9788-4, 2011.

Sinnhuber, M., Friederich, F., Bender, S., and Burrows, J. P.: The response of mesospheric NO to geomagnetic forcing in 2002-2012 as seen by SCIAMACHY, Journal of Geophysical Research (Space Physics), 121, 3603–3620, doi: 10.1002/2015JA022284, 2016.

Spanswick, E., Donovan, E., Friedel, R., and Korth, A.: Ground based identification of dispersionless electron injections, Geophys. Res. Lett., 34, L03101, doi: 10.1029/2006GL028329, 2007.

Stauning, P. and Rosenberg, T. J.: High-latitude daytime absorption spike events, Journal of Geophysical Research, 101, 2377–2396, doi: 10.1029/95JA03125, 1996.

Stewart, B.: On the Great Magnetic Disturbance of August 28 to September 7, 1859, as Recorded by Photography at the Kew Observatory., Proceedings of the Royal Society of London Series I, 11, 407–410, 1860.

Stober, G. and Chau, J. L.: A multistatic and multifrequency novel approach for specular meteor radars to improve wind measurements in the MLT region, Radio Science, 50, 431–442, doi: 10.1002/2014RS005591, 2015.

Stubbe, P.: Modifying effects of a strong electromagnetic wave upon a weakly ionized plasma - A kinetic description, Radio Science, 16, 417–425, doi: 10.1029/RS016i003p00417, 1981.

Szasz, C., Kero, J., Meisel, D. D., Pellinen-Wannberg, A., Wannberg, G., and Westman, A.: Orbit characteristics of the tristatic EISCAT UHF meteors, Mon. Not. R. Astron. Soc., 388, 15–25, doi: 10.1111/j.1365-2966.2008.13374.x, 2008.

Szponarski, P., Honary, F., and McKay-Bukowski, D.: Climatology of high-latitude ionospheric scintillation based on 38.2 MHz IRIS riometer measurements in Northern Finland, AGU Fall Meeting Abstracts, 2015.

Tanskanen, E. I.: A comprehensive high-throughput analysis of substorms observed by IMAGE magnetometer network: Years 1993–2003, Journal of Geophysical Research (Space Physics), 114, A05204, doi: 10.1029/2008JA013682, 2009.

Tanskanen, E. I., Pulkkinen, T. I., Viljanen, A., Mursula, K., Partamies, N., and Slavin, J. A.: From space weather toward space climate time scales: Substorm analysis from 1993 to 2008, Journal of Geophysical Research: Space Physics, 116, n/a–n/a, doi: 10.1029/2010JA015788, 2011.

Thompson, A. R.: Fundamentals of Radio Interferometry, in: Synthesis Imaging in Radio Astronomy II, edited by Taylor, G. B., Carilli, C. L., and Perley, R. A., vol. 180 of *Astronomical Society of the Pacific Conference Series*, p. 11, 1999.

Tingay, S. J., Goeke, R., Bowman, J. D., Emrich, D., Ord, S. M., Mitchell, D. A., Morales, M. F., Booler, T., Crosse, B., Wayth, R. B., Lonsdale, C. J., Tremblay, S., Pallot, D., Colegate, T., Wicenec, A., Kudryavtseva, N., Arcus, W., Barnes, D., Bernardi, G., Briggs, F., Burns, S., Bunton, J. D., Cappallo, R. J., Corey, B. E., Deshpande, A., Desouza, L., Gaensler, B. M., Greenhill, L. J., Hall, P. J., Hazelton, B. J., Herne, D., Hewitt, J. N., Johnston-Hollitt, M., Kaplan, D. L., Kasper, J. C., Kincaid, B. B., Koenig, R., Kratzenberg, E., Lynch, M. J., Mckinley, B., Mcwhirter, S. R., Morgan, E., Oberoi, D., Pathikulangara, J., Prabu, T., Remillard, R. A., Rogers, A. E. E., Roshi, A., Salah, J. E., Sault, R. J., Udaya-Shankar, N., Schlagenhaufer, F., Srivani, K. S., Stevens, J., Subrahmanyan, R., Waterson, M., Webster, R. L., Whitney, A. R., Williams, A., Williams, C. L., and Wyithe, J. S. B.: The Murchison Widefield Array: The Square Kilometre Array Precursor at Low Radio Frequencies, Publ.ASA, 30, e007, doi: 10.1017/pasa.2012.007, 2013.

Ulich, T., Aikio, A., McCrea, I., and Turunen, E.: EISCAT_3D: the European three-dimensional imaging radar for atmospheric and geospace research, in: 38th COSPAR Scientific Assembly, vol. 38 of *COSPAR Meeting*, p. 873, 2010.

van Cittert, P. H.: Die Wahrscheinliche Schwingungsverteilung in Einer von Einer Lichtquelle Direkt Oder Mittels Einer Linse Beleuchteten Ebene, Physica, 1, 201–210, doi: 10.1016/S0031-8914(34)90026-4, 1934.

van Eyken, T., Turunen, E., Wannberg, G., Andersson, H., Behlke, R., Belyey, V., Bergqvist, P., Borg, J., Brekke, A., Delsing, J., Edwall, M., Finch, I., Gabert, A., Grydeland, T., Gustavsson, A., Gustavsson, B., Häggström, I., Iinatti, T., Johansson, G., Johansson, J., Johansson, J., C., L., Laakso, T., Larsen, R., Larsmark, M., Lindgren, T., Lindström, J., Lundberg, M., Lång, U., Markkanen, J., Marttala, I., McKay, D., I., M., Oeschger, S., Postila, M., Puccio, W., Renkwitz, T., Ståbis, J., Söderström, K., Vanhainen, L.-G., Westmann, A., and I., W.: EISCAT_3D Final Design Study Report, Deliverable D11.1, Editors: McKay, D. and McCrea I., EISCAT Scientific Association, D11.1, 2009.

van Haarlem, M. P., Wise, M. W., Gunst, A. W., Heald, G., McKean, J. P., Hessels, J. W. T., de Bruyn, A. G., Nijboer, R., Swinbank, J., Fallows, R., Brentjens, M., Nelles, A., Beck, R., Falcke, H., Fender, R., Hörandel, J., Koopmans, L. V. E., Mann, G., Miley, G., Röttgering, H., Stappers, B. W., Wijers, R. A. M. J., Zaroubi, S., van den Akker, M., Alexov, A., Anderson, J., Anderson, K., van Ardenne, A., Arts, M., Asgekar, A., Avruch, I. M., Batejat, F., Bähren, L., Bell, M. E., Bell, M. R., van Bemmel, I., Bennema, P., Bentum, M. J., Bernardi, G., Best, P., Bîrzan, L., Bonafede, A., Boonstra, A.-J., Braun, R., Bregman, J., Breitling, F., van de Brink, R. H., Broderick, J., Broekema, P. C., Brouw, W. N., Brüggen, M., Butcher, H. R., van Cappellen, W., Ciardi, B., Coenen, T., Conway, J., Coolen, A., Corstanje, A., Damstra, S., Davies, O., Deller, A. T., Dettmar, R.-J., van Diepen, G., Dijkstra, K., Donker, P., Doorduin, A., Dromer, J., Drost, M., van Duin, A., Eislöffel, J., van Enst, J., Ferrari, C., Frieswijk, W., Gankema, H., Garrett, M. A., de Gasperin, F., Gerbers, M., de Geus, E., Grießmeier, J.-M., Grit, T., Gruppen, P., Hamaker, J. P., Hassall, T., Hoeft, M., Holties, H. A., Horneffer, A., van der Horst, A., van Houwelingen, A., Huijgen, A., Iacobelli, M., Intema, H., Jackson, N., Jelic, V., de Jong, A., Juette, E., Kant, D., Karastergiou, A., Koers, A., Kollen, H., Kondratiev, V. I., Kooistra, E., Koopman, Y., Koster, A., Kuniyoshi, M., Kramer, M., Kuper, G., Lambropoulos, P., Law, C., van Leeuwen, J., Lemaitre, J., Loose, M., Maat, P., Macario, G., Markoff, S., Masters, J., McFadden, R. A., McKay-Bukowski, D., Meijering, H., Meulman, H., Mevius, M., Middelberg, E., Millenaar, R., Miller-Jones, J. C. A., Mohan, R. N., Mol, J. D., Morawietz, J., Morganti, R., Mulcahy, D. D., Mulder, E., Munk, H., Nieuwenhuis, L., van Nieuwpoort, R., Noordam, J. E., Norden, M., Noutsos, A., Offringa, A. R., Olofsson, H., Omar, A., Orrú, E., Overeem, R., Paas, H., Pandey-Pommier, M., Pandey, V. N., Pizzo, R., Polatidis, A., Rafferty, D., Rawlings, S., Reich, W., de Reijer, J.-P., Reitsma, J., Renting, G. A., Riemers, P., Rol, E., Romein, J. W., Roosjen, J., Ruiter, M., Scaife, A., van der Schaaf, K., Scheers, B., Schellart, P., Schoenmakers, A., Schoonderbeek, G., Serylak, M., Shulevski, A., Sluman, J., Smirnov, O., Sobey, C., Spreeuw, H., Steinmetz, M., Sterks, C. G. M., Stiepel, H.-J., Stuurwold, K., Tagger, M., Tang, Y., Tasse, C., Thomas, I., Thoudam, S., Toribio, M. C., van der Tol, B., Usov, O., van Veelen, M., van der Veen, A.-J., ter Veen, S., Verbiest, J. P. W., Vermeulen, R., Vermaas, N., Vocks, C., Vogt, C., de Vos, M., van der Wal, E., van Weeren, R., Weggemans, H., Weltevrede, P., White, S., Wijnholds, S. J., Wilhelmsson, T., Wucknitz, O., Yatawatta, S., Zarka, P., Zensus, A., and van Zwieten, J.: LOFAR: The LOw-Frequency ARray, A&A, 556, A2, doi: 10.1051/0004-6361/201220873, 2013.

Verronen, P. T., Seppälä, A., Clilverd, M. A., Rodger, C. J., KyröLä, E., Enell, C.-F., Ulich, T., and Turunen, E.: Diurnal variation of ozone depletion during the October-November 2003 solar proton events, Journal of Geophysical Research (Space Physics), 110, A09S32, doi: 10.1029/2004JA010932, 2005.

Vierinen, J., McKay-Bukowski, D., Lehtinen, M., Kero, A., and Ulich, T.: Kilpisjärvi Atmospheric Imaging Receiver Array — First results, in: Phased Array Systems & Technology, 2013 IEEE International Symposium on, pp. 664–668, doi: 10.1109/ARRAY.2013.6731909, 2013.

Virtanen, I. I.: Station Data Cookbook, ASTRON technical document LOFAR-ASTRON-MAN-064, lOFAR-ASTRON-MAN-064, ASTRON Technical Note, 2012.

Virtanen, I. I., Lehtinen, M. S., Nygrén, T., Orispää, M., and Vierinen, J.: Lag profile inversion method for EISCAT data analysis, Annales Geophysicae, 26, 571–581, doi: 10.5194/angeo-26-571-2008, 2008.

Virtanen, I. I., McKay-Bukowski, D., Vierinen, J., Aikio, A., Fallows, R., and Roininen, L.: Plasma parameter estimation from multistatic, multibeam incoherent scatter data, Journal of Geophysical Research (Space Physics), 119, 10 528, doi: 10.1002/2014JA020540, 2014.

Wijnholds, S. J. and van Cappellen, W. A.: In situ antenna performance evaluation of the LOFAR phased array radio telescope, IEEE Transactions on Antennas and Propagation, 59, 1981–1989, 2011.

Wijnholds, S. J., Bregman, J. D., and van Ardenne, A.: Calibratability and its impact on configuration design for the LOFAR and SKA phased array radio telescopes, Radio Science, 46, RS0F07, doi: 10.1029/2011RS004733, 2011.

Wild, P., Honary, F., Kavanagh, A. J., and Senior, A.: Triangulating the height of cosmic noise absorption: A method for estimating the characteristic energy of precipitating electrons, Journal of Geophysical Research (Space Physics), 115, A12326, doi: 10.1029/2010JA015766, 2010.

Williams, P. J. S., Vaneyken, A. P., Hall, C., and Roettger, J.: Polar mesosphere summer echoes and associated atmospheric gravity waves, in: European Rocket & Balloon Programmes and Related Research, edited by Burke, W. R., vol. 291 of *ESA Special Publication*, 1989.

Wing, S., Gkioulidou, M., Johnson, J. R., Newell, P. T., and Wang, C.-P.: Auroral particle precipitation characterized by the substorm cycle, Journal of Geophysical Research (Space Physics), 118, 1022–1039, doi: 10.1002/jgra.50160, 2013.

Woodman, R. F.: High-altitude resolution stratospheric measurements with the Arecibo 430-MHz radar, Radio Science, 15, 417–422, doi: 10.1029/RS015i002p00417, 1980.

Wucknitz, O.: e-VLBI with LOFAR, in: 10th European VLBI Network Symposium and EVN Users Meeting: VLBI and the New Generation of Radio Arrays, 2010.

Zawdie, K. A., Drob, D. P., Siskind, D. E., and Coker, C.: Calculating the absorption of HF radio waves in the ionosphere, Radio Science, 52, 767–783, doi: 10.1002/2017RS006256, 2017.

Zernike, F.: The concept of degree of coherence and its application to optical problems, Physica, 5, 785–795, doi: 10.1016/S0031-8914(38)80203-2, 1938.

PAPER I

M$^{\underline{c}}$Kay-Bukowski, D., *et al.* (2015) *KAIRA: The Kilpisjärvi Atmospheric Imaging Receiver Array — System Overview and First Results*, in IEEE Transactions on Geoscience and Remote Sensing, vol. 53, no. 3, pp. 1440–1451, March 2015. doi: 10.1109/TGRS.2014.2342252.

PAPER II

McKay, D., R. Fallows, M. Norden, A. Aikio, J. Vierinen, F. Honary, S. Marple, and T. Ulich (2015), *All-sky interferometric riometry*, Radio Science, **50**, 1050–1061, October 2015, doi:10.1002/2015RS005709.

PAPER III

McKay, D., N. Partamies, J. Vierinen (2018), *Pulsating aurora and cosmic noise absorption associated with growth-phase arcs*, Annales Geophysicae, **36**, 59–69, January 2018, doi:10.5194/angeo-36-59-2018.

PAPER IV

McKay, D., N. Partamies, K. Kauristie (2017), *Acquisition of optical and riometric keograms for studying auroral electron precipitation*, in: XVIII Geofysiikan Päivät, Geofysiikan seura r.y., 35–38, available at: `https://geofysiikanseura.yhdistysavain.fi/@Bin/174016/GFP2017_kirja.pdf` (last access: 31 January 2018), 2017.

This section of the publication has been reprinted with the permission of Geophysical Society of Finland.

Appendices

Appendix A

Abbreviations

The following is a list of acronyms and abbreviations used in this work.

AA	Auroral (radio) absorption
ACC	Antenna Cross-Correlation (also Array Covariance Cube)
ADU	Analogue-to-Digital converter Unit
A_{P}	Daily-average of geomagnetic indices
ARA	Averaged Radio Absorption (mean, median, etc.)
ASC	All-Sky Camera
ASTRON	Netherlands foundation for radio astronomy
BPF	Band Pass Filter (Finnish: *kaistanpäästösuodatin*)
BST	Beamlet STatistics (a KAIRA data product)
Cas A	Cassiopeia A (astronomical radio source)
CEP	Central Processing (correlator for the ILT)
CNA	Cosmic Noise Absorption
CPU	Central Processing Unit
Cyg A	Cygnus A (astronomical radio source)
DAB	Digital Audio Broadcasting (radio broadcasting)
DC	Direct Current
DE601	LOFAR station, Effelsberg, Germany
DSP	Digital Signal Processing
EISCAT	European Incoherent Scatter (scientific association and/or radar facility)
ETRS	European Terrestrial Reference System
E-W	East-West
FI609	LOFAR station, Finland #609 (= Kilpisjärvi, LCU only)
FM	Frequency Modulation (radio broadcasting)
FMI	Finnish Meteorological Institute
FR606	LOFAR station, Nançay, France

FWHM	Full-Width Half-Maximum
GB	Gigabyte (= 10^9 bytes)
GiB	Gibibyte (= 2^{30} bytes = 1073741824 bytes)
GK	Gauss-Krüger (map projection)
GPA	Ground Penetrating Radar
GPS	Global Positioning System (also used as a time reference)
GRS	Geodetic Reference System
HBA	High Band Antenna (tile)
HDD	Hard-Disk Drive
HF	High Frequency (3–30 MHz)
HIAB	*Hydrauliska Industri AB* (type of loader crane)
HPF	Low Pass Filter (Finnish: *Ylipäästösuodatin*)
HWHM	Half-Width Half-Maximum
IEEE	Institute of Electrical and Electronics Engineers
IL	Magnetic index; envelope curve of the north-south component
ILT	International LOFAR Telescope
IMF	Interplanetary Magnetic Field
IP	Internet Protocol
IPS	Interplanetary Scintillation
IRF	*Institutet för rymdfysik* (Swedish Institute for Space Physics)
IRIS	Imaging Riometer for Ionospheric Studies
ISR	Incoherent Scatter Radar
IVO	*Imatran Voima Oy*
KAIRA	Kilpisjärvi Atmospheric Imaging Receiver Array
KAS	KAIRA All-Sky (imaging software)
kB	Kilobytes (1×10^3 bytes)
KBT	KAIRA Background Task (observing control software)
KKJ	*Kartastokoordinaattijärjestelmä*, Finnish National Coordinate System, 1970-2005
KLP	KAIRA Local Pipeline (raw-voltage data acquisition software)
KMD	KAIRA Monitoring Data (data transfer/quick-look scripts/software)
KMT	KAIRA Monitoring Task (system monitoring scripts/software)
K_P	*Kennziffer*-index, planetary geomagnetic index
KSW	KAIRA Software (the set of all KAIRA bespoke software)
KUG	KAIRA UDP Get (raw-voltage VLBI data acquisition software)
KUW	KAIRA UDP Writer (data acquisition software)
LAN	Local Area Network
LBA	Low-Band Antenna (inverted-V dipole)

LBH	Low-Band High (LBA input for RCU modes 3 & 4)
LBL	Low-Band Low (LBA input for RCU modes 1 & 2)
LCU	Local Control Unit (control computer)
LMT	Local Magnetic Time
LNA	Low-Noise Amplifier
LOFAR	Low Frequency Array
LPF	Low Pass Filter (Finnish: *Alipäästösuodatin*)
LST	Local Sidereal Time
MMARSY	Middle Atmosphere Alomar Radar System (radar, Andenes)
MB	Megabytes (1×10^6 bytes)
MFIR	Multi-Frequency Interferometric Riometry
MIRK	Meridian Interferometric Riometry Keogram
MLT	Magnetic Local Time
MORRO	Mobile Rocket & Radar Observatory (radar, Ramfjordmoen)
MPIfR	*Max-Planck Institut für Radioastronomie*, Germany
MRA	Meridian Radio Absorption
MRO	Metsähovi Radio Observatory, Finland
NOx	Nitric oxide
N-S	North-South
OERA	Optical Emission / Radio Absorption
ORK	Optical-Radio Comparison
PCA	Polar Cap Absorption
Pc	(Pc4, Pc5, etc.) Micropulsation
PMSE	Polar Mesospheric Summer Echo
PPFB	Poly-phase filter bank (Finnish: *Monivaihesuodatinpankki*)
PVC	Polyvinyl chloride
RAL	Rutherford Appleton Laboratory, United Kingdom
Rb	Rubidium (KAIRA's atomic clock)
RCU	Receiver Unit
RF-container	Shipping container, with Faraday enclosure for DSP electronics
RFI	Radio-Frequency Interference
RIAN	Institute of Radio Astronomy, Ukraine
RIOMETER	Relative Ionospheric Opacity Meter for Extra-Terrestrial Electromagnetic Radiation
SE607	LOFAR station, Onsala, Sweden
SFIR	Single-Frequency Interferometric Riometry
SGO	Sodankylä Geophysical Observatory, Finland
SIC	Sodankylä Ion Chemistry (model)

SST	Subband STatistics (a KAIRA data product)
STFC	Science & Technology Facilities Council, United Kingdom
TEC	Total Electron Content
TECU	Total Electron Content (TEC) Units
UHF	Ultra High Frequency (300–3000 MHz)
UiT	*Universitetet i Tromsø*, Norway
UK608	LOFAR station, Chilbolton, UK
ULF	Ultra Low Frequency (0.3–3 kHz)
UTC	Coordinated Universal Time
VHF	Very High Frequency (30–300 MHz)
VLAN	Virtual Local Area Network
VLBI	Very Long Baseline Interferometry
VLF	Very Low Frequency (3–30 kHz)
VR	*Valtionrautatiet* (Finnish State Railways)
XST	Cross-correlation STatistics

Appendix B

KAIRA technical details

B.1 KAIRA array parameters

Parameter	LBA Array	HBA Array
Number of antennas	48	48 (47 after March 2014)
Antenna type	Inverted-V dipoles	16-element tiles
Number of elements	48	768 (752 after March 2014)
Polarisations per antenna	2 linear	2 linear
X-polarisation alignment	+X = 45°	+X = 137°
Y-polarisation alignment	+Y = 315°	+Y = 47°
Polarisation diagram	Figure E.47	Figure E.27
Array layout	sparse, quasi-random	segmented, rectangular grid
Array physical size	34 m diameter	30 × 50 m
Array alignment	symmetrical	313.95 degrees
Minimum frequency	8 MHz	110 MHz
Maximum frequency	80 MHz	270 MHz
Tile beam-forming	n/a	analogue
Array beam-forming	digital	digital
Longitude	20.76207580° E	20.76103311° E
Latitude	69.07074450° N	69.07105610° N
Height (GRS)	523.371 m	525.336 m
Height (GK/N60)	493.123 m	495.086 m
Geocentric-X	2136832.728 m	2136818.698 m
Geocentric-Y	810088.928 m	810039.764 m
Geocentric-Z	5935285.442 m	5935299.217 m

Table B.1: Parameters for the two KAIRA antenna arrays (Paper I). Observing frequency ranges are not hard edges and are subject to amplifier and antenna response and RFI considerations (see Figure 2.7). Coordinates are for the array centres and are given using ITRF2005 (epoch=2013.5) EUREF-FIN. The geographic height reference system for both global GRS and Finnish national GK/N60 systems are given. Initially, KAIRA had 48 HBA tiles, but one was lost during a blizzard in March 2014 (see Appendix E.20).

B.2 Antenna–RCU assignment

RCUs	LBA	HBA	RCUs	LBA	HBA	RCUs	LBA	HBA	RCUs	LBA	HBA
0,1	0	22	24,25	12	38	48,49	24	54	72,73	36	70
2,3	1	23	26,27	13	39	50,51	25	55	74,75	37	71
4,5	2	24	28,29	14	41	52,53	26	56	76,77	38	73
6,7	3	25	30,31	15	42	54,55	27	57	78,79	39	74
8,9	4	27	32,33	16	44	56,57	28	59	80,81	40	75
10,11	5	28	34,35	17	45	58,59	29	60	82,83	41	76
12,13	6	30	36,37	18	46	60,51	30	62	84,85	42	77
14,15	7	31	38,39	19	47	62,53	31	63	86,87	43	78
16,17	8	33	40,41	20	48	64,55	32	65	88,89	44	80
18,19	9	34	42,43	21	49	66,67	33	66	90,91	45	81
20,21	10	35	44,45	22	51	68,69	34	67	92,93	46	83
22,23	11	36	46,47	23	52	70,71	35	68	94,95	47	96

Table B.2: RCU numbers and the equivalent LBA-aerials and HBA-tiles for the KAIRA station. The two RCU numbers given are for the X and Y polarisations, respectively. For example, RCU 28 is HBA #H41-X and RCU 29 is HBA #H41-Y. The disjunct numbering sequence of the HBA tiles is the result of maintaining numerical compatibility with an International LOFAR station, as described in Appendix E.3.

B.3 Subrack assembly layout

Subrack 0

RCU →	#07	#06	#05	#04	#15	#14	#23	#22	#31	#30	#29
HBA →	25Y	25X	24Y	24X	31Y	31X	36Y	36X	42Y	42X	41Y
LBH →	03Y	03X	02Y	02X	07Y	07X	11Y	11X	15Y	15X	14Y
LBL →	–	–	–	–	–	–	–	–	–	–	–
	#03	#02	#11	#10	#13	#12	#21	#20	#27	#26	#28
	23Y	23X	28Y	28X	30Y	30X	35Y	35X	39Y	39X	41X
	01Y	01X	05Y	05X	06Y	06X	10Y	10X	13Y	13X	14X
	–	–	–	–	–	–	–	–	–	–	–
	#01	#00	#09	#08	#17	#16	#19	#18	#25	#24	
	22Y	22X	27Y	27X	33Y	33X	34Y	34X	38Y	38X	
	00Y	00X	04Y	04X	08Y	08X	09Y	09X	12Y	12X	
	–	–	–	–	–	–	–	–	–	–	

Subrack 1

RCU →	#39	#38	#37	#36	#47	#46	#55	#54	#63	#62	#61
HBA →	47Y	47X	46Y	46X	52Y	52X	57Y	57X	63Y	63X	62Y
LBH →	19Y	19X	18Y	18X	23Y	23X	27Y	27X	31Y	31X	30Y
LBL →	–	–	–	–	–	–	–	–	–	–	–
	#35	#34	#43	#42	#45	#44	#53	#52	#59	#58	#60
	45Y	45X	49Y	49X	51Y	51X	56Y	56X	60Y	60X	62X
	17Y	17X	21Y	21X	22Y	22X	26Y	26X	29Y	29X	30X
	–	–	–	–	–	–	–	–	–	–	–
	#33	#32	#41	#40	#49	#48	#51	#50	#57	#56	
	44Y	44X	48Y	48X	54Y	54X	55Y	55X	59Y	59X	
	16Y	16X	20Y	20X	24Y	24X	25Y	25X	28Y	28X	
	–	–	–	–	–	–	–	–	–	–	

Subrack 2

RCU →	#71	#70	#69	#68	#79	#78	#87	#86	#95	#94	#93
HBA →	68Y	68X	67Y	67X	74Y	74X	78Y	78X	96Y	96X	83Y
LBH →	35Y	35X	34Y	34X	39Y	39X	43Y	43X	47Y	47X	46Y
LBL →	–	–	–	–	–	–	–	–	–	–	–
	#67	#66	#75	#74	#77	#76	#85	#84	#91	#90	#92
	66Y	66X	71Y	71X	73Y	73X	77Y	77X	81Y	81X	83X
	33Y	33X	37Y	37X	38Y	38X	42Y	42X	45Y	45X	46X
	–	–	–	–	–	–	–	–	–	–	–
	#65	#64	#73	#72	#81	#80	#83	#82	#89	#88	
	65Y	65X	70Y	70X	75Y	75X	76Y	76X	80Y	80X	
	32Y	32X	36Y	36X	40Y	40X	41Y	41X	44Y	44X	
	–	–	–	–	–	–	–	–	–	–	
	RSP 0		*RSP 1*		*RSP 2*				*RSP 3*		

Table B.3: Layout of the subrack assemblies, showing the positions of the RCUs for each subrack and the connected HBA and LBA polarisation. The LBAs are connected to the LBH input, with the LBL input not being used. The alternating white/grey bands indicate the RSP with which each RCU is associated.

B.4 RCU modes

RCU Mode	RCU input	Array	Nyquist zone	Filter range (approx. MHz)	Notes
0	–	–	I	–	*"off-position"*
1	LBL	LBA	I	10–90	*Not used at KAIRA*
2	LBL	LBA	I	30–90	*Not used at KAIRA*
3	LBH	LBA	I	10–90	
4	LBH	LBA	I	30–90	
5	HBA	HBA	II	110–190	
6	HBA	HBA	III	170–230	*Uses 160 MHz clock*
7	HBA	HBA	III	210–270	

Table B.4: RCU modes, indicating signal inputs and filter ranges (Paper I). In principle, any RCU mode can use either the 160 or 200 MHz sampler clock. However, in practice Mode 6 is the only one to do so.

B.5 Subband and beamlet parameters

Parameter	Performance			
Sample bit depth	12	8	4	bits
Max. number of simultaneous beamlets	244	488	976	
Polarisations per beamlet	2	2	2	
Cumulative bandwidth (200 MHz)	47.7	95.3	190.6	MHz
Cumulative bandwidth (160 MHz)	38.1	76.3	152.5	MHz
Spectral Resolution (200 MHz)	195.31	195.31	195.31	kHz
Spectral Resolution (160 MHz)	156.25	156.25	156.25	kHz

Table B.5: Signal-processing parameters for the KAIRA facility. The three columns reflect differences when selecting different numbers of sample bits. Where appropriate, different values are given for the two sampler clock settings (160 or 200 MHz).

Appendix C

KAIRA array layout

Tables C.1 and C.2 give the coordinates of the HBA and LBA arrays of KAIRA. The coordinates are provided in metres using ETRS89-GK21, which is the standard Finnish geodetic reference frame, where ETRS89 is the EU-recommended frame of reference for geodata for Europe and GK21 refers to the Gauss-Krüger -projection based on the central meridian of 21 degrees east.

ETRS89-GK21, which was introduced in 2005 and replaces Finland's previous national coordinate system (KKJ). ETRS89 is based on the global reference ellipsoid of the Geodetic Reference System 1980 (GRS80) (Finnish Public Recommendation, 197, 2016).

In Tables C.1 and C.2, the true northing and height are given, but the conventional false easting is used. To convert from the false easting to the true easting, prepend the coordinate system nominal meridian (which is 21 in the case of ETRS89-GK21). For example: 490462.709 → 21490462.709.

During the surveying process, the positions were measured to ±1 cm, in order to lie within the required error budget for the array deployment (±3 cm and ±6 cm for the HBA and LBA arrays, respectively). The tables in this appendix are the original survey data output. Subsequent transformations were done using the online coordinate transformation service provided by the Finnish Geodetic Institute. Ref: `http://coordtrans.fgi.fi/` . These are used to populate the array configuration file (`AntennaField.conf`) which is used for beamforming and post-processing of interferometric data.

A map of the complete array layout is shown in Figure 2.6 on page 11. The numbering arrangement within each individual HBA tile is given in Figure E.25 on page 176.

C.1 HBA array

ID	E (m)	N (m)	ID	E (m)	N (m)
H22	490462.709	7665394.015	H54	490451.947	7665382.939
H23	490466.401	7665390.428	H55	490455.639	7665379.352
H24	490470.094	7665386.840	H56	490459.331	7665375.764
H25	490473.786	7665383.253	H57	490463.023	7665372.177
H27	490481.170	7665376.078	H59	490470.407	7665365.002
H28	490484.862	7665372.490	H60	490474.100	7665361.414
H30	490492.246	7665365.315	H62	490481.484	7665354.239
H31	490495.938	7665361.728	H63	490485.176	7665350.652
H33	490459.122	7665390.323	H65	490448.359	7665379.247
H34	490462.814	7665386.736	H66	490452.051	7665375.660
H35	490466.506	7665383.148	H67	490455.744	7665372.072
H36	490470.198	7665379.561	H68	490459.436	7665368.485
H38	490477.582	7665372.386	H70	490466.820	7665361.309
H39	490481.275	7665368.798	H71	490470.512	7665357.722
H41	490488.659	7665361.623	H73	490477.896	7665350.547
H42	490492.351	7665358.036	H74	490481.588	7665346.959
H44	490455.534	7665386.631	H75	490444.772	7665375.555
H45	490459.226	7665383.044	H76	490448.464	7665371.967
H46	490462.919	7665379.456	H77	490452.156	7665368.380
H47	490466.611	7665375.869	H78	490455.848	7665364.792
H48	490473.995	7665368.694	H80	490463.232	7665357.617
H49	490477.687	7665365.106	H81	490466.925	7665354.030
H51	490485.071	7665357.931	H83	490474.309	7665346.855
H52	490488.763	7665354.344	H96	490478.001	7665343.267

Table C.1: Location of each tile in the KAIRA HBA array. The tile centre is defined as the symmetric centre laterally at the level of the RF ground plane. In all cases, the height of each HBA element is H=495.241 m. Coordinates are in the ETRS-GK21 system. Tile #H75 was destroyed on 8 March 2014 and has not been replaced (see Appendix E.20).

C.2 LBA array

ID	E (m)	N (m)	ID	E (m)	N (m)
L00	490511.219	7665335.032	L24	490520.690	7665332.103
L01	490513.768	7665335.032	L25	490521.206	7665336.458
L02	490512.568	7665337.282	L26	490519.190	7665339.849
L03	490509.869	7665337.282	L27	490515.502	7665342.998
L04	490508.669	7665335.032	L28	490511.002	7665344.234
L05	490509.869	7665332.782	L29	490503.496	7665347.124
L06	490512.569	7665332.781	L30	490500.312	7665345.018
L07	490506.098	7665337.755	L31	490498.998	7665342.182
L08	490505.546	7665333.826	L32	490498.048	7665334.246
L09	490507.647	7665330.461	L33	490496.463	7665331.707
L10	490511.421	7665329.235	L34	490501.379	7665326.054
L11	490515.099	7665330.722	L35	490505.574	7665323.194
L12	490516.962	7665334.225	L36	490509.807	7665319.983
L13	490516.138	7665338.106	L37	490512.739	7665321.618
L14	490513.011	7665340.547	L38	490517.141	7665323.406
L15	490509.046	7665340.410	L39	490522.420	7665328.011
L16	490506.981	7665343.341	L40	490524.104	7665330.233
L17	490503.791	7665341.554	L41	490524.476	7665335.549
L18	490501.139	7665337.270	L42	490525.636	7665339.538
L19	490502.404	7665330.103	L43	490519.834	7665346.243
L20	490504.356	7665327.534	L44	490516.260	7665348.003
L21	490508.103	7665325.436	L45	490510.988	7665349.513
L22	490512.340	7665325.863	L46	490523.798	7665332.702
L23	490517.462	7665328.572	L47	490503.219	7665344.642

Table C.2: Location of each LBA aerial in the KAIRA LBA array. The aerial centre is defined as the intersection of centreline of the mast with the RF ground plane. In all cases the height of each LBA element is H=493.288 m. Coordinates are in the ETRS-GK21 system.

Appendix D

KAIRA project timeline

The following are some significant milestones during the construction of the KAIRA facility. For more detailed notes on the schedule, refer to the document archive at Sodankylä Geophysical Observatory.

24-Apr-2010	Author's first involvement with the project
17-May-2010	Infrastructure funding proposal submitted to U.Oulu
23-Jun-2010	Project funded
30-Jun-2010	Contract for the station procurement
12-Aug-2010	Inspection of two candidate sites
08-Sep-2010	Site mound survey
24-Sep-2010	Ground-penetrating radar tests of the mound
17-Oct-2010	Preparation of winter site testing
18-Oct-2010	Frameset installation
19-Oct-2010	Deployment of winter test tiles
05-Jan-2011	Formulation of the KAIRA science concepts and "science diagram".
04-May-2011	Conclusion of winter monitoring period
11-May-2011	Destructive tests on HBA tile
16-May-2011	Delivery of HBA frameset trusses to site
07-Jun-2011	Grounds works for the site commenced
20-Jun-2011	HBA mark-out survey completed
01-Jul-2011	First non-test frameset assembled
04-Jul-2011	Delivery of the HBAs commences
05-Jul-2011	First frameset deployed into its final location
06-Jul-2011	First HBA tile deployed
18-Jul-2011	Final frameset assembled
19-Jul-2011	Final frameset and HBA tile deployed
27-Jul-2011	HBA array cabling commences
Jul-2011	Temporary mesh snow barriers added to the framesets

02-Aug-2011	Two-day survey of lower field completed
11-Nov-2011	Two test HBA summators installed
20-Jun-2012	Start of groundworks for the LBA field
22-Jun-2012	Main HBA summator installation phase begins
12-Jul-2012	Installation of LBA aerials commenced
15-Jul-2012	HBA summator installation completed
19-Jul-2012	First full HBA (and partial LBA) spectra measured
27-Jul-2012	Last LBA aerial installed
31-Jul-2012	First beacon satellite measurement
05-Aug-2012	LBA array commissioning completed
15-Aug-2012	Timber snow barriers completed
17-Aug-2012	First ISR measurement
31-Aug-2012	First multi-beam ISR measurement
18-Sep-2012	First detection of a pulsar
24-Sep-2012	First IPS together with LOFAR & EISCAT
26-Sep-2012	First dual-LBA/HBA scintillation observation
10-Oct-2012	First all-sky image
18-Oct-2012	New control system and 24/7 operation
05-Nov-2012	Real-time automated image display
26-Mar-2013	Successful VLBI measurement between KAIRA and DE601.
06-Jun-2013	The KAIRA facility was officially opened by the rector of the University of Oulu, Lauri Lajunen
10-Jul-2013	First routine riometry measurements
08-Mar-2014	Blizzard conditions result in the loss of HBA #H75. Other damage was incurred, but later repaired.

Appendix E

History and construction of KAIRA

Traditionally, the scientific process involved the scientist devising the experiment, building their own equipment, and then carrying out the measurements. This project was no exception to that old-world order, with the author taking on a direct role in the construction as project coordinator, site manager and commissioning engineer for build process of the KAIRA facility.

The salient features of the build are mentioned briefly in Paper I, and the capability of the facility is covered in Chapter 2, but this appendix serves as a more comprehensive reference.

It is not part of the scientific results set out in this thesis, but the deployment process of the instrument is critical to the implementation and represents a large body of work on the part of the author; it is thus included here. Additionally, even though there are other LOFAR stations, there are certain aspects of KAIRA that are unique to the site and are not documented elsewhere. The author had previously been the project manager for the construction of the LOFAR facility at Chilbolton, UK, and the experience gained from that, and other projects, was applied to the work at KAIRA.

E.1 Site selection and survey

As described in Chapter 2, the motivation for the use of a Kilpisjärvi site was to place the array within Finland at a suitable distance from the EISCAT radar facility at Ramfjordmoen. Additionally, the road and infrastructure at Kilpisjärvi made this region suitable from a practical point of view.

Two sites were initially identified, both near to the main road (Käsivarrentie, E8-Norway / 21-Finland), just inside Finland from the Norwegian border. They were inspected on 12 August 2010. The selection was initially made on the grounds of topography and land availability.

The first site (approx. $20^\circ\,45'\,40''$ E, $69^\circ\,5'\,30''$ N) was wilderness located just to the east of the road, opposite from a gravel pit. The location made groundwork easier, but it would have taken a “green-field” site. Access would need to be struck from the main road to the area to be developed. A view of the field is shown in Figure E.1.

Figure E.1: Northwest view across the first of two candidate sites for KAIRA. The gravel pit on the opposite side of the road in the centre of the photograph was used for providing supplementary material to the actual KAIRA site. Image: Jyrki Manninen, SGO.

The second site (approx. $20^\circ\,45'\,44''$ E, $69^\circ\,4'\,15''$ N) was located at a roadworks’ spoil site, west of the main road, shown in Figure E.2. As a “brown-field”, this location had an advantage in that it had negligible impact on the reindeer herds, and would generally reduce the impact on the natural environment. Additionally the “mound” of the roadworks’ spoil serves as a natural hill, resulting in an increased wind-shear effect. This places additional requirements on securing the tiles, which ultimately resulted in the loss of a tile (see Appendix E.20). However, the increased wind velocity is advantageous in that snow accumulation is naturally blown away.

A lower field, northwest of the mound, provided a large additional area, shown in Figure E.3. Originally, it was intended that an LBA array would be placed here. However, that proved not to be possible (as described in Appendix E.13).

This second site had the disadvantage that it was adjacent to a snowmobile trail, as well as being nearby the Fenno-Norwegian Border Customs Station (a potential source of RFI from infrastructure, as well as passing and parked vehicles). On the other hand, the close proximity to the Customs Station would increase the security of the site.

Neither site had trees that would require felling. Both sites required comparable amounts of ground-levelling to flatten the terrain to accept the antenna arrays. Both were located close to the road which would make access easy, but would present a more noisy RFI environment because of passing traffic.

Figure E.2: Southeast view of the top of the mound at the second site. The mountains in the background are Korkea-Jehkas (left) and Saana (centre).

Figure E.3: South-southeast view of the lower field of the second site. The roadworks' spoil mound is in the centre mid-distance. The mountains in the background are Korkea-Jehkas (left), Saana (centre) and Pikku-Malla (right).

The facility requires a stable ground surface. For this, the site of roadworks' spoil was chosen, providing a relatively flat, stable surface, which was easy to work on, not subject to tundra ground shift and yet without huge slabs of rock. The site is close to other scientific facilities as well as local infrastructure, access roads and communication. A survey of the spoil mound was carried out on 8 September 2010, and the results shown in Figure E.4.

Ground-penetrating radar

On 24 September 2010, ground-penetrating radar (GPR) sounding were made of the chosen site in order to investigate and analyse the conditions of the subsur-

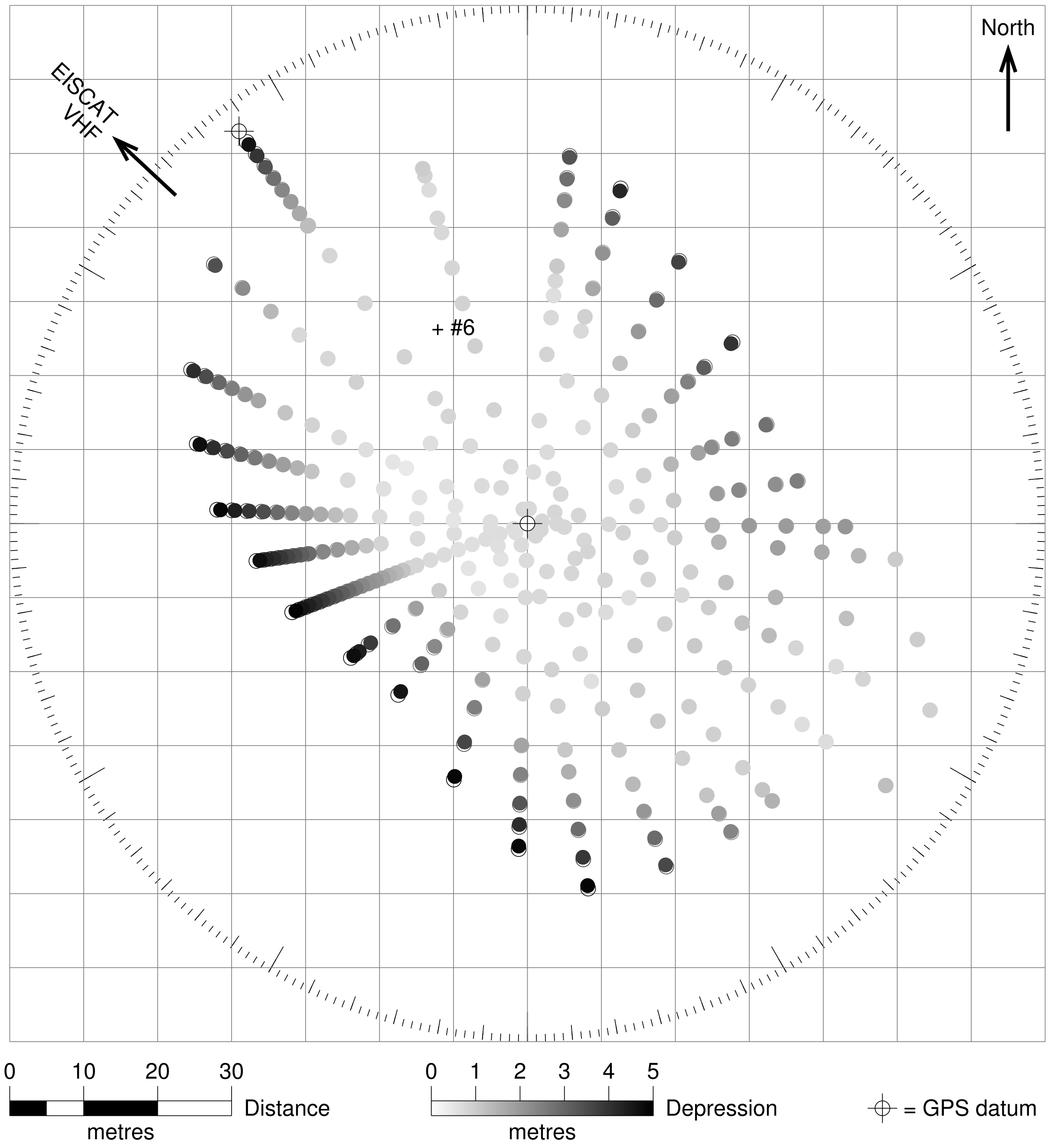

Figure E.4: Site survey data showing the extent of the roadworks' spoil mound. The two GPS data are KKJ27: 3251732, 7678123 (centre) and KKJ27: 3251693, 7678176 (north-west). The snow-depth test registration point is marked #6 (see Figures E.5 and E.8).

face. Measurements were carried out by the personnel of the University of Oulu, Department of Physics and used a Malå GPR system using two different rough-terrain antennas. Nine 100 MHz and seven 50 MHz profiles were measured.

The low tundra area northwest of the mound consisted of well-sorted alluvial deposits of fine sand and silt. Visual observations and 1–2 m test holes indicated that the top layers were not saturated down to a depth of approximately 1 m. Below this, the ground was saturated, rising to a point 100 m northwest of the site, where the terrain drops to the level of the water table, and surface water was evident. Bedrock radar reflections in this area were very distinct, at 4-6 m depth.

Below the landfill area the bedrock layer was not as clear, but still mostly discernible. Bedrock surface measurements indicated an irregular surface, which was indicative of fractured components and loose rock mass, with the largest variations in the western corner of the mound and a depth estimate of 5 ± 1 m. This tapers eastwards to a depth of 2 m at the eastern edge of the mound area.

The deep range of the GPR signal in the mound area, indicated that the spoil material is in a drained condition.

E.2 Winter testing

The LOFAR antenna system used for KAIRA had not been previously tested in Arctic conditions, so it was decided to carry out winter testing for the HBA tiles. Two “dummy” tiles were purchased; the structure was as per a normal HBA tile, but there were no electronics or antenna elements inside.

Winter field tests

An area at the northern edge of the mound was selected for its already-level ground and moderate amount of topsoil, which would assist establishing the test tiles.

Two HBA tiles were to be deployed. The first was put on a raised platform, made of open-timber frames — referred to as a *frameset*. The rationale was to raise the tile even further into the wind shear, to assist in the natural clearing of snow. One of the aims of the winter test was to verify that the increased height results in sufficient reduction in the snow cover. Additionally, it was important to see if the raised height created vulnerability to high wind speeds damaging the tile itself.

The platform was partially pre-assembled at SGO, with final assembly occurring on the site. Deployment occurred on 18 October 2010, with the frame being anchored into position before installation of the tiles. The ground was starting to freeze in places and there was light snow already on the ground.

The HBA tiles themselves were set out using a lorry with HIAB loader crane on 19 October 2010. A description of the tiles and their deployment is given in Appendix E.8. The first tile was set on the timber frameset. The second tile was deployed nearby. It was placed on a bed of sand and light gravel, and anchored directly to the ground as done at other LOFAR sites. These tiles were left undisturbed during the winter months. Regular site checks were made during this time, to monitor conditions and record the snow depth on the site, shown in Figure E.5.

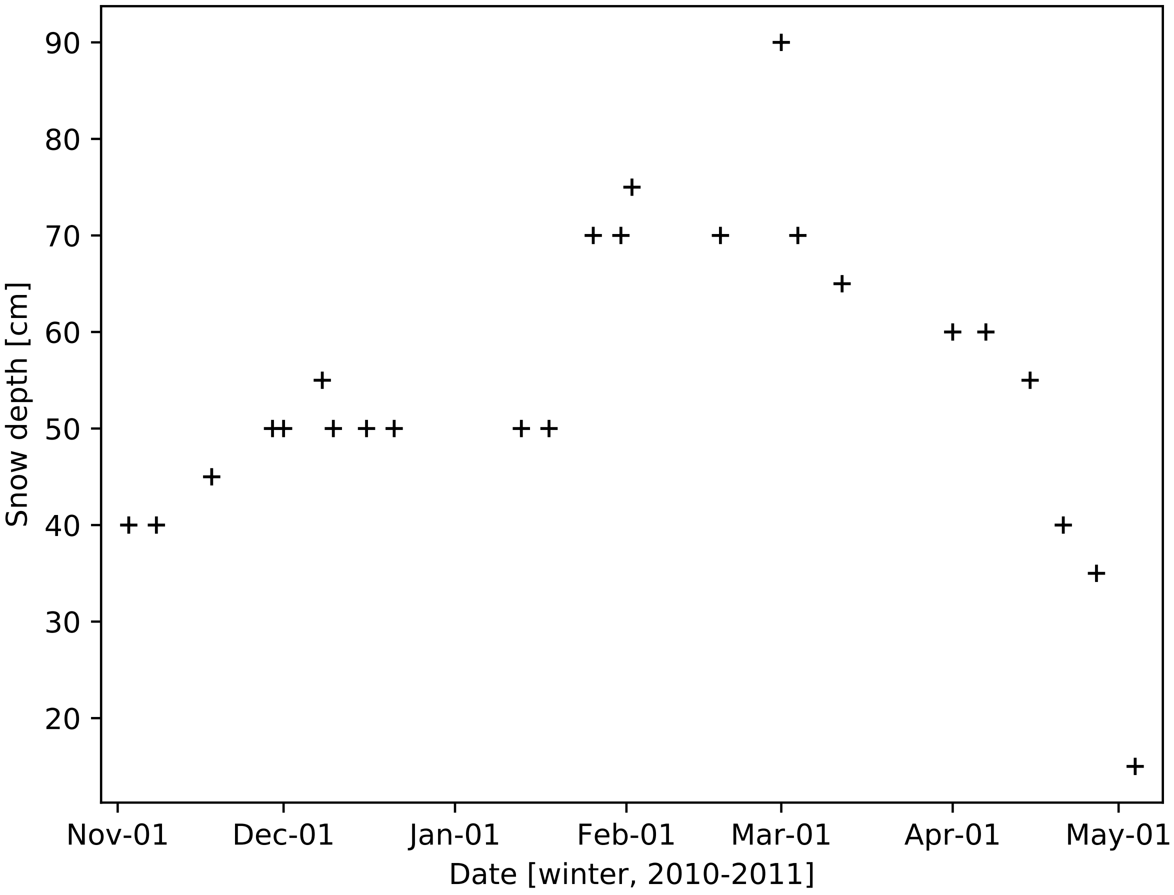

Figure E.5: Snow depth on the KAIRA site during the winter testing period. The location of the measurements is location #6 shown in Figures E.4 and E.8

Example mid-winter conditions are shown in Figure E.6. At the peak of the snow cover on the raised HBA tile (23 March 2011), there was 1–2 cm of dense icy snow above which was a further 15–20 cm of lightly packed snow. On the ground tile, there was 30 cm of snow.

At the end of the winter season, another site visit was made and additional testing was carried out. By this stage, the tiles were clear of snow and the majority of deep snow was gone from the site. On 10 May 2011, a site inspection was carried out. A photograph of the condition of the site is shown in Figure E.7. Both tiles were in good condition. By checking the verticality of the anchor lines, it was determined that the movement of the frameset with respect to the ground had been minimal. There was no visible damage, shift or displacement on either tile. All anchors and

Figure E.6: Condition of the two winter test tiles on 18 February 2011 with the snow-buried ground tile (left) and raised tile and frameset (right). Compare with Figure E.5.

mounting points were still intact, although ground settling had resulted in one of the anchors being slightly loose and several not having sufficient tension.

What was clear from this part of the exercise was that the decoupling of the anchors from the tile cover by use of the intermediate timber frameset significantly helps in the anchoring of the overall tile. Positional flexibility is provided, as well as easier access and the ability to re-position the connection points on the timber, thus improving line tension. In the case of the ground-tile, there was negligible degradation of the sand-gravel base under the tile.

In addition to the visual inspection and measured tile positions, ice-cores were taken about the field to determine the expected snow and ice packing that could be expected at the end of the season (when ice levels are the most solid, due to the thaw-melt cycles). A total of six cores were taken with density measurements as listed in Table E.1.

Figure E.7: Composite image taken on 10 May 2011 of the KAIRA site. The raised test tile is in the forward right of the image, with the ground-placed tile beyond it. The mountains of Saana and Pikku-Malla are in the background (left and right, respectively).

Core	Depth cm	Density (water = 1.0)
#1	21.0	0.34
#2	30.5	0.27
#3	93.5	0.35
#4	36.0	0.24
#5	68.0	0.39
#6	43.5	0.33

Table E.1: Snow samples on the KAIRA site, 10-May-2011. In Core #5, there was a slush of water and ice at the bottom of the core, resulting in a higher density value. Refer to Figure E.8 for the relative positions of the ice cores.

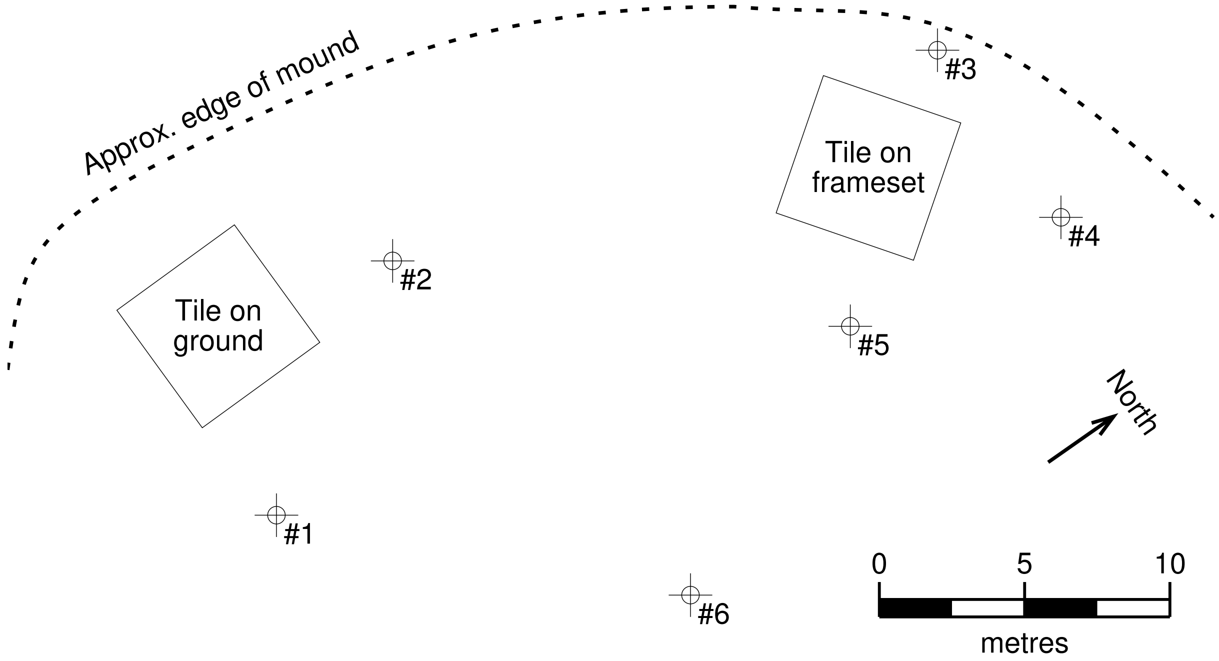

Figure E.8: Location of the winter test tiles and the snow-depth samples, c.f. Table E.1. The reference position (#6) is also indicated in Figure E.4.

Destructive testing

By knowing the snow-depth statistics for the region, and with the snow-density measurements, it was possible to make a first-order estimate for the total snow loading that could be expected on the tiles. The next issue was how much loading could a tile mounted on a frameset tolerate before structural failure. To evaluate that, a deliberate, destructive test of the raised tile was carried out. There were two critical issues:

1. What was the total mass that could be tolerated before collapse?
2. What was the failure mode? A variety of scenarios was anticipated:
    - the polystyrene structure itself would fail, resulting in the tile being crushed due to the collapse of the walls (this was considered to be the most likely),
    - the polystyrene lids on each cell of the HBA tile would fracture and collapse into the cell (but leaving the walls mainly intact),
    - the span of the polystyrene across the gaps between the beams of the frameset would be too great, resulting in localised fracturing, or,
    - the local pressure points of the timber framesets would damage the tiles in an upward direction from underneath.

Because of an included wire ground plane embedded in the tile, it was not anticipated that damage would occur from the suspension of the tile across a sparse frameset. This indeed turned out to be the case.

On 11 May 2011, the destructive testing was carried out. A 15-tonne digger was used to put successive loads of snow onto the tile, as illustrated in Figure E.9. It approached from the east, so at closest approach the front of the digger would be against Cells #07 and #11. (The numbering arrangement within each individual HBA tile is given in Figure E.25 on page 176, although the tile was not aligned at the time of the winter testing.)

Figure E.9: Snow load #8 being deposited onto the raised winter test tile. Details of the snow loads are given in Table E.2.

The digger had a gauge to allow the mass of each load to be roughly measured and the results are shown in Table E.2.

Due to the time needed for the digger to drive to the source of the snow and back, there was a few minutes gap between each load being applied. After Load #8, the tile was still stable, but shortly after the application of Load #9, there was a loud snapping sound and a 5 cm displacement of the underside of the tile (Cells #10 and #11) could be seen. Clicks, snaps and creaks could be heard for the next minute or so, before the tile structure suddenly compressed by approx. 20 cm as the polystyrene structure failed.

Load	Mass kg	Total kg
#1	400	400
#2	550	950
#3	950	1900
#4	1050	2950
#5	850	3800
#6	1400	5200
#7	500	5700
#8	1050	6750
	−100	6650
#9	1000	7650

Table E.2: The approximate load masses of snow that were applied to the test tile and the cumulative total. Note that at Load #8, a small amount of snow toppled off the tile. This was estimated to be equivalent to approximately 100 kg.

After the snow was cleared from the top of the tile, the top PVC cover was removed to inspect the damage. Three images from that clearing and dismantling process are shown in Figure E.10.

Figure E.10: Cell #11 of the test HBA tile. Left: The cover has been removed to show the fractured lid of Cell #11. Centre: the lid has been removed, showing the crushed internal structure. Right: the debris has been removed from Cell #11, showing the profile of Cell #10 behind it, as well as the sagged ground-plane and lower PVC bag.

With the exception of Cell #00, all cells in the tile suffered some form of damage. Yet only Cells #10 and #11 had fractured lids and a disintegration of all internal components. These cells are where the digger was depositing the snow during the loading, so they had been exposed to the impact of the depositions and the bulk of the total snow mass. The maximum snow mass on any given cell was estimated to be 1100 kg (Cell #10).

The failure mode was the internal structure of the cells being unable to support the load across the span between the beams of the frameset underneath. As a result, the span has collapsed, resulting in the fracture of the spanning tile lid above it. It was noted that none of the anchors were damaged, nor was there any tearing of either of the PVC covers. The polystyrene of the tiles was structurally weaker than the supporting timber, so the frame sets were redesigned to use less material, to be higher (from 1.0 m to 1.5 m), and simpler in construction, so that manufacturing would be cheaper and simpler.

The debris of the destroyed tile was removed and disposed of. Undamaged polystyrene components, the ground plane and PVC covers were kept as spares. These parts were later used to repair tiles that had been damaged during delivery as well as tiles that were damaged during a blizzard (Appendix E.20).

The ground deployed tile was also removed from the field on 11 May 2011, to make way for the forthcoming groundworks. This tile was lifted and re-packed, and left in a timber frame support at the edge of the site. It was later dismantled and put into the spares store.

The design conclusions from the winter testing were as follows:

1. The timber frames made securing the tiles much easier. As mounting points on the timber can be in an arbitrary location, the tiles could be attached to the frame in the exact places necessary. Likewise, anchors into ground can be in arbitrary locations to contend with the position of sub-surface rock. Apart from decoupling the ground-to-tile connection, the timber frames meant it would be possible to re-position the anchor points in future, should that be necessary due to, for example, tile compression or ground settling.
2. Raising the tiles onto an open-structured frame was necessary to utilise the wind shear for natural snow clearing.
3. A further increase in height from 1 m to 1.5 m would improve this natural clearing efficiency.
4. The height increase would also increase snow clearing under the structure.
5. That height increase would also make working underneath the structure more practical, allowing workers to stoop, rather than crouch, to move beneath the structure.
6. In the leeward side of the array, the increased height would permit the underside of the array to be utilised as sheltered storage for spare parts (such as tile components).

E.3 Array and site design

There were numerous constraints on the KAIRA layout:

- It had to maintain an elongation in the direction of the EISCAT Tromsø VHF transmitter — approximately 313° azimuth. This was to maintain a suitable beam pattern when looking at target regions of the ionosphere at zenith above the transmitter site.
- There needed to be good access to the site, in order to deploy the tiles, maintain them, and protect them from the Arctic conditions.
- The volume of required ground levelling needs to be minimised. This was to save cost, but it also saved time during the short summer when the array was being installed.
- There needed to be the option to upgrade KAIRA from 48 tiles to a full 96 tiles, thus converting it into a full-size international LOFAR station.
- Such an upgrade would need to be implemented in a way to achieve the standard LOFAR international layout, with minimum disruption to the initial KAIRA array deployment.

The HBA site layout was devised by a team of people including Juha Vierinen, Ilkka Virtanen, Mikko Orispäpä and the author. Several designs were considered, based on simulation of the beam patterns, serviceability and the pragmatism of implementation and upgrade. The two leading concepts were a sparse 4×12 arrangement and a broader sparse 6×8 configuration. Both would have "snow corridors" preventing surplus snow from accumulating on the array, and also have a means to clear it. The 6×8 array had a tighter azimuthal beampattern in the direction of the EISCAT VHF. Additionally it was closer in configuration to the international LOFAR stations, which meant that it would better match the LOFAR network in cases of, for example, joint VLBI experiments. The two layouts are shown in Figure E.11.

Final layout

The final KAIRA HBA array layout is shown in Figure E.12. In the figure, the solid-shaded tiles are those which are part of the KAIRA build. The outlined tiles are the positions and numbers of a conventional LOFAR international station layout. The KAIRA system was designed to be compatible with this numbering scheme. Tile #H75 was part of the initial build, but was destroyed during a blizzard and was not replaced (see Appendix E.20). Tile #H96 is part of the KAIRA build, but is extra to a LOFAR international station layout (there is no #H96 in other LOFAR stations). Tile position #HCC is not part of KAIRA, but in a LOFAR station, this is not an active tile. Instead, a "dummy tile" which is structurally the same, but is devoid of electronics, is included in the array. The purpose of this is to prevent wind turbulence effects

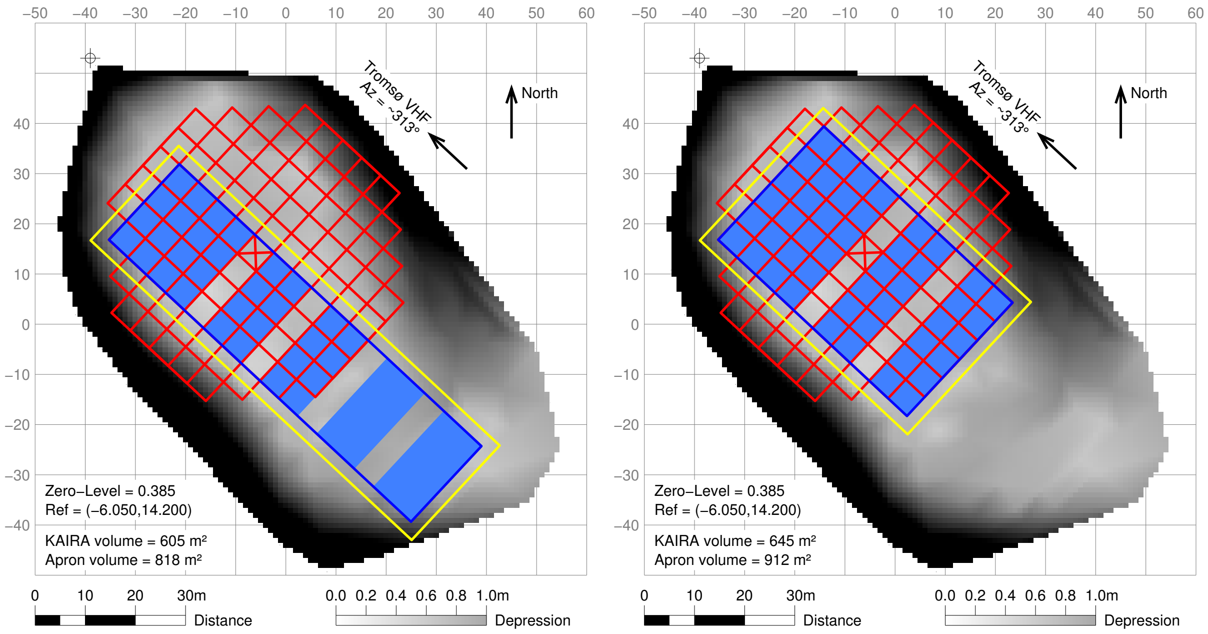

Figure E.11: Two HBA array layouts that were considered, superimposed on a topographic model of the original site. The solid blue tiles are the positions where tiles would be used. The red outlines are the positions of tiles in an international LOFAR station. The yellow outline marks the envelope where level foundations would be required. The configuration on the right was adopted.

in the array centre, which can lead to damage, and also the #HCC tile still has a passive ground plane, which provides RF-continuity across the array centre.

The layout is split into three “blocks” of 6×4, 6×2, 6×2. By splitting the array into a semi-sparse configuration, it permits different sub-array combinations for EISCAT_3D testing. The “corridors” between the blocks can also be used for snow clearing.

The main HBA array required an area of $1500\,\mathrm{m}^2$ level to a surface accuracy of $\pm 3\,\mathrm{cm}$. Based on the survey (Figure E.4), it was estimated that $912\,\mathrm{m}^3$ of extra material would need to be added to the site, with additional gravel required for the top levelling.

E.4 Ground works

Ground works for the site commenced on 7 June 2011. The access track from the main road was improved. The site was roughly levelled with large boulders and one area of higher ground shifted to remove the isolated high spots. This surplus material was used to build up the existing roadworks’ spoil of the mound on the western corner. This is shown in Figure E.13.

Then a “packing layer” of course, mixed-grade material was added to provide the

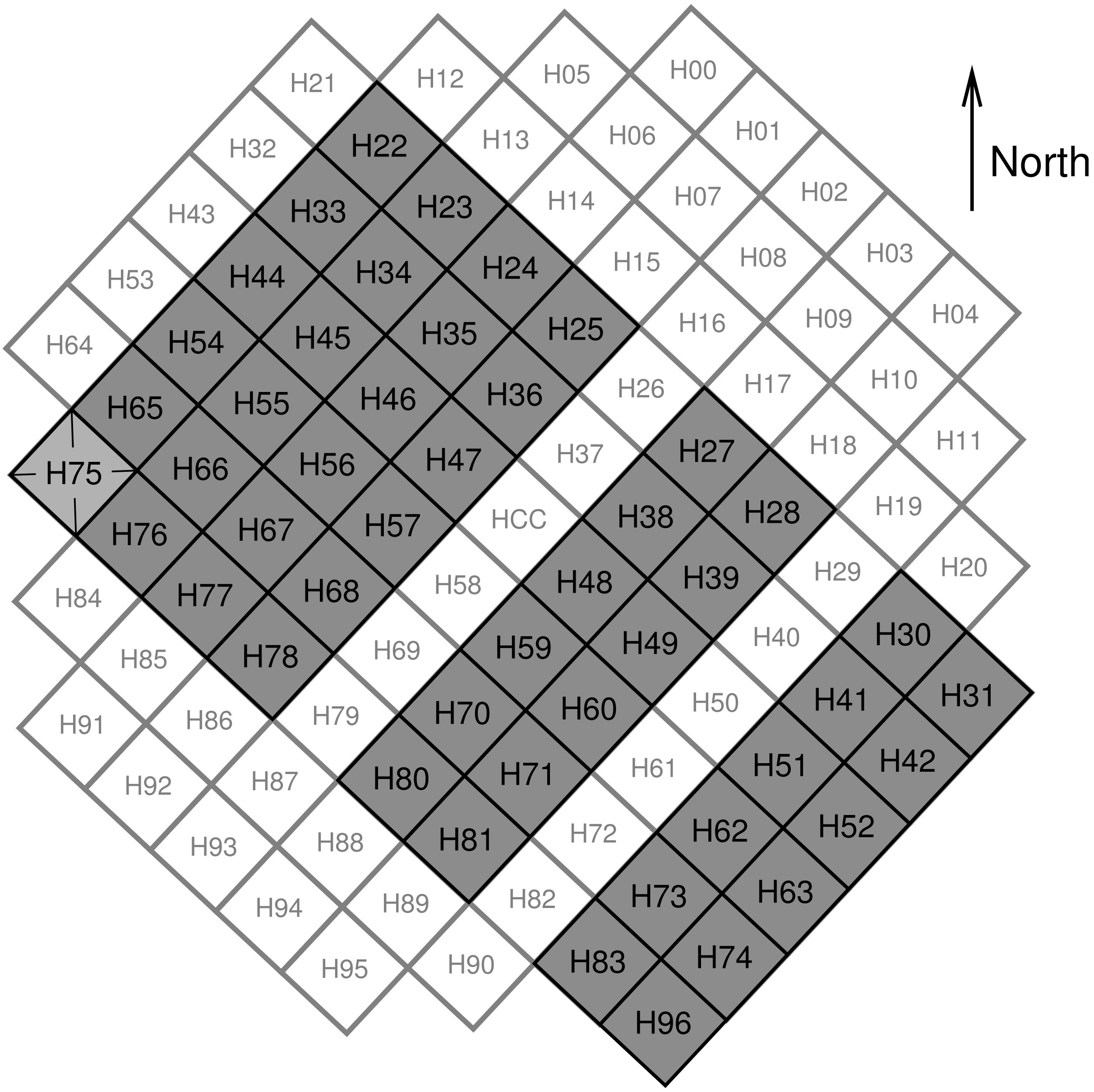

Figure E.12: KAIRA HBA array layout (shaded tiles), with tile identification numbers marked. The outline tiles mark the configuration of a LOFAR international station. Explanation is provided in the text.

Figure E.13: Composite panorama, looking northwest across the site. Existing roadworks' spoil material was moved to provide a roughly-level working surface for the application of fine gravel.

basis for the finer layers and to add material that was devoid of large rock slabs and boulders. This material was deposited one lorry load at a time, with mechanical packing being applied after each to prevent later subsidence (which has proven successful; in 2018, the mound remains intact). The depth of this packing layer was approximately one metre, but with large variation due to the underlying terrain. In the western corner especially, much additional material was added to make up for the deficit in the mound's shape (even after the initial site levelling), as shown in Figure E.14. At the completion of the placement of the packing layer, the surface was level to within 10 cm.

Figure E.14: Composite panorama, looking south at the development of the mound. The lighter, smoother area on the right is the new material. (See also Figure E.32.)

Above the packing layer, a 20 cm "drain layer" of gravel was placed. In this, perforated plastic drain pipes were embedded to minimise the amount of water (and thus ice shift) that would occur. The gravel used here is a uniformly graded material, with each piece being about 15–20mm in size. With fewer fine particles, the material is naturally porous. This permits drainage, especially in the spring when warm weather can result in large amounts of water from snow melt. Removing water from the site before the winter freeze is even more important, as water-saturated ground will distort when it freezes, causing shifts in the antenna array.

To ensure that sufficient water extraction occurs, 100 mm perforated, corrugated, agricultural-type ground drain pipes were laid into the top-level gravel. These are spaced approx. 10 m apart and run in parallel northeast to southwest across the HBA part of the site. Water drainage along these pipes is bi-directional — there is no preference for the destination of the water, just so long as it is leaves from under the HBA array area. The application of the drain-layer gravel and the embedding of the drains is shown in Figure E.15.

Figure E.15: Gravel being applied for the HBA array drain layer (left) and an example of the embedded perforated drainage pipes (right).

The completed drain layer, and an example protruding pipe, is shown in Figure E.16 (left photograph). After completion, pipe ends were stopped with geotextile to prevent animals from entering, but still permit water egress.

The drain layer was also levelled and a layer of geotextile was applied over the entire field. The geotextile hinders new silt from reaching the drain pipes and thus clogging them and disabling their effectiveness. It also helps stabilise the ground against localised settling.

Any silt underneath the geotextile will drain down. With time the drainage of the pipes improves due to fine material washing away, but with no replenishment from new particles.

Over the geotextile layer, a "top layer" of gravel was placed adding a further 20 cm of depth. This is mechanically packed to ensure stability and limit erosion. A laser

Figure E.16: Left: Side view of the drain layer with protruding drainage pipe. Right: application of the final gravel layer over geotextile.

level is used to assess that the surface is accurate to ±3 cm across the entire field.

The additional gravel drain- and top-layers on the HBA field, in addition to the physical height of the framesets themselves, are the two factors that contribute to the difference in height between the LBA and HBA array phase-centres.

Combined, the top layer, drain layer and the upper part of the packing layer provide 50 cm of depth. This material is clear of large boulders and slabs of rock found in the spoil layer, and thus made it possible to use drilled, duck-bill anchors for the securing of the HBA framesets (Appendix E.6). A schematic showing the profile of the completed mound is shown in Figure E.17.

The photograph in Figure E.18 was taking during the groundworks process. From left to right, it shows the packing layer (over which the protruding drain pipes lie, then the drain layer itself, the geotextile and the top-layer.

E.5 HBA array survey

The HBA tiles are 5×5-metre squares and gaps in the array were also designed to be “tile sized” (Appendix E.3). A small gap between tiles for water run-off, fittings and anchors means the actual “grid increment” is 5.148 metres exactly and the site was surveyed and pegged accordingly on 20 June 2011. Reference positions were taken first, from which the precise direction to the EISCAT VHF transmitter at Ramfordmoen was calculated (azimuth = 314.1762 degrees).

The “corner stone” reference mark was then checked with a long-integration GPS

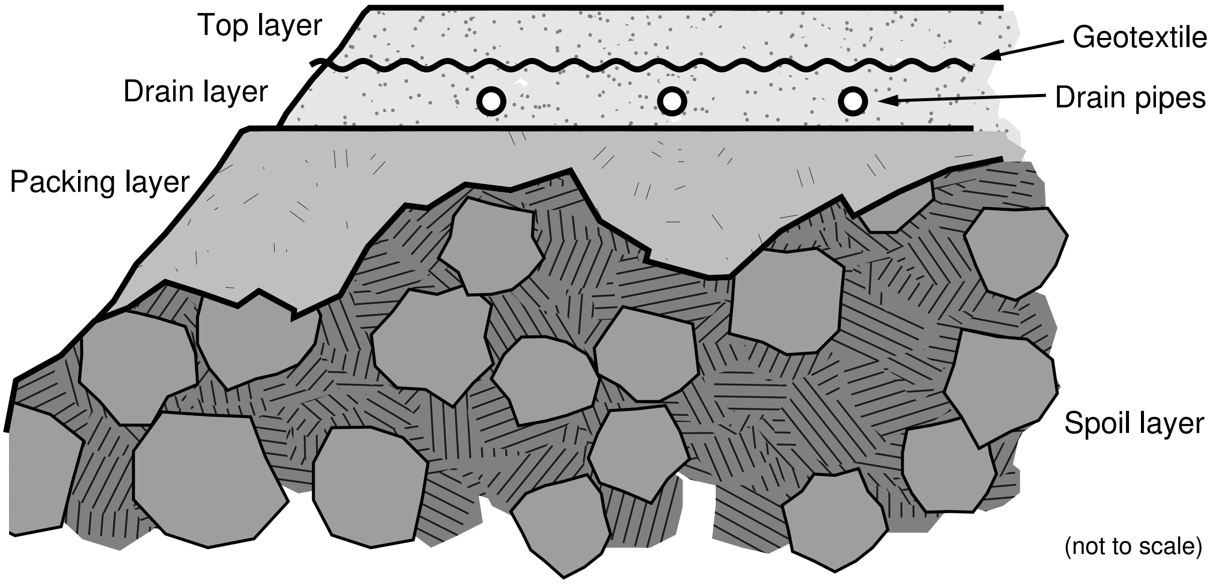

Figure E.17: Representation of the different layers of the HBA mound. The spoil layer is the original material that was already present at the site prior to the commencement of works.

Figure E.18: North-northwest facing composite image of the site, showing the final gravel level being applied over the geotextile. The intermediate layer can be seen in the centre and left, with the drain pipes protruding from this layer on the left.

receiver measurement (total station) and from there the field corners were determined. A slight correction was applied to optimally centre the array on the site to reduce proximity to erodible edges of the mound. A new reference mark was then measured and the corners were re-calculated with the correct azimuth. All the intervening grid points were calculated.

In addition to this, four triangulation points were measured. These then served as the calibration points for the surveyors total station, which was used to do the final mark out. The grid points were then measured and small metal pegs were driven into the ground to mark their locations. These were cross-checked by measuring the grid spacing increments across the field.

The phase centre of each tile in the array is thus the geometric mid-point of the positions of the grid corners for the tile at the level of the RF ground plane mesh. During installation of the framesets on the array (Appendix E.6), a sighting laser was used to check the alignment and make minor corrections where needed. The final survey measurements are given in Appendix C.

E.6 HBA framesets

Following the winter testing, it was decided that the use of a frameset to raise the HBA tiles was essential. Furthermore, it was decided to raise the height of the frameset from 1 m to 1.5 m. Apart from the additional wind-shear effect for natural snow-clearing, the extra height makes it easier to access the underneath side of the array for cable installation, storage space and maintenance.

Frameset base geotextile

Strips of 1 m-wide geotextile were placed in a lattice on the tile outlines on the field prior to the deployment of the framesets. The purpose of the geotextile is to control erosion. On other LOFAR stations, it also serves as a weed suppressant, but that is not a motivation at KAIRA, as ground preparation, arctic conditions and the elevated framesets mean that weeds are not a problem. Water erosion is significant however. During spring, warm weather and rain combine with melting snow to create a lot of liquid water. This runs off the tiles and falls down the gaps between them. However, unlike a conventional LOFAR station, the raised tiles means that this water is falling not 0.5 m (tile height), but 2 m (tile plus frameset height).

The geotextile is deployed from a large roll that is wheeled out onto the field. It is drawn out and cut to length to match the section being completed. Then, small slits are made, and the fabric is placed over the survey pegs. The edges are nailed into the soil to hold it temporarily while waiting for the framesets to be deployed and the anchor lines drilled in and attached.

A second length of fabric goes cross-ways to complete the lattice which is illustrated in Figure E.19.

Figure E.19: Geotextile on the HBA array field, placed along the edges where the HBA framesets would be situated. The orange spray-paint dots mark the positions of the steel survey pegs.

Frameset assembly

Each frameset comprises seven flat-truss frames. Five of these are 4900 mm long and align in one direction at a spacing of 1250 mm. The other two frames in the set are 5000 mm long and are placed in an orthogonal direction to the others. Both the 4900 mm and 5000 mm frames are 1500 mm high. Individual pieces of timber within each frame are held together with gang-nail plates. Figure E.20 shows a scale cross-section of the frameset.

Additional diagonal batons were paced on each frameset to help support the HBA tile that will be placed on top of it. Initially these were fitted after the frameset was in place, but it was noted that they also provided additional stability during the lifting process so the majority of them were fitted during the pre-assembly stage. A completed frameset is shown in Figure E.21

The framesets were assembled from pre-delivered trusses. The final assembly was

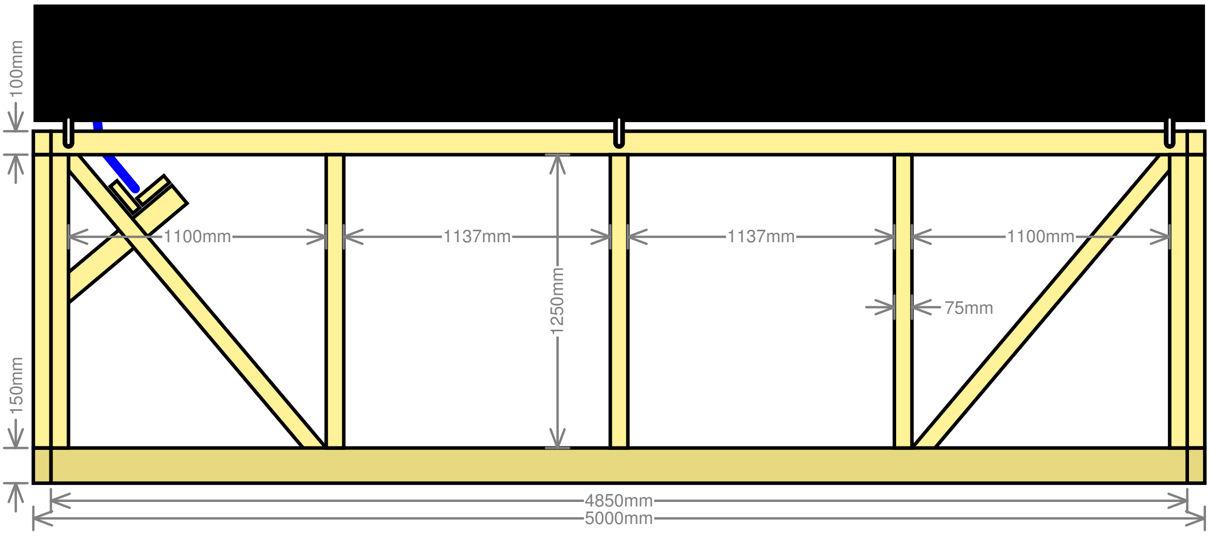

Figure E.20: Scale cross-section of the frameset and HBA tile, showing also the location of the V-section cable trays (see Appendix E.9).

carried out at the array field edge, with each completed unit being placed just prior to the HBA tile. This was necessary to ensure that the loader-crane retained access to the positions where the tiles would be put.

Figure E.21: Left: A completed frameset, prior to being lifted onto the HBA array field. The blue metal hoisting cross is only for lifting the tile into position, and is not part of the final structure. Right: A frameset in position. The additional diagonal braces are being applied. Note the way the frameset sits on the strips of geotextile.

Frameset assembly was carried out between 1 and 18 July 2011, and placement onto the array field lasted from 5 until 19 July 2011. The frameset design has proven satisfactory. However, additional support was added in 2012 due to sagging of the tiles, making the underside of the tile supported along the cell boundaries.

HBA frameset anchoring

The HBA framesets are anchored to the ground using a 0.5 m nylon line and "duck-bill" earth anchor and tests were carried out to determine a suitable depth for these anchors. Figure E.22 shows the ground securing preparation. A hole is first drilled into the ground. Although some soil collapse may occur, it does loosen the ground and ensures that no prohibitive rock pieces are present. The duck-bill anchors are then driven into the hole with a mechanical hammer, allowing for back-draw. A nylon line is attached to the anchor, with a bowline loop-knot at the end, to which a lifting tool can be attached. When tension is applied, the anchor twists into a lateral position to lock into place, leaving the loop as an attachment point, just above ground level.

Figure E.22: Anchor lines are installed by first drilling a pilot hole into the ground (left). The duck-bill anchor is placed on the end of an extended jack-hammer bit (centre), and driving into the pilot hole. A lifting rod (right) is then used to provide tension and lock the anchor into place.

Ground settling requires that lines are re-tightened due to the slight upward movement of the duck-bill anchor; this is carried out in the following year. The insertion of the anchor lines into the ground is completed prior to the frameset being lifted into place, in order to provide sufficient working space for the drilling process.

Once installed, the frameset is connected to the exposed loop on the anchor line via a metal S-hook and rubber O-ring, the latter of which rests over a counter-sunk drywall screw, which is left proud of the timber to accommodate the O-ring, as shown in Figure E.23. Between framesets, a shared anchor line is used.

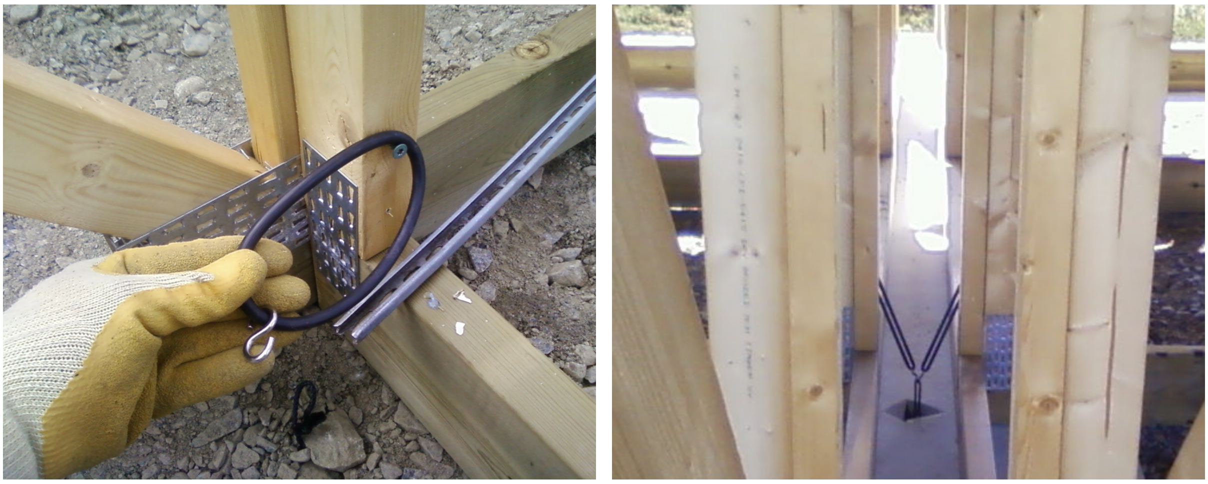

Figure E.23: An O-ring for attaching to the anchor line via an S-hook (left). The bowline loop-knot can be seen protruding from the soil. Between the framesets, it is possible for two O-rings to connect to the same anchor line (right).

E.7 HBA delivery logistics

For the 48 HBA tiles, 12 transport vehicles were needed, each carrying 4 tiles. The transport for the HBA tiles was done with either Tautliner lorries with one trailer of circa 14 m length or combi-volume trailers of 2×7.7 m. Each was a standard 2.50 m wide and 3 m high. Each lorry load comprised four HBA tiles. The tiles were stored folded-down for transportation and were placed on custom-built pallets for lifting with forklift trucks. In this configuration, they are approximately 5 m long, 1 m wide and 2.5 m high. In addition to the four folded tiles, each lorry also contains 4 pallets with "tile lids".

Each HBA tile was pre-fitted with the antenna elements and front-end LNA boards. However, the summators were not pre-installed, and were thus introduced after the tiles were placed on their framesets. The polystyrene lids for each cell in the tile were separate, as were the black PVC tile covers. These were added on at the time of the HBA tile installation. The HBA tile deliveries started arriving on 4 July 2011. An example is shown in Figure E.24.

The loading and unloading of the tiles onto the transport takes place from the sides of the lorries. After delivery, HBA tiles were kept in their packaging and stored against on-site storage containers, which provided stability against the wind. They were removed from storage on an as-needed-basis, for unpack, unfolding assembly and deployment.

The pallets use for the tiles were later dismantled, and the long timber slats recovered. These were later used for two purposes. Firstly, they were used to make the cable trays for routing the signal cables from the HBA tiles back to the electronics cabin (Appendix E.9). The other use was to provide snow shielding batons on the

Figure E.24: Unloading the HBA tiles from the delivery lorry. Such a heavy-duty fork-lift vehicle was not required; however it was the only one available. The folded tiles (including packing material) weigh approximately 250 kg.

sides of the framesets on the edge of the array, preventing excessive snow drifts from going under the tiles (Appendix E.10).

E.8 HBA installation

The HBA tiles are divided into 16 cells, which contain the individual crossed bow-tie antennas and the initial amplifier stages. The tiles are pre-assembled and folded in half, with the fold line being along the centre-line parallel to the EISCAT VHF axis. The numbering scheme used for the individual cells of each tile is given in Figure E.25.

Preparation of a given HBA tile was only started once the relevant frameset had been placed on the array field. It involved moving them from the storage area to an unfolding station, partially fitting them, transporting them to the already placed and anchored framesets, and then securing them with the cover to the frameset.

Unfolding

For other LOFAR installations an unfolding station kit is provided as part of the installation tool set. However, in the case of KAIRA, this was not available. Instead, a temporary construction made of lengths of standard building timber and plywood was prepared. The unfolding station comprised two platforms 2.5×5 m, placed with a 25 cm gap between the two. The platforms sloped very slightly downwards away from each other in a “shallow-roof” configuration, to lift the centre of the tile and thus make it easier to fit the lids. Once in place, the remaining packing material was removed, internal integrity and polarisation alignment checked, and

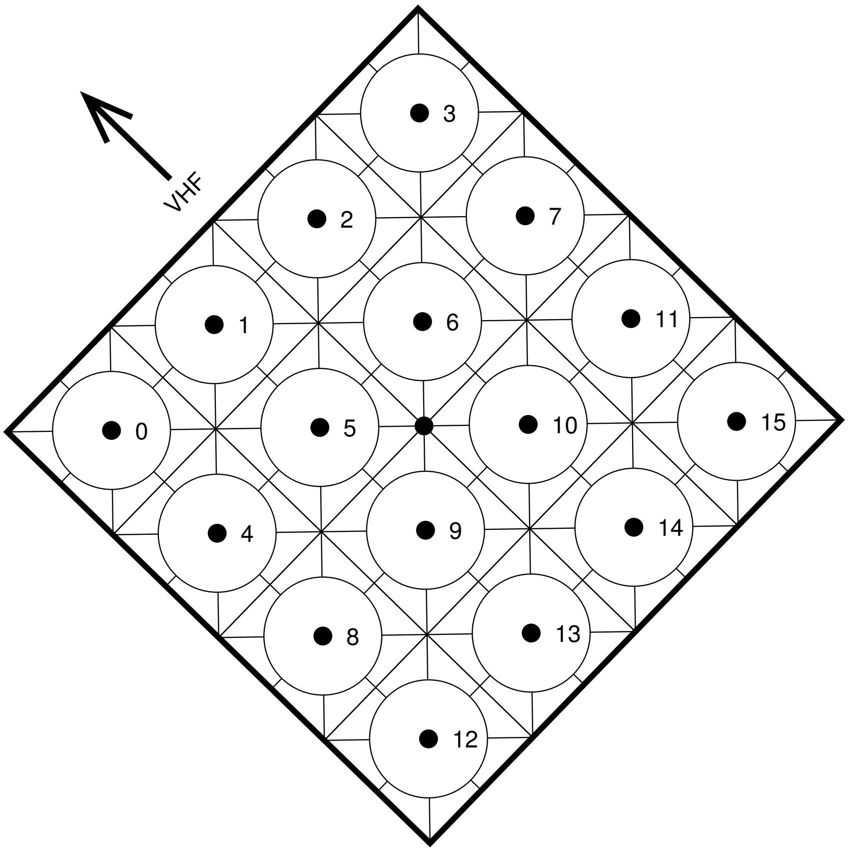

Figure E.25: Numbering scheme for cells within a single HBA tile.

then sixteen polystyrene lids were applied (one per tile cell) and lifting jigs were inserted in the middle of each quadrant of cells. These were attached to a four-arm, centrally suspended steel hoisting cross, which allows the partially completed tile to be lifted in its horizontal configuration and moved onto the HBA array field for final placement.

The tiles were moved from storage by inserting a 6-m long lifting rod between the tile halves above the storage pallet on which it rests and the plastic wrapping and spacer polystyrene is then removed from the remainder of the tile. The lifting rod is then raised up and attached to an inverted-U-shaped unfolding rig on the loader crane.

At this point, the tile comprises the polystyrene internal skeleton, antenna elements and cables. The PVC bottom bag that supports this is folded between the two halves and provides the support for the fragile components. Lining the PVC bottom bag is a galvanised wire mesh (grid-size 5×5 cm), which acts as an RF ground plane. The tile is then lifted off the pallet and slowly moved by the loader-crane lorry to the unfolding station. As it is lowered onto the platforms the lower corners are manually pulled outwards, thus unfolding the antenna tile. These stages are shown in Figure E.26

Figure E.26: Moving the tile from storage to the unfolding station (left) and then unfolding it as it is lowered into position there.

Fitting

Once at rest on the unfolding station, the elastic carrier straps and timber supports are removed. Plastic pins are pushed in the sides at thick polystyrene areas to keep the bottom bag up. The tile is then inspected to check for transport breakage and cell configuration.

The azimuthal orientations of the bow-tie antenna polarisations are +X = 137 degrees and +Y = 47 degrees and is shown in Figure E.27. There is a small ($\approx$3 degrees) offset between the alignment of the X-polarisation of the crossed bow-tie antenna blades and the direction of the EISCAT VHF radar. This was a result of the tile alignment needing to be specified before the array was placed and surveyed and also through the uncertainty of the observation angle, which varies as a function of altitude in the ionosphere. This small mis-alignment has a negligible effect on the data and, as it is a known value, it can be corrected in the post-processing. This configuration was checked for all cells before commencing the enclosure of the tile.

A polystyrene lid covered each cell in the tile, there are two different thicknesses of lid, and they are sloped so that each tile as a slight run-off when complete. This facilitates water drainage from the top of the tile. The lids are fitted 2×4 low lids at the edges away from the fold line and 2×4 high lids in the middle adjacent to the fold line.

Lifting

Four lifting jigs are inserted into manufactured slots centred on each quadrant of the tile. Additionally, securing ropes attach to the sides using plastic guards to prevent damage. The jigs are connected via chains to a hoisting cross which in turn is lifted by the loader crane on the lorry. In addition to the plates on the jigs

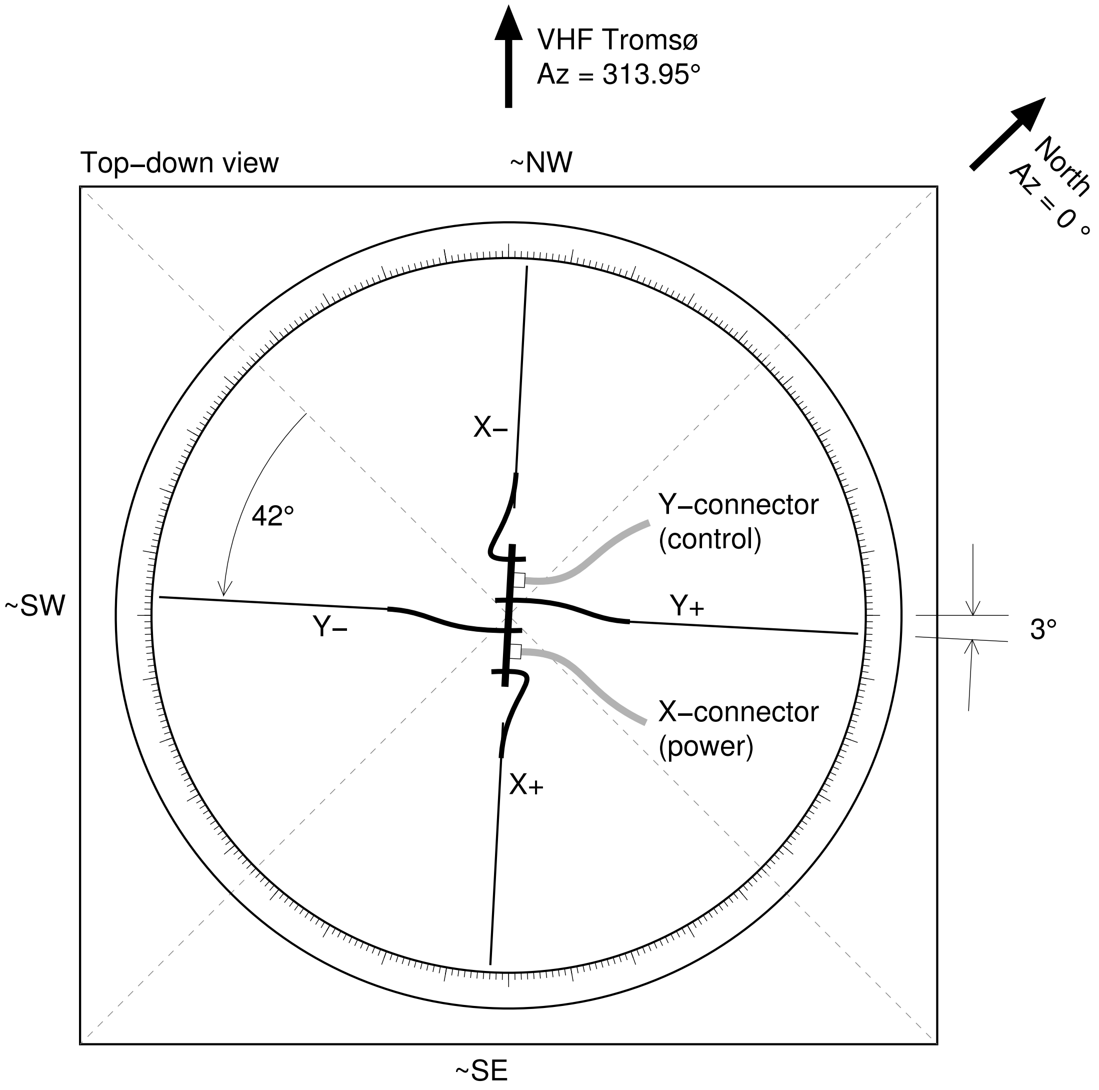

Figure E.27: Configuration of the crossed bow-tie polarisation elements in each HBA cell. See also Figure 2.3, page 9.

themselves, each of the lifting jigs is connected by two elastics to the underside plastic cover to hold it in place during the lift.

With the tile suspended, the lorry is driven in close to the correct square on the KAIRA grid. The loader crane is then used to place the unit either directly in front of the vehicle or to the side. This technique is effective and it was possible to use a single vehicle for both taking the tile from the store to the unfolding station, completing the unfold and in lifting it onto the array. Additionally, the loader crane has sufficient height so that it could lift the tile over the frameset and, when necessary, even over tiles that are already fitted. This meant it was possible to drive through the array to place tiles deep into columns. Examples from HBA tile deployment are shown in Figures E.29.

Figure E.28: A partially-fitted HBA tile on the unfolding station. The lifting/unfolding pin used to transport the tile out of storage is still below the tile in the gap between the platforms. The outer rows of lids have been fitted. Beyond the assembly area are stacks of lids and timber frames for the frameset construction. The tile cover can be partially seen on the left. It is not fitted until after the tile has been lifted into place.

Figure E.29: Moving the partially-completed HBA tile from the unfolding station (left) to the final position on the relevant frameset (right).

Tile cover

Once the HBA tile was in place the lifting jigs, securing ropes and hoisting cross were removed and set aside for use in placing the next tile. The black PVC cover was applied and this was then attached to the frameset, thus providing a water-impervious surface and also securing the tile in place.

Around each tile, there are sixteen attaching positions (five on two of the sides and three on the other two). The edge of the tile cover is folded and plastic welded during the manufacturing process. Fibreglass holding rods, approximately 10 cm long, are incorporated into the edge of the black UV-resistant tile cover. A small punched hole is made and the rods are inserted into the cover edge using long-nose pliers to lock the O-ring into the cover edge. This is shown in Figure E.30.

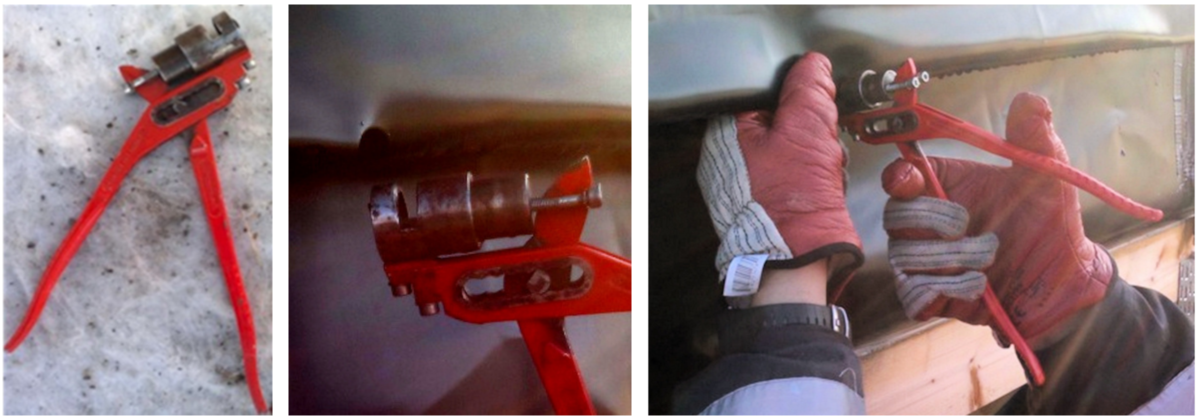

Figure E.30: Punching holes in the plastic-welded top-cover edge, using a bespoke cutter.

The O-ring, then connects to an S-hook, which clips onto a counter-sunk drywall screw, which is left proud of the timber to accommodate the S-hook. O-ring length is adjusted by adding knots to the O-ring itself. This is different to conventional LOFAR installations, where the tile is connected directly to the anchor lines in the ground.

Following the storm damage (Appendix E.20), the S-hook and screw arrangement was replaced with pig-tail hooks, to which the O-ring was attached directly. These provided additional security against complete detachment in the event that the anchor point loses tension. Such a situation might arise in the case, for example, when the polystyrene in the tile is compressed or disintegrates, causing the cover to become loose over the tile's internal structure. A comparison of the two types of connections is shown in Figure E.31.

Figure E.32 shows a side view of the build site on 6 July 2011. It shows the profile of the mound and various stages of the construction. From left to right, there are: four completed HBA tiles in the first array section, the first frameset in the second

Figure E.31: Comparison of the two types of HBA cover securing arrangements. The left-hand image is the original design, with an S-hook attaching to a drywall screw. Note the top of the O-ring, where it connects to the white fibreglass rod embedded in the edge of the top-cover. The right-hand image is the new implementation, with the O-ring connecting directly to a pig-tail hook.

section, in front of the lorry is the geotextile reel. The loader crane on the lorry is preparing to lift the next tile, which has been unfolded and lids applied. (The PVC cover is not put on until the tile is in its final position). To the right of the tile under assembly, are the new framesets. The plastic-shrouded frameset at the far right is a temporary store to collecting packing and waste material. Beyond the site, the summit of Korkea-Jehkas can be seen.

Figure E.32: A composite view from the side of the site during HBA construction, looking northeast. A description of the features is given in the text.

E.9 HBA cabling

For both the HBA array and LBA array, two 75-ohm coaxial cables connect each antenna to the electronics cabin. These allow electrical power and control signals to be sent to each antenna, and transport the RF signals for each of the two linear polarisations from the antennas back to the cabin. The two cables emerge from the lower side of the tiles on the southeast edge, approximately 50 cm either side of the centre line. They are secured to the bottom bag of the tile with a cable gland.

To control cable delays, fixed-length cables were used: 48 × 85 m and 48 × 115 m cables. This results in suplus cable length which is accumulated just outside the electronics cabin. Each of these cables was tested before installation to check for defects and to get an initial assessment of the signal propagation delay. The 85 m cables had a delay of 342.44±0.13 ns The 115 m cables have a delay of 465.50±0.15 ns. Attenuation was measured at 224 MHz and found to be 7.5±0.2 dB and 10.15±0.05 dB for the 85 and 115 m cables, respectively. A schematic representation of the cable plan is shown in Figure E.33.

Cables are routed with timber cable trays, mounted underneath each tile antenna. These are organised so that the cables first run along the V-shaped trays that run under the six antennas in each row, thus a maximum of 12 cables. These trays are pre-constructed using recovered timber from the HBA tile delivery pallets (Appendix E.7) and then are inserted into the framesets which support them. The diagonal bracing timber of the framesets provides a suitable location to attach them. These are shown in Figure E.34 (left); see also Figure E.21.

The V-section trays hold between two and twelve cables (depending location), and bring them to the northeastern edge of the array, where they will link with the main cable trunking. The raised cable trays were necessary due to the difficulty in placing cables underground. Initially there was also worry about ground freezing (and hence shifting), but this concern was unfounded. Another advantage of the raised cabling was to keep the cables away from wildlife; voles, lemmings and mountain hares (Finnish: *jänikset*) all present a threat. The main cable trunking supports are U-shaped box trays which run along the northeastern edge of the array. The hollow-square design, give addition capacity and permits easy mounting on the inside vertical struts of the framesets. Each U-section caters for two rows of the array and thus carries 24 cables. These are shown in Figure E.34 (right).

There were also places where it was necessary to take the cables underground; namely the stretched between the segregated sections of the HBA array and also between the array and the electronics cabin, shown in Figure E.35. In these cases, cable ducting sloping down into pre-buried perforated drain pipes was used. Initially there were problems with cable ducts being crushed by mechanically-placed back fill. This was overcome by pre-filling with layers of sand first, before manually digging back in the back fill (the human-effort limitation would ensure that there would be no large heavy rocks to crush the ducting).

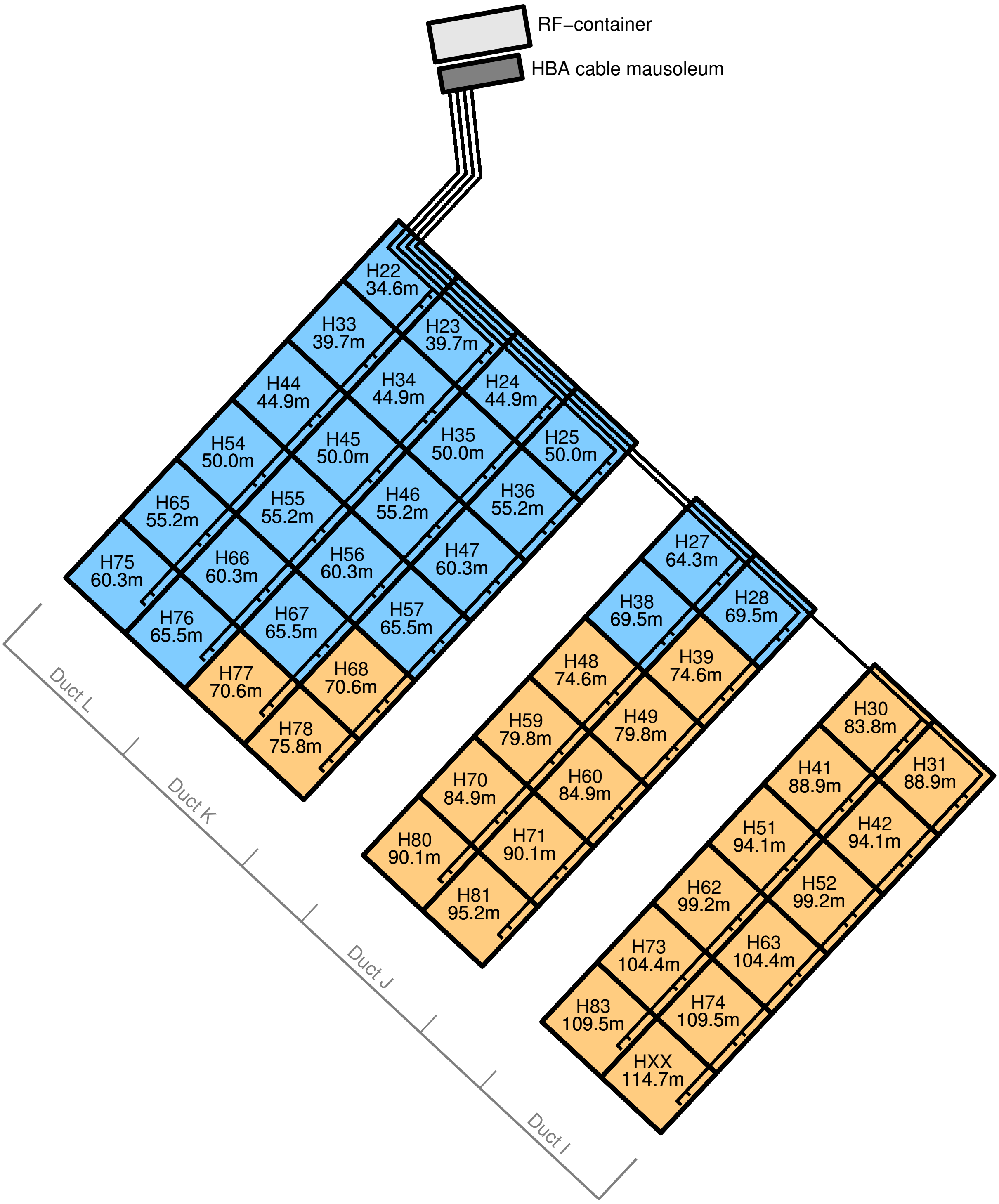

Figure E.33: Schematic representation of the HBA array cabling arrangement. The blue-shaded tiles use 85 m cables and the amber shaded tiles used 115 m cables. Each tile is marked with its tile number, along with the nominal distance of that tile to the electronics cabin (RF-container), including any vertical distance. Different sections of the array feed into different cable ducts (the partitioning of which is also indicated).

Figure E.34: Left: Example V-section cable tray for each row on HBA tiles (per row: 6 tiles = 12 cables; c.f. Figure E.20). Right: U-section cable trays forming the main trunking. In both cases, the cables are not yet in place. Each U-section tray serves two rows (12 tiles = 24 cables).

Figure E.35: Between sections of the HBA array, the cables are routed underground. Perforated drain pipes provide a deterrent against rodents. Likewise, at the point where the cables leave the array area to go to the cable mausoleum, they are routed through perforated ducts (right) which go underground.

HBA cable mausoleum

The final ducting from the array with all HBA signal cabling comes up into are raised timber box against the side of the electronics cabin, where surplus cable is zigzagged back and forth to accommodate the excess lengths. This box is referred to as the cable mausoleum (so named, in comparison to the cable grave, which is the nomenclature used for buried cable arrangements for the similar purpose).

The mausoleum itself is a timber construction with board panelling. The underside and upper sections have ventilation to allow natural circulation of air to keep temperature changes minimal (diurnal variation at Arctic latitudes is gradual). Photographs of the HBA cable mausoleum during construction and after completion are shown in Figure E.36.

Figure E.36: The HBA cable mausoleum during construction (left) and after completion (right). The grey shipping container is the electronics cabin (RF-container). An LBA mausoleum also exists (see Figure E.44), but it is located adjacent to the LBA array.

The white pipes seen in Figure E.36 protect the cables as they pass from the mausoleum, underground, and up into the "lobby" of the electronics cabin. The entry points are further protected with a combination of timber and polystyrene. Geotextile felt was used to block all holes, which provides a guard against snow and rodent ingress, but still permits "breathing" to allow for differences in pressure and humidity. The felt also guarded against sharp edges to reduce possible abrasion of cables.

E.10 HBA snow barriers

Around the sides of the High-Band Antenna array, there are a mix of different snow barrier types. The leading edge of the array was fitted with timber barriers immediately but there was insufficient time in the first year to complete the side panels. As a result, a temporary plastic mesh was put in place. During the second build season, the original meshes were replaced with the proper timber panelling, shown in Figure E.37.

Figure E.37: Application of the snow panelling and mesh on the sides of the HBA framesets. The panelling included several doors, to permit access to the underside of the array. The panels not only prevent excessive snow drift under the array, but also exclude large wildlife (c.f. Figure E.35, right). Image: Arttu Jutila, SGO.

The planks used for this were recycled timber from the pallets on which the HBA tiles were originally delivered. By re-using the packing and transport materials, the volume build waste was reduced to nearly zero. Re-use of shipping material is an important technique that could be used for other large scale projects like the Square Kilometre Array and EISCAT_3D, in order to minimise environmental impact, transport costs and manufacturing waste.

E.11 HBA summators

The HBA summators are electrical units which handle the combination of signals from the individual cells in an HBA tile. There are two per tile, one for each of the two linear polarisations. The X-polarisation summator also has DC-DC converters to distribute power to the individual amplifier boards of each cell. Summation is handled as a binary-tree combination to ensure that there is no variation in path length delay for any given cell in the tile.

There are two designs of casing: the older "Mark-I" design uses a sheet-metal box. They are nominally acceptable, but in the Netherlands where there are high moisture levels, condensation caused some failures. The newer "Mark-II" design is completely encased in black resin (similar to the LBA low-noise amplifier units), and are thus more robust. For KAIRA, the installation comprises Mark-I summators for the X-polarisation and Mark-II summators for the Y-polarisation. Since installation, both summator types have worked successfully.

Normally summators are installed in the tiles as they are assembled in the factory. However due to unit production shortages in 2010 and 2011, this was postponed. Two prototype-sample summators were installed on 11 November, 2011 in order to carry out testing during the first winter. The remainder of the summators were installed in early June 2012, as shown in Figure E.38.

Figure E.38: Fitting summators into the HBA tiles (left). Examples of individual summators are shown (right), including both a light, sheet-metal Mark-I design and some dark, resin-filled Mark-II summators.

E.12 LBA array field survey

Two sets of winter testing were carried out for the LBA aerials. The first was a four-unit system constructed at Pittiövaara, near Sodankylä, Finland. This tested the resilience of the antennas to snow during the 2011–2012 winter, and the suitability of the LBA design for riometry measurements.

A second, more-extensive evaluation was done at Kilpisjärvi. On 1 and 2 August 2011 a survey of the lower field of the KAIRA site (Figure 2.2, page 7) was carried out in preparation for the planned construction of the LBA array in this area. A rough survey was first done with a laser-level and range finder. This allowed the general outline of the field to be marked with posts, as well as one extra post marking the approximate LBA array centre. Then a more thorough survey was carried out with a GPS receiver. The area was slightly sloped with a drop of 220 cm between the highest and lowest parts.

Several test holes were dug into the ground to check the suitability for foundations. This indicated that the surface layer of organic material was 5–20 cm thick. Below it was a wet layer of silt, which acted as a non-Newtonian fluid: hard when forced, but liquid when gentle pressure is applied. When dried, the silt dust became powder-like and easily wind eroded.

Based on this assessment, it was decided that the LBA array would need to be raised up off the tundra, although for ground stability reasons, rather than snow. Three test platforms were constructed in the area (shown in Figure E.39) and left to winter-over from 2011–2012.

Figure E.39: The three test platforms in the lower field at the KAIRA site. All three are fitted with the RF ground plane, but only the centre platform has the LBA aerial erected at the time the photographs was taken.

The winter testing indicated a number of serious problems. The silt/water catchment area meant that the ground was unstable at the time of the annual melt. The presence of permafrost means that additional instability may occur due to the formation of palsas, especially if the natural water courses were altered through the installation of the array. The general gradient across the field means that considerable ice drift can occur, which may rend structures. Additionally, the poor soil means that access would be difficult and the complications of routing cables above ground would be awkward.

Another impediment was the degradation of RF performance of the antennas, because the metal ground plane was small and raised over the natural ground plane of the swamp, which could be of variable height depending on water/ice conditions. Modelling was carried out, indicating sub-peak performance of up to 3 dB for angles with ±45 degrees of zenith. The cost of rectifying these problems would be prohibitive.

Thus the conclusion was that the lower field was unsuitable for the LBA array. Faced with this obstacle, a number of alternative options were considered:

- **Raised LBA on stabilised swamp**
  Stabilise and level the ground, using concrete or other material that fundamentally alters the ground composition, then build individual LBA frames on top of it, with a common wire mesh reflector. This was discarded on grounds of cost and environmental impact.
- **Raised LBA on raw swamp**
  Ignore the ground stability but level and build the frames anyway. This was discard on the grounds of stability and anticipated poor RF performance.
- **Raised Half-LBA on mound**
  Build the frames in the works area of the mound and only build a half-size LBA. The rest of the LBA units could be used at Sodankylä for experiments or kept as spares.
- **Full LBA at SGO**
  Abandon the idea of an LBA array at Kilpisjärvi, move the grids to Sodankylä and either buy or build new DSP electronics. This would be expensive and reduce the usefulness of the KAIRA site.
- **Trenched Half-LBA on mound**
  Deploy a half-size LBA array on the ground (not frames). The cables are either dug in (similar to what was done at the LOFAR station at Chilbolton, UK) or are laid flat then buried (such as was done at the LOFAR station in Onsala, Sweden) to provide the necessary physical and thermal stability.
- **Surface Half-LBA on mound**
  Deploy a half-size LBA array on the ground (not frames). The cables are simply laid on the ground, and are either not covered, or are covered with a light geotextile or gravel (to protect against animals, but not physical loads or thermal cycling). The area must then be fenced off to prevent incursion by people or vehicles, which would crush the cables.
- **Abandon the LBA plan**
  The alternative would be to stockpile the parts and await further funding, ideas, etc.

The final decision was to deploy Trenched Half-LBA array in the works area adjacent to the HBA array and the entry gate. The restricted area would mean a reduction of the array size, and the additional distance from the by-now-installed electronics cabin meant that new cabling arrangements would be required.

On the other hand, having seen the effects of snow during the first winter with the HBA array, it was deemed unnecessary to raise the LBA onto platforms, which thus meant a simplified installation process and better RF performance. Being “on the mound” means that natural snow clearing occurs. Another advantage of the location was the ease of access, especially for vehicles.

E.13 LBA array re-design

There have been a number of factors which have influenced the design of the KAIRA array. The primary aim of the station is to satisfy the VHF reception from the EISCAT radar system. This has determined the layout and position of the HBA array, and has resulted in a layout that is atypical compared to other LOFAR stations. The LBA array, on the other hand, needed to remain secondary to this and a suitable configuration was sought that would still permit the accomplishment of the complicated scientific requirements.

The LBA arrays at other international LOFAR stations comprise 96 aerials, distributed in a quasi-random pattern. At the so-called “core” and “remote” stations in the LOFAR array, the set of aerials are then split into two sub-arrays, antennas from which go into either of the two low-band inputs of the receiver units (described in Section 2.3). With the KAIRA LBA array now limited to the solid-ground area, and constrained from going further away by site access and maximum cable-lengths to the electronics cabin, the “LBA_INNER” configuration from the core/remote stations was chosen for the initial layout of the KAIRA LBA array.

The following limitations restricted the placement of the array on the KAIRA site:

- There must be a 20 degree elevation clearance to any nearby structures.
- The radius of the LBA area should be at least 18 metres.
- Site access needs to be preserved.
- Distances to the electronics cabin should be minimised to reduce the requirements for additional cables.
- The volume of new soil must be minimised (to reduce the number of gravel deliveries).
- The alterations to the ground level should be minimised to prevent soil instability.
- Likewise, the alterations to the ground level should be minimised to reduce the amount of work needed.
- Erosion and draining must be considered during the placement.

The beam pattern of the individual LBA inverted-V dipoles are such that a minimum elevation clearance of 20 degrees is required. For the KAIRA LBA array, the main consideration was the HBA, which was nearby and raised (including the ground plane). Other obstructions in the area included trees and the incoming electricity supply (via posts to the site edge).

Access to the site, in the east-southeast corner) had to be maintained. This had an additional implication that destructive ground alteration would start from the west and work back towards the site entry point. Additionally, the expansion of the HBA to an international LOFAR station layout would also need to be kept possible. This required having hard-packed material that a crane could operate on, or the ability to drive a lorry with loader-crane down the snow corridors — the gaps between sections of the HBA array.

In order to level the site, material was to be brought in to bring the site up to the designated reference. Due to the nature of the material already in place, and the desire not to disturb it, only new material was to be added and nothing removed or re-positioned. This meant that the layout of the array (both as KAIRA and as a potential future LOFAR site) was to be chosen to minimise the volume of new material (sand, soil, concrete, etc.) that needed to be introduced into the site. This reduction in work had additional schedule and financial cost benefits.

A site survey against a reference point of the south-corner of the HBA array, provided a topographic mesh model of the existing area, showing a variation between 620 and 850 mm (depression, with respect to the HBA array reference point). Based on the experience of the HBA array groundworks, any new material would have an edge slope decline of 30 degrees. Thus, the LBA array ground could be approximated as a conical frustrum (truncated cone) and the volume calculation for new material would be the difference between that truncated cone position and the topographic mesh.

Software was written to calculate the volume addition of any given placement, allowing for constraints. This was run for a raster of points across the area, to find an optimum. Due to the slope, there was always a tendency for the optimisation to pull the array closer to the HBA array. That resulted in two problems. Firstly, there was a “lake” (a depression near the east corner of the HBA array). Secondly, it encroached on the access road, thus providing an additional challenge on the required groundworks. To compensate for this, a weighting factor of two was applied to depth differences on the positive-Y (north direction) axis.

The weighted position was then measured for average depth (700 mm) below the HBA array ground reference level, and an elevation clearance to the nearest HBA tile was calculated (14 degrees, which was within the specification).

Practical aspects, such as water run-off and access, were also considered. Analysis of photographs taken on 9 May, 2012, indicated that high-speed wind flow around the edge of the HBA would be problematic, thus encouraging a position that was more in the shadow of the HBA array. Additionally, terrain considerations at the “lake” also required this. Measurement error of the survey and low-precision ground-work operations were also considered.

Lateral variations of up to 2 metres could easily occur with minimal impact on the groundwork costs, which was done, moving the LBA array centre further south-west. An approximate, but conservative, cable-length check was made, estimating the cable distance from the furthest possible LBA aerial to be 123 m (within the limit

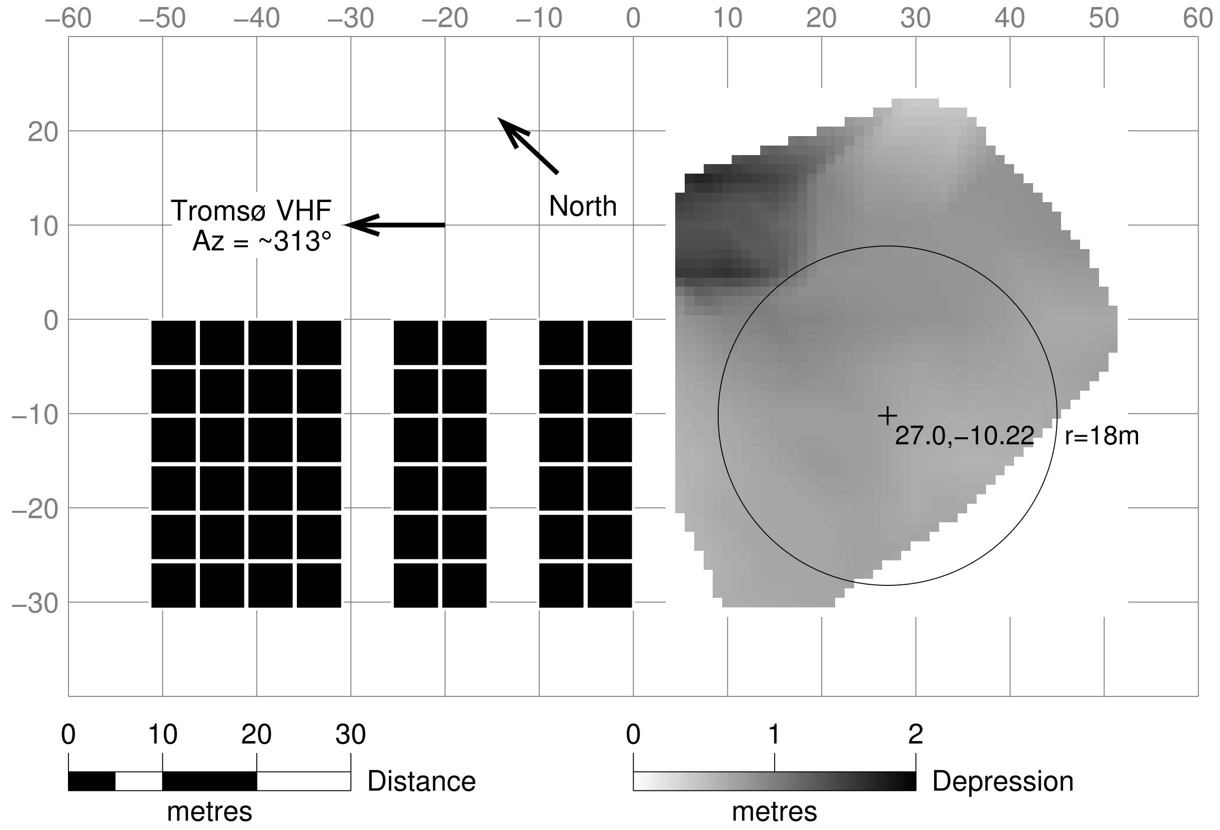

Figure E.40: Survey of the topography of the LBA area with respect to the already-installed HBA array. Additional material was added to the south of the mound to bring it up to level.

of the longest 130 m cable in stock and below the 150 m limit of the subsequent signal processing). Assuming an efficient cable-trenching layout (see Appendix E.15), this validated the proposed location. A volume of $\approx$200 m^3 of additional soil was required to bring the area up to a reference level of 720 mm below the HBA array ground reference and pack the sloped edges appropriately.

LBA array simulations

With the LBA array re-specified to fit the 18 m radius circle, and with a basic antenna layout of the LBA_INNER configuration from LOFAR being used (primarily for compatibility for VLBI observations), it was necessary to change the location of the two outlier LBA aerials (antennas #L46 and #L47) so that they fit within the confines of the designated area.

The method used for doing this was done using an algorithm which placed #L46 and #L47 randomly within the field radius and testing to ensure there was no physical overlap with any existing antennas. These candidate placements were then tested for the sidelobe response of the beam pattern and the best configuration of these was used. Several million candidate positions were assessed, and the best result is the LBA array layout that was used. Final LBA element locations are given in Appendix C.

E.14 LBA array groundworks

On 20 June 2012, work began on levelling the LBA field and took approximately a week to complete. The field was graded, and then a layer of gravel placed and packed on the field (Figure E.41). After levelling, the LBA layout is marked out, to an accuracy of ±1 cm. Each aerial had two kinematic survey pegs: one to define its position and a second to define its orientation. After the array was completed, the survey pegs were removed.

Figure E.41: LBA field groundworks. Image: Joona Keskitalo, SGO.

E.15 LBA array cabling

Like the HBA array, each element of the LBA array has two 75-ohm co-axial cables to transport control and power to the aerials and two polarisation signals from the aerials to the electronics cabin. Cables were encased in perforated agricultural drainage pipe, which were then buried into the ground. The cable plan was devised to:

- Minimise lengths of cables required (cable constrained),
- Avoid all anchor pegs (required to secure the aerials),
- Avoid all survey pegs (required for aerial placement),

- No cable crossings (which cause deployment complications),
- No more than 5 cable pairs per node (due to conduit capacity),
- Nodes cannot be placed under grids (for access),
- Avoid tight cable bends (to protect the cable RF-integrity),
- Keep a good distribution of the entry/exit points on each node,
- Minimise the number of nodes (to conserve pipe),
- Minimise the number of trenches (to preserve worker morale)

The final cable plan was a tree-like arrangement, shown in Figure E.42. In each of the shallow trenches on the LBA field, there are white agricultural drains, which were used as ducting for the cables. Because there is rocky, unforgiving soil from the site levelling, and the fact that ground-moisture freezes each winter, this additional protection for the signal cables was required. This is in contrast to other LOFAR stations, where the cables are buried directly into a sand layer in the ground.

The branch points are referred to as “cable nodes”. The cables themselves are in the flexible agricultural drain pipe. A larger piece of this is then cut to provide the node. A cap then goes on top of this to allow access later for drawing the cables. The cable nodes are shown as black dots with white numbers in Figure E.42.

Cable allocation

The change in the configuration, combined with the now-additional distance from the LBA array to the electronics cabin, resulted in field-modification of the cables. A large stock of short lengths was combined to produce necessary 120 and 130 m lengths. The 130 m lengths were made by joining existing 80 m and 50 m cables from the inventory. The 120 m cables were made by joining existing 80 m cables with 40m cables. There is no standard 40 m cable lengths, so 80 m cables were cut in half — there were surplus 80 m cables in the inventory, due to the reduced size of the LBA array (48, not 96, aerials). Cable propagation delays were measured to ±0.1 ns, and values used as part of the calibration process of the array beamformers.

LBA cable mausoleum

Although cables were adapted to give different lengths, these are still limited to a few set values. The antennas themselves are at quasi random distances, thus there is additional cable to “bury”. Like the HBA, this is done in a cable mausoleum which, for the LBA array, was located near the array itself. Additionally, any cable joins were located in the cable mausoleum, rather than randomly along the buried ducts. This later saved much work. The cable joins suffered from resin ingress,

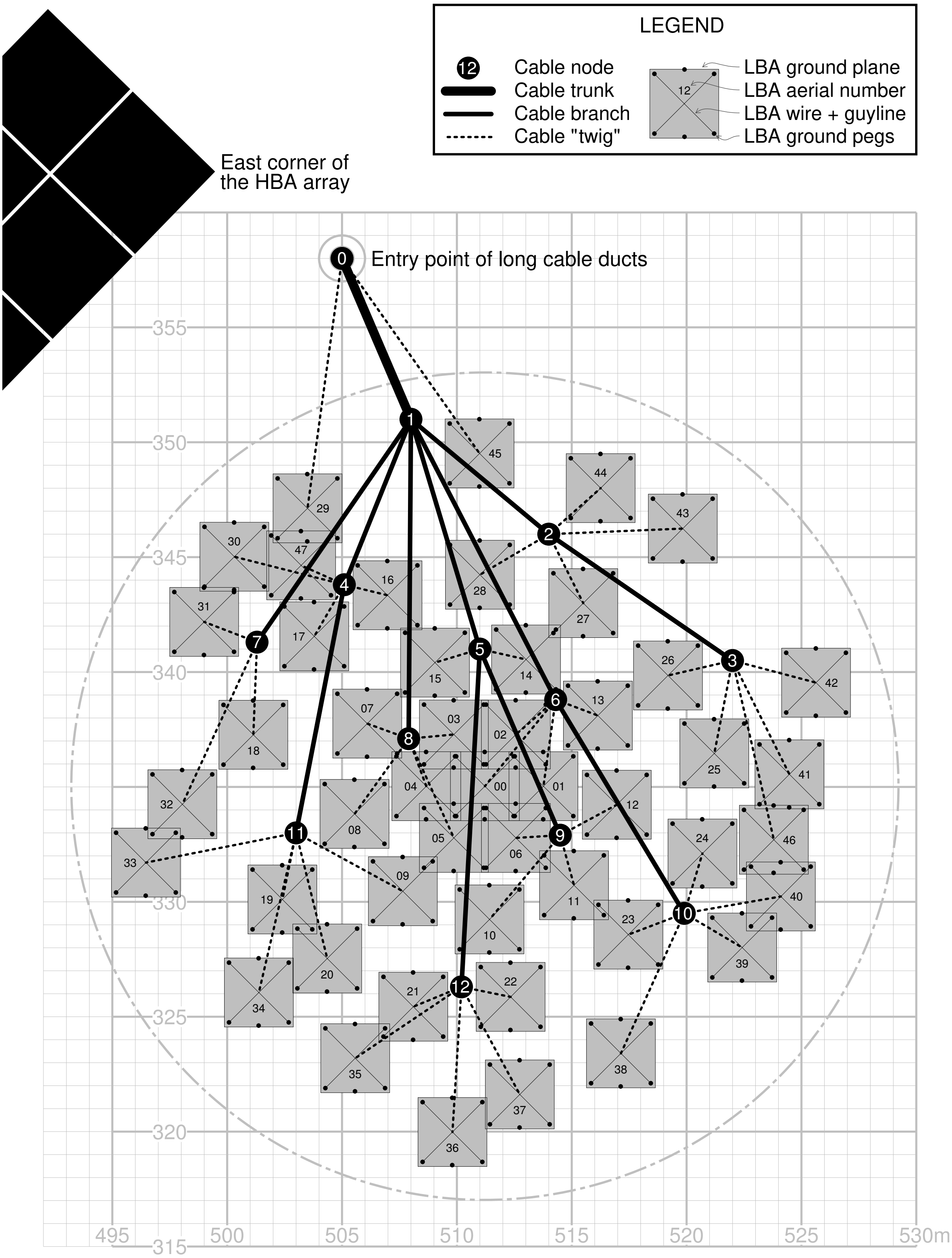

Figure E.42: Trenching plan for the underground cable ducts on the LBA array. The background grid-scale is in metres, with respect to a local survey point. A detailed schematic of an individual LBA aerial is shown in Figure E.47.

Figure E.43: Digging shallow trenches and adding the cable ducting drain pipe (left) and the feeding of cables into the ducts in the backfilled area, after the RF ground planes had been placed (right).

which resulted in them needing to be completely re-stripped and re-connected. The ability to access the cable joins comparatively easily through the above-ground mausoleum made rectifying this problem possible without re-opening trenches. Even so, from the initial detection of the problem in September 2012, it still took several months to effect the repairs. Pictures of the partially-built and completed stages of the LBA cable mausoleum are shown in Figure E.44.

Figure E.44: The LBA cable mausoleum during construction (left) and after completion. The cables zig-zag back and forth without any loops, before going into the subterranean main duct (the large black entry point to the left). Compare the LBA cable mausoleum to the HBA cable mausoleum (shown in Figure E.36).

Between the LBA cable mausoleum and the electronics cabin, there are two buried ducts. As additional cables were passed through these ducts, it became increasingly congested and difficult to introduce new cables. To ease this problem, part of the duct trench was re-opened and access hatches were cut mid-way along the duct to provide an intermediate cable-draw point, shown in Figure E.45.

Figure E.45: The LBA main cable trenching with the main ducts being buried (left) and the mid-point access hatches removed (right), showing the cables inside. Photos: Toivo Iinatti & Arttu Jutila, SGO.

E.16 Aerial installation

The steel ground plane for each LBA aerial is 3 m × 3 m, with a gridsize of 10 cm and manufactured from 8 mm machine-welded steel bar. These are placed against the kinematic survey pegs. Once aligned, four anchor pegs are used to secure the grid to the ground. These pegs also serve as the connection point for the guy lines of the LBA aerial wires. Two of these are nylon, and provided the fixed angle. The other two guy lines are elastic and provide tension to keep the LBA mast upright. To accommodate the KAIRA ground and ease installation and maintenance of the LBA aerials, a bespoke peg design was devised. Once the anchor pegs were in place, the two survey pegs were removed.

The LBA aerials comprise a 1.8 m long, 40 mm PVC pipe which serves as the mast and protects the two co-axial cables. They were erected after the cables had been installed. At the ground point between the pipe and the buried duct, 40 cm of metal armoured sleeving covers the cable to protect it from damage and provide flexibility between the precision-surveyed antenna position and the coarsely-buried duct. At the top of the mast is a resin-potted cap, which contains the low-noise amplifiers (LNA) for the inverted-V dipole wires. The azimuthal orientations of the LBA aerial, and thus polarisations are +X = 45 degrees and +Y = 315 degrees. These alignments, as well as the construction details, are shown in Figure E.47.

Installation of the LBA array aerials started on 12 July 2012 and was completed on the 27-Jul-2012. A completed LBA aerial is shown in Figure 2.5 (page 10).

Figure E.46: A newly completed LBA with respect to the cable node and routing pipes (left). The two signal cables are protected with a flexible metal armour at the point where they leave the LBA mast and go into the underground ducts. A wad of geotextile is pressed into each to hold the cables steady and prevent access by rodents.

E.17 Signal path

The signal processing of the antennas can be summarised as per Figure E.48. It shows the antenna signal paths for two polarisations, which ultimately become the input of a single receiver unit (RCU) board.

Each HBA polarisation element comprises a bow-tie antenna and initial low-noise amplifier (LNA). A remote on/off control can be used to configure which elements within a tile are used. Analogue delay is provided in 0.5 ns steps up to 31.5 ns. This provides tile-level beam control. Balance amplifiers are used to ensure matching between elements within the tile. Summation is delay-neutral, passive, analogue addition. Fixed-length 75-ohm cable takes the signal to the electronics cabin Faraday enclosure patch panel. The LBA polarisation elements are simpler. As there is no summation, only a single dipole and LNA exist per polarisation element, with fixed-length 75-ohm cable returning the signal to the electronics cabin.

E.18 Electronics cabin

The electronics cabin (also known as the "RF-container") is an industry-standard 20 ft sea container. The outside dimensions of the container are 606×250×290 cm (L×W×H) cm with a total weigh is approximately 4000 kg. It was installed on 26 July 2011. The foundations for the cabin are two 3 m×30 cm×30 cm reinforced concrete beams which are located at either end of the container. The blocks are placed on compacted ground, which has been fine-levelled with sand and confirmed with a laser-level. The container itself then sits freely on timber blocks which are placed on top of these beams. The delivery and final placement is shown in Figure E.49.

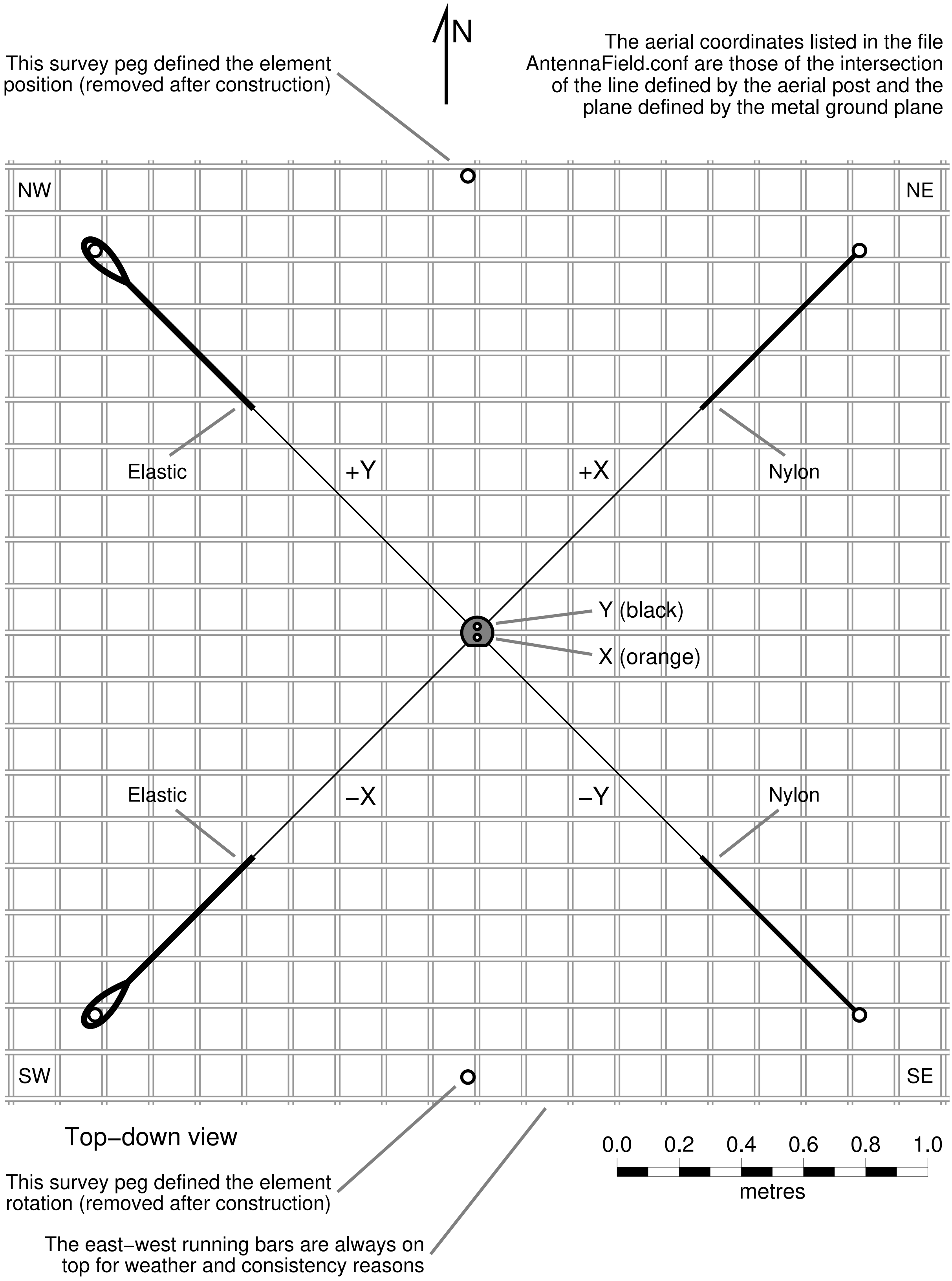

Figure E.47: Scale diagram of an LBA aerial. The LNA unit is in the centre, with two cables that run vertically down the mast. These carry power (X) and control data (Y) to the LNA unit, in addition to the X- and Y-polarisation signals back to the electronics cabin.

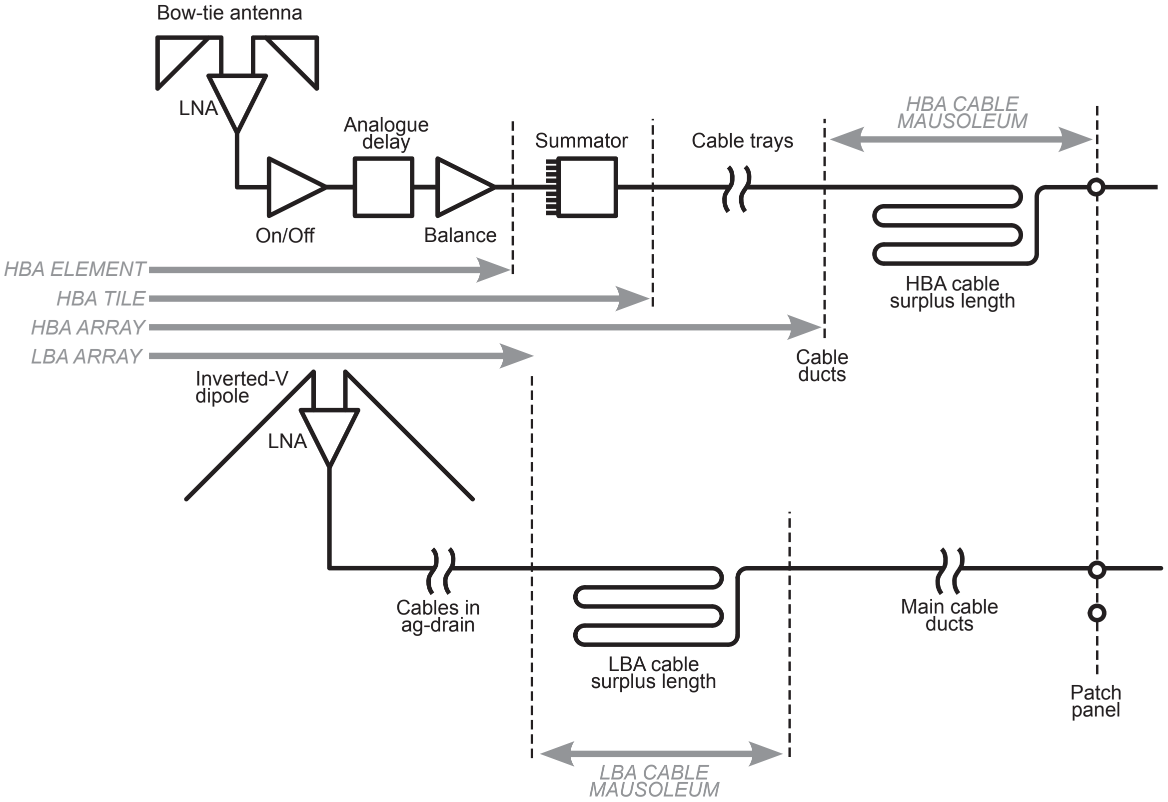

Figure E.48: Schematic of the KAIRA antennas and field cables. This is indicative of a single polarisation for an LBA/HBA pair (the input for a single RCU), up to the point of the patch panel leading into the Faraday enclosure. Refer to the text for a detailed description.

Figure E.49: Unloading the electronics cabin from the delivery lorry. Note the air-conditioning unit embedded in the end of the container (left). The cabin was placed on two concrete foundation blocks (right). After placement, a metal cowl was put over the air-conditioning unit to prevent ice build-up from fouling the radiator fan. See also Figure E.36, which shows the completed electronics cabin.

Internally, it contains a Faraday-enclosure, a small “lobby” area, which permits service and signal cables to enter the unit and protects the RF-safe patch-panel, which couples the external connections into the container, shown in Figure E.50.

Once inside the RF-container, there are 6 m patch cables that go from the back of the patch-panel under the false floor and into the signal processing racks (Figure E.51).

Figure E.50: Just inside the electronics cabin is an RF-tight patch-panel, which interfaces cables going into the Faraday enclosure.

The enclosure has a raised floor (under which the signal cables are passed) and four, full-height, full-depth, 19-inch electronics racks, which contain the signal processing and local computing. The end opposite to the container doors has an air-conditioning unit. Externally, this was covered by an additional cowling structure to prevent snow and ice from obstructing the fans or building up about the unit and reducing its cooling efficiency (Figure E.49, right).

The receiver unit (RCU) boards are the first part in the signal processing chain as the signals come into the RF-container and are shown in Figure E.52. There are 96 of these in total in the KAIRA system (which is the equivalent of a LOFAR Remote Station). There is one RCU per polarisation per antenna and each RCU has three

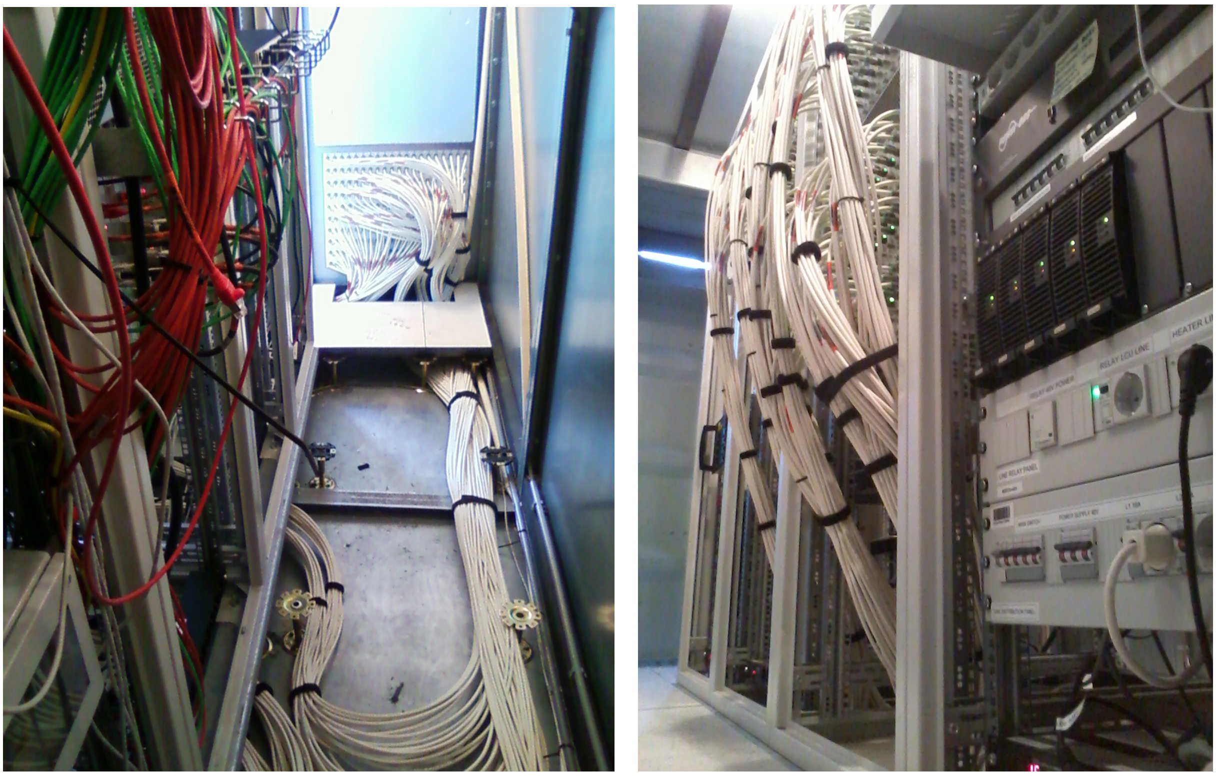

Figure E.51: The left image is the inside of the electronics cabin. The photograph was taken during the installation and the floor has been removed showing the cabling. The cables enter the cabin via the patch panel at the back of the image (this is the opposite side of the patch-panel shown in Figure E.50). The right-hand image shows the other side of the racks, with the signal cables coming up from the floor to go into the RCUs (c.f. Figure E.52.)

input channels. These are the high-band antennas (HBA), low-band-high (LBH) and low-band-low (LBL). On KAIRA, and other international LOFAR stations, only the HBA and LBH channels are used which have the signals from the HBA and LBA arrays respectively. The third channel, LBL, is for a second LBA array field. At the time of writing, there were no plans to utilise this additional capacity.

The internal filter arrangements in each RCU are shown schematically in Figure E.53, from the three F-type connections on the front panel (HBA, LBH and LBL), which include 75–50 ohm impedance conversion.

For the HBA signal path within the RCU, an initial 110–290 MHz bandpass filter (Finnish: *kaistanpäästösuodatin*) excludes out-of-band noise to minimise the linearity requirements on the following LNA. A pair of band switches (input and output) then selects the necessary bandpass filter associated with RCU modes 5, 6 and 7. There is then a higher-noise figure amplifier to ensure sufficient gain for at least three-bits of sky-noise on sampling. A 270 MHz low-pass filter is then present to suppress aliasing and out-of-band noise prior to sampling.

For the LBA, there are the two possible inputs (LBH and LBL) followed by a se-

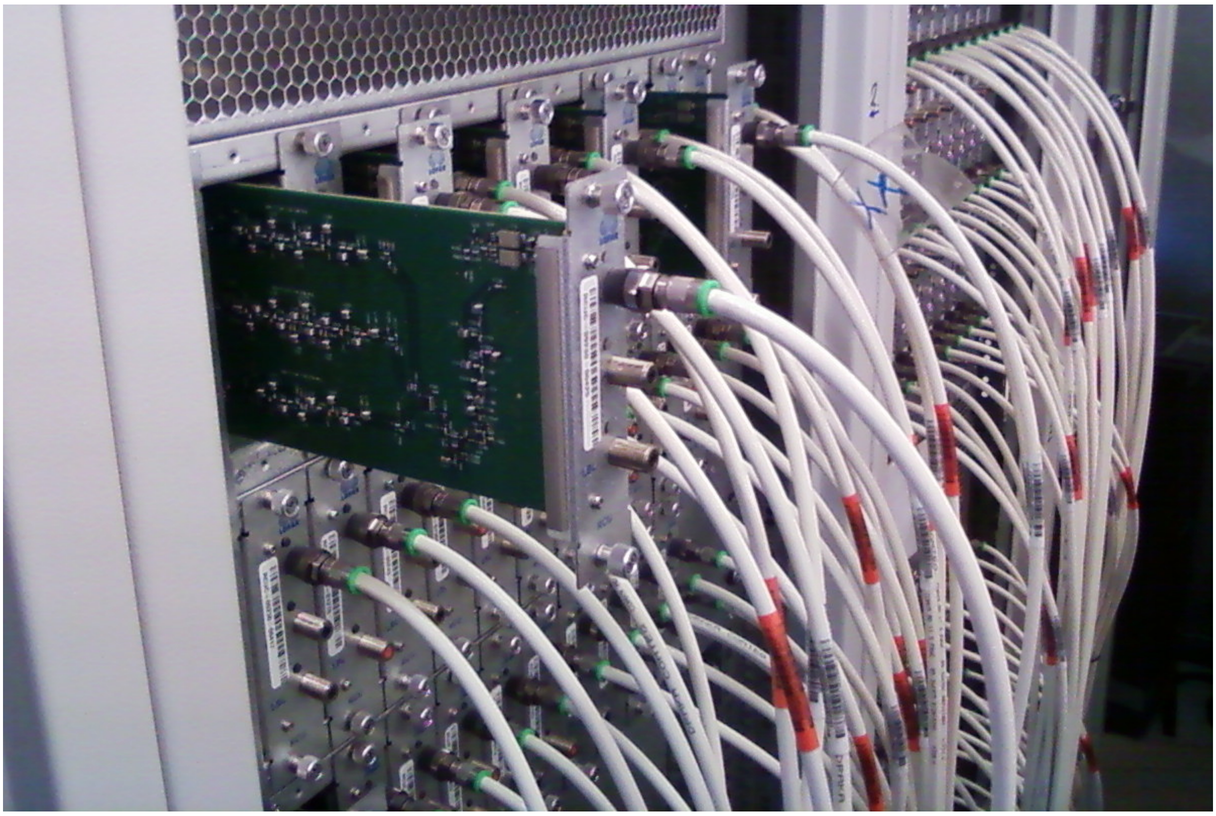

Figure E.52: The RCU subracks, with one of the RCU boards pulled out (c.f. Figure E.53). At the time the photograph was taken, the subracks were only partially populated with RCU boards and only HBA signal cables had been attached.

lectable highpass filter (10 or 30 MHz). Normally 10 MHz is selected, but the 30 MHz highpass filter can be used when nearby shortwave radio transmitters cause severe RFI.

A 90–110 MHz bandstop filter is used to suppress FM radio broadcast RFI, this is followed by a high-gain LNA and then the band-selecting filter. Like the HBA signal path, there is then a higher-noise figure amplifier to ensure sufficient gain for at least three-bits of sky-noise on sampling. Finally, a 90 MHz lowpass filter is used as an anti-aliasing filter.

Because of the input select switch just before the analogue-to-digital (A/D) converter, it is not possible to use the HBA and LBA simultaneously on a given RCU. However, it is possible to configure some boards to use the HBA and others to use the LBA inputs (see Section 2.6).

Digitisation is performed using a 12-bit A/D-converter, sampling at 160 or 200 megasamples per second (selectable). Time and frequency standards are provided by a rubidium atomic frequency standard, which phase-locked to a GPS receiver to correct for long-term drift and to establish a reference-frame time.

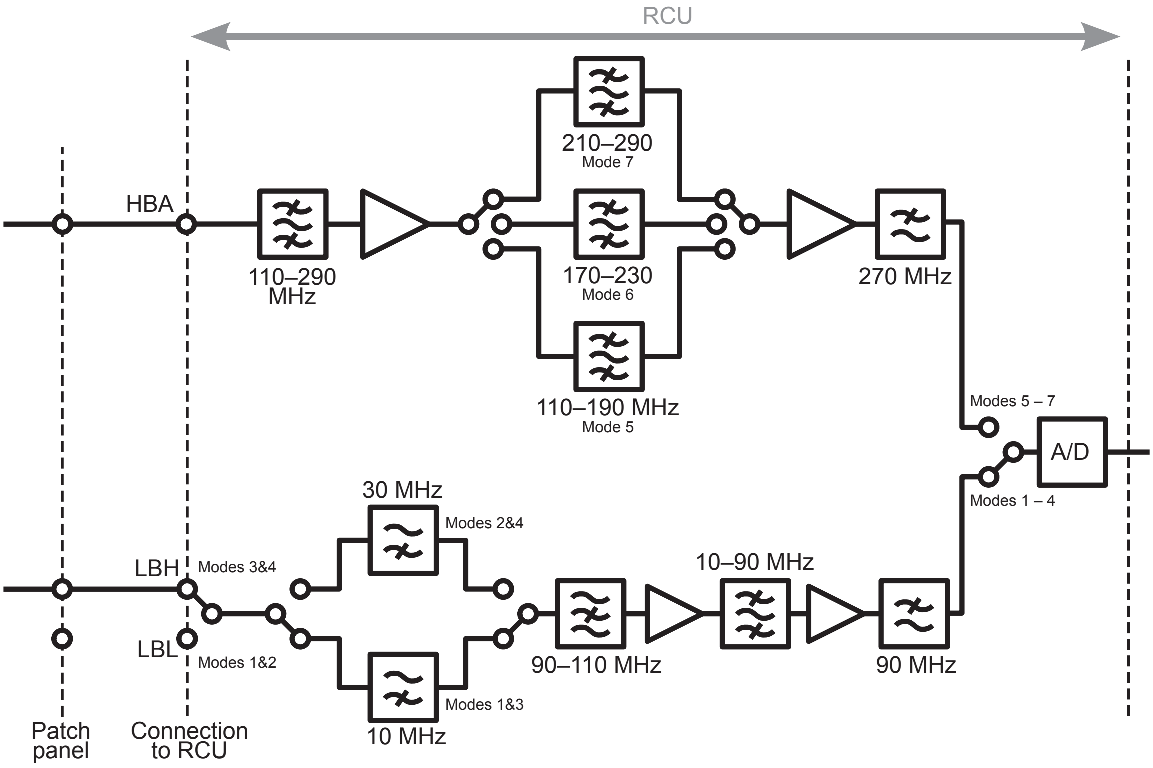

Figure E.53: Schematic of a single receiver unit (RCU). It shows the filters, indicating the paths taken under different RCU modes; c.f. Figure E.52. The final stage of the RCU is the analogue-to-digital converter (A/D).

The 96 RCU boards are arranged in three subrack assemblies, the configuration of which is provided in Table B.3 (page 142). On the back of each subrack assembly, there are the remote signal processing (RSP) boards, which handle timing, beamforming, etc.. These are shown schematically in Figure E.54, and are also described in Paper I.

As the system is then processing in the digital domain there is an initial first-in-first-out (FIFO) buffer to ensure synchronisation between inputs. Additionally, receiver statistics (RxS) are extracted which are used as part of the control processes and also for monitoring. All digital signals are passed into a poly-phase filter bank (PPFB, Finnish: *Monivaihesuodatinpankki*)

Every signal path records subbands statistics (SST) for all channels of the PPFB. A switch unit (Sel) can select which subband (PPFB channel) is used, thus defining the frequency of a given signal stream. There is a Sel unit for each beamlet, and whether a signal path is selected or not, defines the sub-arrays being used. Signals from different paths can be cross-correlated to form antenna covariance cubes (ACC) or cross-correlation statistics (XST).

A beamformer (BF) is used to apply phase-rotation to each selected channel and the result is passed around a ring-buffer to accumulate partial products and thus

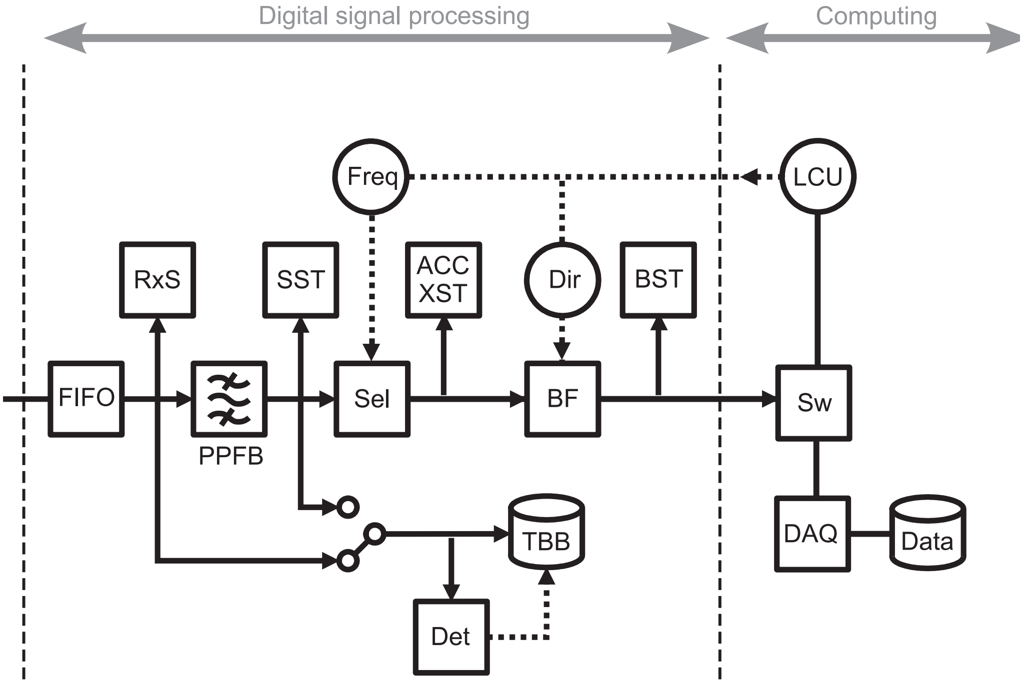

Figure E.54: Simplified schematic of the digital signal processing and computing. Refer to the text for the explanation of the components.

form the complete beamlet. Beamlet statistics (BST) are accumulated at this point. The output for the beamformers goes to a network switch (SW) via conventional Ethernet communications. Attached computers perform the data acquisition (DAQ) and storage to data disk. The local control unit (LCU) is a computer used for managing the configuration of the signal processing. In addition to general parameter setup, it provides control of the frequency channel selection (Freq) and beamformer direction control (Dir).

On a conventional LOFAR station, the network switch has an external connection for conveying data to the central processor of the LOFAR network. KAIRA does not have such a connection. Although there is limited-bandwidth Internet to the site, there is no high-speed link and the station can run sans-connection autonomously.

E.19 Site infrastructure

In addition to the KAIRA phased arrays and the RF-container for signal processing, there are a variety of other infrastructure on the site. An ex-VR railway carriage was converted into a site-office and a buried duct between the RF-container and the site office is used to provide it network and power. Two additional 20-ft shipping containers are used for storing surplus parts and site equipment. A perimeter fence is installed to keep reindeer away from the antennas and to delineate the site.

In addition to the mobile-broadband network connection, there is also the installation of optical fibre. This is connected around the northwest and north edges of the site and is buried into the ground. The fibre end terminates inside the RF-container. At the time of writing, there was no network termination equipment and the fibre remains unutilised.

E.20 Blizzard damage

On 8 March 2014 a blizzard swept through the Kilpisjärvi area. Estimates, based on the meteorological records from the top of Saana and in Kilpisjärvi village suggest that the wind speed was 38 ± 3 m/s. During the onslaught, one HBA tile (#H75) came loose and was ripped from its anchors. It was blown over the HBA array and then through the LBA array, damaging or destroying several LBA aerials. The LBA aerials were later repaired or replaced. One other HBA tile (#H65) was damaged, but was also later repaired. The dislodged tile #H75 was not replaced and was beyond any possibility for repair. Thus the KAIRA HBA array now only has 47 elements. `:-(`

Throughout this thesis, both 48 and 47 elements are mentioned, depending on the context and whether the full array was available at the time of the measurements. At the time of writing there are no plans to replace the missing tile.

Appendix F

Control and data systems

KAIRA control is provided by a single computer, referred to as the Local Control Unit (LCU). Software to control the digital signal processing (and hence control KAIRA) is provided using the standard software that was developed for the LOFAR project (Virtanen, 2012). These commands enable or set the different signal processing modes (such as the clock frequency or the number of bits; Section 2.5).

In addition to these provided tools, a complete suite of packages (the KAIRA Software, KSW) has been written to accommodate the following tasks.

- experiment scheduling and robotic observing tools
- site and electronics power and reset control
- data transport, archiving and indexing
- data reduction and processing
- automated monitoring, alerts and recovery
- computer system management utilities
- plotting utilities (incl. real-time displays)

With the exception of the KLP and KUG data acquisition software (discussed below), all KAIRA software was written by the author.

F.1 Control and scheduling

The initial stages of this project involved establishing the equipment and the technique. This includes the development of the necessary control programmes and facility software to ensure robust data acquisition in an autonomous observing mode. Additionally, the system must be calibrated and configured so that data integrity is assured. This work is an integral part of the project.

KBT (KAIRA Background Task) is a system for setting-up and running routine experiments. These are specified once using configuration and command files and then, once started, they will run autonomously. The KBT software manages data space and will create necessary directory structures to keep data and metadata organised. It will also restart the experiment in the event of failure. KBT produces observing logs to assist analysis of the data later. It also creates metadata, which is otherwise not present in the default LOFAR data products. These features of KBT allow long-term monitoring experiments to be established and run without ongoing effort.

Each experiment comprises a sequence of commands that start the observation from scratch, that check to ensure the system is running, that perform the recovery of the operation (in case the running script indicates failure), and the sequence that will terminate the experiment. An example KBT experiment is described in Appendix K.

F.2 Attenuation and 4-bit mode

KAIRA can transport data in 16-, 8- or 4-bit words, as described in Section 2.3. With 4-bit mode, it is possible to sample nearly the entire free spectrum range from LBA and HBA (although there are large areas of some bands which are unavailable due to RFI). Beamlets are not restricted to a single pointing direction, so the provision of addition beamlets through reduced numbers of bits gives additional flexibility in scheduling multiple-pointing experiments (such as multibeam riometry).

In Figure F.1 dark blue horizontal bands around 100 and 200 MHz are due to filter cut-off (see also Figure 2.7). The coloured vertical strips are (mostly) ionospheric scintillation. However, the pale blue band that runs from 50 to 70 MHz in Figure F.1 (left), is where the signal is being clipped due to a limited number of sampling bits, and thus insufficient dynamic range.

The saturation can be mitigated by selectively applying varying levels of attenuation. The system has the ability to apply up to 31-levels of attenuation in 0.25 dB steps. In Figure F.1 (right), full attenuation is applied to all LBA beamlets.

F.3 Data acquisition

KAIRA data is divided into statistics data (summary or averaged data from different stages of the signal chain) and high-speed data.

Statistics data products

Table F.1 gives an overview of the statistics data products that are available.

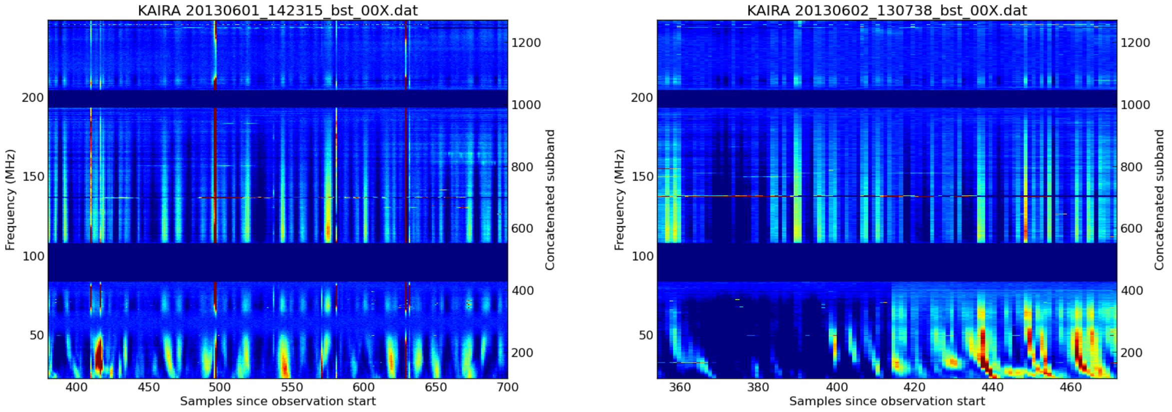

Figure F.1: KAIRA mode-357, 4-bit beam-formed observation of Cas A from 22 to 249 MHz. The left-hand plot has no attenuation and the right-hand plot has full attenuation on the LBA beamlets.

Data product	Abbrev.	Description
Subband statistics	SST	all 512 subbands, for each RCU min. 1 s integration
Beamlet statistics	BST	244, 488 or 976 beamlets, both polarisations min. 1 s integration
Array covariance cubes	ACC	antenna cross-correlations, steps through all 512 subbands, 1 s integration only
Cross-correlations	XST	antenna cross-correlations, single subband, 1 s integration only

Table F.1: Summary of standard LOFAR data products. It is not possible to record both ACC and XST files simultaneously.

The integration time for statistics data must be an integer number of seconds. The exception is the ACC data. These are matrices of signal covariances (cross-correlations) between each antenna. The data starts with subband 0 on the first integration, then proceeds to subband 1, 2, and so on. At the end of the 512 seconds, corresponding to subband 511, the file is written to disk (taking approximately 8 seconds to do so) and the process repeats.

As both ACC and XST data require the use of the station correlator, it is not possible to record both ACC and XST files simultaneously. All of these statistics data files are generated by the standard LOFAR software supplied with the station and specified in Virtanen (2012).

High-speed data acquisition

The LOFAR DSP electronics also capable of generating high-volume data products. These are the beamlet raw data streams and transient-buffer data. The beamlets from the signal processing are equally divided over four channels, each of which has its own 1 Gbit/s Ethernet network connection. These connections are additionally supported by a VLAN and each is referred to as a "lane". Each lane is a stream of UDP/IP packets, the format of which is described by Virtanen (2012). In a typical ILT station, these are sent to the central processor (CEP) in Groningen, The Netherlands. However for KAIRA these data streams are intercepted and stored/processed locally.

KUW

KUW (KAIRA UDP Writer) is a high-speed data recorder which can write either linear polarisation data or Stokes parameters. It restricts the number of samples by applying realtime averaging in frames of 16 samples. This reduces the maximum sampling rate, but it does result in more robust operation by easing disk access.

KUG

KUG (KAIRA UDP Get) is a local port of the `read_udp_gen2` software written by Olaf Wucknitz *et al.*. It is used for VLBI measurements.

KLP

KLP (KAIRA Local Pipeline) is a simple, high-performance data acquisition system written by Juha Vierinen *et al.*. This is used for high-speed scintillation observations and incoherent scatter radar experiments.

KSC

In addition to these data recorders, the KAIRA Software Correlator also makes use of the standard UDP/IP data stream. It is independent from the LOFAR station correlator and is described in detail in Appendix H.

Data rates

At the time of writing, KAIRA was running the `kbt3a_e` experiment as the default background task. This is an 8-bit experiment, permitting 488 beamlets. Table F.1 indicates the data products that are recorded as part of this current experiment. These comprise low-speed (statistics) and medium-speed (KUW) data. For occasional campaigns, high-speed data (KLP, KUG, etc.) is recorded. Examples include VLBI, MAARSY and EISCAT ISR campaigns.

The data rates that can be expected during routine operation are given in Table F.2. The KUW data rate is variable, but a cadence of ≈10 ms is typically used and the data rates for that are shown here:

Type	Files per day	Size per file	Daily total	Rate
BST	2	168652800	3.4 GB	3.9 kB/s
SST	96	353894400	34.0 GB	393.2 kB/s
XST	24	530841600	12.7 GB	147.5 kB/s
ACC	166	75497472	12.5 GB	145.2 kB/s

Table F.2: Statistics data rates for normal operation. Note that it is not possible to record ACC and XST files simultaneously.

ACC files are buffered, and there is an 8 s write time due to bandwidth limitations on the data disk, meaning that the data rate is slightly lower than the continuously written XST files.

In addition, there are a small number of daily log files. These are typically 3 MB per day. However, the data files generated by KUG and KLP have considerably higher data rates. These are given in Table F.3.

Note that it is not possible to record KUG/KLP/KUW data simultaneously on a given lane. To run either VLBI with KUG or radar echoes with KLP, it is necessary to terminate the KUW acquisition.

Type	Files	Individual rate	Total rate
KUW	4	0.2	0.8
KUG	4	96 MB/s	383 MB/s
KLP	≈244/s	90 MB/s	380 MB/s

Table F.3: Data rates for high-speed operation. The data rates for KUW data are those typically used (resulting in 100 Hz sampling).

Table F.3 assumes that all four signal processing lanes are being recorded. The reason why KLP has slightly lower data rates, is that it does not record packet header information. The difference in file numbers is because KUG records one monolithic file per lane, which continues to grow as acquisition continues. In contrast, KLP records ≈30 files per second per polarisation per beamlet.

The numbers given are the maximum rates for high-speed data acquisition. In some cases, a reduced number of beamlets are recorded.

Meta data

As there are no meta data associated with LOFAR BST files, KAIRA uses the automatic observing system (KBT) which records the additional data in ancillary files. Additionally, naming conventions assist in data curation. For example, KAIRA observations typically use the convention “a” for 8-bit and “b” for 4-bit after the RCU number. For example: `cal6a_tsys` is an 8-bit, RCU mode 6 experiment. However, this is not a hard rule and there are no checks in the case of error or mis-naming.

Appendix G

Software packages

In addition to the low-level driver software in the LOFAR system, and the standard LOFAR access utilities for telescope control, a large number of software packages were written specifically for this project. These are listed here.

G.1 KAIRA software

KAS	KAIRA All-Sky imager — metascript for KPM and KPX.
KAW	KAIRA Aurora Warning[1]
KBT	KAIRA Background Task — Primary autonomous control software
KCB	KAIRA Cut BST — splits BST files[1]
KCD	KAIRA Change Directory — software development tool
KCM	KAIRA Create Manuals and Documentation
KCR	KAIRA Cut RCU-set — split RCU spectrum data[1]
KCS	KAIRA Cut SST — split subband statistics data
KCT	KAIRA Cron Tasks — meta-management of automated scripts
KCX	KAIRA Cut XST — splits XST data files
KDA	KAIRA Data Archiver — automatically retrieves data products
KDC	KAIRA Data Coverage — tracks the amount of successful observing
KDD	KAIRA Desktop Display — public relations/outreach display software
KDF	KAIRA Disk Free — Data storage management
KDI	KAIRA Data Index — Create an index of KAIRA data[1]
KDK	KAIRA After Dark — public relations/outreach display software
KDT	KAIRA Data Transfer — automatically move data off-site
KDV	KAIRA Data VLBI transfer — transfer data from archive to the MPIfR correlator
KDX	KAIRA Data eXternal — automatically backup data to external USB disks
KDZ	KAIRA Data Zstd-compression — compress data data storage/transport
KEA	KAIRA E-mail Alert — automatic notification of system failure
KEB	KAIRA Extract Beamlet statistics — extract numeric data from a BST file

KEU	KAIRA Extract UDP-data — extract numeric data from KUW files
KFD	KAIRA Find Data — data search function for the KAIRA data archive
KHR	KAIRA Horizon RFI — generate azimuthal radio-interference plots
KIR	KAIRA IVO reset — power reset software for recovering from failures
KJB	KAIRA Join BST — re-join BST fragments into a single file[1]
KJS	KAIRA Join SST — re-join SST fragments into a single file[1]
KKP	KAIRA K_P Index — automatically recover the K_P (planetary) index
KLC	KAIRA Local pipeline Correlator — software cross-correlator for KLP files
KLK	KAIRA Local Kombiner — real-time combiner for meteor radar observations[1]
KLN	KAIRA Link — symbolic link software development tool
KLP	KAIRA Local Pipeline — high-speed data recorder[2]
KLS	KAIRA List — lists files but also displays UTC metadata
KMA	KAIRA Monitor All — meta-monitoring programme[1]
KMB	KAIRA Monitor Beamlet-statistics — realtime display of beamlet data
KMD	KAIRA Monitor-Data distributor
KME	KAIRA Monitor web E-mail
KMH	KAIRA Monitor Host — monitors computer systems
KML	KAIRA Monitor Logfiles
KMP	KAIRA Median Power — used for beamformed riometry experiments
KMS	KAIRA Monitor Subband-statistics — realtime display of subband spectra
KMT	KAIRA Monitoring Task — meta-script for handling monitoring tasks
KMX	KAIRA Monitor XST — realtime display of correlated data (XST or ACC)
KPA	KAIRA Plot ACC — (obsolete, replaced with KPX)
KPB	KAIRA Plot Beamlet statistics — plotting utility
KPC	KAIRA Pointing Catalogue
KPD	KAIRA Plot Data — array plotting utility
KPF	KAIRA Plot Frame — plotting utility for individual XST frames
KPK	KAIRA Plot KUW — plotting utility for high-speed KUW data
KPR	KAIRA Plot RCU spectra — plotting utility, especially for RFI monitoring
KPS	KAIRA Plot SST — plotting utility for subband statistics spectra
KPW	KAIRA Plot beamlet Waterfall — frequency-corrected beamlet statistics data
KPX	KAIRA Plot Cross-correlation images — all-sky imaging using ACC or XST files
KQD	KAIRA Quick DIsplay — experimental plotting software
KRA	KAIRA Rsync Alert — monitors presence rsync data transfers
KRM	KAIRA ReMove surplus files — deletes redundant and partial-product files
KRS	KAIRA Real-time Status — (obsolete, replaced with KEA, etc.)
KSB	KAIRA Subband frequency-wavelength — unit/channel converter utility
KSC	KAIRA Software Correlator — see Appendix H

KSI	KAIRA Stellarium Image — public outreach display[1]
KSL	KAIRA Status Label generator — used for online status displays
KSR	KAIRA Computer Reset — automatic computer reset for robotic operation[1]
KSS	KAIRA System Status — monitors KAIRA basic status parameters
KST	KAIRA Software Test — development unit test tool
KSV	KAIRA Software Versions — lists installed packages, version & creation dates
KSW	KAIRA Software — master package for KAIRA software setup
KTD	KAIRA Test Data — sample data for unit testing
KTT	KAIRA Test Timestamps — data integrity checking
KUG	KAIRA UDP Generator — VLBI recording software[3]
KUT	KAIRA Up-Time — observing statistics[1]
KUW	KAIRA UDP Writer — high-speed data recorder
KWG	KAIRA Web Get — Internet-based transfer system
KWM	KAIRA Web Mail — e-mail alert distribution system
KWP	KAIRA Web Put — Internet-based transfer system
KWS	KAIRA Web Services — Internet-based transfer system[1]
KWT	KAIRA Web Transfer — Internet-based transfer system

[1] Not yet complete at time of writing
[2] Written by Juha Vierinen, *et al.*
[3] Written by Olaf Wucknitz

G.2 Interferometric riometry

In addition to the generic KAIRA observing software, the following software packages were developed for the interferometric riometry work that was carried out for this thesis.

cccp	Cas A, Cyg A Convolution Pattern experimental scintillation removal software
ltss	Long-Term Scintillation Statistics, initially used for scintillation deconvolution later used as statistics software in its own right
mirk	Meridional Interferometric Riometry Keograms (e.g. Figure 4.2; Figure 6.3; Paper IV, etc.)
oera	Optical Emission / Radio Absorption comparison software (e.g. Figure 5.5, etc.)
orka	Optical & Riometry Keogram Automation (Paper IV)
sfir	Single-Frequency Interferometric Riometry (e.g. Figure 5.2; Paper II, etc.)
sras	Seasonal Radio Absorption Statistics

Appendix H

Multi-frequency software correlator

There is a correlator built into the digital signal processing of each LOFAR station. This "station correlator" has a fixed integration time of 1 second and operates in a single subband (de Vos et al., 2009). There are 512 subbands across 100 MHz (assuming the 200 MHz sampler clock) of sampling space, giving each subband a bandwidth of approximately 195 kHz. The station correlator can be set to either repeatedly observe a single subband (generating a so-called XST file), or to step through each subband sequentially (generating what is known as an antenna covariance cube, ACC, file), as described in Appendix F.3.

Although it is not readily possible to alter the configuration of the station correlator beyond these two modes, it is possible to develop a separate software correlator which makes use of the raw data products from the beamformers. The KAIRA Software Correlator (KSC) has been written in such a way that interferometric antenna pairs for multiple frequencies could be correlated simultaneously and that the integration time could be set to any arbitrary duration.

The software correlator method assigns beamlets to individual antennas, rather than to the entire array (as in a conventional experiment) or a large sub-array (such as that used for "Mode-357", Section 2.6). Conceptually, each beamlet is a single-antenna sub-array.

In the case of regular beamforming, each antenna filters and digitises its signal with the Receiver Unit (RCU) and then divides that signal with a Polyphase Filter Bank (PPFB) into frequency channels (subbands). Each beamformer (BF) takes a set of these subband outputs for a set of antennas, applies digital phase rotation and adds the resultant products to generate the beam-formed beamlet output. This is shown in Figure H.1.

However, in the software correlator case, each beamlet makes use of only a single antenna. There is no digital phase rotation applied (i.e. the pointing direction is zenith) and the outputs from beamlets with identical subbands can then be correlated, as illustrated in Figure H.2.

The KSC receives beamlet UDP/IP packets and correlates those beamlets which

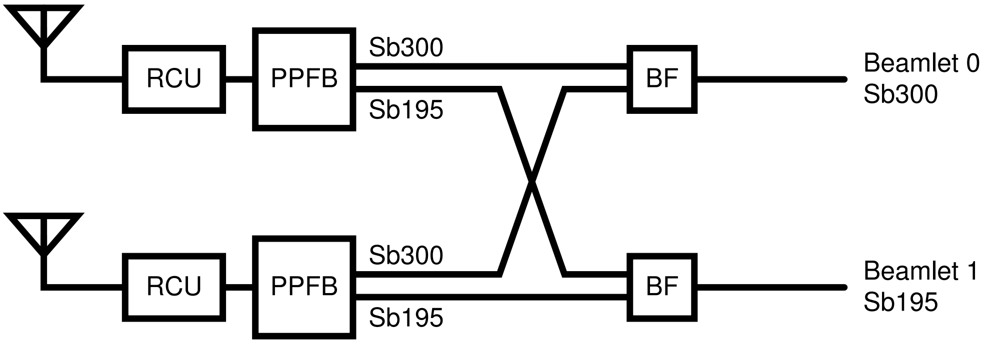

Figure H.1: A reduced example, showing how conventional beamforming functions for a couple of subbands (in this case Sb195 and Sb300). Each beamformer (BF) takes the Polyphase Filterbank (PPFB) output for a given subband from all available antennas. The beamlet outputs are directional and with a full-array beam pattern. (Compare with Figure H.2.)

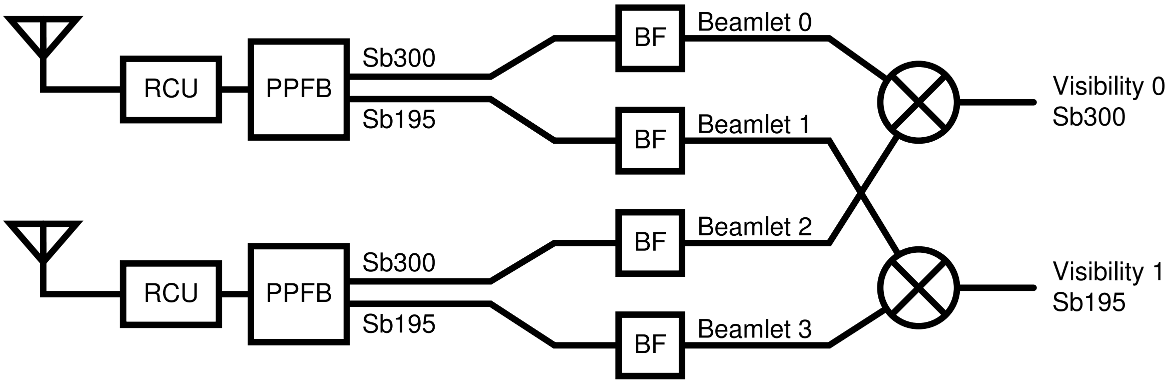

Figure H.2: A reduced example showing the multi-frequency software correlator configuration for a couple of subbands (Sb195 and Sb300). Each beamlet is a single antenna, single subband. See the text for a full explanation.

are using the same subband. As the assignment of antenna sets and subbands to beamlets is arbitrary, it is possible to arrange beamlets for sets of antennas and subbands, correlate those of similar subband, and thus form uv-data sets for different frequencies simultaneously. A further advantage of this method, is that the cadence can be set arbitrarily low, allowing faster imaging that normally possible with the station correlator.

Capacity

The typical data transport mode for software correlation is 8-bit mode (Section 2.3) as this gives the greatest number of beamlets without any saturation clipping that is present in 4-bit mode. In 8-bit mode, a total of 488 beamlets are available. As there are 48 LBA aerials, this makes it straight forward to produce 10 full-array all-sky images at different subbands (as shown in Section 2.6. In principle, the same technique can be used for the HBA array, however, the beamforming of the individual tiles means that either reducing the number of cells in use by each tile is required, or a restricted field of view will be obtained.

In addition to using 4-bit mode (resulting in 20 all-sky images), the other way to improve the number of frequencies that can be imaged is by reducing the number of antennas.

As beamlets can be selectively selectively assigned antennas and subbands, it is possible to use different sets of antennas for each frequency. Thus baselines can be selected to match the frequency (and hence beam shape), or to match the frequency sensitivity (the LBA antennas and amplifiers have a better response at 50–60 MHz, (c.f. KAIRA spectral bandpass, Figure 2.7).

The LBA array layout has redundant baselines (e.g. the baseline #L00 to #L01 is the same baseline as #L05 to #L06). Removal of certain antennas, especially in the centre of the array, has negligible impact on the overall beam pattern.

For example, by reducing the number of LBA aerials from 48 to 40, the number of subbands that can be simultaneously imaged increases from 10 to 12. The overall loss of sensitivity of the array is 1.5 dB, which is not significant when observing bright sources (such as Cas A or the Galactic synchrotron background).

By carefully choosing the LBA aerials to remove, the affect on the sidelobe pattern can also be reduced. In one test case, LBA aerials #L01, 03, 04, 06, 14, 20, 22, 24 were omitted. The relative sidelobe pattern only rose by 0.3 dB, with the additional spurious power increase being diverted into previous nulls in the beampattern. The full- and reduced-array beam patterns are compared in Figure H.3.

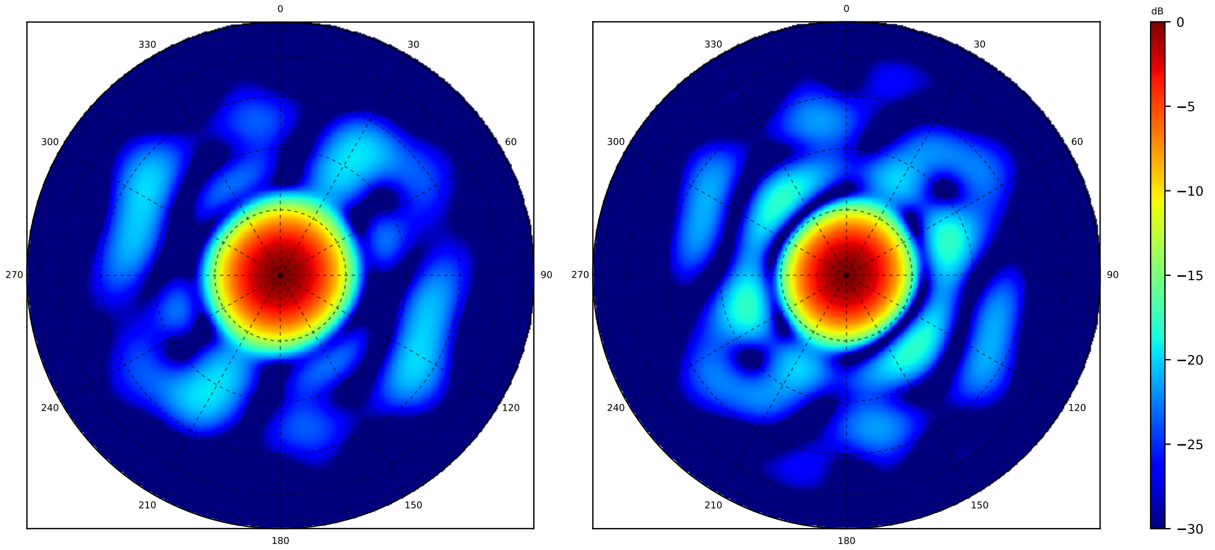

Figure H.3: The KAIRA LBA array zenith point-spread function. Left: full array of 48 LBA aerials. Right: reduced array with only 40 LBA aerials (#L01,03,04,06,14,20,22,24 removed).

Sample results for the multi-frequency software correlator have already been presented in Section 2.6 and limitations of the technique were discussed in Section 4.3.

Appendix J

Calibration and commissioning

Quality control procedures were carefully followed during the construction of KAIRA, with error budgets being defined and then strictly adhered to. This made the calibration process straight-forward and there were no problems with inability to acquire fringes or unexpectedly low signal gains. Positional accuracy of all antennas was also carefully surveyed, which allowed successful first-light observations.

Addition calibration of KAIRA requires the calculation of a direction-independent complex-valued gain for each signal path, a direction dependent gain toward each calibration source, and a noise covariance matrix that includes compensation for short baselines ($<$4 wavelengths), where antenna-antenna coupling is non-negligible (Wijnholds et al., 2011).

The procedures for complex gain and delay calibration made use of the standard LOFAR procedures, which had been independently verified (Wijnholds and van Cappellen, 2011). The area where KAIRA calibration exceeded this was in the sensitivity calculations, which required additional attention as a result of strong ionospheric scintillation and abnormal system configuration.

J.1 Sensitivity calibration

Although some studies (e.g. riometry), rely only on relative power measurements, other experiment types require some degree of absolute calibration in order to place limits on the physical conditions being observed. The conventional way to do this is to determine the System Equivalent Flux Density (SEFD), which is a measure of the system's contribution to the detected power. Unlike LOFAR, which has a network of linked radio telescopes, KAIRA is isolated and therefore must self-determine the calibration. Additionally, as a LOFAR-based system, KAIRA does not have any noise diode or any other internal calibration mechanism. In order to determine the system sensitivity, it is necessary to perform controlled observations on external sources.

The SEFD is established by considering a source of flux S_{src}. The ratio between the on- and off-source measured power, P_{on} and P_{off}, is equal to a comparable ratio in flux of the source plus instrument, to that of the instrument alone. It is expressed as follows:

$$\frac{S_{\text{src}} + \text{SEFD}}{\text{SEFD}} = \frac{P_{\text{on}}}{P_{\text{off}}} \tag{J.1}$$

This can be re-formulated as

$$\text{SEFD} = \frac{S_{\text{src}} P_{\text{off}}}{(P_{\text{on}} - P_{\text{off}})} \tag{J.2}$$

To calculate SEFD, the median of the "on-source" and "off-source" data for each beamlet is taken, as measured in the beamlet statistics (BST) files. These data are in ADUs — the raw counts from the digital signal processing chain — linearly equivalent to power. Determination of P_{off} is complicated by the fact that the sky background a haze of Galactic synchrotron emission (as seen in Figure 4.1, page 34).

The nominal flux of the "on-source" is calculated based on parametric models of the bright radio sources Cas A and Cyg A (Baars et al., 1977). As Cas A is a slowly fading supernova remnant, additional corrections for this flux decay are used (Helmboldt and Kassim, 2009). Details of the method used at KAIRA are described in Appendix J.4, below. Once the SEFD is known, the reverse formulation can be applied:

$$S_{\text{src}} = \text{SEFD}\,(\frac{P_{\text{on}}}{P_{\text{off}}} - 1) \tag{J.3}$$

J.2 T_{sys} determination

The alternative formulation for expressing the sensitivity of a radio telescope is a system-equivalent temperature, which is the equivalent black-body temperature (Rayleigh-Jeans limit). In a similar manner to the power calculations in the previous section, an astronomical source is used with noise temperature, T_{src}. This could be determined by measuring the brightness and noise temperatures, on-source and off-source, as

$$T_{\text{src}} = T_{\text{on}} - T_{\text{off}} \tag{J.4}$$

where T_{on} is the temperature when the telescope is pointing "on source" and T_{off} is when it is pointing elsewhere: the "off source" temperature, including contributions from the sky, antenna, electronics, etc.. For the measurement of a source of temperature T_{src}, the signal-to-noise ratio, SNR, is related to the ratio of the temperatures.

$$\text{SNR} = T_{\text{src}} / T_{\text{sys}} \tag{J.5}$$

The measurement that is made by the system is power, P, which is proportional to the square of the measured voltage, V^2. This has an associated coherence time, τ_{c}:

$$\tau_{\text{c}} \approx 1/\Delta\nu \tag{J.6}$$

where $\Delta\nu$ is the bandwidth. This coherence time places a limit on the number of independent power measurements, N, related by:

$$N = t/\tau_{\mathsf{c}} = \tau\Delta\nu \tag{J.7}$$

Because SNR improves as the square root of the number of independent measurements, we can modify Equation J.5 to:

$$\mathsf{SNR} \ = \ \frac{T_{\mathsf{src}}}{\sqrt{N}\,T_{\mathsf{sys}}} \ = \ \frac{T_{\mathsf{src}}\sqrt{\tau\Delta\nu}}{T_{\mathsf{sys}}} \tag{J.8}$$

Consider now an astronomical source that wholly fits within the primary beam of the telescope of flux density S_{src}. The radiation of this source is assumed to be unpolarised. Because KAIRA has linearly polarised antennas, this means the received power, P, on only one polarised element will be half of the total and is thus given as:

$$P_{\mathsf{src}} = \frac{S_{\mathsf{src}}A_{\mathsf{eff}}\Delta\nu}{2} \tag{J.9}$$

where A_{eff} is the effective telescope area and $\Delta\nu$ is the bandwidth. The power is related to the noise temperature, T, by:

$$P = kT\Delta\nu \tag{J.10}$$

where k is Boltzmann's constant ($k \approx 1.38 \times 10^{-23}$ J.K^{-1}). Combining Equations J.9 and J.10 gives:

$$k\,T_{\mathsf{src}}\Delta\nu = \frac{S_{\mathsf{src}}A_{\mathsf{eff}}\Delta\nu}{2} \tag{J.11}$$

$$T_{\mathsf{src}} = \frac{S_{\mathsf{src}}A_{\mathsf{eff}}}{2k} \tag{J.12}$$

This can then be incorporated into Equation J.8 to give:

$$\mathsf{SNR} = \frac{S_{\mathsf{src}}A_{\mathsf{eff}}\sqrt{\tau\Delta\nu}}{2kT_{\mathsf{sys}}} \tag{J.13}$$

A signal-to-noise ratio using bright astronomical sources can now be measured. Here the SNR is given by:

$$\mathsf{SNR} = \frac{P_{\mathsf{src}}}{P_{\mathsf{sys}}} = \frac{P_{\mathsf{on}} - P_{\mathsf{off}}}{P_{\mathsf{off}}} \tag{J.14}$$

This can be combined with Equation J.13 to give:

$$\frac{P_{\mathsf{on}} - P_{\mathsf{off}}}{P_{\mathsf{off}}} = \frac{S_{\mathsf{src}}A_{\mathsf{eff}}\sqrt{\tau\Delta\nu}}{2kT_{\mathsf{sys}}} \tag{J.15}$$

$$T_{\mathsf{sys}} = \frac{S_{\mathsf{src}}A_{\mathsf{eff}}\sqrt{\tau\Delta\nu}}{2k}\frac{P_{\mathsf{off}}}{(P_{\mathsf{on}} - P_{\mathsf{off}})} \tag{J.16}$$

which relates the system temperature, T_{sys} in terms of either constants, measured- or known-quantities, with the exception of the antenna efficiency, A_{eff}.

J.3 Antenna efficiency

Antenna efficiencies for individual LOFAR elements have been reported by Nijboer et al. (2009), stating a generic formula for a dipole effective area as:

$$A_{\text{eff}} = \lambda^2/\Omega_e \tag{J.17}$$

where λ is the observed wavelength and Ω_e is the effective solid angle covered by the antenna beam. Nijboer et al. (2009) reports that for an isotropic beam pattern, $\Omega_e = 2\pi$; for an isolated dipole, $\Omega_e \approx 3$; and for a dipole in a half-wavelength spaced dense array, $\Omega_e \approx 4$. Response inhibition due to the presence of neighbouring elements can therefore be approximated by:

$$A_{\text{eff,elt}} = \text{min}\{\frac{\lambda^2}{3}, \frac{\pi d^2}{4}\} \tag{J.18}$$

from which the lower bound of the effective area of the station can be approximated by summing the effective areas of the individual elements as:

$$A_{\text{eff,stn}} = \sum_{i=1}^{n_{\text{elts}}} A_{\text{eff,elt},i} \tag{J.19}$$

LBA array area

Some sample antenna layouts are given in Figure J.1. Each layout shows circles of equivalent A_{eff} plotted at the physical location of the element itself. At lower frequencies, “clustering” of the array elements limits the effective area.

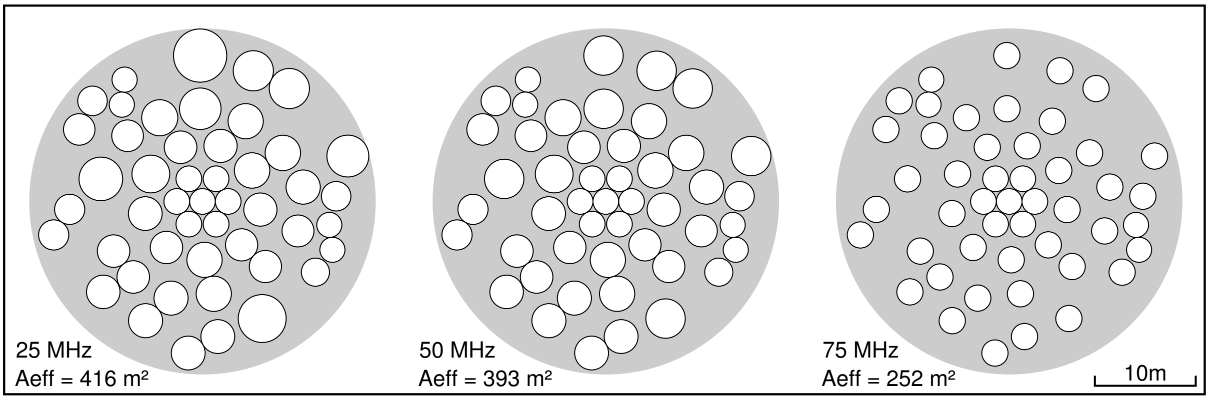

Figure J.1: Effective areas of the KAIRA antennas on the field layout. Relative positions and areas are to scale.

Figure J.2 shows the calculated $A_{\text{eff,stn}}$ for the KAIRA LBA array. KAIRA has a slightly better response than LOFAR core-, or remote-inner-, stations because it has 48, not 46 LBAs in the field. Note also that the inner antennas do not contribute additional area proportional to their number as a result of the packing. In future array design, these could be omitted (or re-positioned) without significant loss of sensitivity at lower frequencies.

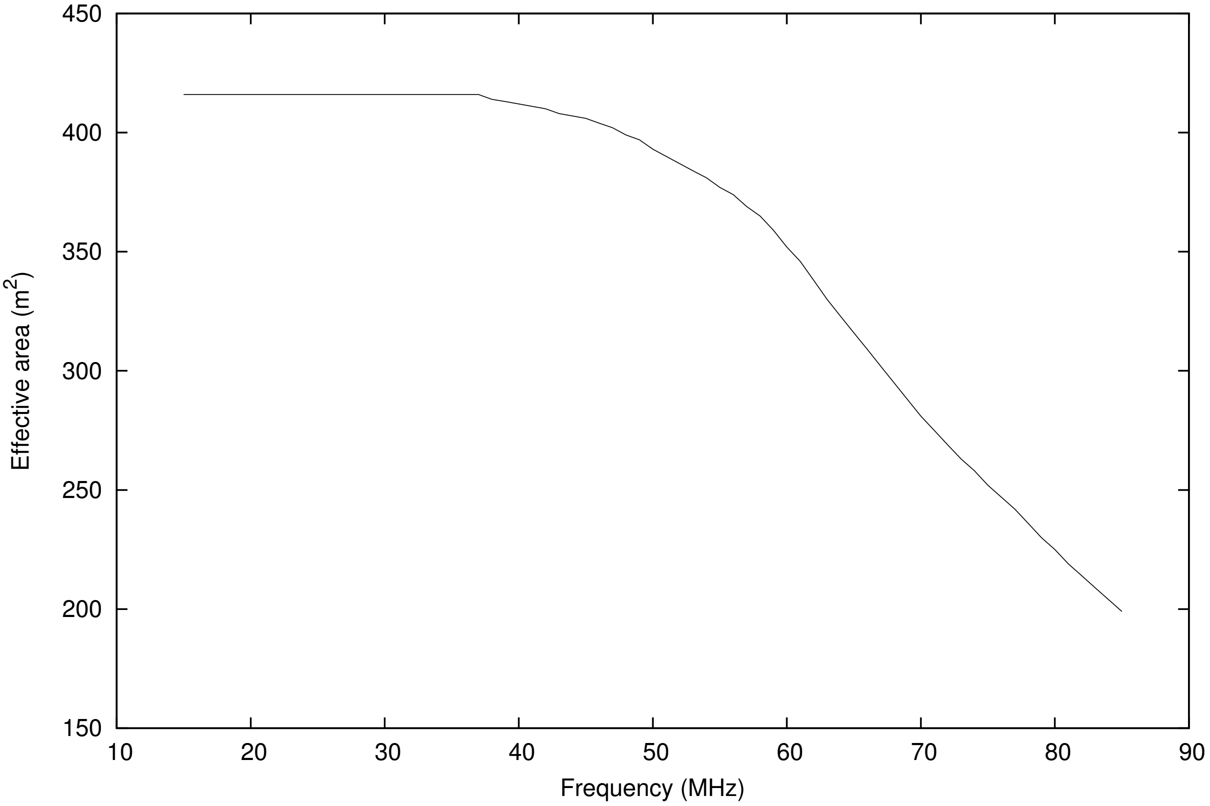

Figure J.2: Approximate KAIRA LBA array area, based on the field layout and Equation J.18.

HBA array area

At high frequencies, the bow-tie antennas inside each HBA tile act as isolated antennas. At the low-end, the effective area is the tile area divided by the number of cells in each tile 16, which is ≈1.56. The overlap range where there is a transition between the two regimes is not exact, but the difference is small and may be neglected.

$$A_{\text{eff,elt}} = \text{min}\{\frac{\lambda^2}{3}, \frac{25}{16}\} \tag{J.20}$$

The effective area of the HBA array as a function of frequency is shown in Figure J.3.

J.4 SEFD calculation

In the experiments made for the SEFD calculations for Paper I, both Cas A and Cyg A measurements were employed. A variety of carefully-chosen “off-source” directions were used to ensure that no additional effects were introduced via beam-patterns, source elevations, etc..

The details in the previous sections assume a zenith position. As the zenith angle increases, there is a degradation in the sensitivity, as well as a distortion to the beam pattern. This is caused by factors such as the reduced gain of individual

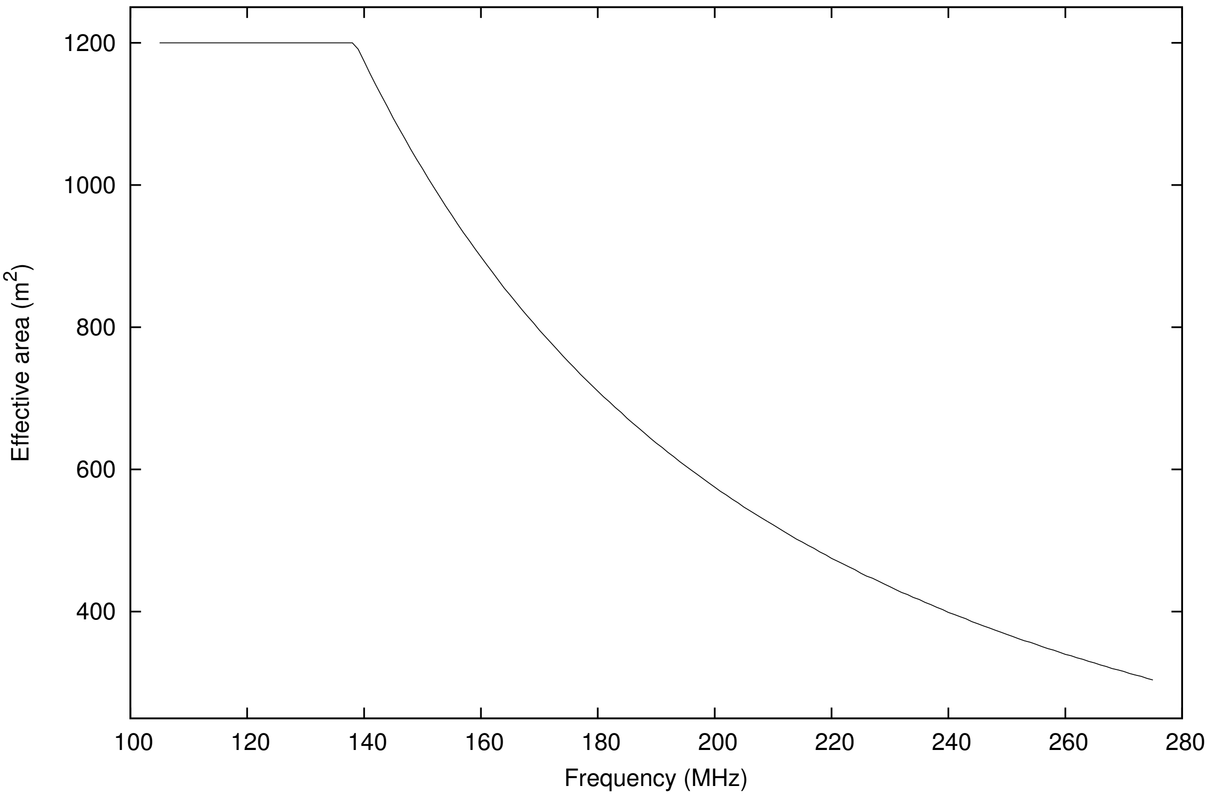

Figure J.3: Approximate KAIRA HBA array area, based on the effective area of an individual elements determined using Equation J.20.

dipoles, the reduced $A_{\text{eff,elt}}$ due to projected coupling, and the longer path-lengths through the ionosphere.

Sky noise

The sky brightness temperature is dominated by the Galactic synchrotron radiation, which has a strong dependency on wavelength (de Oliveira-Costa et al., 2008; Guzmán et al., 2011).

$$T_{\text{sky}} = T_{\text{s0}} \lambda^{2.55} \tag{J.21}$$

where $T_{\text{s0}} = 60 \pm 20$K, for Galactic latitudes $10 < b < 90^\circ$ (Nijboer et al., 2009).

Beamsize considerations

Because KAIRA has low resolution, the target sources are much less than the beamsize. Therefore Equation J.16 does not hold directly. Instead, the more complex case of:

$$T_{\text{src}} + T_{\text{sky}} = T_{\text{on}} - T_{\text{off}} \tag{J.22}$$

must be used.

J.5 Sensitivity experiment

In order to carry out a T_{sys} or SEFD calibration, a number of considerations need to be made to accommodate various limiting factors. These are:

Scintillation
Observations on/off source must last at least 30 minutes in order to average out the effects of ionospheric scintillation.

Frequency coverage
There needs to be a larger selection of frequencies used in order to obtain better coverage of the spectrum

Galactic latitude
The on/off source positions need to account for galactic emission. This presents a problem when analysing the data using Cas A, Cyg A or Tau A as both these sources lie in the Galactic plane, where background emission is very high.

Array projection
The beam locations must allow for the projection of the array, namely the foreshortening effect that ensues when the beam direction is off-zenith.

Array symmetry
Although the LBA array is roughly symmetric, the HBA array is not and the azimuth will play a critical role.

Source selection

Cas A and Cyg A are sufficiently bright and rise high in the sky. Vir A is detectable, but only reaches an elevation of $e = 32°$ at transit and has low brightness compared to the surrounding Galactic synchrotron background. Cas A and Cyg A fluxes are known from Baars et al. (1977). Because Cas A is a relatively young supernova remnant, its flux decays with time. Helmboldt and Kassim (2009) indicate that Cas A is exhibiting a flux decrease of 0.7–0.8% yr^{-1}, which is also taken into account. Cyg A is a radio galaxy that does not exhibit variations in flux, making it possible to use the Baars parametric model directly.

Observation technique

Cas A and Cyg A were observed for durations of approximately 1 hour. This time was chosen so that ionospheric scintillation would be smoothed out. These are the “on-source” observations. Additionally, areas of “blank-sky” were observed at similar times. The four source beams were pointing at:

- Cas A (beamlets 0:121)

- Cyg A (beamlets 122:243)
- Cas*A (beamlets 244:365)
- Cyg*A (beamlets 366:487)

where Cas*A is the equivalent azimuthal beam conjugate of Cas A. Mathematically, if Cas A is at geodetic coordinates (Az,El), then Cas*A is the point with geodetic coordinates (Az+180°,El). The motivation for this configuration was to provide uv-symmetry, thus resulting in equivalent beam patterns. The azimuthally-symmetric equivalent position ensures that the beam pattern of the array was the same as the equivalent "on-source" observations.

The beam conjugate point is not fixed on the celestial sphere (and thus the galactic sphere), and therefore will record different backgrounds from the galactic synchrotron emission. This is beneficial as it will show the variance that can arise from a non-accurate background measurement.

Additionally, the beam-shape will also vary as a function of time, due to both projected array rotation and different foreshortening effects due to the projection with respect to different zenith angles.

Observations of the North Celestial Pole (NCP) are interleaved in the measurements. The NCP is well off the Galactic Plane (at $\ell =$122.9°, $b =$27.1°) and is always at fixed zenith angle ($Z =$20.9°).

The measurements were made using 8-bit mode, with a distribution of subbands for each beam. This results in good spectral coverage of the band for each source.

From the data, we take the median of the "on-source" and "off-source" data for each beamlet in ADUs. These are used with Equation J.2 to derive the SEFD. The results of this SEFD calibration are reported in Paper I (Figure 11)

Appendix K

Background task experiment

KAIRA experiments are run autonomously using the KBT control software (described in Appendix F.1). This appendix describes the multi-faceted experiment that is running at the time of writing. It was first run on 16 January 2015, with the current version of it starting on 29 April 2016. Different versions have corrected errors or improved checking and efficiency, but the basic experiment design remains the same. This is important for continuity of data and to make processing easier.

K.1 Experiment kbt3a_e

The `kbt3a_e` experiment is based solely on the LBA array, operating in RCU mode 3 and using the 200 MHz sampler clock. It comprises a number of beams for carrying out multi-frequency riometry. These beams have been arranged to provide a distribution of pointing directions at several different elevations, so that multi-frequency measurement of absorption spatial evolution can be made.

Experiment `kbt3a_e` includes the recording of all subbands statistics (SST) and beamlet statistics (BST) products with 1-second integration times. The KAIRA station correlator is configured to record antenna cross-correlation statistics (XST) for subband 195 (38.1 MHz). These cross-correlations are used for riometric imaging, such as shown in Papers II and III. The XST data are also used to produce routine riometric keograms as part of the KAIRA online monitoring, and as a summary index for the data archive (Paper IV).

High-speed data recording is also enabled for the `kbt3a_e` experiment, recording Stokes parameters for all beamlets at $\approx$100 Hz cadence.

Position selection

Figure K.1 shows the distribution of beams on the sky. The position of each beam is only marked as a dot; the size of the beam is frequency dependent and as most beams have multiple frequencies, there is a variation in size for each (see also Paper I, Figure 8).

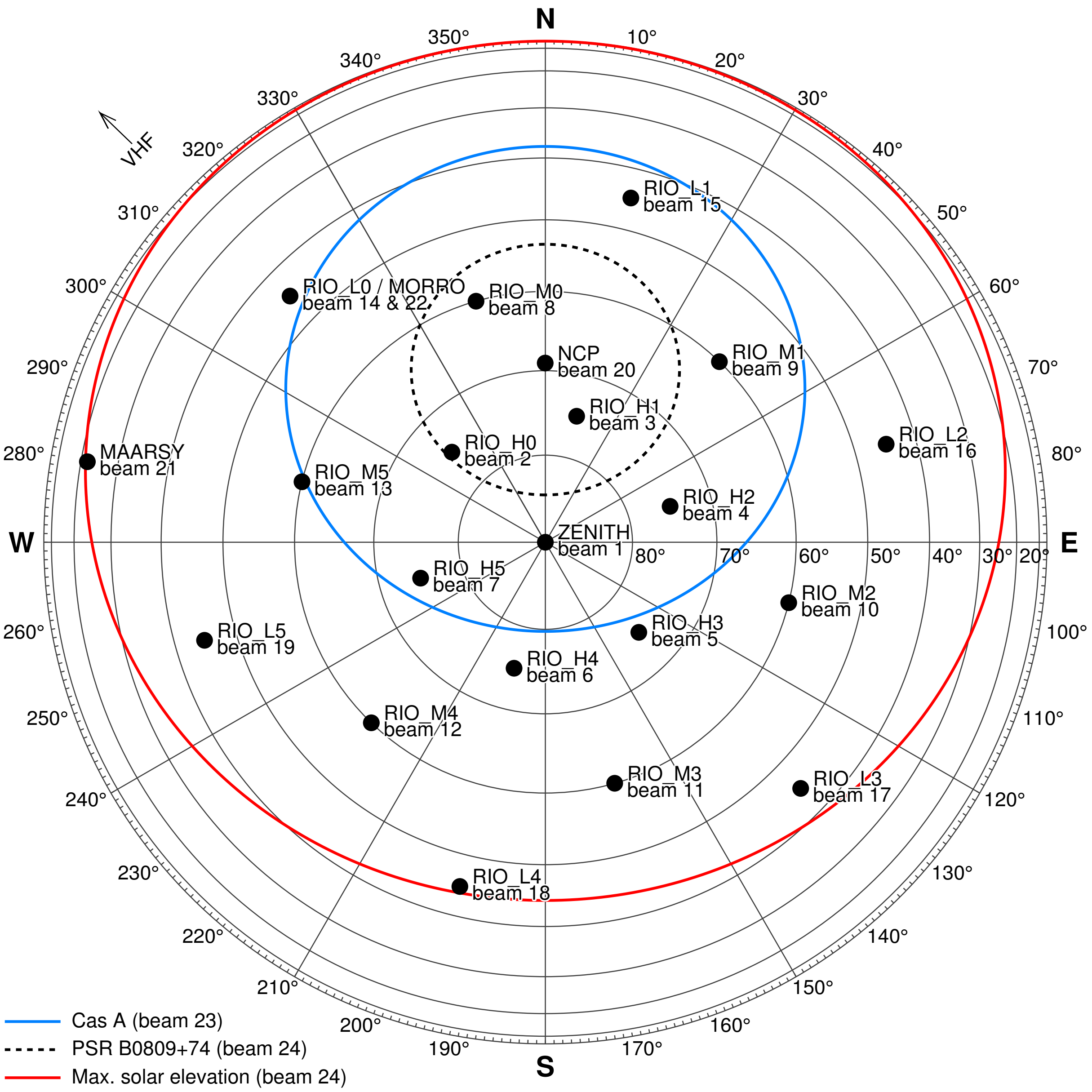

Figure K.1: Top-down view of the beam positions of experiment `kbt3a_e` in orthographic projection.

Most of the beams are at fixed azimuth and elevation. However, there are a number of tracking beams, which have been marked as the path taken during a full sidereal day.

Beam 24 is a switching beam. When the sun is above the horizon, KBT tracks it with beam 24. When no, then KBT switches to tracking the circumpolar pulsar PSR B0809+74. The solar declination varies throughout the year, and in Figure K.1, only the track of the Summer Solstice (i.e. maximum declination) is shown.

The final beamlet (487) is not beamformed. Instead, this beamlet processes a single antenna (#L00) for Subband 195 (38.1 MHz). This is an all-sky monitor. However, although the subbands statistics are recorded from all antennas at 1-second cadence, the use of a beamlet for monitoring one subband from one antenna means that high-speed KUW data can also be recorded for it. This final beamlet, therefore, provides a high-speed, all-sky monitor. It is used to supplement the station correlator measurements and to provide a high-speed monitor for RFI.

Beamlet allocation

Each beamlet is a subband-pointing-direction combination (see also Section 2.3, page 12). In most cases, multiple beamlets are allocated to a single pointing direction, to provide the necessary multi-subband, and thus multi-frequency, capability. As `kbt3a_e` is an 8-bit experiment, the maximum number of beamlets is 488. The allocation of these 488 beamlets for this experiment are shown in Table K.1.

Subband selection

The subbands allocated to each beamlet is arbitrary, but to ease the data analysis task, a few specific sets of subbands were chosen for experiment `kbt3a_e`. The main riometry beams: zenith, North Celestial Pole (NCP) and beam L0, each have 32 subbands. Zenith is given priority as this represents the geographic point measurement and is the most sensitive due to the beampattern and thinness of the ionospheric screen overhead. The NCP is also high-priority, as it is a relatively faint area of the sky (in terms of Galactic synchrotron emission) and it is a stationary point in both Galactic, celestial and topocentric reference frames. This makes it suitable for calibration and system performance determination (see Appendix J.5). Riometry beam L0 is the position directly above the EISCAT VHF transmitter at the altitude of the D region. It is selected for use in conjunction with EISCAT experiments and for providing supplementary data in case interesting phenomena are serendipitously observed over the EISCAT site.

A number of other riometry beams are included for general all-sky coverage. These are allocated the same 11 subbands each. These subbands are a sub-set of the 32 used for the main riometry beams.

The two tracking beams are for scintillation statistics measured against Cas A and for observing the Sun (when above the horizon) or a reference pulsar (when the Sun has set). These tracking beams have 99 subbands in total.

The subband numbers for the 11-, 32- and 99-subband sets are given in Table K.2.

Also included are two beams that point at the D region over nearby radars: MAARSY (Andenes) and MORRO (Ramfjordmoen). The subbands used are specifically to match the transmitter frequencies of those systems. The intention is to use them for routine monitoring of meteor statistics. At the time of writing, only the MAARSY system has been tested for such purposes (Chau et al., 2018).

Beam	From	To	Number	Description
1	0	31	32	Zenith riometry beam
2	32	42	11	Riometry beam H0
3	43	53	11	Riometry beam H1
4	54	64	11	Riometry beam H2
5	65	75	11	Riometry beam H3
6	76	86	11	Riometry beam H4
7	87	97	11	Riometry beam H5
8	98	108	11	Riometry beam M0
9	109	119	11	Riometry beam M1
10	120	130	11	Riometry beam M2
11	131	141	11	Riometry beam M3
12	142	152	11	Riometry beam M4
13	153	163	11	Riometry beam M5
14	164	195	32	Riometry beam L0
15	196	206	11	Riometry beam L1
16	207	217	11	Riometry beam L2
17	218	228	11	Riometry beam L3
18	229	239	11	Riometry beam L4
19	240	250	11	Riometry beam L5
20	251	282	32	Riometry beam NCP
21	283	285	3	MAARSY
22	286	288	3	MORRO (untested)
23	289	387	99	Cas A scintillation
24	388	486	99	Psr / Sun scintillation (swapping experiment)
–	487	487	1	Correlator testing and RFI monitoring

Table K.1: Summary of beamlet allocation in experiment `kbt3a_e`. The beamlet numbers (“From” and “To”, inclusive) for each beam are shown, with the total “Number” of beamlets for each pointing direction, which is thus also the number of subbands. See also Table K.2.

Sample output

Figure K.2 shows the way that the beamlets can be assigned arbitrary channels and thus provide sparse frequency sampling to conserve processing resources. In this case, the sampling is quasi-uniform in wavelength, which results in continuous sampling at low frequencies, but sampling only every 9 subbands at the highest frequency.

```
SB11="88,103,119,132,153,174,195,216,237,258,279"

SB32="88,94,103,107,113,119,126,132,139,146,153,160,167,174,181,188,195,202,
      209,216,223,230,237,244,251,258,265,272,279,286,293,300"

SB99="114,115,115,116,117,118,119,120,121,122,123,124,125,126,127,128,129,130,
      131,132,133,134,135,136,138,139,140,141,143,144,145,147,148,149,151,152,
      154,155,157,158,160,162,163,165,167,169,170,172,174,176,178,180,182,184,
      187,189,191,193,196,198,201,203,206,209,212,215,218,221,224,227,230,234,
      237,241,244,248,252,256,261,265,270,274,279,284,289,295,300,306,312,318,
      325,332,339,346,354,362,371,380,389"

SB_MAARSY="273,274,275"

SB_MORRO="285,286,287"

SB01="195"
```

Table K.2: Sets of subbands used in KAIRA experiment `kbt3a_e`. See also Table K.1.

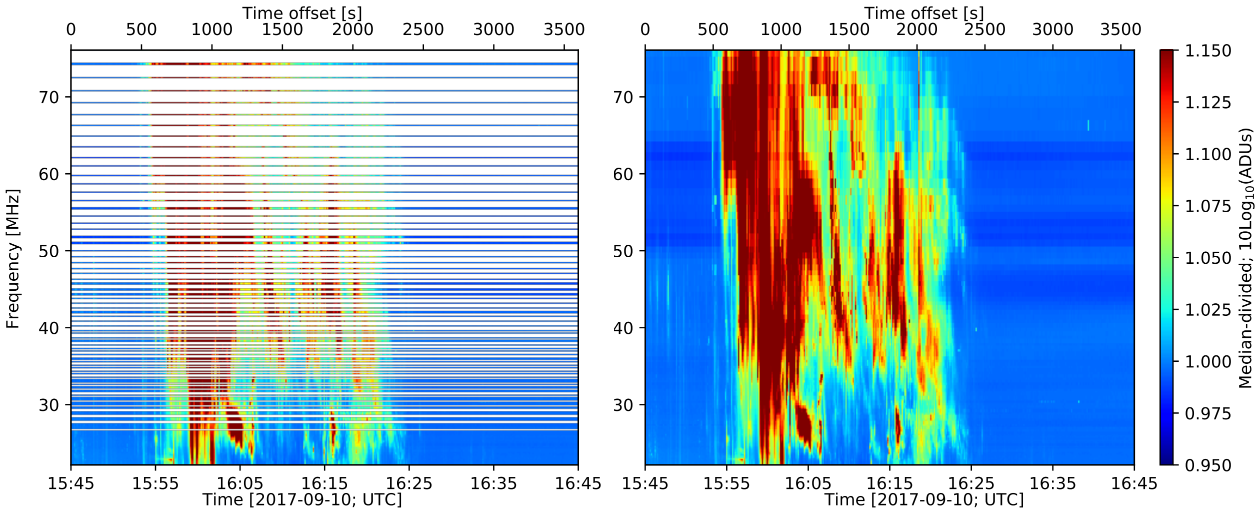

Figure K.2: Example plot of beamlet statistics, showing a Type II solar flare, measured on 10 September 2017. The plot on the left is the actual data recorded, illustrating the sparse distribution of subbands at higher frequencies. The plot on the right is the same data, but with a linear interpolation to provide continuous frequency coverage. The data for each subband are mean-divided, raw analogue-to-digital converter units (ADU), on a dB-scale.

* * *